8-2016

Pinpointing the Molecular Basis for Metal Ion Effects on Plasminogen Activator Inhibitor-1 (PAI-1)

Joel Cullen Bucci
University of Tennessee, Knoxville, jbucci@vols.utk.edu

To the Graduate Council:

I am submitting herewith a dissertation written by Joel Cullen Bucci entitled "Pinpointing the Molecular Basis for Metal Ion Effects on Plasminogen Activator Inhibitor-1 (PAI-1)." I have examined the final electronic copy of this dissertation for form and content and recommend that it be accepted in partial fulfillment of the requirements for the degree of Doctor of Philosophy, with a major in Biochemistry and Cellular and Molecular Biology.

Cynthia Peterson, Major Professor

We have read this dissertation and recommend its acceptance:

Elizabeth Howell, Engin Serpersu, Rebecca Prosser, Michael Best

Accepted for the Council:
Dixie L. Thompson

Vice Provost and Dean of the Graduate School

(Original signatures are on file with official student records.)

Pinpointing the Molecular Basis for Metal Ion Effects on Plasminogen Activator Inhibitor-1 (PAI-1)

A Dissertation Presented for the

Doctor of Philosophy

Degree

The University of Tennessee, Knoxville

Joel Cullen Bucci

August 2016

Acknowledgements

I first would like to thank my mentor, Dr. Cynthia Peterson, for her expert guidance, experience, and encouragement. I feel as though I have made significant improvements in experimental design, technical writing, and presenting of scientific data throughout my graduate career. These improvements would not have occurred without hard work and the guidance I received from Cynthia. I would also like to thank my committee members (in alphabetical order) Drs. Michael Best, Elizabeth Howell, Rebecca Prosser, and Engin Serpersu. Your expertise and advice have been integral to my project and my progression as a successful graduate student. Next, I'd like to thank all of my lab mates during my tenure in the Peterson lab. Drs. Larry Thompson and Sumit Goswami completed work that was the foundation for my research project, and helped familiarize me with basic lab techniques. I'm thankful for the help of Dr. Tihami Qureshi; the time she spent making edits to my writing or presentations, and giving advice on lab work. I had frequent, prolonged conversations with Nancy Horn and Dr. Carlee McClintock, who were so helpful in resolving technical issues I encountered in my project. I also want to thank my lab mate Letitia Puster, along with the rest of the BCMB graduate students that I began with in the Fall of 2009. We were a tight group who were happy to help out one another at every step during graduate school. Much thanks to multiple undergraduates that helped me with various aspects of my project: Caleb, Scott, Joanna, Greg, and Anna-Claire. Thank you to my collaborators Drs. Morten Beck Trelle, Thomas Jørgensen, Jenny Yang, and the American Heart Association, which partially funded my work. Finally, I would like to thank my parents John and Mary Jane, and brothers Jason, and Joseph for their overwhelming support of my professional endeavors.

Abstract

Plasminogen activator inhibitor type-1 (PAI-1) specifically inhibits the proteases tissue-type plasminogen activator (tPA) and urokinase plasminogen activator (uPA) to control the activation of fibrinolysis. Vitronectin (VN) interacts with PAI-1 primarily through the somatomedin B (SMB) domain to stabilize and localize PAI-1 to sites of injury. Our laboratory observed that transition metals ions such as copper^{2+} have VN dependent, reciprocal effects on how long PAI-1 remains active. We aim to determine the molecular basis for effects of copper^{2+} on PAI-1 activity. We employed a computational algorithm (MUG) to predict metal binding clusters, and introduced amino acid substitutions hypothesized to create metal binding deficiency. We compared variants to wild-type by: measurement of stability kinetics, thermodynamic parameters using isothermal titration calorimetry, and protein dynamics using hydrogen deuterium exchange. Active PAI-1 binds copper^{2+} in the low nanomolar range. In a variant lacking the N-terminal histidines of PAI-1, we observed reduced copper^{2+} binding, but this does not abolish accelerated transition to the latent form. PAI-1 variants lacking the carboxylate containing resides in the gate region require more copper^{2+} than wild-type to promote accelerated latency formation, making these residues candidates for further metal binding characterization. SMB-PAI-1 complex binds copper^{2+} with comparable affinity and stoichiometry as PAI-1 alone. Finally, the SMB domain stabilizes PAI-1 by localized effects on dynamics in the same regions that are affected by copper^{2+}. Thus, binding of SMB does not sterically interfere with copper binding to PAI-1, but rather negates copper^{2+} effects directly through changes in dynamics.

Table of Contents

List of Figures

Chapter 1

Chapter 2

List of Abbreviations

14-1B	Stable PAI-1 variant (N150T, K154T, 319L, M154I)
ATP7A, 7B	P-type ATPases 7A, 7B
cAMP	Cyclic AMP
CD	Circular Dichroism
CCS	Cytosolic Copper Chaperone
Ctr1,2	Transmembrane copper transporter 1, 2
DC	Direct current
ESI	Electrospray Ionization
ΔG	Gibb's free energy change
GPI	Glycophosphotidylinositol anchored
ΔH	Enthalpy change
hA	PAI-1 helix A
HDX-MS	Hydrogen Deuterium Exchange Coupled to Mass Spectrometry
HPLC	High Pressure Liquid Chromatography
IDD	Intrinsically Disordered Domain
IL-1	Interleukin-1 cytokine
IMAC	Immobilized Metal Affinity Chromatography
IR	Infrared Spectroscopy
ITC	Isothermal Titration Calorimetry
K_a	Association constant
K_d	Dissociation constant
k_{ch}	Chemical isotopic exchange rate

k_{close}	Rate of amide hydrogen in the closed state
k_{lat}	Rate of latency transition
k_{open}	Rate of amide hydrogen in the open state
MALDI	Matrix Assisted Laser Desorption Ionization
MAPK/ERK	Mitogen activated protein kinase/extracellular response kinase
MOPS	3-Morpholinopropane-1-sulfonic acid
MS	Mass Spectrometry
MUG	Multiple Geometries Algorithm
n	Stoichiometry
NF-κB	Nuclear Factor- kappa B
NMR	Nuclear Magnetic Resonance
PAI-1	Plasminogen Activator Inhibitor-1
PKA, B	Protein Kinase A, B
q_i	Reaction heat due to injection
RCL	Reactive Center Loop
RF	Radio Frequency current
s1A	PAI-1 strand 1 of beta sheet A
SAXS	Small Angle X-ray Scattering
SELEX	Systematic evolution of ligands by exponential enrichment
Serpin	Serine Protease Inhibitor
SMB	Somatomedin B domain
SPR	Surface plasmon Resonance
SOD	Superoxide Dismutase

$t_{1/2}$	Half-life of latency transition
TGF-β	Transforming growth factor beta
TNF-α	Tumor necrosis factor alpha
TOF	Time of Flight mass analyzer
tPA	Tissue type plasminogen activator
TΔS	Entropy change
uPA	Urokinase plasminogen activator
uPAR	Urokinase plasminogen activator receptor
VLDL	Very low density lipoprotein
VN	Vitronectin

Chapter 1 PAI-1, Metals, and Disease

1.1 Introduction

1.1.a. PAI-1 Biological Function

The serine protease inhibitor (serpin) superfamily of proteins functions in biological systems ranging from prokaryotic bacteria to eukaryotic human life forms. Serpins perform essential regulatory functions in a breadth of physiological processes, including control of inflammation, the circadian clock, and hemostasis [2]. Serine proteases cleave and activate each other in an incremental fashion to form intricate functional cascades. However, when protease activity lacks the appropriate regulation by a cognate serpin, disease states may arise. Plasminogen activator inhibitor type-1 (PAI-1) is a serpin that has known functions in a variety of tissues from zebrafish to humans [3]. The anti-proteolytic properties of PAI-1 are required to maintain a strict balance between coagulation, blood clot formation and breakdown, or fibrinolysis (**Figure 1.1**). The process of coagulation occurs through the proteolysis and activation of the serine protease pro-thrombin into thrombin [4]. Active thrombin converts fibrinogen into insoluble fibrin clots. Similarly, fibrinolysis is activated by serine proteases, namely the plasminogen activators including tissue type plasminogen activator (tPA) and urokinase plasminogen activator (uPA) [5]. The plasminogen activators are responsible for cleavage and subsequent conversion of dormant plasminogen into active plasmin for breakdown of insoluble fibrin clots [6]. PAI-1 inhibits the plasminogen activators to control the levels of active plasmin, and subsequent clot breakdown. In the absence of PAI-1, hyperfibrinolytic bleeding states can occur [7-9], while higher than normal levels of PAI-1 result in thrombotic states that could occlude blood vessels [10-12].

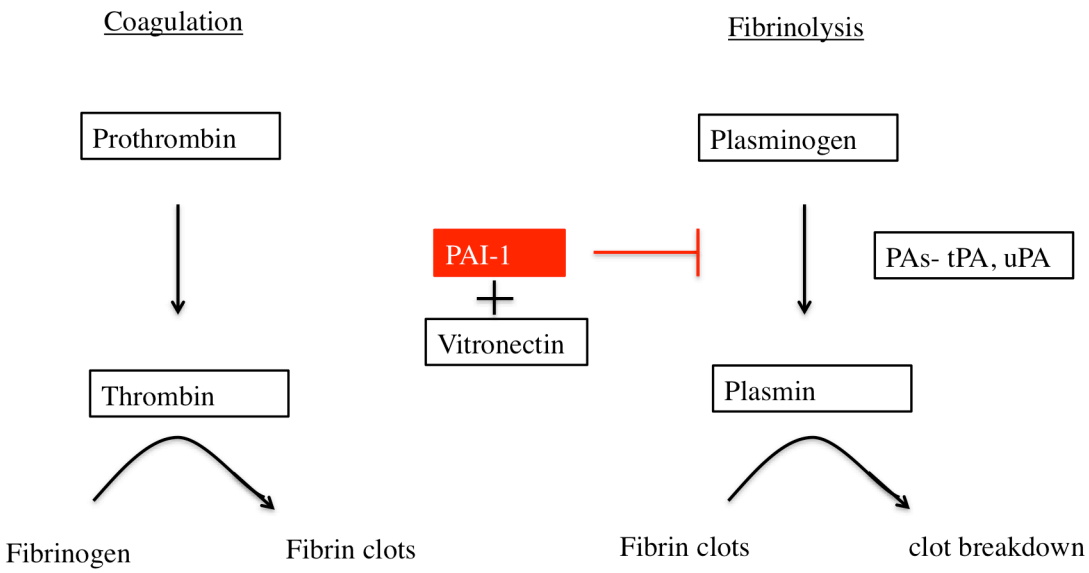

Figure 1.1 PAI-1 Regulation of Fibrinolysis. Blood clot formation and breakdown are catalyzed by cleavage mediated activation of serine proteases. In coagulation, pro-thrombin is cleaved and activated into thrombin, which is responsible for forming insoluble fibrin clots from fibrinogen. In fibrinolysis, the plasminogen activators (tPA, uPA) are responsible for cleaving and activating plasminogen to active plasmin, resulting in the breakdown of fibrin clots. PAI-1 regulates this process by inhibiting the plasminogen activators, and thus plasmin activity. PAI-1 circulates in 1:1 complex with another glycoprotein cofactor vitronectin. Vitronectin aids in stabilization and directing PAI-1 to sites of injury.

PAI-1 interacts with another circulatory glycoprotein vitronectin (VN) in the circulation, at sites of injury, and within the extracellular matrix. Circulating PAI-1 associates with VN to form a tight 1:1 complex, whereby VN associates with the fibrin matrix of the blood clot [13-15]. However, within the extracellular matrix PAI-1 and VN interact to form higher order oligomers. VN is important in localizing PAI-1 to fibrin blood clots as well as stabilizing PAI-1 in the active form, as it turns over quickly *in vivo* [16, 17]. VN is responsible for binding to the GPI-linked cell surface receptor urokinase receptor (uPAR), which cleaves uPA on the surface of migrating cells [18, 19]. VN also interacts with α-β heterodimeric cell surface integrins, namely αvβ3, αvβ5 [20, 21]. These receptors are located at focal adhesions connected to the cell cytoskeletal machinery, and through these interactions, VN binding confers coordination of cell adhesion and migration tendencies [22-24]. Interestingly, VN and PAI-1 dysregulation have been implicated in a number of overlapping disease states, such as atherosclerosis [25] and angiogenesis [26].

The imbalance of PAI-1 levels can lead to numerous complications as it is involved in several biological processes (**Figure 1.2, 1.3**). Elevated PAI-1 levels shift the balance towards coagulation and are thus pro-thrombotic; increased levels of PAI-1 are associated with greater risks to cardiovascular disease [27-30]. Atherosclerotic plaques are known to form, which hardens blood vessels to cause tissue scarring and inflammation [31]. The system is also implicated in different types of stroke, in which blood vessels are significantly obstructed (ischemic) or ruptured (hemorrhagic) and there is lack of sufficient blood flow to the brain [32]. In addition to thrombosis, PAI-1 is intimately involved in angiogenesis and vascular remodeling [33-35]. Disease to the vessel wall often involves hyperplasia or increased production of smooth muscle cells, macrophages, and endothelial cells, all of which are involved in the atherosclerotic process

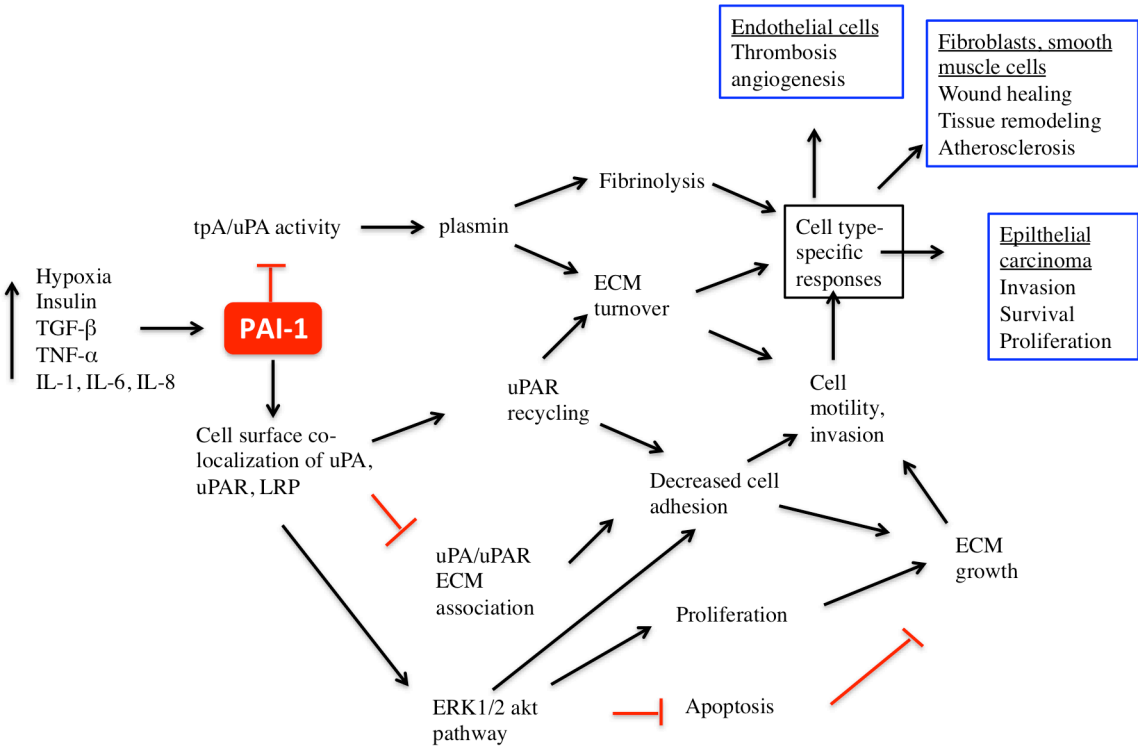

Figure 1.2 Regulatory Agents of PAI-1 Expression and the Pleotropic Physiological Effects. Several hormones, including insulin, TGF-β, TNF-α, IL-1,6,8 upregulate PAI-1 expression through binding to the regulatory sequence before the PAI-1 gene. Through the inhibition of plasminogen activators fibrinolysis and extracellular matrix turnover are regulated. PAI-1 binding to uPA can affect localization to cell surface receptors, causing changes in mobility, proliferation, and apoptosis. The downstream effects of which in endothelium cause thrombosis and angiogeneis. In fibroblasts and smooth muscle, the effects cause wound healing, tissue remodeling, and atherosclerosis. Changes in proliferation, mobility, and apoptosis in different cell types are involved in cancer. Adapted from Gramling, Church et al. Thrombosis Research. 2010

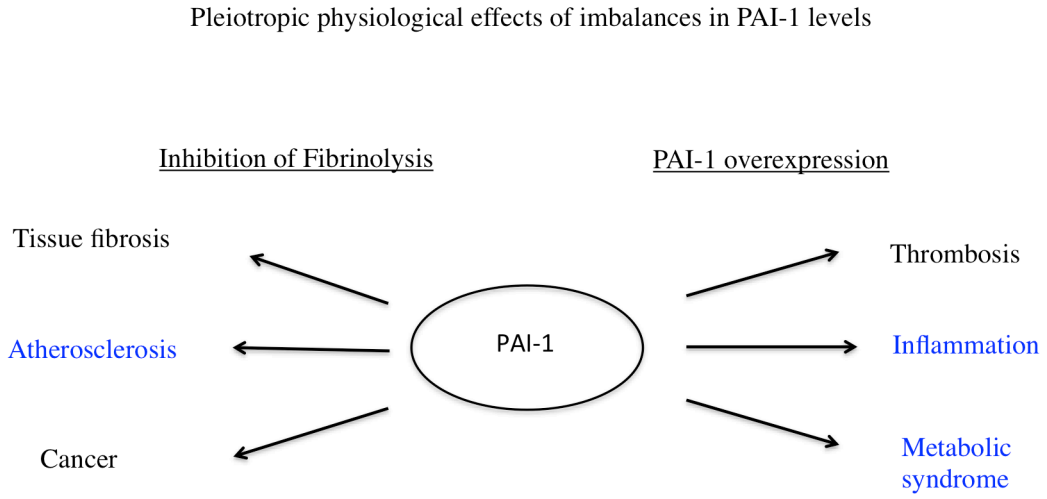

Figure 1.3 Diseases Associated with PAI-1 Imbalances. Knock-out, or inhibition of PAI-1 in vivo results in fibrosis of the heart, liver, and lungs. Also, there is increased build up of atherosclerotic plaques, leading to myocardial infarction or heart attacks. Loss of PAI-1 also leads to carcinogenic states due to the ability of PAI-1 to alter cell adhesion and migration properties, as well as PAI-1 having a role in angiogenesis. Overexpression of PAI-1 in vivo results in thrombotic states, inflammation, and metabolic syndrome. Interestingly, there is significant overlap in the disease states that also are linked to imbalances in metal ion homeostasis.

and all express PAI-1 [33]. Furthermore, PAI-1 is associated with reduced as well as enhanced cellular migration, due to pro- and anti- adhesive properties [36, 37] mediated by the extracellular matrix. The manifestation of pathophysiology in angiogenesis is the cause of metastasis of several cancers [38], including breast [39-41], lung [42], and ovarian [43], among others.

PAI-1 contributes to metabolic syndrome through expression in adipose tissue, which is typically more abundant in patients with this ailment (**Figure 1.2**). In turn, more PAI-1 is produced, causing a decreased fibrinolytic response, providing a link with its role in cardiovascular disease [44]. PAI-1 secreted from adipose tissue significantly increases blood levels that can enhance further aspects of metabolic syndrome, including hypertension, type 2 diabetes, hyperlipidemia, and obesity [45]. PAI-1 is also involved in inflammatory response, as a number of pro-inflammatory cytokines, such as tumor necrosis factor alpha (TNF-α) [46], interleukin-1 (IL-1) [47] as well as growth factors such as transforming growth factor beta (TGF-β) [48]. Interestingly, defects in the plasminogen activation system can cause several of the aforementioned disease states, but addition of PAI-1 for inhibition to mitigate issues often exacerbates their severity, commonly known as the as the "PAI-1 Paradox" [49-51]. Altogether, it is apparent that cells have established robust regulation of PAI-1 levels, which is required to maintain homeostasis in healthy individuals.

1.1.b. Control of PAI-1 Expression

The human PAI-1 gene is located on the long arm of chromosome 7, spanning approximately 12.2 kilobases (kb), containing 9 exons and 8 introns [52]. The PAI-1 gene can be transcribed into either a 2.3 kb or 3.2 kb, with the sole difference between the mRNA transcripts being the latter contains a larger 3' untranslated region, which may account for greater mRNA stability [52]. The 5' flanking region contains a TATA box, transcription initiation site, and a regulatory region that confers transcriptional responsiveness to TGF-β [53], TNF-α [46], IL-1 [47], angiotensin II, glucocorticoids, very low density lipoprotein (VLDL), glucose, insulin, and glucagon [28, 54-57] (**Figure 1.2**). Glucagon or cAMP activate liver PAI-1 expression through the protein kinase A (PKA) pathway, while glucocorticoids bind directly to response elements in the flanking region [58]. Glucose activates liver PAI-1 expression through increases in nuclear factor kappa B (NF-κB) and IL-1 [58]. Insulin and TGF-β binding to their respective liver cell surface receptors activate PAI-1 expression through the mitogen activated protein kinase/extracellular response kinase (MAPK/ERK) pathway [58]. These key elements link the expression of PAI-1 to metabolic and inflammatory disorders [58]. Additionally, several microRNAs can bind to the non-coding PAI-1 mRNA sequence to regulate transcription in a tissue specific manner [59]. The 4G/5G polymorphism in the regulatory region 675 base pairs from the start site is located in an important transcription factor binding site [60]. The allele containing 4 guanines results in increased PAI-1 expression, while a PAI-1 allele with 5 guanines is down regulated. This results in higher PAI-1 levels in the 4G allele and higher risk for thrombotic events in a variety of tissues and organs [60]. There are no observable developmental disorders as a result of PAI-1 gene deletion, apart from mild bleeding states individuals develop normally [7].

PAI-1 is expressed as a 45 kilodalton (kDa) protein sequence consisting of 402 total amino acids residues, including the signal peptide at the N-terminus. (MQMSPALTCLVLGLALVFGEGSA). Because the signal endopeptidase is able to cleave at two separate sites, the N-terminus of PAI-1 can start as VHHPPSY or SAVHHPPSY and contain either 379 or 381 residues, respectively (The former version and all numbering will be henceforth used through out this document). Unlike many other serpins, PAI-1 is an acute response protein circulating at relatively low concentrations (5-20 ng/mL), with a fast turnover rate in blood [61]. PAI-1 is expressed by liver hepatocytes, endothelial cells, epithelial cells, adipocytes, megakaryocytes, fibroblasts, and smooth muscle cells [62]. Despite stringent regulation of PAI-1 expression, there is further regulation subjected to PAI-1 at the protein level, particularly the amount of available active fraction in circulation.

1.1.c. PAI-1 Inhibitory Function

Serine proteases perform necessary biological functions through highly specific cleavage of peptide bonds for digestion, protein turnover, or, as in the case of tPA or uPA, activation to perform a function. Peptide bonds can be broken in a thermodynamically favorable hydrolysis reaction, although they are kinetically trapped in bonded form with planar, double-bond like character. Serine proteases employ an active site triad consisting of a serine, histidine, and aspartate residues to perform the acid-base catalyzed reaction. The histidine acts as a base, accepting a hydrogen ion from the serine hydroxyl group, forming a potent alkoxide nucleophile. The negatively charged aspartate interacts with the histidine to aid in orientation and stabilization throughout the reaction. The alkoxide performs nucleophilic attack on the carbonyl α carbon, forming an unstable tetrahedral intermediate that is then stabilized by the oxyanion hole. The

histidine donates a hydrogen ion to the peptide bond nitrogen, resulting in collapse of the intermediate, peptide bond cleavage, release of the N-terminal portion of the peptide, and an acyl enzyme intermediate. In the second step, water acts as a nucleophile to repeat the process, forming a tetrahedral intermediate, which collapses into a carboxylic acid as the C-terminal half of the peptide is released, regenerating the active site serine for future reactions.

PAI-1 utilizes a canonical serpin suicide inhibitory mechanism that parallels the proteolytic reaction until the final inhibitory step: E + I <-> EI* <-> EI <-> E~I -> E-I [63] (**Figure 1.4**). PAI-1 has a solvent exposed loop termed the reactive center loop (RCL) that contains the arginine-methionine scissile bond, which is also located on the natural substrate of tPA, plasminogen. Initially, PAI-1 uses proximal RCL loop residues to engage in non-covalent interaction with the exosite residues of tPA, in a non-covalent Michaelis complex (EI*). This Michaelis complex structure has been determined by x-ray crystallography with PAI-1 bound to either uPA or tPA, with each active site serine mutated to alanine to prevent the mechanism from progressing further [64, 65]. Formation of Michaelis complex is followed by nucleophilic attack of the PAI-1 scissile bond carbonyl to form the loop-bound acyl-enzyme complex (EI) [66], followed by release of the C-terminal half of the loop forming the loop-displaced acyl-enzyme (E~I). In the final inhibitory step, the N-terminal acyl bound half of the loop inserts into the central beta sheet of the protein body, translocating the protease with a distorted active site approximately 70Å to the opposite pole of the inhibitor [67]. The PAI-1-protease complex remains quite stable, due to a negligible rate of deacylation of the bond that joins them (E-I) [67]. However, if loop insertion is delayed, deacylation will occur, and results in release of the intact serine protease, leaving a cleaved or "substrate-like" PAI-1 form [68].

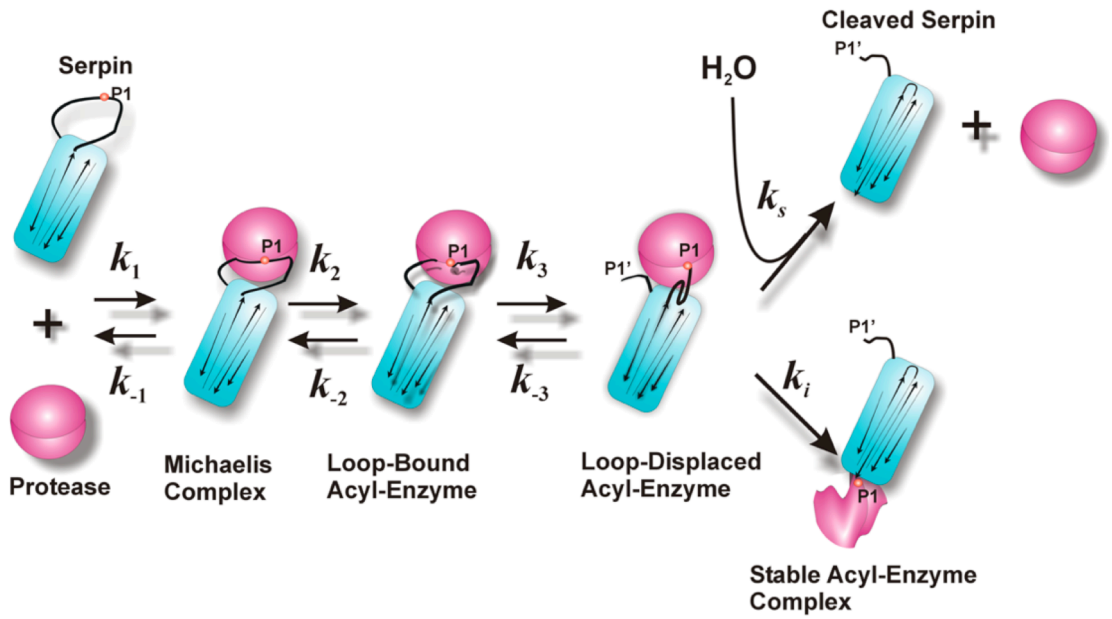

Figure 1.4 Serpin Mechanism. Serpins are folded around a core β-sheet from which protrudes a surface-exposed loop (the reactive- center loop or RCL). Within this loop region are the residues recognized as substrates by the target protease (uPA or tPA), with the reactive center peptide bond denoted P1-P1'. Initial binding of the protease to the target site in the RCL forms a noncovalent Michaelis complex. Upon attack by the protease, this P1-P1' peptide bond is cleaved by nucleophilic attack of the active-site serine, and an acyl-intermediate is formed. In contrast to the normal progression of proteolysis, this acyl-intermediate is extremely long-lived due to a negligible rate of deacylation. Structural rearrangements occur so that the two ends of the cleaved loop separate, and the P1 end is inserted into the central β-sheet, with the covalently coupled protease transferred to the opposite "pole" of the serpin.

PAI-1 is a fast acting inhibitor that has a reaction rate constant (3.5×10^7 $M^{-1}S^{-1}$) approaching the diffusion limit [69]. Approach to equilibrium kinetics has determined the interaction rates of PAI-1 with tPA or uPA at each step of the inhibition mechanism [70]. The rate of Michaelis complex formation is fast, so the overall inhibition rate is limited by the rates of the subsequent steps [69-71]. These rates can vary depending on the protease, presence of VN, as well as the presence of amino acid substitutions [71-73] [74] [75]. If the limiting rates are faster than the inhibitory rates, then PAI-1 will exhibit "substrate-like" behavior (**Figure 1.5**) [68]. Native PAI-1 inhibits two-chain tPA with the highest rate constant, followed by uPA, and single chain tPA [71]. Binding of VN slows the overall rate of inhibition by stabilizing the loop displaced acyl enzyme [71], just before the peptide insertion and destruction of the protease active site occurs.

1.1.d. PAI-1 Structure/Latency Conversion

Interestingly, PAI-1 is relatively unique in the serpin protein family in that it has a tendency to spontaneously insert into the protein body, due to its metastable fold in the active conformation [76]. Despite serpins having rather low sequence homology, they fold into highly similar tertiary structures [77]. This fold consists of nine α-helices, and sixteen total β-strands that are organized into three β-sheets (**Figure 1.6**). The secondary structural features of PAI-1 will be referred to as helices hA-hI, and numbered strands of each sheet A-C (ie. s1A). The properly folded active form of PAI-1 is a flexible, kinetically trapped intermediate, which readily relaxes into a rigid, compact fold of lowest thermodynamic energy [78]. This folding process involves RCL peptide insertion into the protein body, the loop is no longer solvent accessible, and thus unavailable for interaction with target proteases, and this conformation is called the latent conformational state (**Figure 1.7**) [1]. PAI-1 is by far the most labile of all serpins, with the conformational shift to the latent form

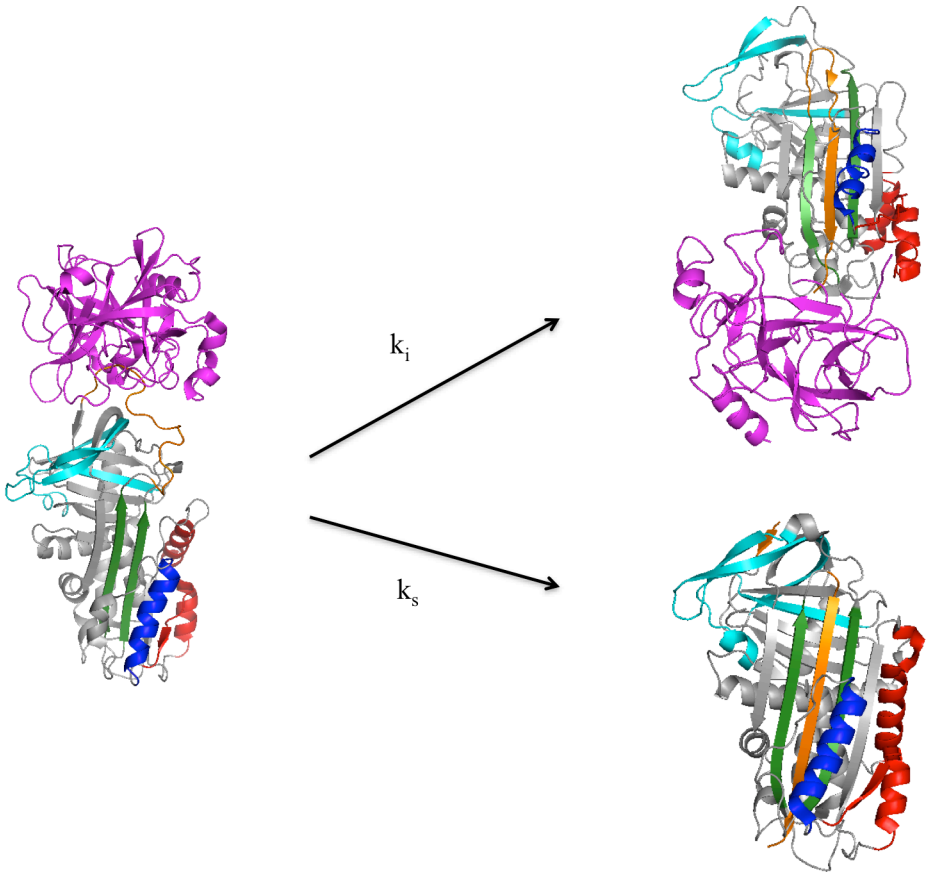

Figure 1.5 Structures of PAI-1-S195A tPA Michaelis Complex, Protease-Serpin Complex, and Cleaved PAI-1. PAI-1 and tPA initially interact in a michaelis complex (pdb 5BRR) in which the loop makes non-covalent interactions with the protease (magenta) exosite residues. In the final inhibitory step, the N-terminal half of the RCL (orange) of PAI-1 inserts into the protein body at a rate of k_{lim} which can be influenced by the presence of cofactors, mutations, pH, temperature, as well as other factors. Full peptide insertion results in a stable protease-serpin complex (top right, protease in magenta). PAI-1-tPA complex has not been solved, so α-1-proteinase inhibitor in complex with elastase is shown (pdb 2D26). If the rate of peptide insertion is too slow, the intact protease can be released post RCL cleavage. This is termed the cleaved or substrate like PAI-1 (bottom right pdb 9PAI).

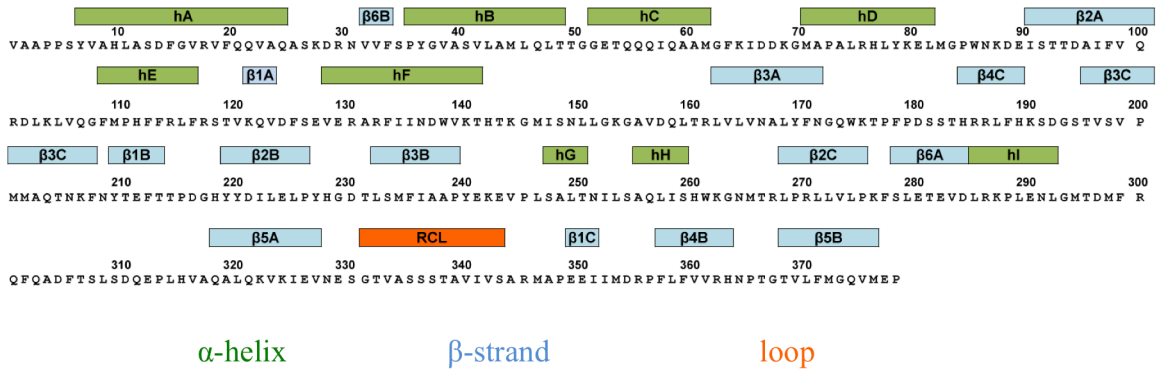

Figure 1.6 PAI-1 Primary Sequence and Secondary Structure. PAI-1 is composed to 379 or 381 amino acids, depending on the cleavage of the signal peptide by the signal peptide peptidase. PAI-1 is composed of nine α-helices (shown in green), three β-sheets (shown in blue), and the inhibitory RCL loop (shown in orange). The nomenclature of PAI-1 secondary structure: helicies A to I are named hA to hI; the strands are classified into three sheets A-C, and named in order of the sequence by number (ie. s1A is strand 1 of sheet A).

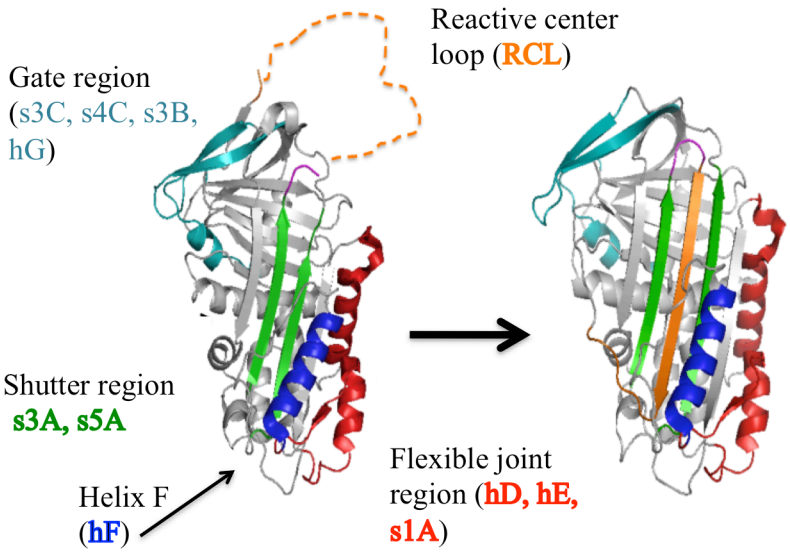

Figure 1.7: The Active and Latent Conformations of PAI-1. The crystal structures of active PAI-1 (pdb code 3Q02, left) and latent PAI-1 (pdb code 1DVN, right) are shown. The RCL (orange) is the contains the same scissile bond proteases target, but it spontaneously inserts into the central β-sheet A strands 3 and 5, converting PAI-1 to an inactive, or latent conformation. Multiple steps during the latency transition process have been proposed, including local unfolding of the hydrophobic core. The shutter region strands 3 and 5 (green) open up, as well as the gate region loops (teal) for RCL insertion to occur during the latency conversion process. Helix F (blue) and the underlying shutter region may be transiently rearranged to allow for the RCL to fully insert in the shutter. The flexible joint region (red), contains the binding interface of the SMB domain of VN, as well as other important protein - protein interactions. As a point of reference, the "top" of PAI-1 will be described as the pole that contains the RCL, and the "front" of PAI-1 will be described as the side that central β-sheet A faces. PAI-1 helices A-I are abbreviated as hA-hI, and β strands are abbreviated as follows: strand 1 of sheet A is written as s1A.

occurring over a half-life of 1-2 hours [79]. Antithrombin and neuroserpin also undergo latency conversion, although over a much longer timespan [80, 81].

Although structural information is available for the active and latent forms of PAI-1, the mechanism of how this conformational change occurs is not completely understood. There appears to be concerted movement that involves communication between many important regions of PAI-1, named after their involvement in PAI-1 inhibition and/or latency conversion. At an absolute minimum the gate region (s3C, s4C, s3B, hG) of strands of PAI-1 must open up to allow for the uncleaved RCL to pass through [82]. Directly C-terminal of the loop, strand s1C becomes unstructured and detached to facilitate this task [83]. Opening of the shutter region (s3A, s5A) strands occurs next to accommodate loop insertion, forming a sixth beta strand in in the central beta sheet A [1]. For complete insertion, hF, which sterically blocks the lower part of the shutter, must be transiently displaced [84]. The flexible joint region (hD, hE, s1A) is an important region for protein-protein interactions that have an effect on the stability and inhibitory function of PAI-1 [71]. Additionally, the underlying shutter region and other areas of the hydrophobic core have been identified to undergo transient unfolding events that are consistent with the timescale of latency conversion [85]. Calorimetric studies monitoring the latency conversion show no detectable changes in enthalpy, indicating that the process is largely entropically driven [86]. Since the major difference between the fast acting inhibitory mechanism and relatively slower latency conversion is the lack of RCL cleavage, passage of the RCL through the gate region is regarded as the rate-limiting step in the process [87]. The latency conversion process is irreversible under physiological conditions; reversing the process requires the presence of denaturants or negatively charged phospholipids [88]. Latent PAI-1 in platelets is suggested to be in a “pro-form” that is

activated by the significant amount of negative phospholipids on the outside of platelets [89], but this method of activation has yet to be confirmed.

1.1.e. Factors Influencing PAI-1 Latency Conversion

Why PAI-1 may have evolved a regulatory mechanism to inactivate itself has remained elusive to investigators of the field. Many intrinsic factors contribute to how long PAI-1 remains active before converting to the latent form. Directed evolution studies comparing PAI-1 to other serpin protein sequences indicate that the metastability of PAI-1 is the result of positive evolutionary selection [87, 90]. Mutating a PAI-1 amino acid residue to the consensus identity at that position in most serpins typically results in significantly stabilizing the variant PAI-1 compared with wtPAI-1 [87]. PAI-1 in the active form is highly dynamic as evidenced by hydrogen deuterium exchange (HDX) experiments, and this is thought to play a key role in the latency transition process [91]. Environmental pH has an effect on how long PAI-1 remains active, as PAI-1 is increasingly more stable in the active form as pH drops from the physiological range to pH 5 [92]. This effect has been pinpointed to the stabilizing interactions that PAI-1 histidines make in the protonated state [92]. Additionally, the basic residues in the s3C/s4C loop are proposed to stabilize the active form, because mutation to acidic residues in those positions accelerates latency transition [93]. Further, introducing double cysteine mutations to cross-link areas that must be mobile to allow for the latency transition, such as the hinges of the RCL, significantly delayed latency transition [94]. It should be noted that many of the mutations also alter the thermodynamics of protein folding, as determined from chemical denaturation experiments [95]. For example, the 14-1B PAI-1 quadruple variant (N150H, K154T, Q319L, M154I) creates a hydrogen bonding network at the hF-s3A loop-shutter and s1C-gate region

interactions extends the half-life of PAI-1 to approximately 145 hours [96]. This also results in altered protein folding thermodynamics, in which 14-1B has a significantly higher melting temperature compared with wild-type PAI-1 [95]. However, a recent crystal structure of active PAI-1 containing only one mutation in the N-terminal hinge prior to the RCL (W175F) retains wild-type like thermodynamics of protein folding [95]. This currently represents our most accurate structural model for active PAI-1.

The metastable structure and overall stability of PAI-1 is influenced by ligand binding. A cofactor glycoprotein, VN, binds PAI-1 with high affinity (K_d ~0.1nM); this interaction is required to direct circulating PAI-1 to blood clots for thrombolysis [16]. VN binding to PAI-1 results in a delay in latency transition, which increases the half-life by ~1.5 fold. [79]. VN has an N-terminal somatomedin B domain (SMB) responsible for the primary high-affinity interaction with PAI-1 (**Figure 1.8**) [97]. Interaction of SMB with PAI-1 has been investigated through mutagenesis (**Figure 1.9**), x-ray crystallography, and NMR, determining that SMB binds through the flexible joint region residues R103, M112, and Q125 [97]. The primary interactions responsible for stabilization observed when VN is bound to PAI-1 have been pinpointed to the SMB-PAI-1 interaction [97, 98]. The SMB is flanked in primary sequence by a region that is predicted to be intrinsically disordered (IDD), and central and C-terminal domains that are hemopexin-like and have predicted beta-propeller structure [99]. Interestingly, VN is still able to bind PAI-1 even when the SMB domain is removed, albeit at a lower affinity (Kd ~ 50nM), indicating that the interaction includes regions of VN other than the SMB domain [98, 100]. Mutagenesis studies mapped the lower affinity interaction the more distal regions of helices D and E of PAI-1 [98].

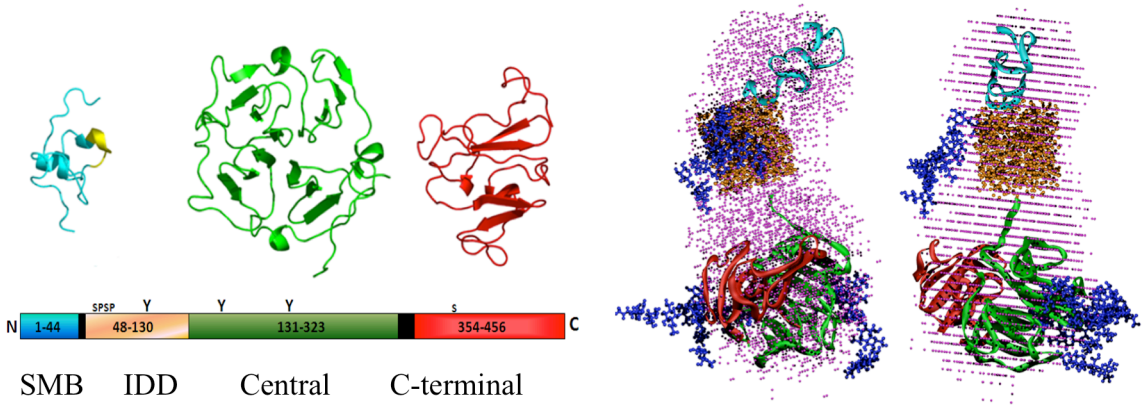

Figure 1.8 Vitronectin Domains, Structural Model. VN is composed of four domains, the SMB domain, which is the primary binding interface with PAI-1, the intrinsically disordered domain, containing the integrin binding sequence, the central domain, and C-terminal domain. The IDD region has prevented crystallization of VN, but our lab has produced a model of VN structure. The SMB has been crystallized, and the central/C-terminal domains homology modeled to similar proteins. A combination of small angle X-ray scattering and computational modeling of the domains determined the overall shape, which is peanut-like. Data from Zhou et al., Nat Struc Bio, 2003 ; Peterson lab, JBC, 2004; Proteins, 2001; Biochemistry, 2005.

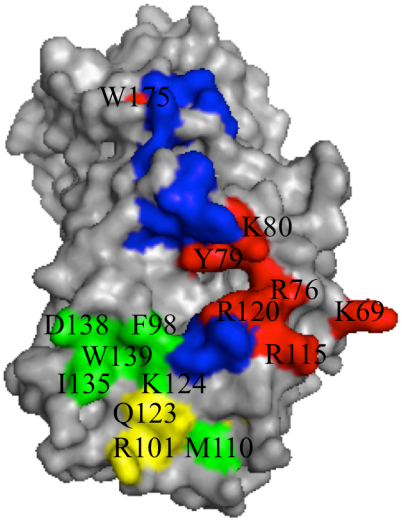

Figure 1.9 PAI-1/VN Interaction Interface. The interaction of PAI-1 and VN was investigated by surface plasmon resonance (SPR) and site directed mutagenesis. The SMB domain, full length VN and a VN deletion variant lacking the SMB domain (ΔSMB VN) were tested against a battery of PAI-1 variant for binding. The effects of VN binding to these constructs were mapped on the PAI-1 structure (3q02). The residues in red were those that only influenced binding to ΔSMB VN, the residues in green are important for SMB binding, and the residues in yellow were important for all VN proteins tested. The residues in blue were tested by had no effect on the VN proteins tested.

Using a combination of SAXS, NMR and crystallography on SMB [101], and molecular modeling [99], a structural model for VN has been proposed by our lab [102].

PAI-1 binding of RNA aptamers, glycans, and antibodies in different areas of PAI-1 have produced significant effects on latency transition. SELEX library generation of high-affinity RNA aptamers identified two aptamers that can significantly stabilize PAI-1 in the active form (**Figure 1.10**) [103]. Human PAI-1 is a glycoprotein that can be post-translationally modified by N-linked glycosylation at three residues (N209, N265, N309) (**Figure 1.11**) [104]. Purified plasma PAI-1 is only modified at residues 209 and 265, the latter modification protects a hydrophobic cleft at s1C, resulting in stabilization in the active form [83, 104, 105]. Otherwise, PAI-1 expressed in bacteria that lacks these modifications has the same biochemical properties as plasma purified protein fraction [104]. There are examples of PAI-1 monocolonal antibodies in which binding either delays or facilitates latency conversion. Antibodies have been particularly useful in identifying different conformational states of PAI-1. Several antibodies (Mab-2,6, 55F4C12, 33H1F7) have binding epitopes located on hF or the loop to S3A, and disrupt hF translocation to form a substrate-like or cleaved form of PAI-1. Similarly, Mab-8H9D4 blocks the active site distortion of the target protease by binding to the shutter region, rendering PAI-1 in the substrate-like form. Mab-1 binds to hC and is stabilizing, whereas a H4B3 epitope is in the gate region and destabilizes, likely due to favoring the formation of a pre-latent state [83, 106]. The predicted pre-latent state resembles a partial insertion of the N-terminal part of the RCL into beta-sheet A, and partial detachment of s1C, much like a pre-latent state in another serpin, alpha-1-antichymotrypsin [107]. Another antibody Mab-33B8 binds at the pre-inserted N-terminal hinge and hD to accelerate latency

paionap-5 GGGGCCACCAACGACAUU**GAACCACGUAGGCUCGUUUCUGAGCCGAUCUCGAU**GUUGAUAUAAAUAGUGCCCAUGGAUC
paionap-40 GGGGCCACCAACGACAUUU**AUCGAAUUGAUAACCUUACGCGAGAGCGUAGUUC**GUUGAUAUAAAUAGUGCCCAUGGAUC

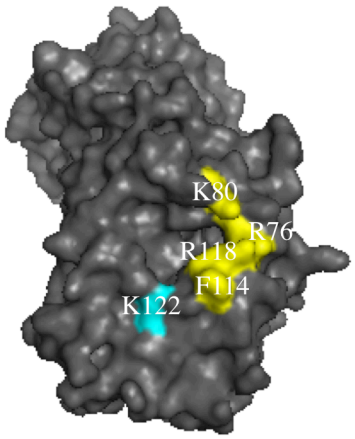

Figure 1.10 RNA Aptamer Binding to PAI-1. The nucleotide sequences of paionap-5 and paionap-40 are shown (top) with regions of variable sequence bolded. A gel shift assay was used to monitor PAI-1 RNA-aptamer binding in the nanomolar range. The migration of the nucleotides are reduced due to protein binding, separating free aptamer from complex in the experiment (bottom left). Site directed mutagenesis was used to identify important residues in aptamer binding on PAI-1 (bottom right). The residues shown in red are implicated for their importance to binding both aptamers, while K122 in pink is only important in binding paionap-40. Adapted figure from Madsen et. Al. Biochemistry, 2010.

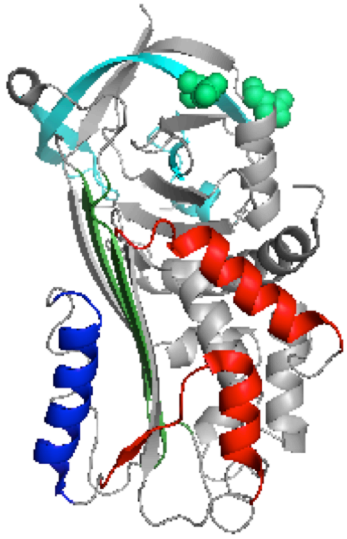

Figure 1.11 Functional Glycosylation Sites of PAI-1. PAI-1 has three potential glycosylation sites for N-linked glycosylation: N209, N261, and N309. However, only N209 and N261 are glycosylated in PAI-1 isolated from plasma samples. The glycosylation sites are shown in green space filling spheres on the active PAI-1 structure (pdb 3q02). PAI-1 is stabilized by glycosylation, particularly at N265 due to protection of a hydrophobic cleft at s1C.

conversion. Finally, the initial Michaelis complex formation with tPA can be inhibited through a variety of antibodies that have varying binding epitopes in the gate region and some partial overlap with the RCL [83] [108].

1.1.f. Copper^{2+} Effects on PAI-1

Our lab has recently uncovered an interesting and unusual effect of transition metal ions on PAI-1 stability, which is dependent on the presence or absence of VN [79]. Physiologically relevant metals such as calcium^{2+}, magnesium^{2+}, and manganese^{2+} confer a modest stabilizing effect on PAI-1 in the presence as well as the absence of VN. VN stabilizes PAI-1 modestly ($t_{1/2}$ ~ 1.5 hours with VN; $t_{1/2}$ ~ 1 hour alone) [79]. However, in the presence of different transition metals such as nickel^{2+}, copper^{2+}, and cobalt^{2+}, PAI-1 is significantly destabilized ($t_{1/2}$ ~10 minutes) [79]. PAI-1 bound to any of these three transition metal ions along with VN is significantly stabilized ($t_{1/2}$ ~ 3 hours with Cu^{2+}), representing a longer half-life than observed upon binding of VN alone [79]. Competition experiments determined that transition metal ion binding occurs at the same site(s) in PAI-1 [109]. Furthermore, metal ions bind to the active form and the latent form, albeit with a weaker affinity for latent PAI-1 [109]. Monitoring intrinsic tryptophan fluorescence of PAI-1 in the presence of metal ions using approach-to-equilibrium kinetics yielded a triple exponential. The first exponential is concentration dependent and likely the binding event, a second exponential captures a currently uncharacterized conformational change, and the third exponential occurs with kinetics close to the timescale of latency transition [109]. The copper ion binding affinity to PAI-1 determined from the binding exponential (K_d ~ 90nM) is well within physiologically relevant range, considering the micromolar copper^{2+} concentrations of liver and brain [109-114].

1.1.g. Eukaryotic Copper Ion Metabolism/Physiology

Copper ions are an essential cofactor for enzymes and are required for proper physiological function, but levels must be intricately controlled to prevent toxic effects. The use of copper^{2+} as a cofactor originated 2.7 billion years ago, as photosynthetic cyanobacteria mass-produced atmospheric oxygen, leading to the oxidation of iron to Fe^{2+} to Fe^{3+}. This subsequently lead to less soluble iron, and organisms adapted by using copper^{2+}, which was best suited for red-ox reactions in the new atmosphere [115] [116] [117]. Copper ions are found in $^{1+}$ and $^{2+}$ oxidation states, and in excess amounts this presents the opportunity for oxidative damage. Compounds such as ascorbic acid or glutathione are able to reduce copper^{1+} to copper^{2+} if the coordination has a negative reduction potential [117]. Subsequent re-oxdiation by O_2 or H_2O_2 results in the generation of hydroxyl radicals, which are highly reactive and damaging to a variety of biomolecules, such as creating DNA strand breaks or peroxidation of lipids [117]. Copper toxicity has been strongly linked with many overlapping disease states as PAI-1, such as angiogenesis, cancer, cardiovascular disease, and diabetes (**Figure 1.3**). The chelation of copper ions has resulted in the suppression of several pro-angiogenic cytokines and growth factors that are required for early tumor growth [118]. The localization of physiological copper ions during angiogenesis has been monitored by X-ray fluorescence [119]. Copper ions are subjected to large scale reorganization which is strictly controlled during angiogenesis [120]. Copper is found in atherosclerotic plaques, and is known to interfere with platelet endothelium interaction, and cause vascular leakages [121]. The levels of plasma copper transporting ceruloplasmin are significantly increased in individuals with type 1 and 2 diabetes [122]. Cellular and extracellular copper trafficking is only partially understood at the molecular level.

Copper is ingested through the diet and initially stored in the liver, entering hepatocytes via the high affinity transmembrane protein human copper transporter-1 hCtr1 (**Figure 1.12**) [123]. Virtually all intracellular copper ions are bound to a copper ion chaperone or transporter until trafficked to a destination, like the CuA/CuB clusters of the mitochondrial electron transport chain, for example [124]. Intracellular copper ion homeostasis is not completely understood, but an emerging hypothesis is "one transporter for each destination" [125]. Copper ion transporters include superoxide dismutase (SOD), the cytosolic copper chaperones CCS and atox1, and copper transporter 2 (Ctr2) [125]. Copper ions can be shuttled to the golgi network, whereby they can be internalized via the Menke's disease p-type ATPase ATP7A for distribution to several cupro-proteins [126]. Likewise, another p-type Wilson's disease ATPase ATP7B controls copper distribution in and out of tissues, also using the golgi network [127]. Copper ions are either distributed to ceruloplasmin destined for the serum, or excreted when levels are too high [128]. Polymorphisms to these two p-type ATPases results in widespread imbalances in copper ion levels across all tissues, leading to the aforementioned disease states [126, 127]. Wilson's disease is an autosomal recessive disorder that is characterized by an extreme excess of $copper^{2+}$ within brain and liver tissue[127]. Approximately 1 in 100 people are carriers for the disease, and two carriers have a high chance of producing offspring with the disease [127]. Symptoms of the disease include various liver diseases, neuropsychiatric problems such as dementia, depression, loss of cognitive abilities, seizures, and migraines [127]. Patients with the x-linked Menkes's disease have an even worse fate, including sparse, wooly hair, nervous system breakdown, defects in growth development, and often death by age 3 [128]. In this case, many proteins in many tissues lack the

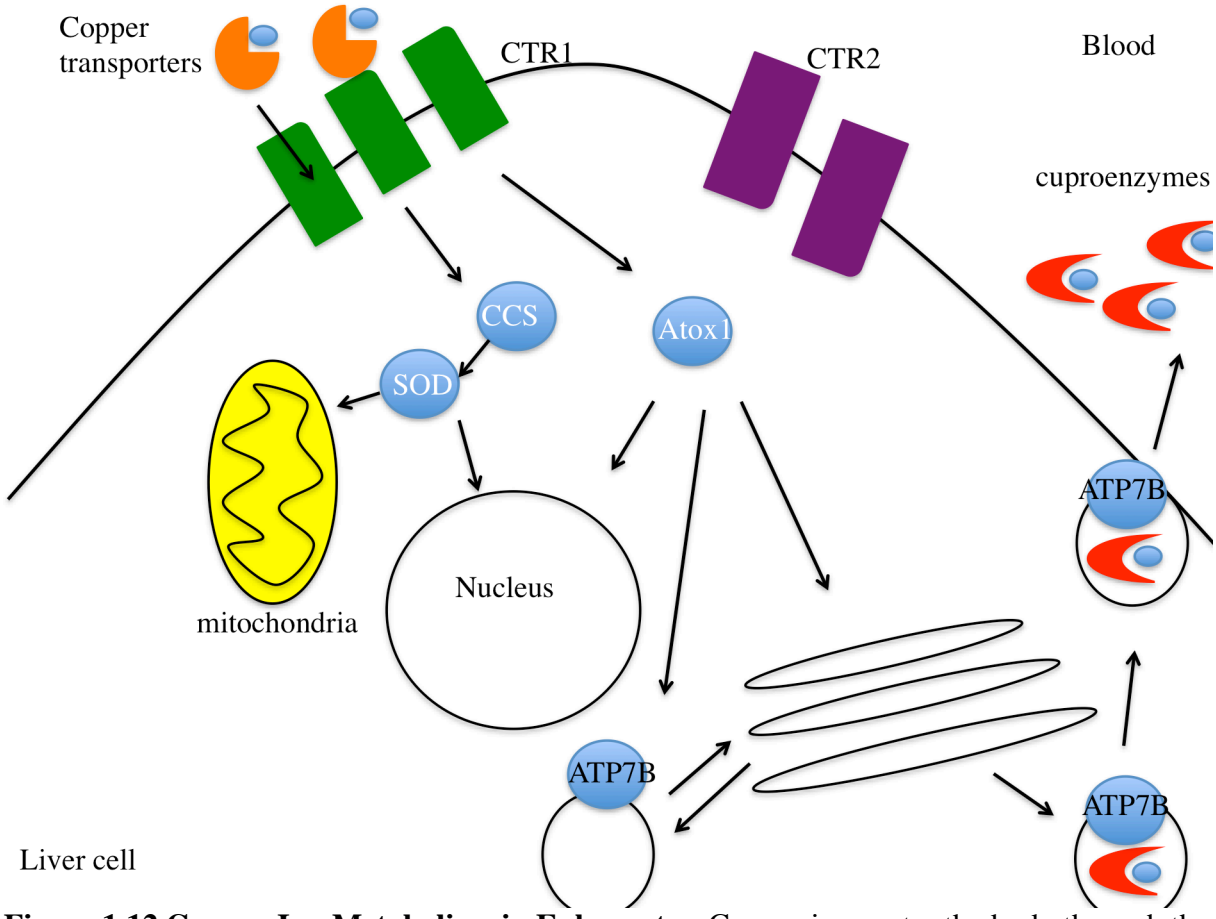

Figure 1.12 Copper Ion Metabolism in Eukaryotes. Copper ions enter the body through the diet, and initially enters a hepatocyte cell in the liver. Copper ions are bound to transfer or carrier proteins within a cell to prevent causing harmful side reactions that could cause formation of reactive oxygen species. Copper reaches its destination through a specific transporter, or is sent in a vesicle to ceruloplasmin for distribution throughout the body.

delivery of required copper ions to function properly [128]. Taken as a whole, copper ion binding could be one of many regulating physiological factors on PAI-1.

1.1.h. Metalloprotein Interactions

Copper ions are considered soft acids and thus require coordination through soft ligands; sulfur and nitrogen containing cysteine, histidine, and methionine residues tend to dominate coordination centers of cuproproteins [129]. $Copper^{1+}$ prefers binding strongly to the anionic thiolate group of cysteine and somewhat weaker to the thioether group of methionine [129]. $Copper^{2+}$ preferentially binds to the deprotonated nitrogen in the imidazole of neutral histidine at physiological pH [129]. Given their differences in d-orbital valence electrons, $Copper^{1+}$ and $^{2+}$ also differ in their coordination geometries. $Copper^{1+}$ is most often found in linear, trigonal planar, or octahedral coordination geometry, while $copper^{2+}$ usually coordinates in tetrahedral, square planar, or square pyramidal forms [117]. The red-ox active proteins that interconvert $copper^{1+}$ and $^{2+}$ most often bind copper ions in tetrahedral coordination geometry [117].

Several coordination centers have been determined through a variety of techniques. The $copper^{1+}$ binding ATPase family of proteins uses linear binding using two cysteine residues, while many chaperones coordinate through trigonal planar geometry with two cysteines and a histidine. Superoxide dismutase uses tetrahedral binding geometry with four histidines to coordinate and transport $copper^{2+}$ to the mitochondria (**Figure 1.13**) [130]. Likewise, Plastocyanin and umecyanin are photosynthetic electron transport proteins that use tetrahedral $copper^{2+}$ binding; both using two histidines, a cysteine, with the fourth ligand in each being methionine in the former [131], a carboxylate containing residue in the latter [132]. Within the circulation and extracellular matrix, the physiologically relevant oxidation state of copper is $^{2+}$ [129], which is complementary to the

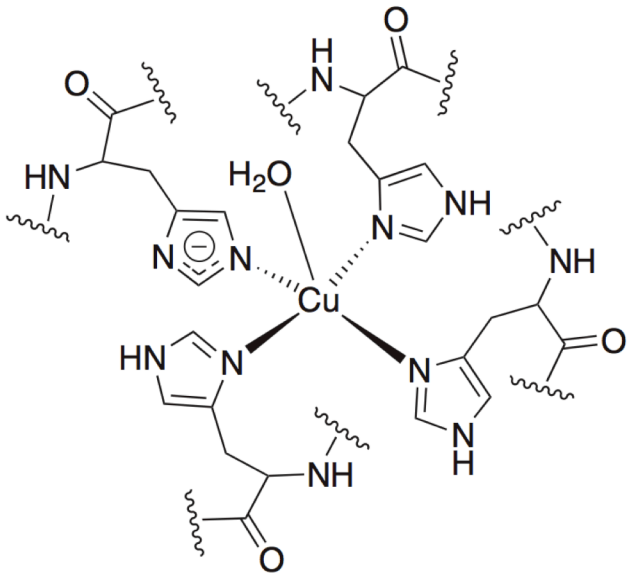

Superoxide Distmutase copper^{2+} binding motif
(tetrahedral, 4x His)

Figure 1.13 Copper^{2+} Coordination by Superoxide Dismutase. Superoxide dismutase coordinates copper^{2+} by using four tetrahedral histidine ligands and water. Illustration based on crystal structure of copper^{2+} bound superoxide dismutase (pdb 4BCY).

lack of cysteine residues within PAI-1. Several additional binding geometries have been proposed that are relevant for PAI-1, including a two histidine motif possibly including water or another anion, and a two histidine, two amide backbone coordination (**Figure 1.14**) [129]

1.2 Rationale for Study and Organization of Dissertation

In this dissertation work, we further probe the observations in which transition metal ions incur an interesting and unusual regulatory effect on PAI-1, which is dependent on the presence of the cofactor VN. There are unquestioned parallels between the dysregulation of PAI-1 and copper ion levels and the disease states that arise. A physiological relevance of the interaction between $copper^{2+}$ and PAI-1 is apparent from the strength of their interactions, their relative concentrations, and their particular localization *in vivo*. In order to understand the molecular basis for metal ion effects on PAI-1, we must identify the metal ion binding site or sites. To this end, we are unable to use several traditional structural methods such as X-ray crystallography due to the fast timescale by which copper promotes latency conversion. Alternatively, we have opted to use kinetic, thermodynamic, and isotopic exchange measurements to answer several key questions regarding $copper^{2+}$-PAI-1-VN interactions. Where is $copper^{2+}$ binding on PAI-1? How does $copper^{2+}$ binding promote the latency transition? Are the $copper^{2+}$ effects mediated directly through PAI-1 or through interactions that involve VN? How does PAI-1 ligand binding influence protein dynamics? Does PAI-1 protein dynamics play a role in the latency conversion process? This work aims to address these questions to explain the molecular basis of $copper^{2+}$ binding on PAI-1 function. This work sheds significant light on PAI-1 metal ion interaction, but also aims to investigate the role of protein dynamics in the latency conversion process, which is yet to be completely understood.

Theoretical copper coordination chemistries

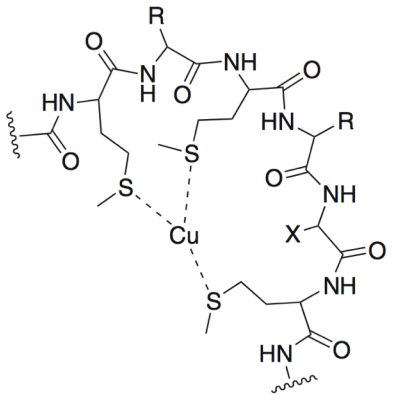

Trigonal, 3x Met

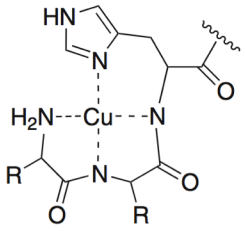

Tetrahedral, 1x His, 2x amide, 1x amine

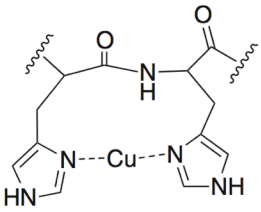

linear, 2x His

Figure 1.14 Potential N-terminal copper coordination chemistries. The following coordination strategies are suspected to be used by the N-terminus of copper binding proteins, but none have been structurally characterized to date.

In chapter 2, we investigate the effects of ligands on PAI-1 protein dynamics using hydrogen deuterium exchange coupled to mass spectrometry (HDX-MS). Copper^{2+} destabilizes PAI-1, significantly accelerating latency transition, but copper^{2+} and SMB domain are able to stabilize PAI-1, slowing down the latency transition process. If PAI-1 latency is tied to protein dynamics, then we would expect to see localized increases in dynamics in the presence of copper^{2+}, but localized decreases in dynamics in the presence of both ligands. PAI-1 in the presence and absence of copper^{2+} and SMB are compared in active, as well as latent forms of PAI-1. In addition, a PAI-1 variant hypothesized to bind copper^{2+} is compared with wild-type.

Our approach has been to combine computational prediction and targeted mutagenesis. In Chapter 3, we describe prediction of metal binding clusters using a computational algorithm that accounts for clusters of metal ion ligands. With a goal of producing a PAI-1 variant that is insensitive to metal ion effects, we have used site directed mutagenesis to engineer mutations at several regions of PAI-1 hypothesized to contain metal ion binding clusters. A battery of PAI-1 variants that are hypothesized to be metal ion binding deficient have been generated. The inhibitory activity of each PAI-1 variant has been tested as well as measurement of the rate of latency transition for comparison with wild-type PAI-1. This is to ensure that incorporation of the mutations does not significantly alter the biochemical properties independent of metal ion effects. Metal-binding properties were assessed by measurement of PAI-1 latency transition in the presence of copper^{2+}. A complementary assay was also used to monitor formation of PAI-1-tc-tPA in a gel in which PAI-1 is incubated with titrating amounts of copper^{2+}. This assay offers a more direct perspective on PAI-1 metal ion sensitivity as it relates to function. Finally, we use isothermal titration calorimetry (ITC) to measure the thermodynamic characteristics- enthalpy

change, stoichiometry, and affinity of copper^{2+} PAI-1 interaction in active and latent conformations for wild-type PAI-1 and the variants with targeted amino acid substitutions.

Chapter 4 focuses on the active W175F PAI-1 crystal structure, highlighting the differences from previous structures of the active form. The study of PAI-1 from a structural perspective is disadvantaged by its conversion to the latent form. The existing structures typically have several mutations that favor the active form, so that the protein is not latent at the end of the crystallization process. For example, the first crystal structure for active PAI-1 is the 14-1b quadruple variant with four amino acid substitutions. However, introduction of these amino acid switches incurs structural and functional effects that can change the thermodynamics and functionality of the protein. While W175F PAI-1 is highly stable and retains similar thermodynamic characteristics to that of wild-type PAI-1, the structure of W175F PAI-1 revealed several interesting differences, including the presence of a halogen-binding site in the gate region. In this work, we aim to characterize halogen binding in terms of structure and function to determine the physiological relevance of halogen binding on PAI-1. We measured wild-type and W175F PAI-1 latency conversion kinetics in the presence of several halogens. Additionally, we investigate the existence of a preference for different halogens binding to PAI-1.

Throughout the studies described in Chapters 2 through 4, we have aimed to investigate the binding of ligands to PAI-1 and determine effects on protein dynamics and overall function. At the end of these chapters, we present overall conclusions and future directions for work on the molecular effects of copper^{2+} on PAI-1 protein function. A summary of the findings from chapters 2-4 are described with relation to PAI-1 involvement in human disease. The aforementioned PAI

questions research questions are addressed, and a model for the effects of copper^{2+} on PAI-1 function is illustrated. Of course, this work opens up further questioning of how ligands can affect 1 stability, inhibitory function, and dynamics. The final portion of this chapter will outline new questions, potential future experiments, and directions for this area of research.

Chapter 2 Ligand Effects on PAI-1 Protein Dynamics Measured by HDX-MS

2.1. Introduction

This chapter was adapted from the manuscript currently in the submission process to the American Chemical Society Journal *Biochemistry*. It has been reviewed favorably and revisions are pending:

Copper (II) Ions Increase PAI-1 Dynamics in Key Structural Regions that Govern Stability. Joel C. Bucci, Morten Beck Trelle, Carlee S. McClintock, Tihami Qureshi, Thomas J.D. Jørgensen, Cynthia B. Peterson

2.1.a. Hydrogen Deuterium Exchange

The exchange of hydrogen atoms from different groups on the surfaces of proteins with their immediate solvent surroundings was observed some time ago. This phenomenon goes unnoticed unless the protein is placed under conditions of heavy isotopes of hydrogen, including deuterium or tritium. The hydrogen-deuterium exchange (HDX) can be monitored by several analytical techniques, such as radioactive scintillation, nuclear magnetic resonance (NMR), infrared spectroscopy (IR), or mass spectrometry (MS). Using mass spectrometry to measure HDX takes advantage of the mass difference between hydrogen and deuterium, which are 1.008 amu and 2.014 amu, respectively. A mass spectrometer is capable of making highly sensitive measurements to differentiate the mass difference between the two isotopes. As the heavier deuterium incorporates into the protein, the degree of mass shift indicates how much exchange occurs over a specific experimental timeframe. The experiments monitor global exchange from a structured perspective, but can be investigated at peptide level resolution.

The exchange reaction itself is acid-base catalyzed, so several factors need to be considered when designing experiments. Hydrogen atoms are bound to several chemical groups in proteins that exchange at differing rates (**Figure 2.1**). For example, hydrogen bound to electronegative atoms (either nitrogen, oxygen, or sulfur) on amino acid side chains exchange too quickly to monitor by current analytical techniques. Conversely, carbon bound side chain hydrogen exchange at negligible rates for HDX experiments. However, the amide hydrogens of the protein backbone exchange at an intermediate rate that is measureable by the analytical techniques. This is useful because each amino acid in the protein has one backbone amide hydrogen, with the exception of proline, in which it is incorporated into the main chain. The intrinsic exchange rate constant (k_{int}) can be defined as $k_{int} = k_H[H+] + k_{OH}[OH-]$; where k_H is the acid catalyzed rate constant, k_{OH} is the base catalyzed rate constant, and [H+] and [OH-] are the relative proton and hydroxide concentrations (**Figure 2.2**) [133]. The environmental pH, temperature, accessibility to solvent, and tendency to form intra- and inter-molecular hydrogen bonding are chief components governing HDX rates within proteins. Amide hydrogen bonding is integrally involved in formation and stability of protein secondary structure, making HDX a useful tool to assess protein dynamics.

Amide hydrogen exchange dependence on pH has implications on overall experimental conditions. Exchange rates are slowest at acidic conditions (~ pH 2.5) increase as the pH steadily becomes alkaline. Each reaction is completed at physiological (7.4) pH, where exchange readily occurs. At specific time points, samples are taken and quenched by addition of small amounts of concentrated formic acid, and flash frozen. The purpose of acid/temperature quenching is two-fold. Acid and temperature reduction lowers the pH and stops further exchange, so that no back-exchange occurs when the samples enter protiated solvent in the liquid chromatography separation and gas phase ionization process. Secondly, the acid quenching ensures that basic

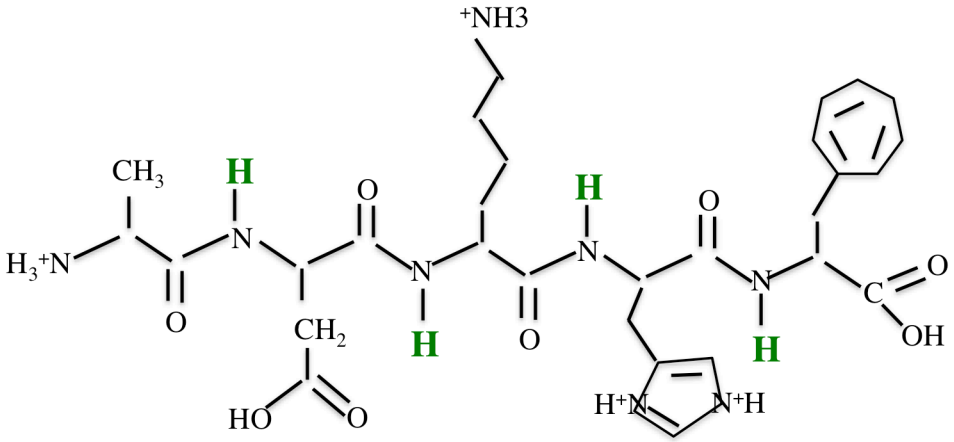

Figure 2.1 HDX of Functional Groups in Proteins. The peptide Gln-Asp-His-Pro-Lys-Leu is used as a representative peptide to illustrate the rates of hydrogen deuterium exchange of different functional groups on proteins. Hydrogens on non-electronegative atoms such as carbon will not exchange with the surrounding solvent at any appreciable rate. HDX can not be measured on the methyl hydrogens of the alanine due to negligible exchange. Likewise, HDX measurements are not possible on hydrogens of electronegative atoms such as nitrogen or oxygen within amino acid side chains. For example, the hydrogen on the carboxylic acid group of aspartate will exchange with the surrounding solvent at a rate so fast it can not be measured by instrumentation. However, Amide backbone hydrogens (shown in green) exchange with the solvent at an intermediate rate that is measureable by instrumentation such as NMR or mass spectrometer.

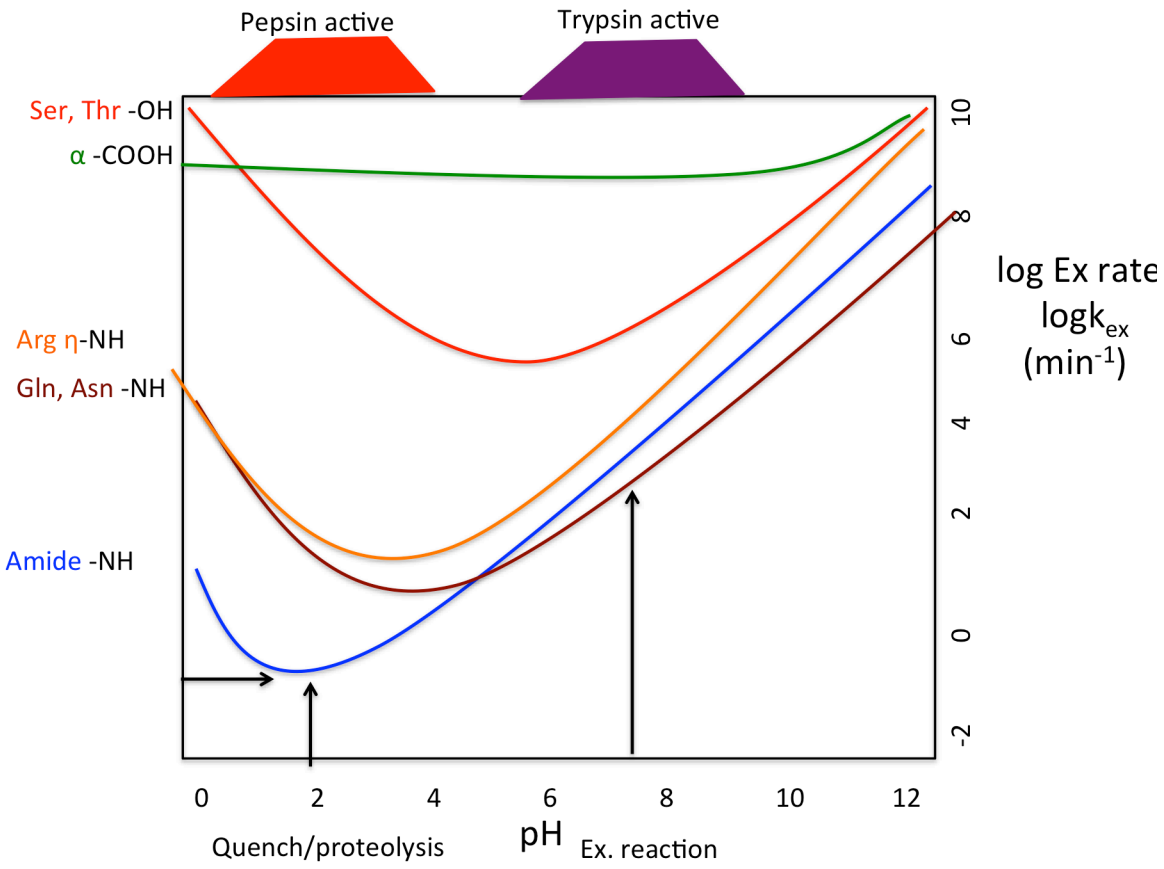

Figure 2.2 Hydrogen Deuterium Exchange Rates of Protein Functional Groups in the pH Spectrum. The y-axis represents the logarithm of the intrinsic hydrogen deuterium exchange rate (k_{ex}) in inverse minutes. This value is plotted as a function of the pH scale on the x-axis. HDX is an acid-base catalyzed reaction, where as the pH becomes more alkaline, the isotopic exchange generally within all functional groups, although the signatures do vary somewhat. Amide backbone hydrogens offer an intermediate rate at physiological pH 7.4, but also importantly the exchange can be quenched at low pH (2-2.5). This is important to protect against back exchange during analysis, and to charge the analyte for viewing in the instrument. Pepsin is used to cleavage the protein into peptides prior to instrumentation because it is optimally active in acidic conditions.

amino acid side chains (arginine, lysine, histidine) as well as peptide N-termini remain in the protonated and charged state required for monitoring in the mass spectrometer instrumentation.

To achieve peptide level resolution of HDX, the protein is cleaved by a protease into several peptides. The most used protease is typically trypsin, having predictable cleavage at basic residues along with the N-terminus guarantees two charges per peptide. However, Pepsin is used in HDX, taking advantage of its robust activity in acidic conditions. Pepsin cleavage is less predictable than trypsin, but nonetheless is experimentally reproducible. Pepsin cleaves C-terminal peptide bonds of hydrophobic residues, with specific preference for cleavage of aromatic amino acids. Following cleavage, the peptides are separated prior to monitoring of mass shift change.

Isolation of each peptide is completed using reverse phase liquid chromatography (LC), followed by ionization and separation by mass to charge ratio (m/z) in the MS. Peptides are bound to a hydrophobic C18 column under non-polar conditions, followed by peptide separation and elution under a linear gradient of increasing aqueous phase. As peptides elute, they enter the ion source of the MS to undergo electrospray ionization in which the aqueous droplets are converted to an aerosol gas phase (**Figure 2.3**). The taylor cone from the LC sprays the solvent into an area under high voltage. Under high voltage, the droplets evaporate, making each more charged. At a point, called the Rayleigh limit, the concentration of charge on a droplet exceeds the amount it can harbor physically, causing explosive dissociation of ions into the gas phase as they enter the MS. Inside the instrument ions are subjected to separation by quadrupole mass analyzer, followed by a

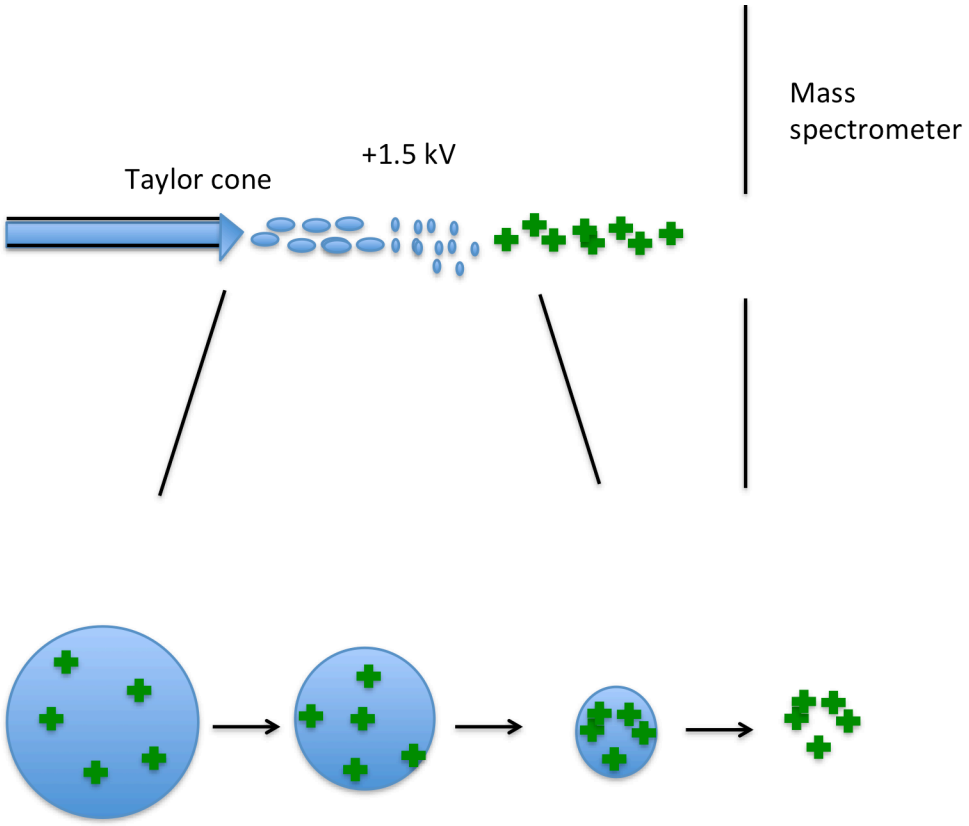

Figure 2.3 Electrospray Ionization. Peptides are separated by a reverse phase chromatography to be separated on basis of hydrophobicity. As they elute from the C18 column, they enter the mass spectrometer. The fine needle sprays the analyte ions through the taylor cone to create a jet of liquid phase ions. The liquid phase ions are subjected to a high voltage and heat, which causes the droplets to gradually evaporate, as they are in a mixture of aqueous and volatile solution such as acetonitrile. Evaporation of each droplet concentrates the charge to the extent that is can not be contained reaching the Rayleigh limit. At this point, the liquid phase ions burst into the gas phase for separation by the mass spectrometer. Electrospray ionization is a soft ionization technique fit for biomolecules such as proteins, and allow for multiply charged ions that increases the range of masses that can be detected by the instrument.

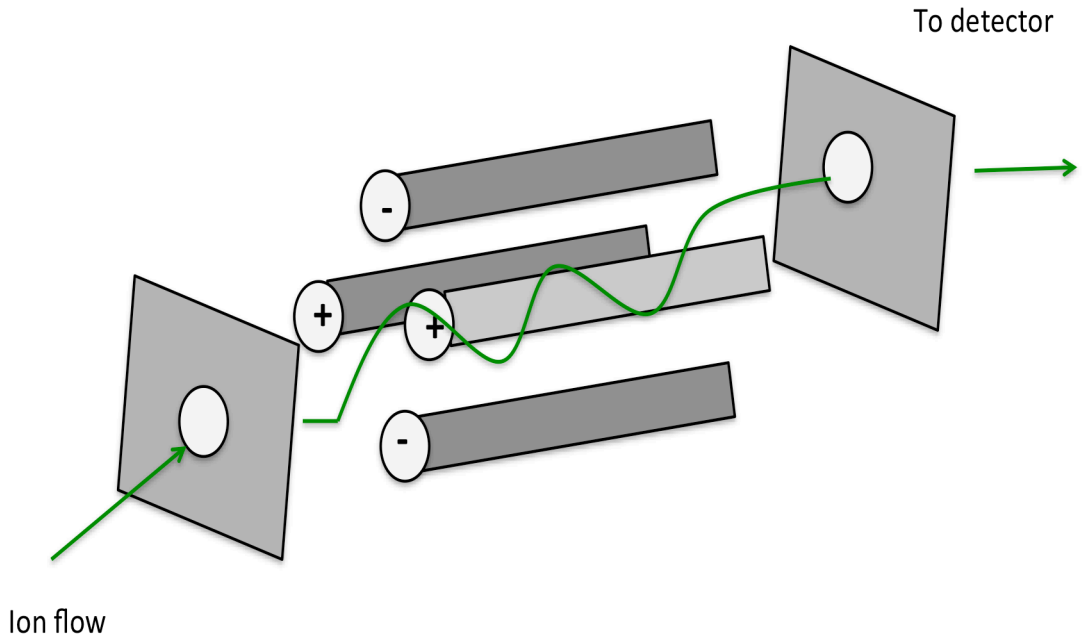

Figure 2.4 Quadrupole Mass Analyzer. Ions enter between four long metal rods, separated into two pairs. They are charged by radio frequency voltage (RF) and also an offset direct current voltage (DC) applied to the two pairs. The charge of the two pairs is controlled simultaneously to keep ions of a specific m/z range on a stable, periodic, hyperbolic, trajectory between the center of the rods, to the detector. Ions that have a m/z that is not within this range will enter unstable trajectories, collide with the rods, and never reach the detector. In this way, quadrupole mass analyzers separate on the basis of m/z to analyze ions of a desired m/z range.

time of flight mass analyzer. A quadrupole is a set of four metal rods that are parallel to one another in space (**Figure 2.4**). The two pairs are connected electrically through radio frequency current (RF), and direct current (DC) voltage is applied between one pair and the other in a concerted fashion. Since the electronics and voltage guide the ion flight based on their m/z ratio, the desired ions in the m/z range will proceed through to the detector, while ions not in this m/z range will enter trajectories that collide with the rods and will not appear in the ion chromatograms. The time of flight mass analyzer uses a known electric field strength, which gives each ion a velocity that depends directly on m/z ratio (**Figure 2.5**). This method separates by m/z ratio because lighter molecules will travel faster and hit the detector before heavier ones.

Each amide hydrogen in a protein can be found in a closed, open or exchanged state defined by: closed <-> open -> exchanged, where closed is an amide hydrogen participating in a hydrogen bond, and open is available for exchange. The rate of amide opening is k_{open}, while the rate of amide closing is k_{close}, and k_{ch} refers to the rate of hydrogen/deuterium exchange when the amide hydrogen is in the open state (ch for deuterium chemical exchange rate) [133]. The EX2 exchange limit (EX2 kinetics) is defined as the limit at which the rate of amide closing is markedly faster than the rate of chemical deuterium exchange, or $k_{close} >> k_{ch}$ [133]. Most proteins exist in a stable fold and usually exhibit exchange in EX2 kinetics. Many openings are required for this type of exchange for each event, resulting in a mass shift of a single population peak in the mass spectra as a function of labeling time due to incorporation of the heavier deuterium isotope. The EX1 exchange limit (EX1 kinetics) is defined as the limit at which the chemical exchange rate is significantly faster than the rate of amide closing, or $k_{ch} >> k_{close}$ [133]. In this observed exchange, the rate of chemical exchange becomes equal to k_{open}. EX1 kinetics is less common, but when it

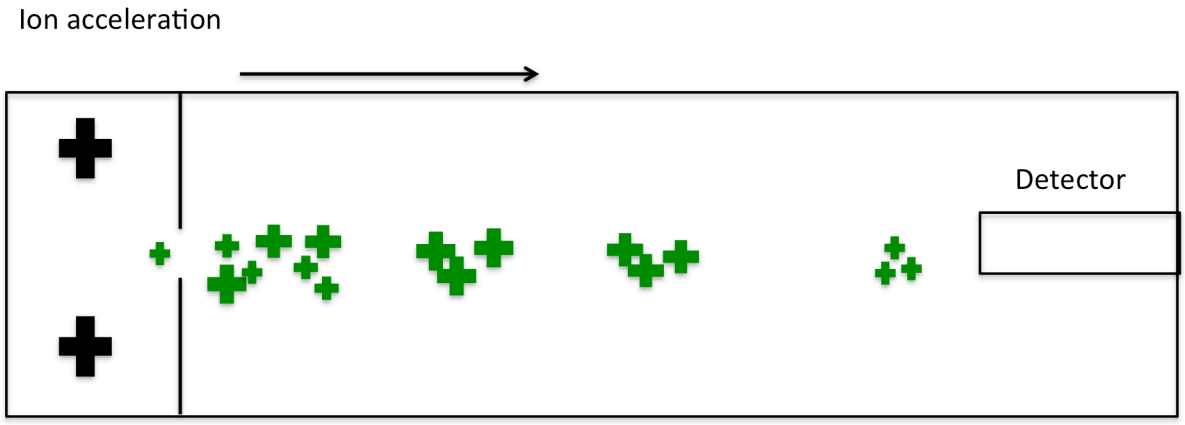

Figure 2.5 Time of Flight Mass Analyzer. Ions of the analyte containing ions of ranging masses are accelerated toward the detector using an electric field. Each ion has the same kinetic energy in this state, but their velocity towards the detector is directly dependent on their mass to charge (m/z) ratio. Ions of lowest m/z reach the detector in the shortest time period, and ions with the largest m/z reach the detector in the longest time period. In this way, time of flight mass analyzers separate ions on basis of m/z.

is observed, there is broadening of the peaks in the isotopic packet or even a bimodal isotope distribution detecting an unfolding event. If the two isotopic population peaks in a bimodal distribution are adequately separated by mass (deuterium content), then it is possible to determine the rate of unfolding as it is equal to the rate at which the lower mass population peak (folded form) interconverts with the higher mass population peak (unfolded form).

2.1.b. Serpin Protein Dynamics

Previous studies using hydrogen/deuterium exchange coupled to mass spectrometry (HDX-MS) have shown that wild-type PAI-1 is highly dynamic in the active form [91]. Peptides covering hD-s2A, hE-s1A of the flexible joint region quickly reach full deuteration early in the experimental time course, which is consistent with weak structural protection against isotopic exchange and high dynamics [91]. Additionally, peptides spanning the N-terminal half of hF, s3A-s4C, and s5A-N-terminal RCL loop of the shutter region also exchange rapidly, and are thus highly dynamic regions within active wtPAI-1 [91]. However, several peptides covering beta sheet B core undergo much slower exchange, and do not become fully deuterated during the time course [91]. These peptides spanning s6B-hB, s1B-s2B, s2B-s3B, s4B, and s4B-s5B are significantly protected from exchange, and comprise the least dynamic regions of PAI-1. In contrast, the latent form of PAI-1 is much more structurally resistant to isotopic exchange, featuring lower dynamics in almost all regions [91]. A peptide covering s4C to the N-terminal half of s3C is a lone example of a more dynamic area in the latent form compared with the active [91]. This observation is consistent with the opening of the gate region loops as a result of latency conversion, as well as the loss of secondary structure to s1C proximal to the gate [83].

HDX experiments were utilized in several stabilized serpins to compare with active wtPAI-1 in evaluating the role of protein dynamics in the latency transition process. The highly stabilized 14-1b PAI-1 variant contains N150H, K154T, Q319L reinforcing interactions between the hF-s3A loop and the shutter and M354I in the gate result in reduced dynamics [1, 91]. Peptides near the site of three of the four the amino acid substitutions (N-terminal half of hF, s2C-s6A) had lower exchange, as expected [91]. Interestingly, regions more remote from the stabilizing mutations also featured moderate protection, particularly peptides spanning s6B to N-terminal part of hB, hB-hC, C-terminal half of hE-s1A, s2B-s3B, and hI) [91]. Neuroserpin [134] (tm ~ 51-56°C, latency $t_{1/2}$ > 24h) and α-1-antitrypsin [135] (t ~ 59°C, do not undergo latency at physiological conditions) are also stabilized compared with PAI-1 and feature structural differences within HDX patterns. Some similarities shared with PAI-1 include a protected core consisting of β-sheet B and part of β-sheet C [136, 137]. These two serpins feature some of the same highly dynamic regions in peptides spanning the N-terminal part of hA, hD, and the RCL [136, 137]. Key regions of difference were observed in the shutter region (peptides spanning s3A and s5A) and the underlying shutter (hC) of α-1-antitrypsin, compared with neuroserpin or PAI-1 [136, 137]. A summary of the current understanding of these serpin thermodynamics, dynamics and latency transition is found in **Figure 2.6**.

HDX has also been used to detect partial unfolding events within the hydrophobic core of PAI-1 [85] that offer new insight to how PAI-1 converts from the active to latent form. Peptides spanning hA-s6B-hB and s5A-RCL undergo local unfolding events on timescale that is consistent with being on the path to latency conversion ($t_{1/2}$ ~ 24, 18 minutes, respectively) [85]. A peptide spanning hB-hC undergoes unfolding on a timescale very early in the latency conversion process ($t_{1/2}$ ~ 1 minute) [85]. These findings identified new regions of PAI-1 that have functional

Serpin thermodynamic stability, dynamics, and latency transition $t_{1/2}$

PAI-1	**T_m (°C)**	**HDX dynamics observed**	**Latency $t_{1/2}$ (hrs)**
wtPAI-1 active	50	FJ, gate, shutter, hF	1.2
wtPAI-1 latent	68	global protection	-----
W175F PAI-1	51	?	2.5
14-1b PAI-1	65	localized FJ protection	~145
Other SERPINs			
Neuroserpin	56	FJ, gate, shutter, hF	~24
α-1-anti-trypsin	59	protection in shutter, hC	not under physiological conditions

Data compiled from: Trelle et al., 2013, Biochemistry; Jensen et al., 2011; Takehara et al., 2009, J. Mol. Bio.; Belorgey et al., 2009, J. Bio. Chem.; Kaslik et al., 2002, Biochemistry; Tsutsui et al., 2001, Biochemistry; Sarkar et al., 2011, Biophys.;

Figure 2.6 Serpin Thermodynamics, Dynamics, Latency Transition Summary. The thermodynamic melting point in degrees (°C), hydrogen deuterium exchange dynamic regions, and latency conversion kinetics half-life ($t_{1/2}$ in hours) are summarized for comparison. The serpins to be compared are wild-type PAI-1 in the active form, latent form, as well as two variants, W175F, and 14-1b, that stabilize PAI-1 through varying mechanisms. They are also compared against neuroserpin and α-1-anti-trypsin, serpins that do not convert to latency as readily (or at all) as PAI-1.

relevance to the latency transition process. As a technique, HDX proves to be powerful in uncovering the structural changes that occur during the path to the latent state.

2.1.c. Ligand Effects on PAI-1 Dynamics

PAI-1 ligands such as the SMB domain of VN, Mab-1 monoclonal antibody and RNA aptamers prolong the length of time PAI-1 remains active [79, 103, 138]. Ligand binding is expected to protect against isotopic exchange by sterically blocking the binding interface, but the protected regions often extend beyond the interface [91, 139]. The binding of the SMB domain significantly protects against exchange in peptides spanning s2A-hE, hE-s1A, and N-terminal half of hF constituting or proximal to the binding interface [91]. In addition, SMB protects against exchange in peptides of hA, hB-hC, hD, C-terminal hF-hF-s3A loop, hI, and hI-s5A [91]. Thus, SMB binding confers stabilization on peptides that are not at the PAI-1:SMB interface and are positioned at the bottom pole of the molecule [91]. The mab-1 antibody binds at E53 of hC, Q56 of hC, and D305 of hI and stabilizes PAI-1 similarly to SMB domain (1.4 fold increase) [138]. Mab-1 binding results in HDX protection to several of the same peptides, although in this case the changes are more localized to the binding epitope [91]. Peptides spanning hB-hC, hI are significantly affected, while only peptides s6B-hB and hF-s3A away from the epitope exhibit protection from exchange [91]. Two RNA aptamers paionap-5, and paionap-40 bind to flexible joint residues R76, K80, F114, and R118. Paionap-40 additionally binds to K122. The two aptamers strongly stabilize the active form of PAI-1 (t1/2 ~ 2, 28 hours respectively) [103]. The protection signatures of the aptamers are similar to that of SMB, with some notable differences. In addition to where SMB protects, the aptamers also protected exchange in hA, s4B, s5B, s6B, and

hB. Paionap-40 strongly protects the peptide containing K122 spanning s1A-hF [139]. Despite the highly similar HDX patterns between ligands, the mechanism for the most potent stabilization of PAI-1 by paionap-40 is not completely understood [103]. Overall, PAI-1 conformational flexibility in the active form allows for binding of several different stabilizing ligands and influences in dynamics are uniformly observed.

2.2. Rationale for Study

Copper^{2+} binding to PAI-1 accelerates the latency transition in the absence of VN and slows latency transition in the presence of VN [79]. This work aims to further understand the influence of copper^{2+} ions on PAI-1 dynamics, either in destabilizing or stabilizing the inhibitor in the active form. A zinc^{2+} ion was identified in the most recent PAI-1 structure (3Q02), coordinated to two N-terminal histidines (H2 and H3) of one PAI-1 molecule and carboxylate-containing residues from the gate region of a second PAI-1 molecule, forming an asymmetric dimer interface [95]. To determine whether the PAI-1 N-terminal histidines coordinate copper^{2+} to influence structural effects, we have also engineered and analyzed a variant form of PAI-1 that has alanine substitutions at those positions (H2AH3A PAI-1). We hypothesize that ligands govern the stability of PAI-1 conformations through protein dynamics. This work aims to address many unanswered questions using HDX. Copper^{2+} causes destabilization of PAI-1 and acceleration of latency, while binding of SMB domain stabilizes, causing a delay in latency. Does copper^{2+} binding increase the dynamics in regions of PAI-1 important to latency transition? Are these same regions stabilized in the presence of copper^{2+} and the SMB domain? Are the structural effects imparted by copper^{2+} specifically targeted to the active conformation?

2.3. Materials and Methods

2.3.a. Expression, Purification, Activity Assessment of PAI-1

Wild-type and PAI-1 variants were cloned into the pET-24d expression vector plasmid for recombinant expression in Rosetta 2 (DE3) pLysS *Escherichia coli* cells (Novagen-EMD). PCR based mutagenesis was used to introduce mutations, in which primers developed to incorporate the intended triplet codons necessary for alanine substitution at residues H2, H3, E81, E212, D222, E242, E350, H364 in the sequence of PAI-1 (Several of these variants will be tested in Chapter 3). **Figure 3.3** shows the relative locations of the investigated residues on the three dimensional PAI-1 structure. Verification of mutations was completed by sequencing of each variant plasmid DNA at the UTK molecular biology and sequencing center (Walters Life Sciences Building). Wild-type and variant plasmids were transformed into the expression cell line using a standard heat shock method of 42°C for 45 seconds. Bacterial colonies were grown on LB agar plates, which contained 50 μg/mL kanamycin and 34 μg/mL chlorphenicol for antibiotic selection. A single colony was isolated for growth in a 12 mL TB liquid culture with the same antibiotics at 37°C, and shaking at 250 rpm. The cell growth proceeded to an optical density (OD_{600}) of 1.0 absorbance unit, at which time the temperature was lowered to 15°C in order to express PAI-1 that is predominantly in the active form. After one hour of growth at 15°C, 1mM IPTG (Research Products International) was added to start protein expression for 16 hours. The cell harvest was performed via centrifugation at 10,000xg for 30 minutes.

Cell lysis was performed using 50mM phosphate buffer 1mM EDTA, pH 6.5 at 25°C containing 20mg lysozyme and protease inhibitor cocktail (1mg/100mg of cell pellet), followed by cell sonication, and centrifugation at 10,000xg for 30 minutes at 4°C. Wild-type PAI-1 and

variants are purified according to standard published procedures [79] using three column steps. Sulfopropyl sepharose (SP) cation exchange column (volume 120mL), in which PAI-1 is bound using a buffer of 50mM sodium phosphate, 80mM $(NH_4)_2SO_4$, and 1mM EDTA, pH 6.5 at 4°C. PAI-1 is eluted from the SP column using an $(NH4)_2SO_4$ gradient of 80-500mM, pooled, and extensively dialyzed to remove the EDTA. Next, PAI-1 is bound to a nickel charged immobilized metal affinity (IMAC) column (volume 20mL), in a buffer of 50mM sodium phosphate, 20mM imidazole, and 500mM NaCl, pH 7 at 4°C. PAI-1 is eluted from the IMAC column using a gradient of 20-200mM imidazole. Final purification of PAI-1 is achieved using a Sephacryl (s-100) gel filtration column (volume 600mL) in a buffer of 50mM sodium phosphate, 300mM NaCl, and 1mM EDTA pH 6.25 at 4°C to separate PAI-1 from any contaminants based on size. Purification of variants lacking the N-terminal histidines required modifications to the procedure, because there were difficulties in binding SP and IMAC columns. For variants lacking H2 or H3, the pH was lowered to 5.5 for more adequate binding to the SP column. Instead an of IMAC step, these variants were purified using a phenyl sepharose column with a reverse 600-10mM salt gradient; otherwise the steps were the same as for wild-type PAI-1. Protein purity was verified using a 10% polyacrylamide SDS-PAGE gel in reducing conditions and protein concentration was measured using at 280 nm using Beer's law, where the PAI-1 extinction coefficient: e_{280} = 0.93 mL mg^{-1} cm^{-1} and a molecular weight of 43,760 g/mol.

Two activity assays are performed to determine adequate inhibitory ability of the purified forms of PAI-1. First, PAI-1 is buffer exchanged into a buffer composed of 50mM MOPS, 100mM $(NH_4)_2SO_4$ pH 7.4 at 37°C for all metal ion studies, since sodium phosphate and EDTA significantly interact with metal ions. Inhibition was tested by titration against two chain tPA in a

plate based assay. Two chain tPA at 100nM is in a buffer of 50mM MOPS, 100mM $(NH_4)_2SO_4$, 2mM EDTA, and 1% bovine serum albumin (w/v), pH 7.4 at 37°C. The proteins are mixed at PAI-1:tPA ratios ranging from 0.25 up to 4, followed by 1mM tPA substrate Spectrozyme tPA addition (in the same buffer as tPA). Activity of tPA is directly measured through cleavage of the para-nitro-aniline group on the substrate by tPA that absorbs at 405 nm over 20 minutes. Wild-type PAI-1 with proper and timely preparation results in a protein fraction that adequately inhibits tPA activity with 1.25 equivalents of PAI-1. Additionally, an activity assay in an SDS-PAGE gel using similar PAI-1/ single-chain tPA ratios can be used to monitor their complex formation, latent, and cleaved PAI-1 forms. This is completed using 4uM tPA and ratios of PAI-1 ranging from 0.25 to 3 molar equivalents relative to that. This assay is completed in 50mM MOPS, 100mM $(NH_4)_2SO_4$, pH 7.4 at 37°C. Electrophoresis is completed in a 4-12% gradient gel to resolve PAI-1/tPA complex, latent, and cleaved PAI-1 forms in non-reducing conditions for 75 minutes, at 150 volts. The equivalents of a new PAI-1 stock required to fully inhibit tc-tPA are 1-1.25 equivalents, or 85% inhibition. Adequate wild-type PAI-1 inhibition is 85% active using this method. To produce latent PAI-1 for experiments, protein expression is performed at 25°C. The purified protein samples from the s100 column in this case are converted completely to the latent state by incubating at 37°C, with shaking at 75rpm for one week. Latent protein stocks are confirmed to have no activity by the previously mentioned plate based activity assay, where no observable inhibition of tPA at a minimum of 10:1 (PAI-1:tPA) is considered adequate for use in experiments.

2.3.b. Preparation of the N-terminal VN Protein Fragment, SMB Domain

The SMB domain and RGD sequence (amino acids 1-47 of VN) DNA sequence was cloned into the pET-32b expression plasmid vector with a preceding thioredoxin protein, N-terminal 6x histidine tag, and a region encoding for a thrombin cleavage site. Recombinant expression of SMB domain was completed using Rosetta-gami 2(DE3) pLysS E. *coli* cell line equipped to fold disulfide-bonded proteins. SMB domain plasmid DNA was transformed into the cells using a standard heat shock method of 42°C for 45 seconds, and colonies were grown LB agar plates that contained antibiotic selection of 50μg/mL ampicillin, 34 μg/mL chloramphenicol, and 12.5 μg/mL tetracycline. A single colony was isolated for liquid culture, which was grown in 12mLs of TB with the same antibiotics at 37°C, and 300 rpm shaking to an OD_{600} of 1.0 absorbance unit. Protein expression is induced by addition of 1mM IPTG for a total of 16 hours. Cells were harvested by centrifugation at 10,000xg for 30 minutes at 4°C. Cell lysis is performed using 50mM sodium phosphate, 500mM NaCl, and 20mM imidazole which contains 20mg lysozyme and (1mg/100mg cell pellet) protease inhibitor cocktail, followed by sonication, and centrifugation at 10,000xg for 30 minutes.

The cell lysate containing overexpressed, his-tagged SMB domain is bound to an IMAC column, and isolated using an imidazole gradient of 20mM-1M. Eluted protein fractions are pooled, and dialyzed thoroughly in a thrombin cleavage buffer of 20mM Tris, 150mM NaCl, and 2.5mM $CaCl_2$, pH 8.3 at 25°C, removing the large concentration of imidazole. Biotinylated thrombin (15U/400mg of SMB) is added for overnight cleavage of the thioredoxin-his-tag from SMB. The engineered histidine tag would add non-native metal ion binding site to the protein, and must be removed. Cleavage results in an N-terminal extension of four amino acids (GSAM), in

addition to the first 47 residues of VN. Complete cleavage was confirmed by running the mixture over the IMAC column again, collecting the flow through, and analyzed by electrophoresis on a 10% polyacrylamide SDS-PAGE gel under reducing conditions. Next, the mixture is run over a streptavidin column for complete removal of thrombin, and passed over the S100 column (volume 600mL) in 50mM sodium phosphate, 300mM NaCl, and 1mM EDTA pH 6.25 at 4°C. In the final step, a column with active W175F PAI-1 bound is used as an affinity chromatography step for isolation of correctly folded SMB domain. SMB protein mixture is bound column which is equilibrated in 50mM sodium phosphate, 300mM NaCl, and 1mM EDTA at 4°C. SMB fractions are eluted using the same buffer, but lowering the pH to 4.0. Sample purity was confirmed by running 10% polyacrylamide SDS-PAGE in reducing conditions. Protein concentration is measured by absorbance at 276 nm, using beer's law, where SMB extinction coefficient ε276 = $4500 M^{-1} cm^{-1}$, and with a molecular weight of 5678.26 g/mol. SMB binding is verified using an SPR assay in which a 1:1 PAI-1:SMB mixture is flown over a CM5 chip coated with VN. A correctly folded SMB should bind PAI-1, competitively inhibiting PAI-1 binding to the VN chip in the SPR assay.

2.3.c. Hydrogen-Deuterium Exchange Reactions

PAI-1 and SMB protein stocks were diluted into a pre-incubation buffer, consisting of 5 mM MOPS, 100 mM $(NH_4)_2SO_4$, 6.5 mM NaCl, 2 mM sodium acetate, and 0.1 mM EDTA pH 7.4 at 25°C. This resulted in PAI-1 at 5 μM, in which the buffer and salt components were identically balanced in composition among all experimental conditions. This permitted complex formation and/or rapid exposure to $copper^{2+}$ ions preceding addition of deuterium (D_2O) buffer.

For the copper^{2+} conditions, the buffer also included 215 μM total $CuSO_4$, having a final calculated free copper^{2+} concentration of 2.3 μM. After copper^{2+} addition, the pH was adjusted to pH 7.4 at 25°C using NaOH. The experimentally determined first sphere MOPS/copper^{2+} affinity value β_1 is 4.00 [140]. The following quadratic formula was employed to calculate free copper^{2+} concentration $10\text{^}\beta_1 = K_a$; $K_a = 1/K_d$; $M_f = M_t - [(M_t + B_t + K_d) - ((M_t + B_t + K_d)^2 - 4B_t M_t)^{1/2}]/2$ where M_f is the concentration of free copper^{2+}, M_t is the concentration of total copper^{2+}, and B_t is the buffer concentration (MOPS), and the K_d is the dissociation constant between copper^{2+} and MOPS. It should be noted that EDTA is present to prevent trace metal ion effects and for protein stability; it was subtracted from the total metal ion concentration prior to free copper^{2+} calculation. For conditions including the SMB domain, there was a 2-fold molar excess (10 μM) relative to the PAI-1. A scheme of HDX reactions is illustrated in **Figure 2.7**. Pre-incubation solutions (8 μL) are diluted 20-fold (final volume of 160 uL) into deuterium buffer (5 mM MOPS, 100 mM $(NH_4)_2SO_4$, 6.5 mM NaCl, 2 mM sodium acetate, and 0.1 mM EDTA pD 7.8 at 25°C) and incubated at 25°C, and time-point aliquots (10, 30, 180, 600 seconds) were taken by quenching with 1.38% (3.2 μL) formic acid and flash-freezing in liquid nitrogen. Quenched samples underwent proteolysis using 16 μL of pepsin (final concentration of 0.5 mg/mL) on ice for two minutes. The peptides are then injected using an ice-cold Hamilton syringe into an Acquity HDX liquid chromatography system kept at 4°C (Waters, Milford, MA). Samples flow through a Vanguard BEH C18, 2x5 mm pre-column (Waters) at a rate of 300 μL/min and then eluted using a Acquity BEH 1x100 mm C18 analytical column using a gradient of: 8-15% B over 0.5 minutes, 15-35% B in 5.5 minutes, and 35-85% B over 0.5 minutes at a rate of 40 µL/min and into the mass spectrometer. A sample total ion chromatogram of LC elutions for undeuterated active wtPAI-1 is shown in **Figure 2.8**. Peptide ions were analyzed on a Waters Synapt G1

quadrupole-time-of-flight (Q-TOF) mass spectrometer. The instrument underwent daily calibrations to 3ppm accuracy. Deuterium uptake plots were constructed by plotting average mass shifts of each peptide as a function of the incubation time in logarithm form (**Figure 2.10**). Normalized exchange was calculated from experimental peptides with respect to fully deuterated controls (100%). Fully deuterated control samples were generated through PAI-1 incubation in 4 M deuterated guanidine in D_2O for four hours, then identical reaction quenching, treatment, and analysis. calibrations to under 3ppm accuracy. Undeuterated wild-type and variant PAI-1 peptic peptides were fragmented using tandem (MS2) CID to identify each peptide to be analyzed using MASCOT (Matrix science) (**Figure 2.9**). The following equation was used to calculate average mass of each peptide in all experiments: average mass = $\sum_i(m_iI_i)/(\sum_i I_i)$ where i is each isotope peak and running from 1 to the total number of isotope peaks in the isotopic packet, the centroid mass of isotope peak i is shown by m_i, and I_i represents the intensity of isotope peak i.

2.4. Results

2.4.a. Adapted HDX-MS Conditions are Required to Measure Metal Ion Effects

The previous HDX-MS studies using N-terminally histidine-tagged PAI-1, and phosphate buffered saline (PBS) [91] rendered incompatible conditions for these metal ion experiments on wild-type PAI-1. Similar to our previous work on metal ion effects with PAI-1 [109], we employed a MOPS buffer system to preserve metal ion solubility. We also have expressed a PAI-1 construct without a His-tag to diminish non-specific metal interactions. Because of this, it was first important to test whether our wild-type PAI-1 in MOPS buffer yields reproducible HDX results compared with previous studies [91] [139]. Initial HDX reactions on wild-type PAI-1 and His-tagged PAI-1 in both PBS and MOPS determined that the presence or absence of a N-terminal

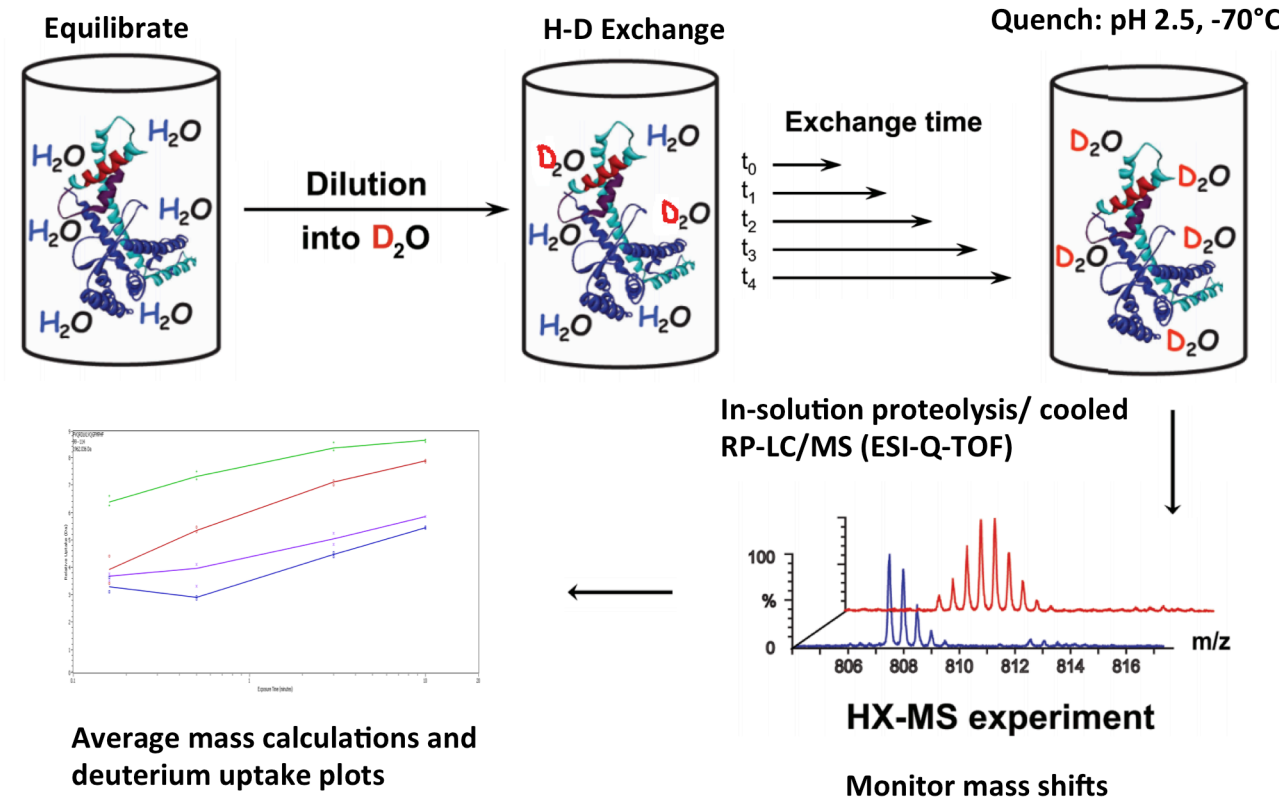

Figure 2.7 HDX Reaction Scheme. Hydrogen deuterium reactions are completed using a protiated protein that is diluted into 95% deuterium oxide to start exchange. The reactions are conducted at a specific temperature, pH, and time frame that allows for monitoring of dynamic changes within the protein. After specific time points, samples are removed and the HDX is quenched by addition of formic acid to drop the pH, and then are flash frozen in liquid nitrogen. This prevents the possibility of isotopic back exchange, and also protonates basic groups on the protein for detection in the mass spectrometer. Following, the samples are individually thawed on ice, and immediately subjected to proteolysis by pepsin on ice. The resulting peptides are injected into a cooled liquid chromatography system with a C18 hydrophobic column for separation prior to entry into the mass spectrometer. The peptides are ionized through electrospray ionization and are subsequently separated by quadrupole and time of flight mass analyzers before entering the detector to be viewed as spectra. The undeuterated versions of the peptide (blue) are identified by MASCOT, each peptide mass shift is monitored and analyzed by DynamX software. Finally, the mass shifts in daltons of a time course are plotted as a function the logarithm time to produce HDX uptake plots.

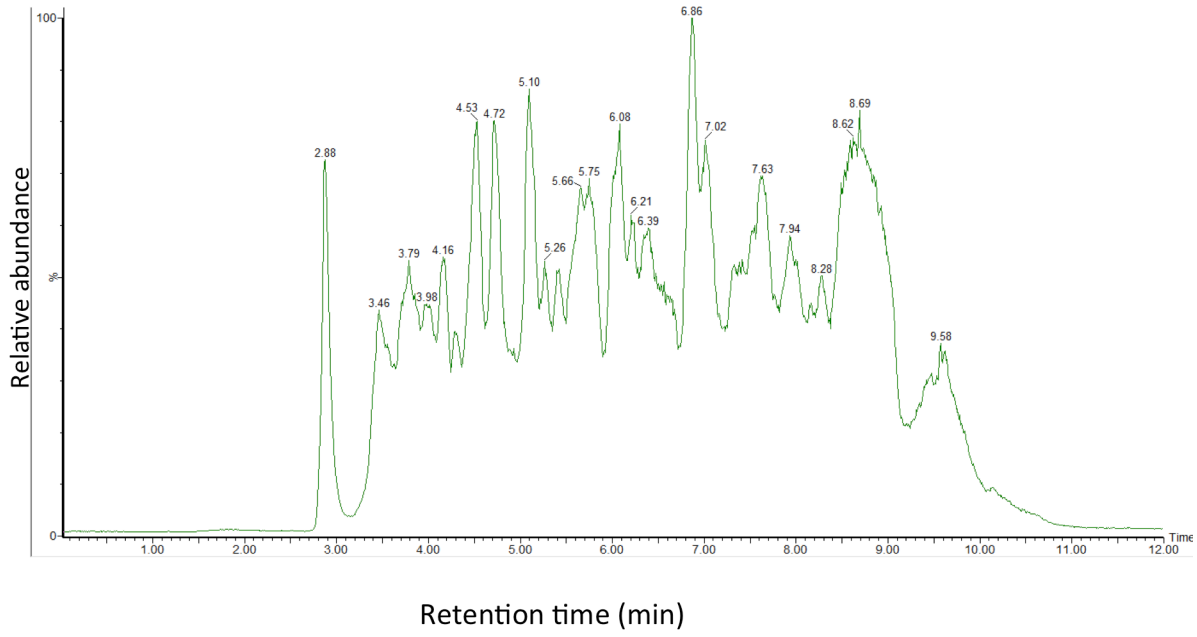

Figure 2.8 Liquid Separation of PAI-1 Peptides by RP-LC. Directly after proteolysis by pepsin, a sample is injected into the high pressure liquid chromatography system. The peptides bind to the C18 hydrophobic analytical column under aqueous conditions, and are then eluted by a gradient of increasing acetonitrile. Shown above is the total ion chromatogram of the peptides, with the relative abundance of peaks at each retention time as peptides elute from the column. This chromatogram is of active wild-type PAI-1 in the undeuterated form, it was used initially to identify peptic peptides spanning all regions of PAI-1, for later comparison with deuterated time course samples under a number of experimental conditions.

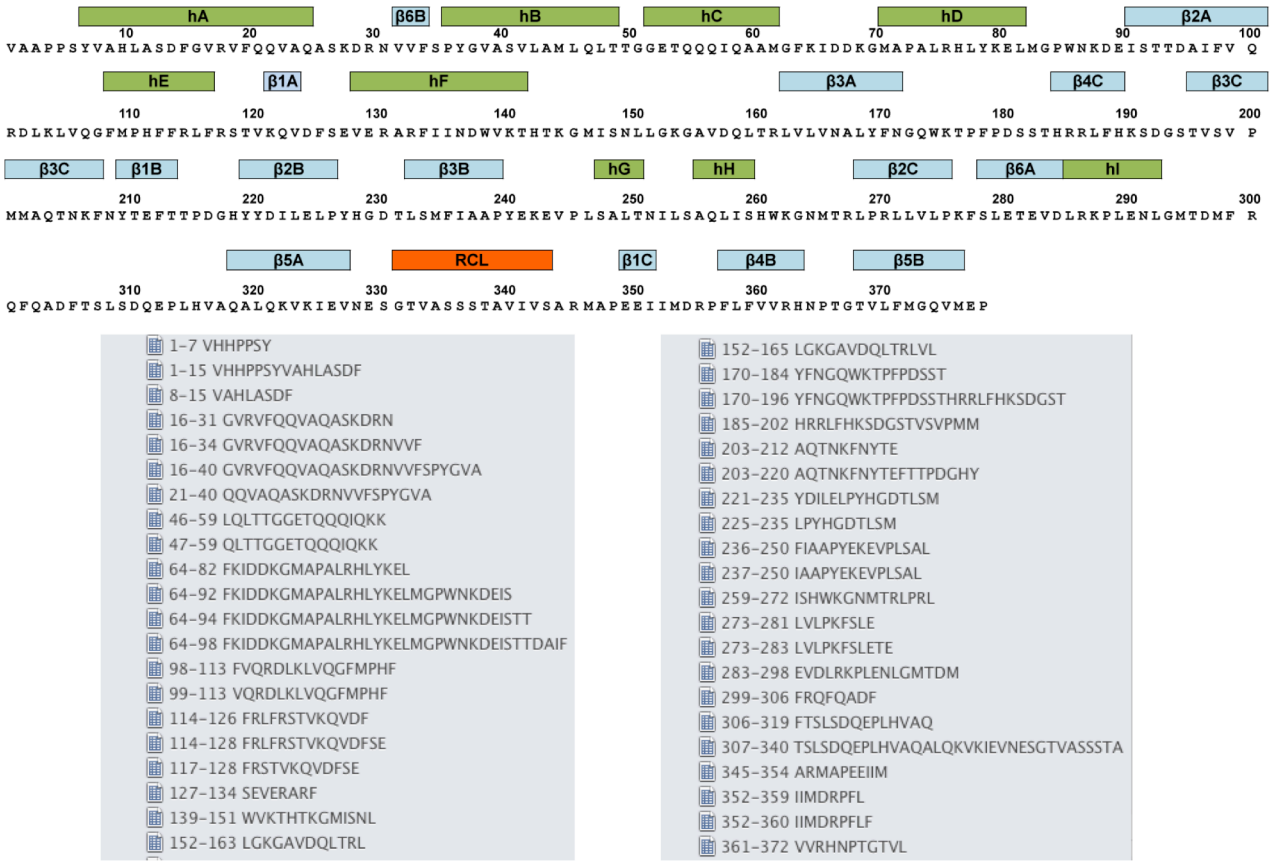

Figure 2.9 MASCOT Identified PAI-1 Peptic Peptides. After MS/MS fragmentation of PAI-1 peptides, we were able to identify 42 PAI-1 peptic peptides using the program MASCOT. This program predicts the cleavage patterns of multiple proteases, and calculates the theoretical masses for the peptides. Our mass spectrometry results lead to 42 direct peptide matches to our MASCOT potential matches. Their relative locations along the primary sequence and secondary structure of PAI-1 are listed above.

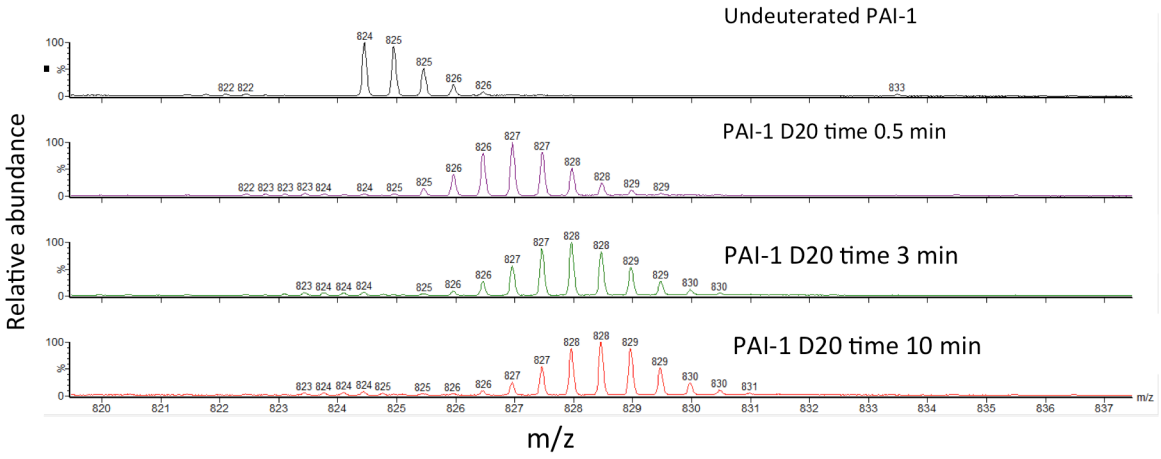

Figure 2.10 Mass Shifts Due to Deuterium Incorporation. The mass shift due to isotopic exchange of heavier deuterium is shown over 3 experimental time points in comparison to an undeuterated active wtPAI-1 peptide. The peaks shown are the isotopic packets of naturally occurring isotopes of H, N, C, and O in the peptide, which changes to a bell shape when deuterium incorporates into functional groups of each atom. The average masses of each isotopic packet are plotted in duplicate for each deuterium uptake plot as a function of logarithm time.

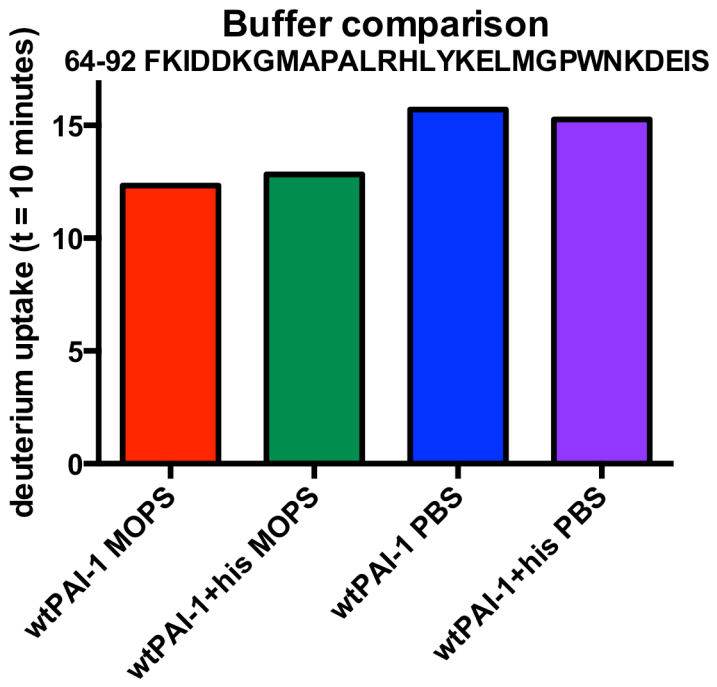

Figure 2.11 Representative Deuterium Uptake Plots Comparing the Deuterium Uptake of PAI-1 +/- N-terminal His-tag, in PBS Buffer and MOPS Buffer. A deuterium uptake bar graph for the same PAI-1 peptide spanning residues 64-92 (hD-s2A) after 10 minutes of exchange using active wild-type PAI-1 (red) or active PAI-1 with an N-terminal histidine tag (green) in 5 mM MOPS, 100 mM $(NH_4)_2SO_4$, 6.5 mM NaCl, 2 mM NaOAc, and 0.1 mM EDTA. Deuterium uptake bar graph are also shown for this peptide in after 10 minutes of exchange on active wtPAI-1 (blue), and active wtPAI-1 with the histidine tag (purple) in 10 mM phosphate buffer, 2.7 mM KCl, and 137 mM NaCl. Pre-incubation samples (8uL) were diluted 20-fold (160uL) into deuterated buffer, exchange occurring at 25°C, and aliquots were taken after 10 minutes by quenching upon addition of 1.38% (3.2 uL) formic acid and flash-freezing in liquid nitrogen. The PAI-1 peptides, including 64-92, were generated using pepsin proteolysis. The peptides were injected into a cooled HPLC and analyzed using ESI-qTOF mass spectrometry as described in the Materials and Methods section.

His-tag has no effect on PAI-1 dynamics in each buffer; results for all peptides were compared and peptide 64-92 (hD-S2A) is shown as an example from the data set (**Figure 2.11**). While the HDX results were comparable in PBS buffer for both forms of PAI-1, a surprising 20% reduction in deuterium uptake was generally observed using the MOPS buffer system. We attribute this reduction in D-uptake to the presence of ammonium sulfate in the MOPS buffer, which is known to have a stabilizing effect on proteins. The only exception to this trend was observed with highly dynamic peptides that were fully deuterated within the experimental timeframe. Moreover, the reduction in deuterium uptake in MOPS *vs*. PBS buffer offers an advantage for observing differences in HDX that will arise from ligands that increase protein dynamics. In PBS, many peptides reach fully exchanged levels very quickly, so the dynamic range in HDX experiments on PAI-1 is expanded using the MOPS buffer to slow the exchange.

2.4.b. Addition of Increases Dynamics of PAI-1 in Functionally Relevant Regions

The effect of copper^{2+} ions on the amide backbone dynamics of active wtPAI-1 was investigated in the presence as well as the absence of the SMB domain of VN. All of the deuterium uptake plots for these experiments conditions are displayed in (**Figure 2.12**). Representative deuterium uptake plots are presented in **Figure 2.13** to illustrate copper^{2+} exchange effects on three PAI-1 peptic peptides (**Figure 2.13**). In the absence of ligands, active form of wtPAI-1 is highly dynamic. Peptides comprising the lower backside underlying the shutter (hB, hC), flexible joint region (hD, hE, s1A), shutter region (s3A, s5A) and gate region (s3C, s4C, s3B) experience substantial deuterium uptake as a function of time in the experiment (**Figure 2.12**). The only regions structurally resistant from isotopic exchange are located in β-sheet B in the protein

core, which is in line with previous work [91]. Addition of the SMB domain of VN resulted in extensive protection to exchange to the binding interface in the flexible joint region, but also to the peptides spanning the backside underlying shutter, comprising the better part of the lower half of wtPAI-1 (**Figure 2.12**). Addition of copper^{2+} results in an increase in isotopic exchange, meaning increased dynamics in regions covered by representative peptides 46-59 and 99-113, compared with active unligated wtPAI-1 (**Figure 2.13**). As seen in previous work [91], SMB domain binding to PAI-1 resulted in lower isotopic exchange, consistent with reduced structural dynamics in the regions spanning these peptides. When copper^{2+} and SMB domain are incubated with PAI-1, comparable exchange is observed relative to the addition of SMB for the peptides in **Figure 2.13.** However, the effect was not for all peptides; an example of a peptide that is unaffected by copper^{2+} addition in the presence or absence of the SMB domain is 152-163 (**Figure 2.13**).

Since several PAI-1 peptides likewise exhibited an increase in deuterium uptake as a result of copper^{2+} binding, it was first important to examine where this effect corresponded to on the primary sequence of PAI-1. To facilitate this analysis the relative deuterium content, presented as percent of the full deuteration level, was calculated for each peptide, with and without copper^{2+} bound to PAI-1, and the difference in relative deuterium content was plotted as a heat map along the primary sequence (**Figure 2.14**). Peptide 46-59 (hB-hC loop) exhibited a significant increase of exchange in the presence of copper^{2+}, indicative of an increase of dynamics in this region underlying the shutter. Immediately following this peptide in the sequence, peptides representing the flexible joint region (64-94 (hC-hD), 99-113 (s2A-hE), 114-128 (hE-s1A), and 139-151 (hF)) also exhibit increased exchange consistent with elevated dynamics. In addition, peptides spanning 283-298 (s6A-hI) and 299-306 (loop between hI & s5A), immediately before strand 5A of the

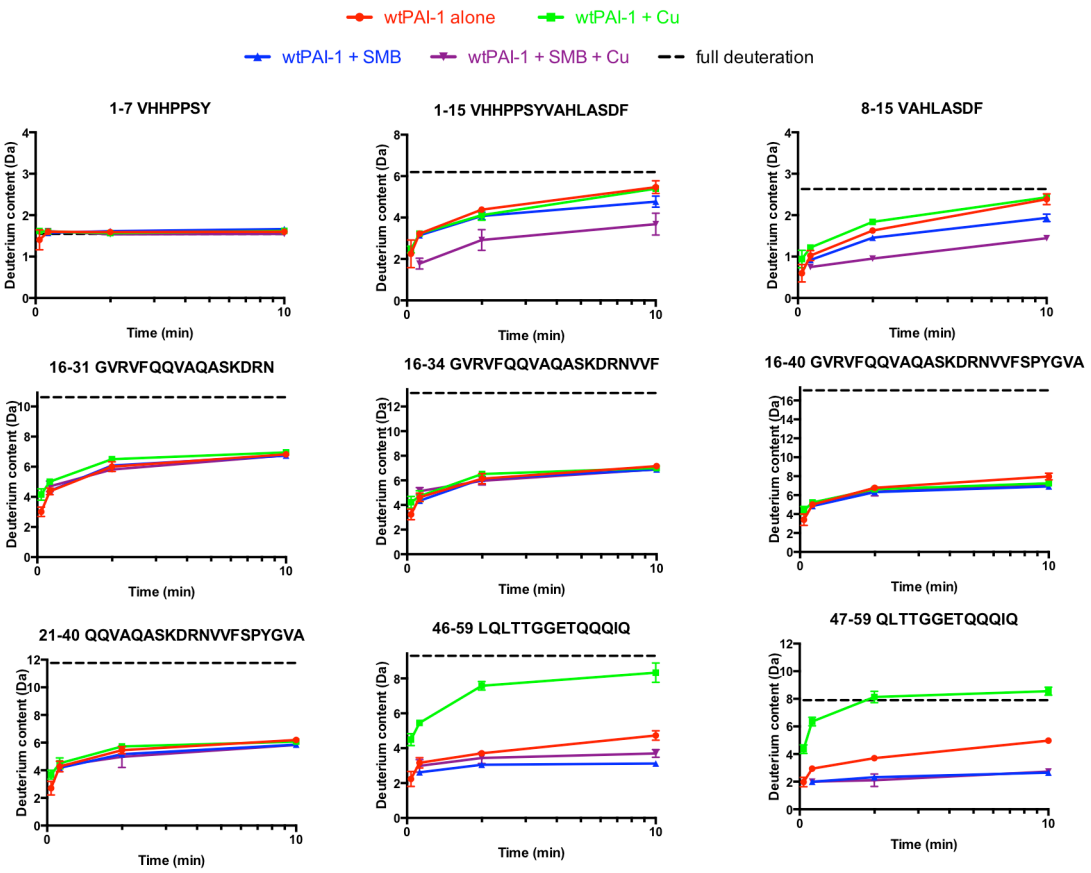

Figure 2.12 Deuterium Uptake Plots Active wtPAI-1 in the Presence and Absence of Copper^{2+} and SMB domain: HDX-MS experiments were performed on wtPAI-1 (red), wtPAI-1 + copper^{2+} (green), wtPAI-1 + SMB domain (blue), and wtPAI-1 + SMB + copper^{2+} (purple). Deuterium uptake plots represent the increase in mass (Da) for each individual PAI-1 peptide as a function of time. The mass shift of each PAI-1 peptide having reached full experimental deuteration is denoted by the dashed black line.

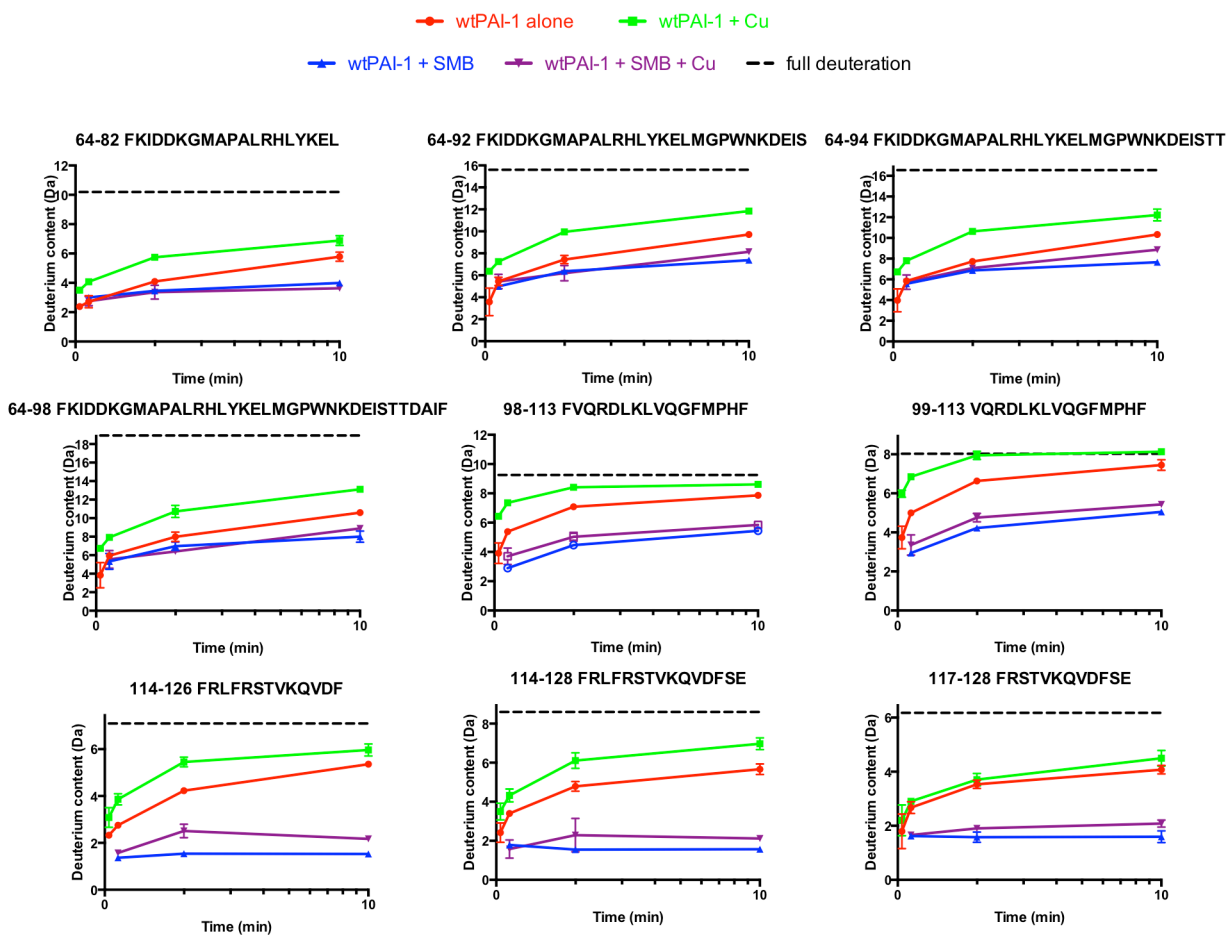

Figure 2.12 Deuterium Uptake Plots Active wtPAI-1 in the Presence and Absence of Copper^{2+} and SMB domain (cont.): HDX-MS experiments were performed on wtPAI-1 (red), wtPAI-1 + copper^{2+} (green), wtPAI-1 + SMB domain (blue), and wtPAI-1 + SMB + copper^{2+} (purple). Deuterium uptake plots represent the increase in mass (Da) for each individual PAI-1 peptide as a function of time. The mass shift of each PAI-1 peptide having reached full experimental deuteration is denoted by the dashed black line.

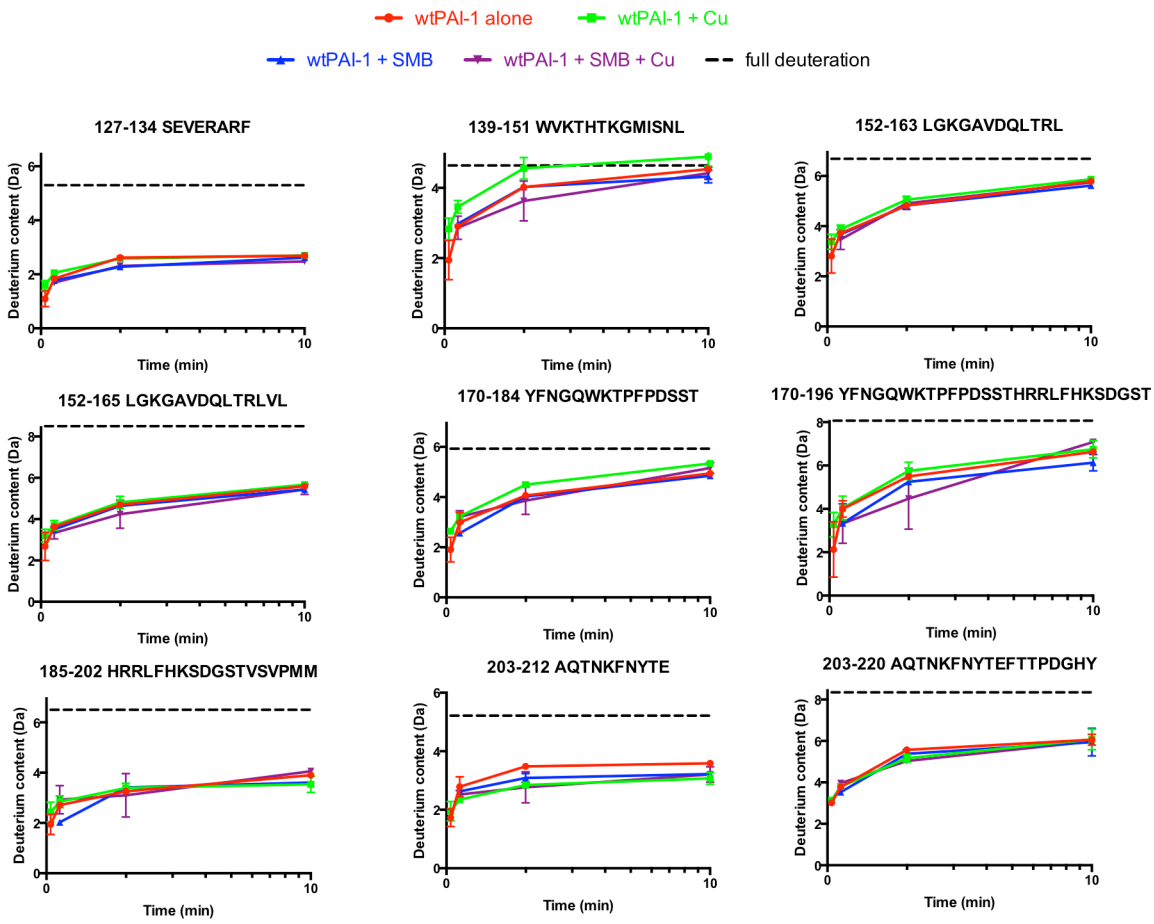

Figure 2.12 Deuterium Uptake Plots Active wtPAI-1 in the Presence and Absence of Copper^{2+} and SMB domain (cont.): HDX-MS experiments were performed on wtPAI-1 (red), wtPAI-1 + copper^{2+} (green), wtPAI-1 + SMB domain (blue), and wtPAI-1 + SMB + copper^{2+} (purple). Deuterium uptake plots represent the increase in mass (Da) for each individual PAI-1 peptide as a function of time. The mass shift of each PAI-1 peptide having reached full experimental deuteration is denoted by the dashed black line.

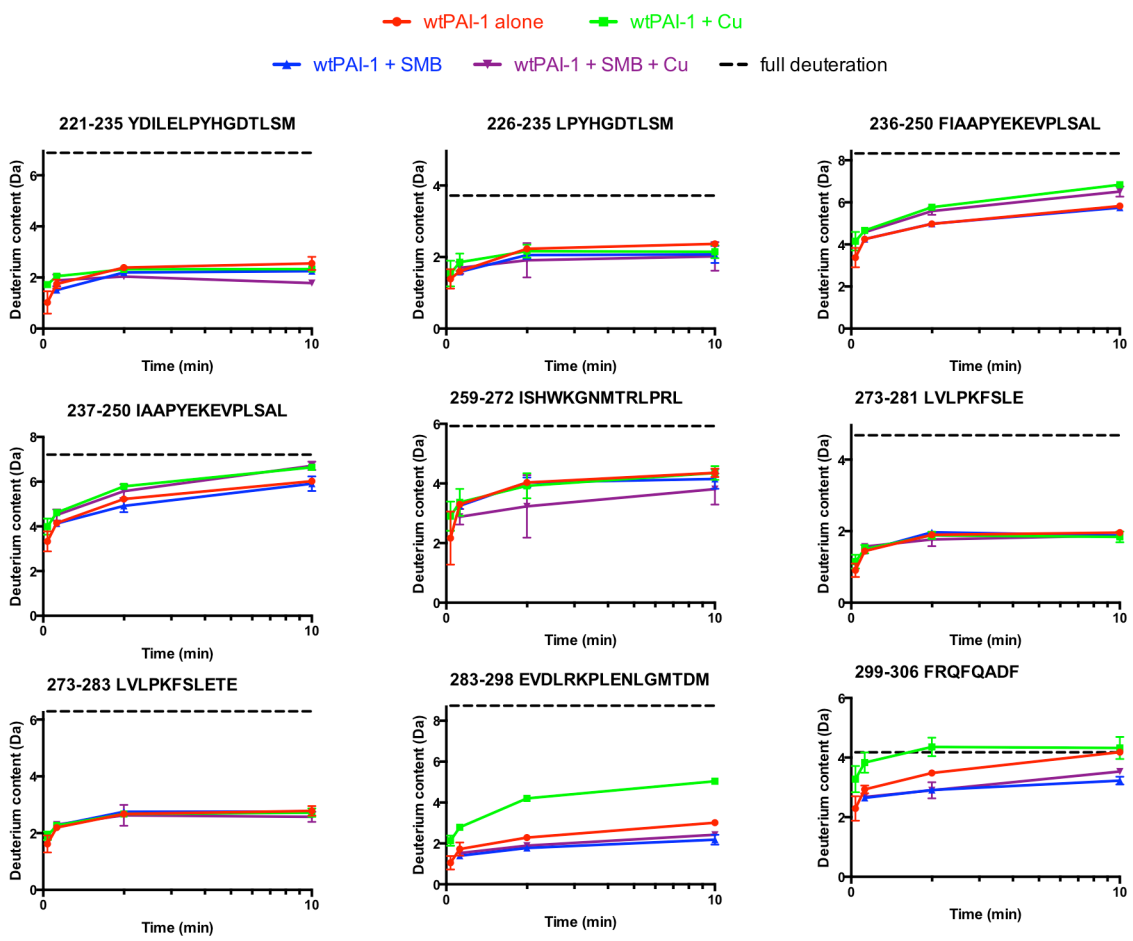

Figure 2.12 Deuterium Uptake Plots Active wtPAI-1 in the Presence and Absence of Copper^{2+} and SMB domain (cont.): HDX-MS experiments were performed on wtPAI-1 (red), wtPAI-1 + copper^{2+} (green), wtPAI-1 + SMB domain (blue), and wtPAI-1 + SMB + copper^{2+} (purple). Deuterium uptake plots represent the increase in mass (Da) for each individual PAI-1 peptide as a function of time. The mass shift of each PAI-1 peptide having reached full experimental deuteration is denoted by the dashed black line.

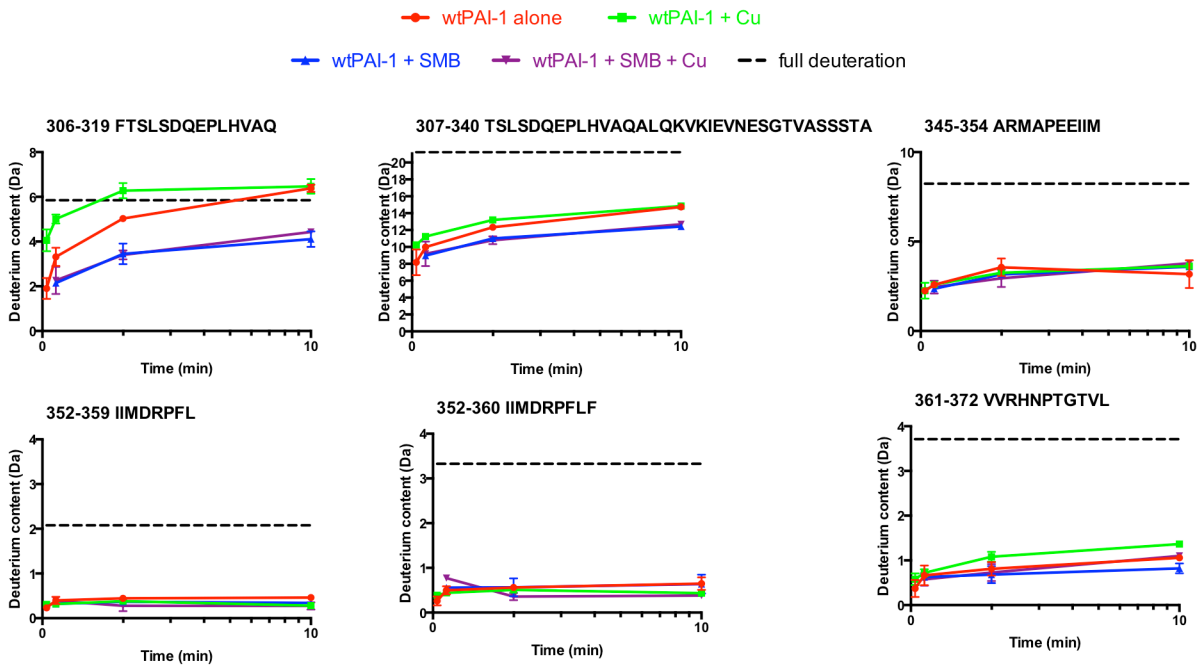

Figure 2.12 Deuterium Uptake Plots Active wtPAI-1 in the Presence and Absence of Copper^{2+} and SMB domain (cont.): HDX-MS experiments were performed on wtPAI-1 (red), wtPAI-1 + copper^{2+} (green), wtPAI-1 + SMB domain (blue), and wtPAI-1 + SMB + copper^{2+} (purple). Deuterium uptake plots represent the increase in mass (Da) for each individual PAI-1 peptide as a function of time. The mass shift of each PAI-1 peptide having reached full experimental deuteration is denoted by the dashed black line.

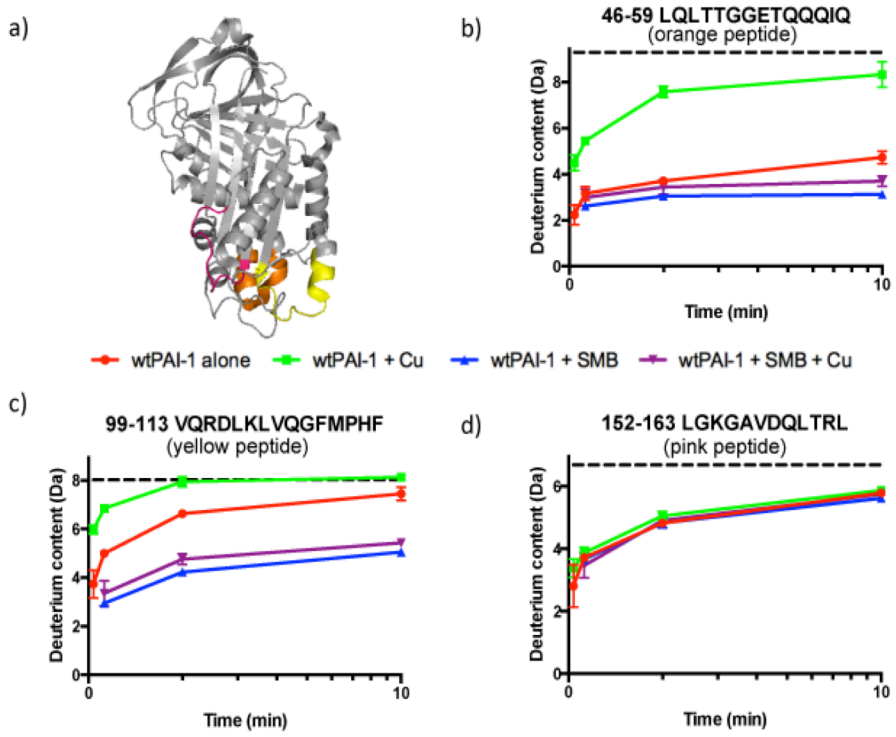

Figure 2.13: Representative Data from HDX-MS on Active wtPAI-1.
Panel a: PAI-1 structure depicting the location of three representative HDX peptides. The HDX peptide spanning residues 46-59 of hB, hC and the loop connecting them is colored orange. The HDX peptide spanning residues 99-113 of C-terminal end of s2A, hE and the loop connecting them is colored yellow. The HDX peptide spanning residues 152-163 of the N-terminal portion of s3A and part of the preceding loop connecting to hF is colored pink. *Panel b, c and d: HDX plots of representative peptides comparing the effects of copper^{2+} addition (+/- SMB)*. Deuterium uptake plots are shown for three PAI-1 peptides: 46-59 (LQLTTGGETQQQIQ) (panel b), 99-113 (FVQRDLKLVQGFMPHF) (panel c), and 152-163 (LGKGAVDQLTRL) (panel d). HDX-MS experiments were performed on wtPAI-1 (red), wtPAI-1 + copper^{2+} (green), wtPAI-1 + SMB domain (blue), and wtPAI-1 + SMB + copper^{2+} (purple). Deuterium uptake plots illustrate the increase in mass (Da) as a function of time for the individual peptic peptides.

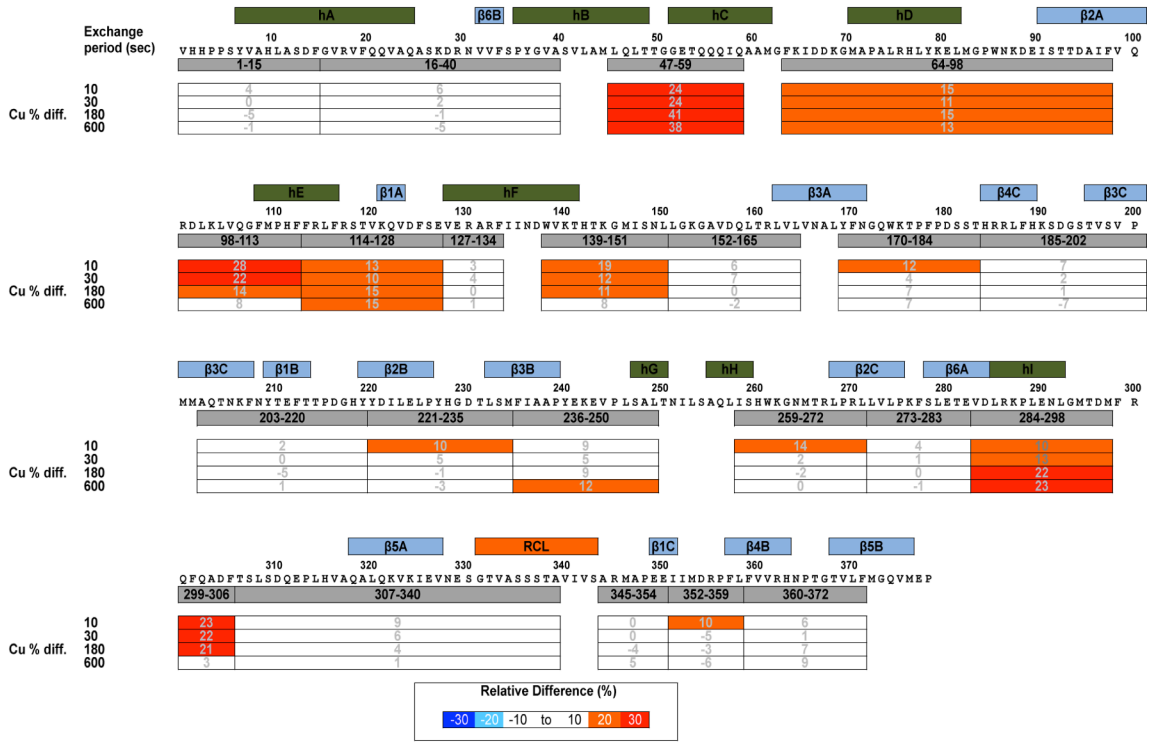

Figure 2.14 The Effects of Copper^{2+} on PAI-1 Dynamics: Examining the Primary Sequence. HDX-MS data were collected for various periods of exchange listed on the far left. For each of the 4 time points, deuterium exchange of wtPAI-1+copper^{2+} is given as a percentage difference relative to that observed for wtPAI-1 alone. The data +/- copper^{2+} were normalized with respect to a fully deuterated control (100%) in which PAI-1 is denatured by guanidine in the presence of D_2O for 4 hours to evaluate deuterium exchange in the unfolded form. The primary sequence of PAI-1 is shown along the top of each row, with locations of secondary structure elements α-helices (green) and β-strands (blue) throughout the sequence. The identity of individual peptic peptides that were analyzed is depicted by the gray boxes along the sequence, and uptake results for each peptide at the four time points is shown in the columns below each peptide. The proteolysis yielded peptides spanning the majority of the PAI-1 sequence, giving essentially complete coverage in the HDX-MS experiments. The observed deuterium uptake values shown are the percentage difference between the two experimental conditions ([wtPAI-1 + Cu] – [wtPAI-1 alone]). The normalized percent difference was color coded using the following scheme: Percent difference of > -20% in dark blue, -20 to 10% in light blue, -10 to 10% in white, 10 to 20% in orange, and > 20% in red.

shutter region, feature increased dynamics when copper^{2+} is bound. It is important to note that copper^{2+} binding has no effect on exchange in peptides of several regions of PAI-1. In our measurements, peptides covering the first two N-terminal peptides, which include hA and preceding N-terminal residues, beta sheets B and C, hG, hH, and the C-terminus are not affected by copper^{2+} binding. To interpret the spatial signature of copper^{2+} binding on PAI-1 dynamics we transferred the heat map shown in **Figure 2.14** and onto the three-dimensional structure of PAI-1 (**Figure 2.15**). Each of the peptic peptides affected by copper^{2+} addition is localized to the flexible joint region and areas underlying the shutter strands of beta sheet A. Taken together, our observations from the experimental conditions indicate that copper^{2+} binding causes localized rather than global changes in PAI-1 dynamics, at the time scale investigated. Furthermore, it is apparent that copper^{2+} binding increases dynamics in regions of PAI-1 that are important for maintaining anti-protease active, metastable PAI-1 conformation; namely the flexible joints region and underlying helices in the shutter region.

2.4.c. SMB Domain Binding Negates Copper^{2+} Effects on the Dynamics of PAI-1

As the SMB domain of VN binds PAI-1, containing the primary high-affinity binding site for PAI-1 [97], this results in significant resistance against isotopic exchange in several peptides. This includes peptides 46-59 (hB-hC), 99-113 (s2A-hE), 114-128 (hE-s1A), 299-306 (hI loop-s5A) (**Figures 2.12, 2.16**), This is consistent with previously published results [91], although the SMB effect is generally less pronounced in the present study due to the reduced dynamics of PAI-1 in MOPS buffer compared to PBS. The noted peptides are located in or proximal to the flexible joint region, including the SMB binding interface. Likewise, binding of both copper^{2+} and the

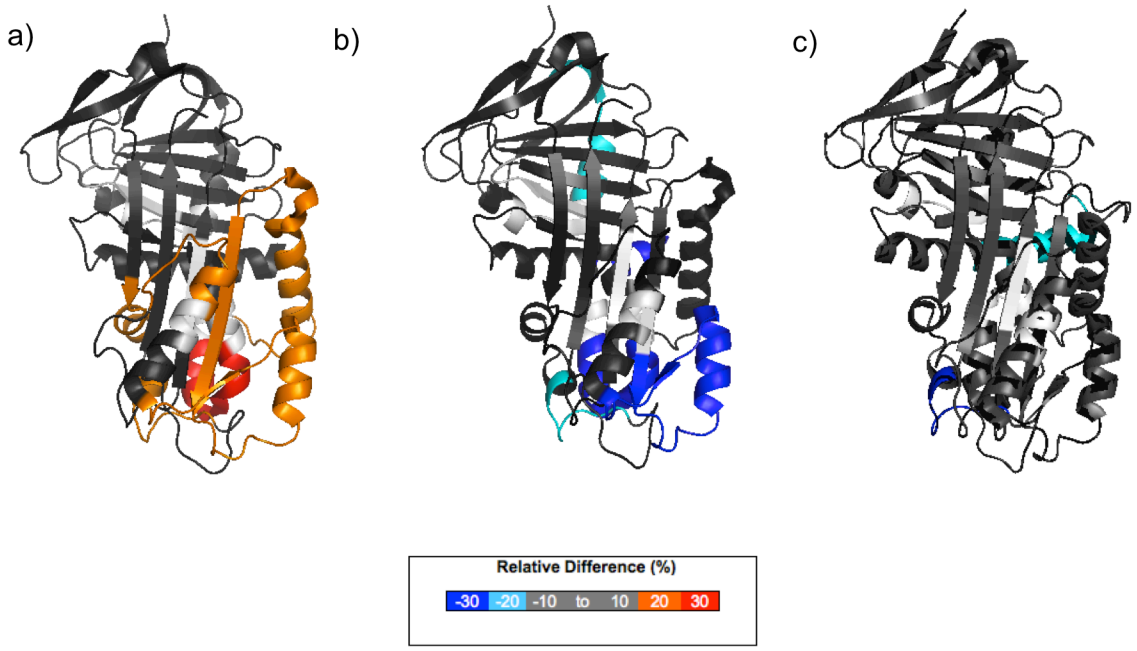

Figure 2.15 Copper^{2+} Increases Localized Dynamics in the Flexible Joints Region and Underlying Shutter Helices, SMB negates copper^{2+} effects.
Panel a: Structural heat map of copper^{2+} effects on wtPAI-1. The normalized percent difference of deuterium uptake of wtPAI-1 + copper^{2+} *versus* wtPAI-1 alone for the peptic peptides in **Figure 2.14** was represented on a crystal structure for active PAI-1 (pdb: 3Q02). The percent difference in deuterium uptake is determined for the three minute HDX time point, represented by the following color scheme: > -20% in dark blue, -20 to -10% in light blue, -10 to 10% in dark gray, 10 to 20% in orange, and > 20% in red. Areas of light gray signify residues for which there was no sequence coverage.
Panel b: Structural heat map of copper^{2+} + SMB effects on PAI-1. The normalized percent difference of deuterium uptake of wtPAI-1 + SMB + copper^{2+} *versus* wtPAI-1 alone for peptic peptides in **Figure 2.16** was represented on a crystal structure for active PAI-1 (pdb: 3Q02). The percent difference in deuterium uptake is determined for the three minute HDX time point. The same colors representing percent differences apply for the heat map key.
Panel c: Heat map of copper^{2+} effects (+/- SMB) on a PAI-1 structure. The normalized percent difference of deuterium uptake comparing wtPAI-1 + SMB + copper^{2+} *versus* wtPAI-1 + SMB for the same peptic peptides was represented on a crystal structure for active PAI-1 (pdb: 3Q02). The percent difference in deuterium uptake is determined for the three minute time point. The same colors representing percent differences apply for the heat map key.

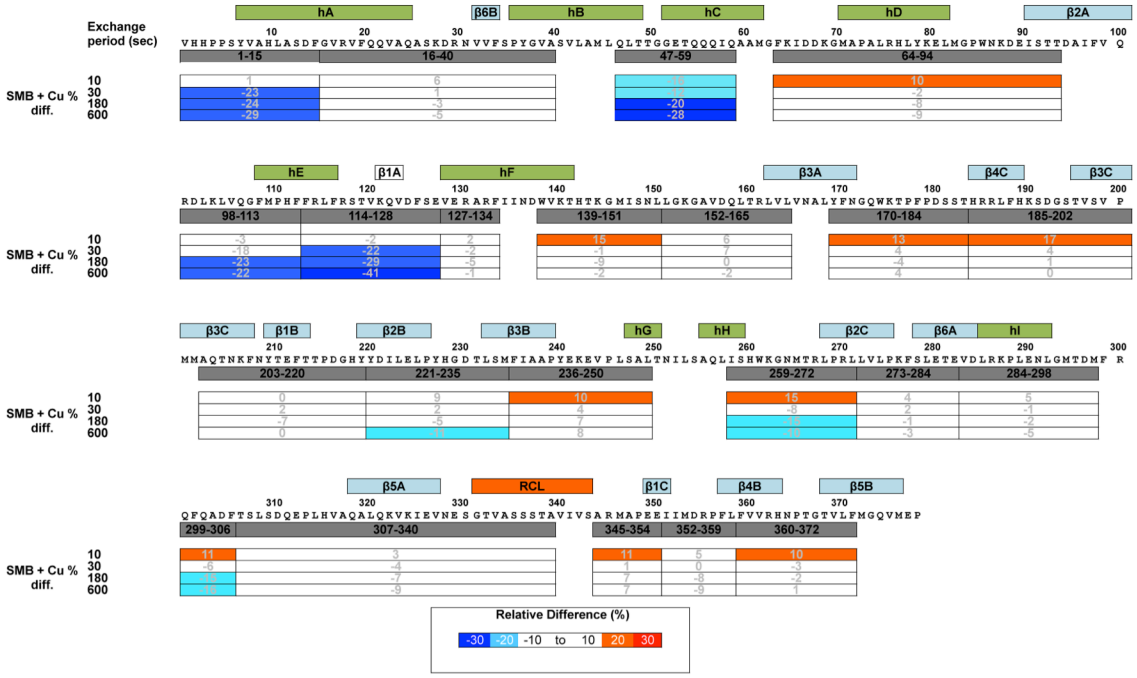

Figure 2.16 Determining the Effect of SMB and Copper^{2+} on PAI-1 Dynamics: Examining the Primary Sequence: HDX-MS data were collected for various periods of exchange listed on the far left. For each of the 4 time points, deuterium uptake of wtPAI-1+SMB+copper^{2+} is given as a percentage relative to that observed for wtPAI-1 alone. The data for the experimental conditions +/- copper^{2+} and the SMB domain were normalized with respect to a fully deuterated control (100%) in which PAI-1 is denatured by guanidine in the presence of D_2O for 4 hours to determine the deuterium exchange in the unfolded form. The primary sequence of PAI-1 is shown along the top of each row, with secondary structure elements α-helices (green) and β-strands (blue) at their respective locations throughout the sequence. The identity of individual peptic peptides that were analyzed is represented in the gray boxes along the sequence, and uptake results for each peptide at the four time points are listed in the columns below each peptide. The deuterium uptake values listed are the percentage difference between the two experimental conditions ([wtPAI-1 + Cu +SMB] – [wtPAI-1 alone]). The normalized percent difference was color coded using the following scheme: Percent difference of > -20% in dark blue, -20 to 10% in light blue, -10 to 10% in white, 10 to 20% in orange, and > 20% in red.

SMB domain produced similar patterns of HDX protection observed upon the binding of the SMB alone, a general phenomenon illustrated by the example peptides in **Figure 2.13**. As observed with binding of just the SMB domain, peptides 47-59 (hB-hC), 99-113 (s2A-hE), 114-128 (hE-s1A), and 299-306 (hI loop-s5A) (**Figures 2.12, 2.16**) are areas highly protected from exchange when both ligands are bound. Mapping of the results for binding of SMB and $copper^{2+}$ shows similar protection patterns observed with binding of the SMB alone [91], and shows reduced dynamics in the flexible joints region (**Figure 2.15**). Importantly, the high affinity of $copper^{2+}$ for PAI-1, previously measured with a $K_d < 100nM$ [109], appears unaffected upon the binding of the SMB domain. This is apparent from isothermal titration calorimetry experiments (See Chapter 3) in which the $copper^{2+}$ binding isotherm is unchanged comparing PAI-1 and the PAI-1-SMB complex. Furthermore, there is no binding of $copper^{2+}$ to the isolated SMB domain by calorimetry. Thus, the changes in dynamics observed in these HDX experiments are due to binding and conformational effects of SMB and $copper^{2+}$ and not to changes in affinity, which would alter saturation levels.

Only the N-terminal peptide (residues 1-15) was substantially protected with both ligands bound, compared to the binding of SMB (**Figure 2.12, 2.15**). Since peptide 1-7 is unaffected, and peptide 1-15 is protected (**Figure 2.12, 2.15**) the protection by the combined binding of SMB and $copper^{2+}$ must be sub-localized to the second half of the peptide (8-15). The N-terminal histidine residues in positions 2 and 3 are part of a potential $copper^{2+}$ binding site. However, these residues are located in an unprotected, dynamic region and it is not possible to predict whether complex formation with $copper^{2+}$ would cause protection of their backbone amide hydrogens. Therefore, the absence of $copper^{2+}$-SMB-induced protection in peptide 1-7 does not rule out possibility interaction between $copper^{2+}$ and the N-terminal histidine residues. Nevertheless, our data show

that in the presence as well as the absence of copper^{2+}, SMB domain binding protects against changes in dynamics that are correlated with the destabilization that is promoted as a result of copper^{2+} binding.

2.4.d Copper^{2+} Affects Protein Dynamics in the Same Regions within H2AH3A-PAI-1 and Wild-Type PAI-1

As the recent crystal structure of W175F-PAI-1 revealed a zinc positioned proximal to the two N-terminal histidines of PAI-1 at positions 2 and 3 in the protein chain (pdb: 3Q02), experiments were designed to assess whether copper^{2+} asserts its effect on PAI-1 dynamics through binding to these same residues. A form of PAI-1 was engineered with alanine substitutions for these two histidines, and HDX experiments were performed to test for copper^{2+} effects on dynamics. The example uptake plot in **Figure 2.17** compares exchange rates for active wtPAI-1 with active H2AH3A-PAI-1 in the presence and absence of copper^{2+}. Data are shown for representative peptides 46-59 (hB-hC loop) and 99-113 (hE-s1A). A complete set of uptake plots of H2AH3A-PAI-1 with and without addition of copper^{2+} are presented in **Figure 2.18**. Comparing wild-type PAI-1 to H2AH3A-PAI-1 revealed a decrease in HDX rates as a result of incorporating this double amino acid substitution into PAI-1 (**Figure 2.17**). Also, as with wild-type PAI-1, the variant shows an increase in deuterium exchange in the presence of copper^{2+} compared with H2AH3A-PAI-1 alone. Across the primary sequence, changes in dynamics due to Copper^{2+} addition occur in similar regions seen with active wild-type PAI-1 upon copper^{2+} binding (**Figure 2.18**). The regions that experience changes are apparent when the copper^{2+} effects are mapped onto the structure of H2AH3A-PAI-1 (**Figure 2.17**). The peptides spanning the hB-hC loop, hD,

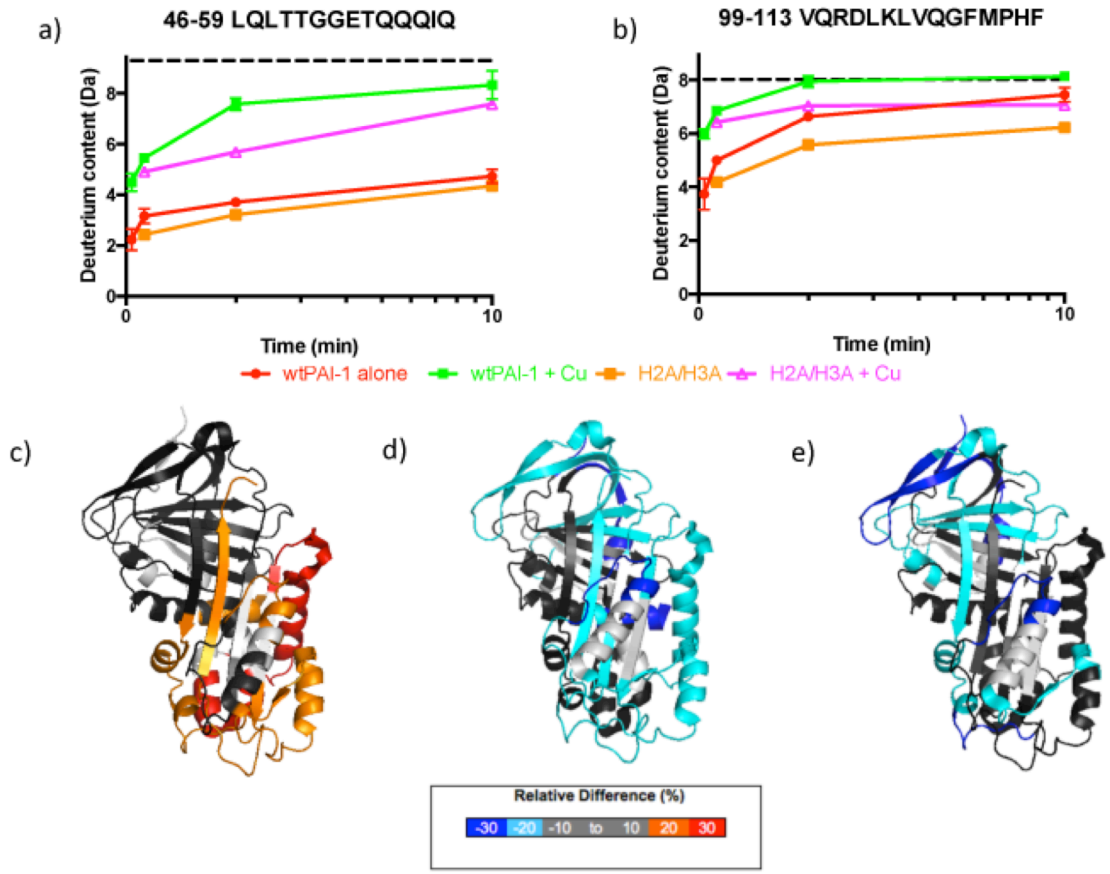

Figure 2.17 Comparing the Effects of Copper^{2+} Addition on H2AH3A-PAI-1.
Panels a and b: Deuterium uptake plots for two PAI-1 peptides in H2AH3A-PAI-1 and wtPAI-1: a- 46-59 (LQLTTGGETQQQIQ) and b-99-113 (FVQRDLKLVQGFMPHF). HDX-MS experiments were performed on wtPAI-1 (red), wtPAI-1 + copper^{2+} (green), H2AH3A-PAI-1 (purple), and H2AH3A-PAI-1 + copper^{2+} (orange). Deuterium uptake plots illustrate the increase in mass (Da) as a function of time for each peptic peptide.
Panel c: Structural heat map of copper^{2+} effects on H2AH3A-PAI-1. The normalized percent difference of deuterium uptake of H2AH3A-PAI-1 + copper^{2+} *versus* H2AH3A-PAI-1 alone for the peptic peptides **Figure 2.19** was represented on a crystal structure for active PAI-1 (pdb: 3Q02). The percent difference in deuterium uptake is determined for the three minute HDX time point, represented in the following color scheme: > -20% in dark blue, -20 to -10% in light blue, -10 to 10% in dark gray, 10 to 20% in orange, and > 20% in red. Areas of light gray signify residues for which there was no sequence coverage.
Panel d: Structural heat map of H2AH3A-PAI-1 dynamics compared with wtPAI-1. The normalized percent difference of deuterium uptake of H2AH3A-PAI-1 *versus* wtPAI-1 for the peptic peptides was represented on a crystal structure for active PAI-1 (pdb: 3Q02). The same colors representing percent differences apply for the heat map key.
Panel e: Structural heat map of copper^{2+} effects on H2AH3A-PAI-1 compared with wtPAI-1. The normalized percent difference of deuterium uptake of H2AH3A-PAI-1 + copper^{2+} *versus* wtPAI-1 + copper^{2+} for the peptic peptides was represented on a crystal structure for active PAI-1 (pdb: 3Q02). The same colors representing percent differences apply for the heat map key.

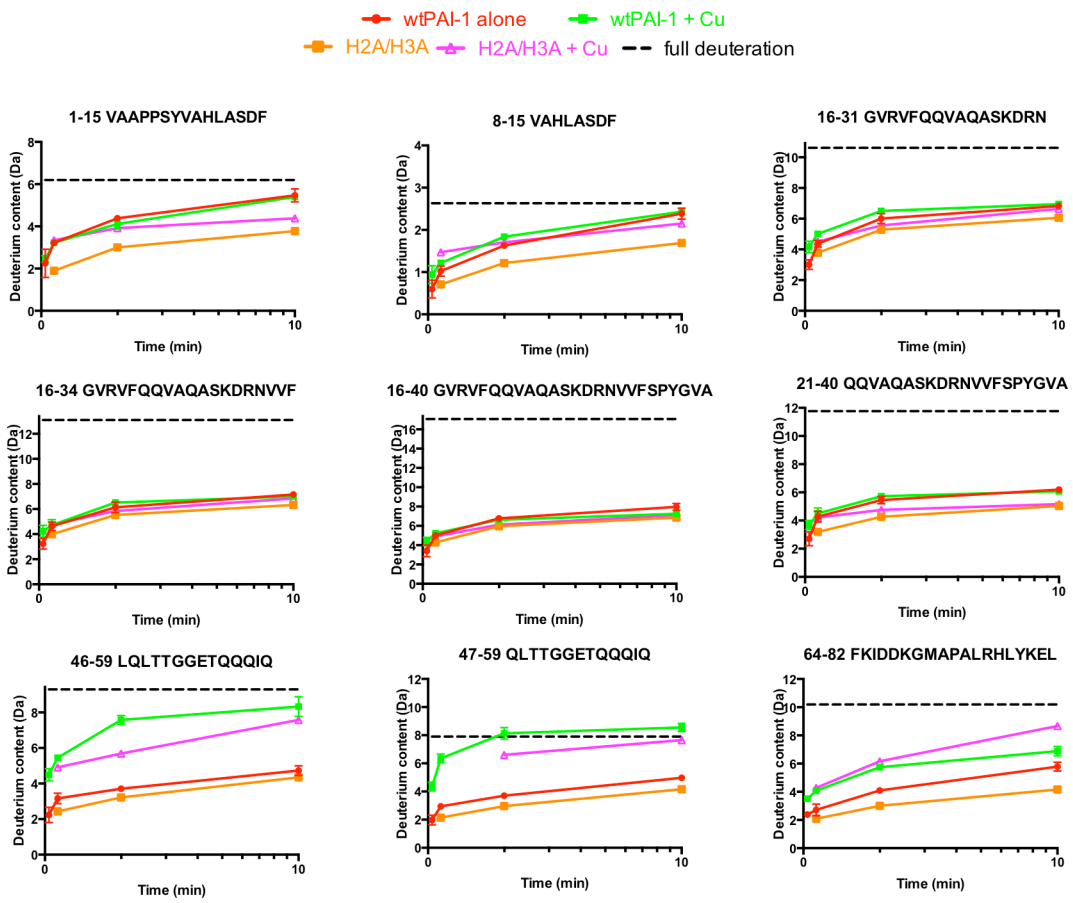

Figure 2.18 Deuterium Uptake Plots Active wtPAI-1 versus H2AH3A PAI-1 in the Presence and Absence of Copper^{2+}: HDX-MS experiments were performed on wtPAI-1 (red), wtPAI-1 + copper^{2+} (green), H2AH3A PAI-1 (magenta), and H2AH3A PAI-1 + copper^{2+} (orange). Deuterium uptake plots represent the increase in mass (Da) for the each individual PAI-1 peptide as a function of time. The mass shift of each peptide having reached full experimental deuteration is denoted by the dashed black line.

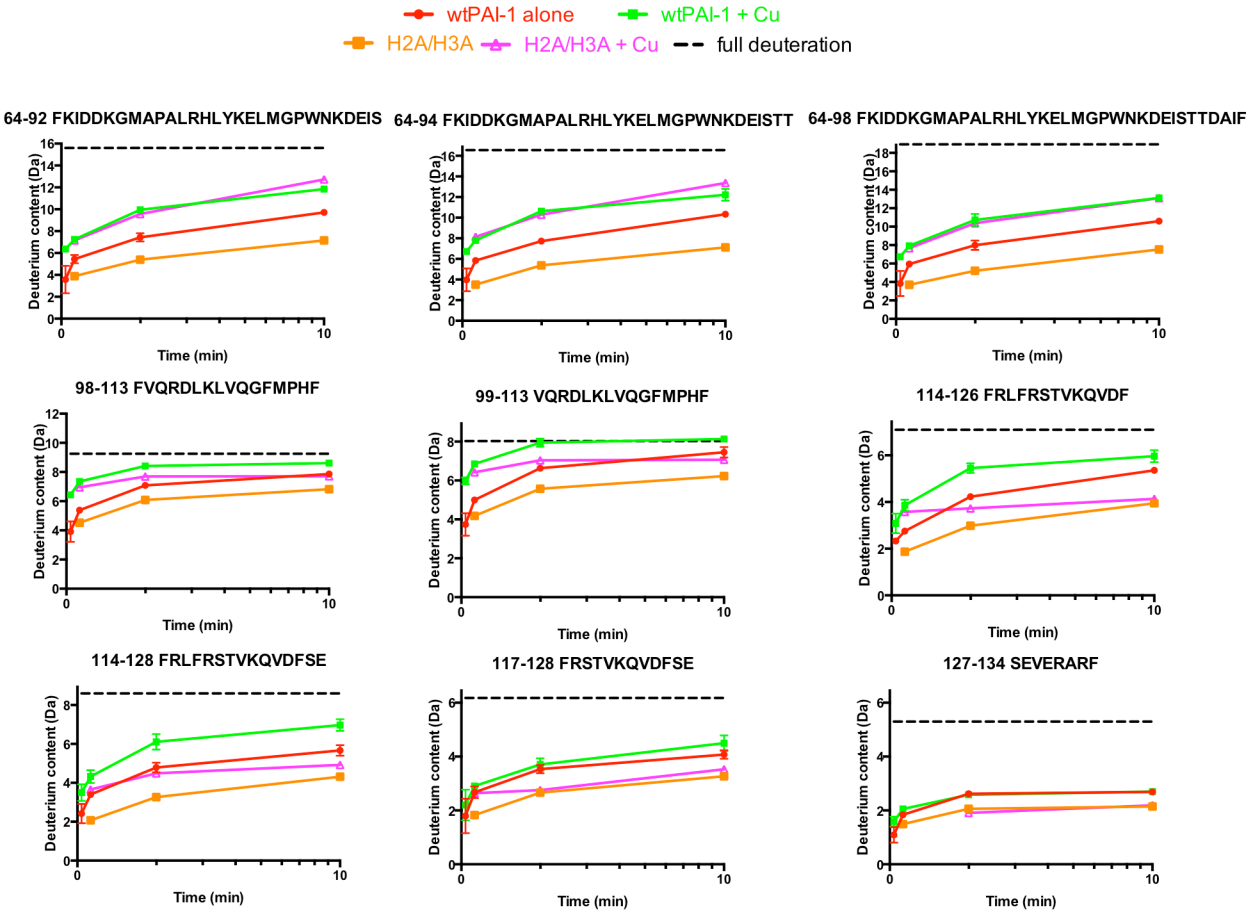

Figure 2.18 Deuterium Uptake Plots Active wtPAI-1 versus H2AH3A PAI-1 in the Presence and Absence of Copper^{2+} (cont.): HDX-MS experiments were performed on wtPAI-1 (red), wtPAI-1 + copper^{2+} (green), H2AH3A PAI-1 (magenta), and H2AH3A PAI-1 + copper^{2+} (orange). Deuterium uptake plots represent the increase in mass (Da) for the each individual PAI-1 peptide as a function of time. The mass shift of each peptide having reached full experimental deuteration is denoted by the dashed black line.

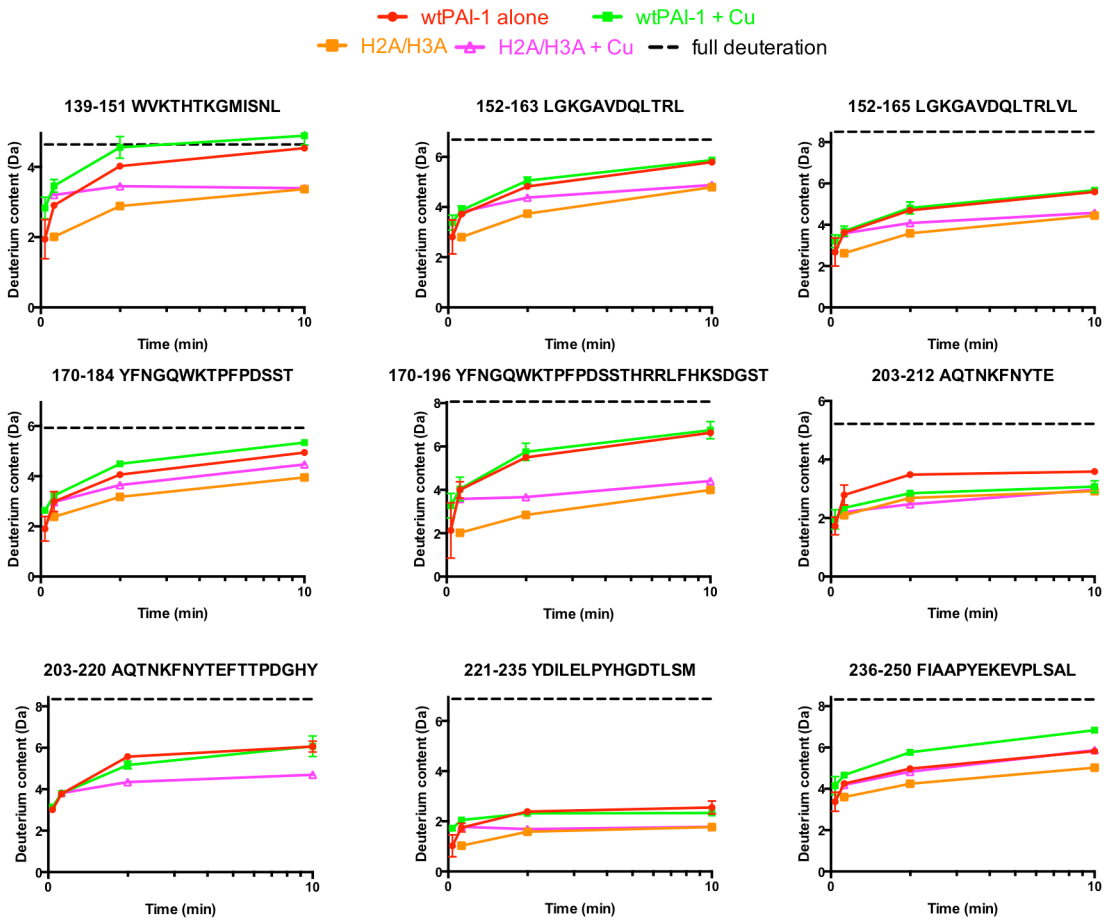

Figure 2.18 Deuterium Uptake Plots Active wtPAI-1 versus H2AH3A PAI-1 in the Presence and Absence of Copper^{2+} (cont.): HDX-MS experiments were performed on wtPAI-1 (red), wtPAI-1 + copper^{2+} (green), H2AH3A PAI-1 (magenta), and H2AH3A PAI-1 + copper^{2+} (orange). Deuterium uptake plots represent the increase in mass (Da) for the each individual PAI-1 peptide as a function of time. The mass shift of each peptide having reached full experimental deuteration is denoted by the dashed black line.

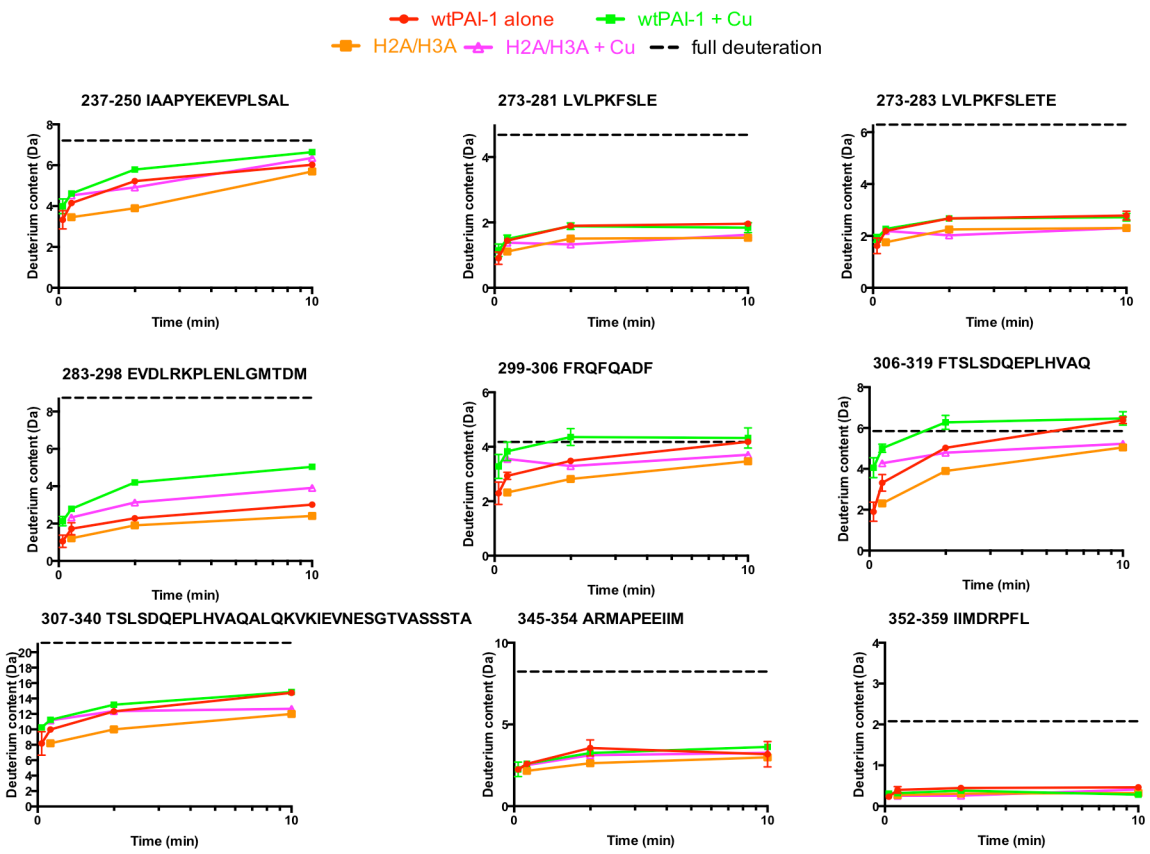

Figure 2.18 Deuterium Uptake Plots Active wtPAI-1 versus H2AH3A PAI-1 in the Presence and Absence of Copper^{2+} (cont.): HDX-MS experiments were performed on wtPAI-1 (red), wtPAI-1 + copper^{2+} (green), H2AH3A PAI-1 (magenta), and H2AH3A PAI-1 + copper^{2+} (orange). Deuterium uptake plots represent the increase in mass (Da) for the each individual PAI-1 peptide as a function of time. The mass shift of each peptide having reached full experimental deuteration is denoted by the dashed black line.

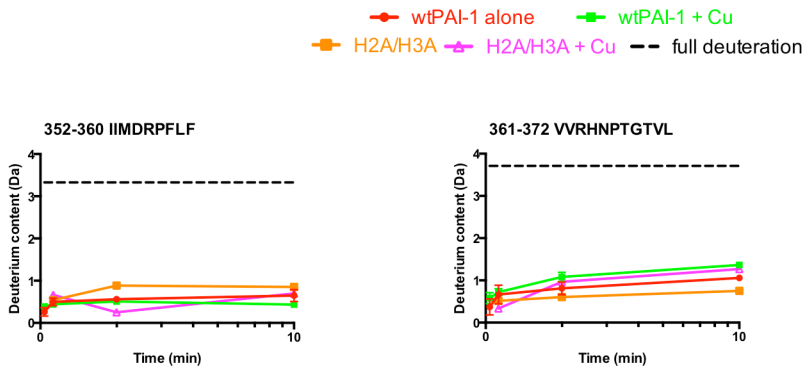

Figure 2.18 Deuterium Uptake Plots Active wtPAI-1 versus H2AH3A PAI-1 in the Presence and Absence of Copper^{2+} (cont.): HDX-MS experiments were performed on wtPAI-1 (red), wtPAI-1 + copper^{2+} (green), H2AH3A PAI-1 (magenta), and H2AH3A PAI-1 + copper^{2+} (orange). Deuterium uptake plots represent the increase in mass (Da) for the each individual PAI-1 peptide as a function of time. The mass shift of each peptide having reached full experimental deuteration is denoted by the dashed black line.

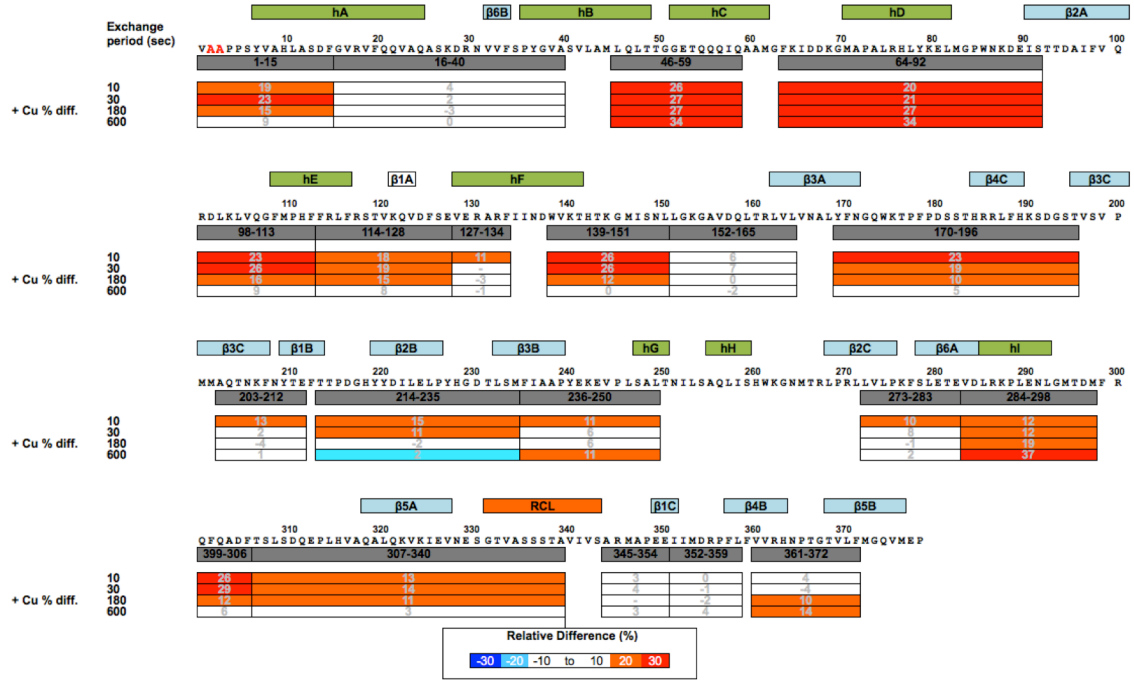

Figure 2.19 Effect of Copper^{2+} on H2AH3A-PAI-1 Dynamics, Examining the Primary Sequence. HDX data of H2AH3A-PAI-1 alone and H2AH3A-PAI-1 + copper^{2+} were acquired for comparison with wild type. Exchange data were collected for various periods listed on the far left. For each of the 4 time points, deuterium uptake of H2AH3A-PAI-1+copper^{2+} is given as a percentage relative to that observed for H2AH3A-PAI-1 alone. The data in both experimental conditions were normalized with respect to a (100%) fully deuterated control in which PAI-1 is denatured by guanidine in the presence of D_20 for 4 hours to determine the deuterium exchange in the unfolded form. The primary sequence of PAI-1 is shown along the top of each row, with secondary structure α-helices (green) and β-strands (blue) in their locations throughout the sequence. The identity of individual peptic peptides that were analyzed is represented in gray boxes along the sequence, and uptake results for each peptide at the four time points are displayed in the columns below each peptide. The listed deuterium uptake values are the percentage difference between the two experimental conditions ([H2AH3A-PAI-1 + Cu] – [H2AH3A-PAI-1 alone]). The normalized percent difference was color coded using the following scheme: Percent difference of > -20% in dark blue, -20 to 10% in light blue, -10 to 10% in white, 10 to 20% in orange, and > 20% in red.

hE, hF, hI, and s5A all have elevated exchange as a result of copper^{2+} addition, like wild-type PAI-1 (**Figure 2.15**). A structural comparison of the H2H3A and wild-type PAI-1 both in the presence of copper^{2+} exposes changes in the gate region. The dynamics of the gate region are lower in wild-type, compared with the variant, indicating a possibility of a metal ion-binding site in the region. From a structural perspective, H2AH3A variant and wild-type PAI-1 are affected by copper^{2+} in largely similar regions, including the flexible joints region and helices that border the shutter region, although there are some differences. If we compare dynamics in the absence of ligands, we observe the regions of lower dynamics that appear to result directly from the mutation at the N-terminus. **Figure 2.17** shows the difference in dynamics comparing H2AH3A-PAI-1 and wild-type PAI without ligands, and **Figure 2.17** shows the differences mapped onto the structure for the two forms of the protein with added copper^{2+}. The decreased dynamics in H2AH3A-PAI-1 at multiple sites in the protein is apparent, either in the presence or absence of copper^{2+}. One intriguing difference of note between the variant and wtPAI-1 is observed with peptides 1-15, 8-15 (hA) that include the substituted residues. These peptides are protected from exchange in the presence of copper^{2+} and SMB in wtPAI-1, but show no differences when copper^{2+} alone is added to wtPAI-1 (**Figure 2.12**). Conversely, addition of copper^{2+} results in an increase in exchange for the same peptides in H2AH3A-PAI-1. Apart from this difference, the overall response in dynamics to copper^{2+} complexation is quite similar for wtPAI-1 and H2AH3A-PAI-1 suggesting that the copper^{2+}-induced destabilization is not mediated through the binding of copper^{2+} to the two N-terminal histidines of PAI-1.

2.4.e Copper^{2+} has Modest Effects on the Dynamics of Latent wtPAI-1

Previous binding studies showed that metals ions bind to the active as well as the latent form of PAI-1, although the latter binds somewhat weaker [109]. It is therefore important to determine

whether copper^{2+} affects the dynamics of both the active and latent form of PAI-1. HDX studies were thus pursued with latent wild-type PAI-1 in the presence and absence of added copper^{2+}. In the absence of copper^{2+}, results from peptides throughout PAI-1 illustrate an almost global reduction in HDX rates that accompanies the conformational change to the latent form, consistent with previous work [91]. Furthermore, there are only minor changes in dynamics with the latent form in the presence of added. This is illustrated by deuterium uptake for all peptides (**Figure 2.20**) and also by representative uptake plots of peptides 46-59 (hB-hC loop) and 99-113 (s2A-hE) (**Figure 2.21**) and the map along the primary sequence (**Figure 2.22**). The representative uptake plots in **Figure 2.21** compare latent wtPAI-1 in the presence and absence of copper^{2+} with active wtPAI-1 in the presence and absence of ligand. A view of the copper^{2+} effect on latent wtPAI-1 is represented on the three-dimensional structure in **Figure 2.21**. While there are modest changes in dynamics for a few peptides, the differences are not localized to one region on the structure; nor are they located in regions known to influence latency conversion, or protease inactivation.

2.4.f. Copper^{2+} Accelerates Local Unfolding of an Underlying Shutter Peptide on a Time-Scale Relevant for the Latency Transition

Recent work has identified local unfolding events in PAI-1 HDX peptides that transpire on timescales relevant to the latency process [85]. The signature of an unfolding event in the HDX-MS data is the presence of bimodal isotope distributions (see methods for further explanation). In the case of a transient unfolding event, protein molecules which have not yet visited the unfolded state will yield a low mass population in the mass spectrum; whereas protein molecules that have visited the unfolded state will yield a high mass population. The mass difference between the two

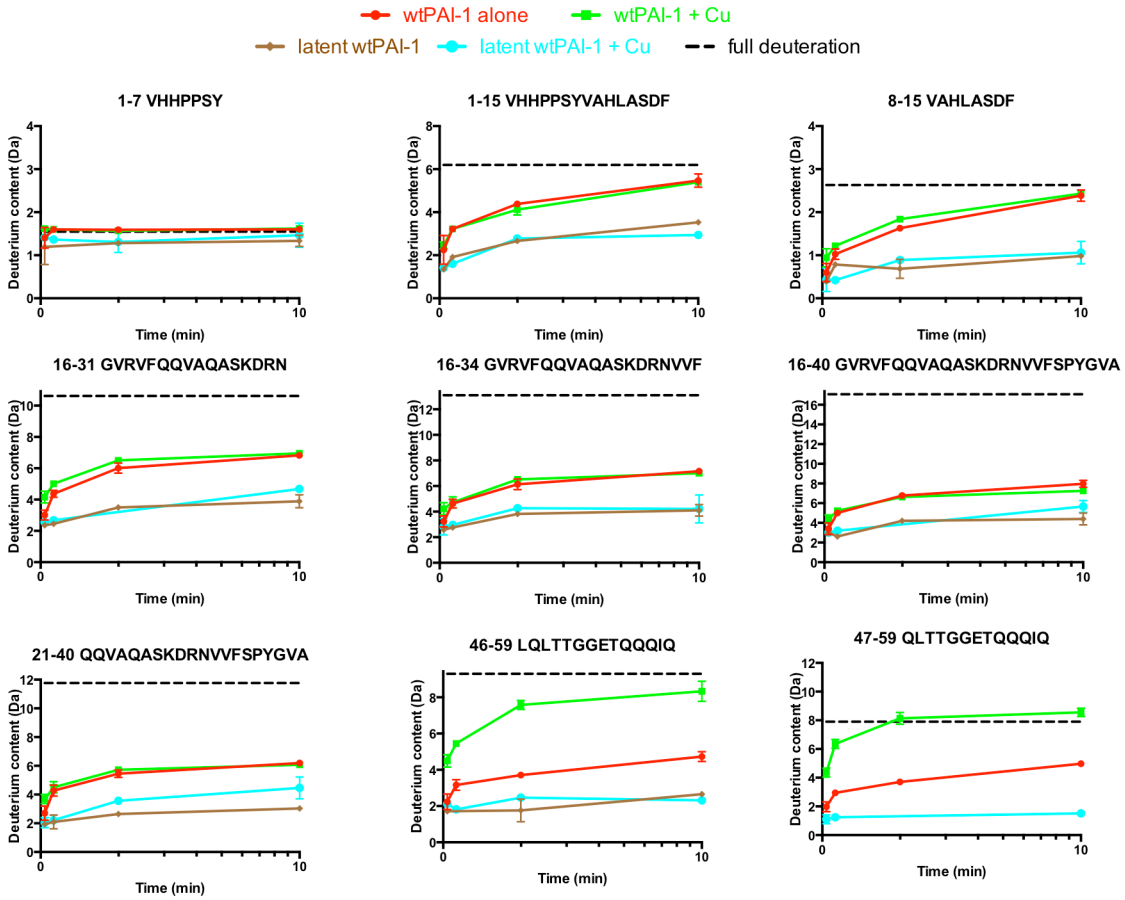

Figure 2.20 Deuterium Uptake Plots Active wtPAI-1 versus Latent wtPAI-1 in the Presence and Absence of Copper^{2+}. HDX-MS experiments were performed on wtPAI-1 (red), wtPAI-1 + copper^{2+} (green), latent wtPAI-1 (brown), and latent wtPAI-1 + copper^{2+} (teal). Deuterium uptake plots represent the increase in mass (Da) for the individual PAI-1 peptides as a function of time. The mass shift of each peptide having reached full experimental deuteration is denoted by the dashed black line.

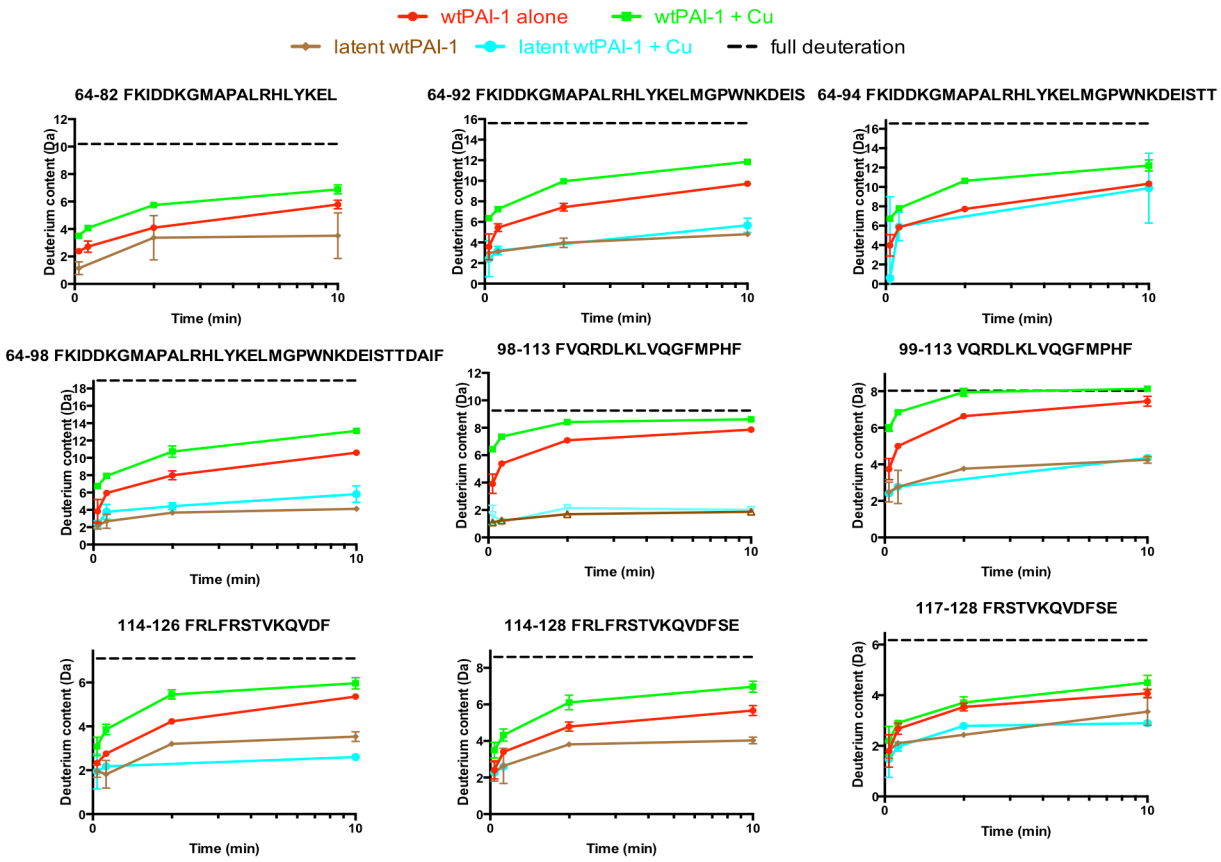

Figure 2.20 Deuterium Uptake Plots Active wtPAI-1 versus Latent wtPAI-1 in the Presence and Absence of Copper^{2+} (cont.): HDX-MS experiments were performed on wtPAI-1 (red), wtPAI-1 + copper^{2+} (green), latent wtPAI-1 (brown), and latent wtPAI-1 + copper^{2+} (teal). Deuterium uptake plots represent the increase in mass (Da) for the individual PAI-1 peptides as a function of time. The mass shift of each peptide having reached full experimental deuteration is denoted by the dashed black line.

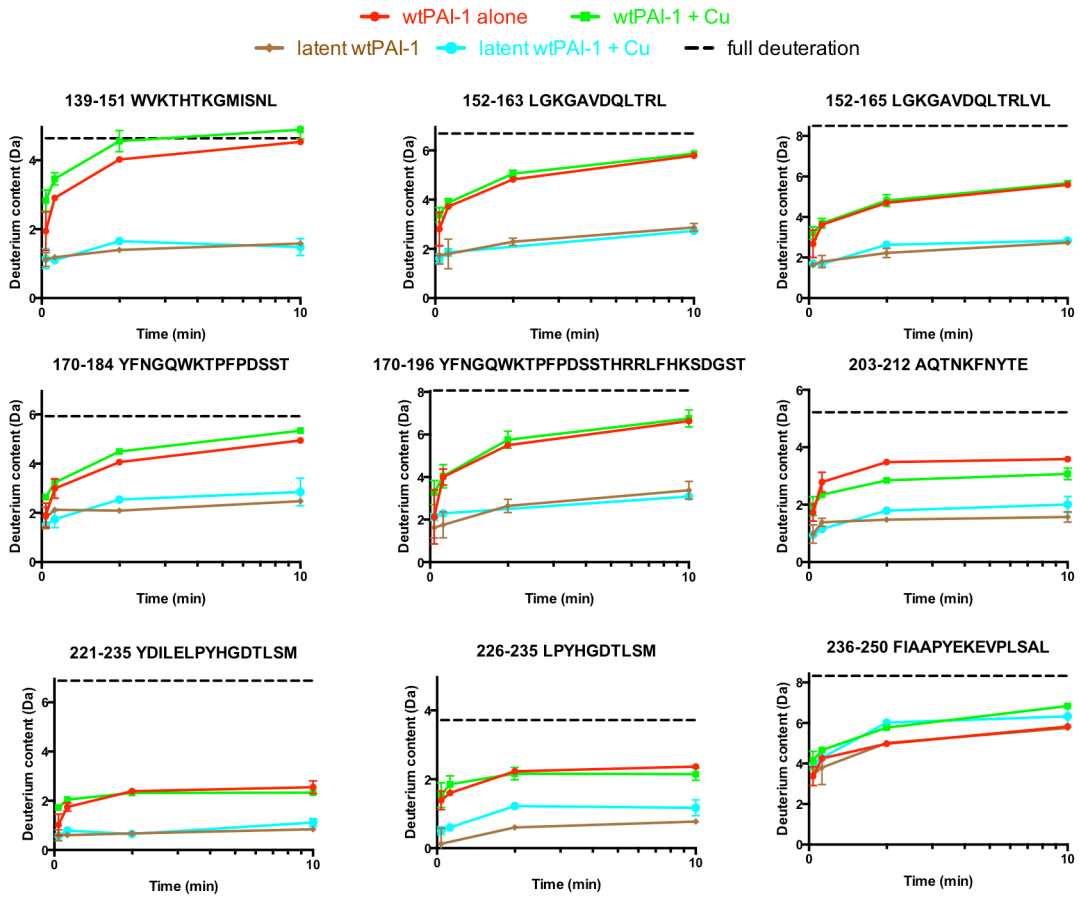

Figure 2.20 Deuterium Uptake Plots Active wtPAI-1 versus Latent wtPAI-1 in the Presence and Absence of Copper^{2+} (cont.): HDX-MS experiments were performed on wtPAI-1 (red), wtPAI-1 + copper^{2+} (green), latent wtPAI-1 (brown), and latent wtPAI-1 + copper^{2+} (teal). Deuterium uptake plots represent the increase in mass (Da) for the individual PAI-1 peptides as a function of time. The mass shift of each peptide having reached full experimental deuteration is denoted by the dashed black line.

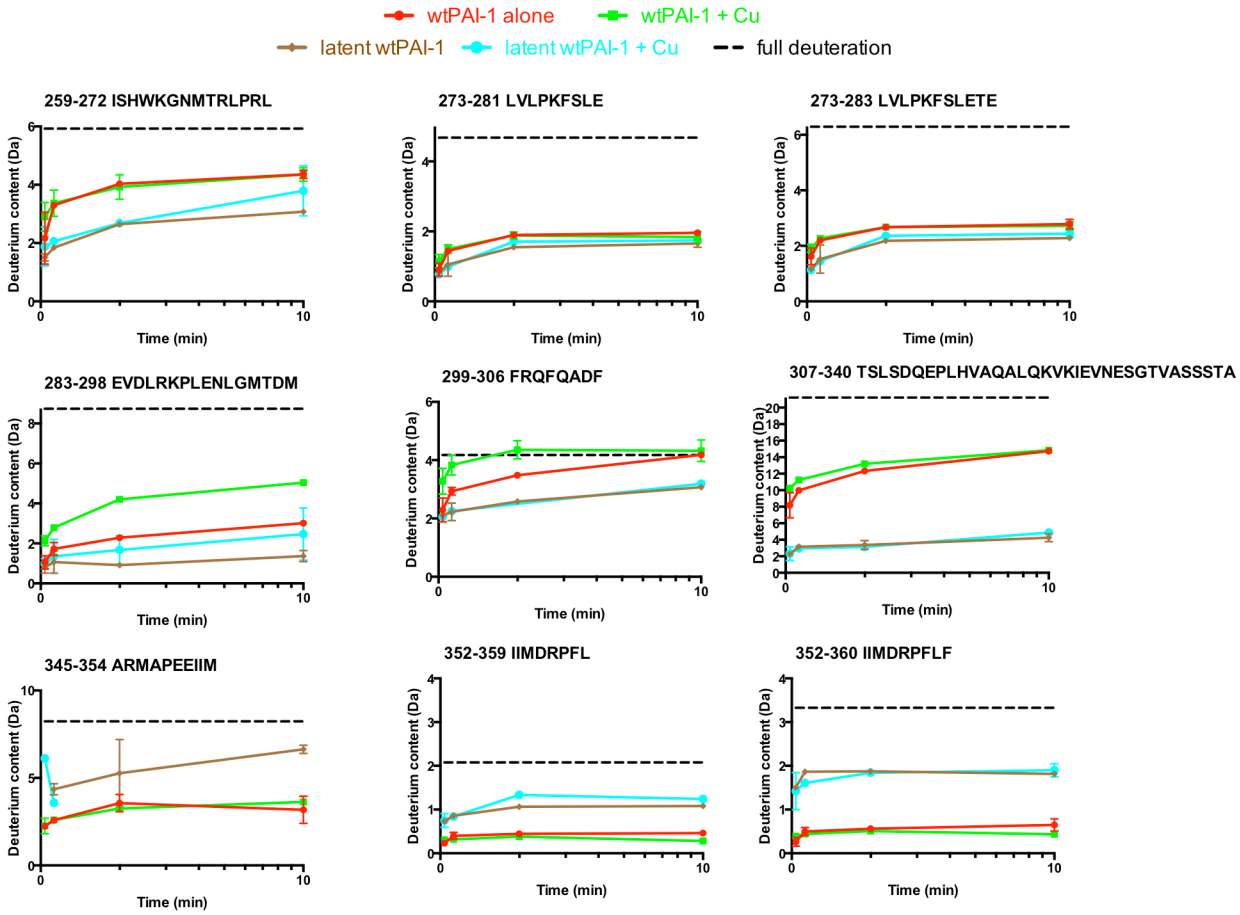

Figure 2.20 Deuterium Uptake Plots Active wtPAI-1 versus Latent wtPAI-1 in the Presence and Absence of Copper^{2+} (cont.): HDX-MS experiments were performed on wtPAI-1 (red), wtPAI-1 + copper^{2+} (green), latent wtPAI-1 (brown), and latent wtPAI-1 + copper^{2+} (teal). Deuterium uptake plots represent the increase in mass (Da) for the individual PAI-1 peptides as a function of time. The mass shift of each peptide having reached full experimental deuteration is denoted by the dashed black line.

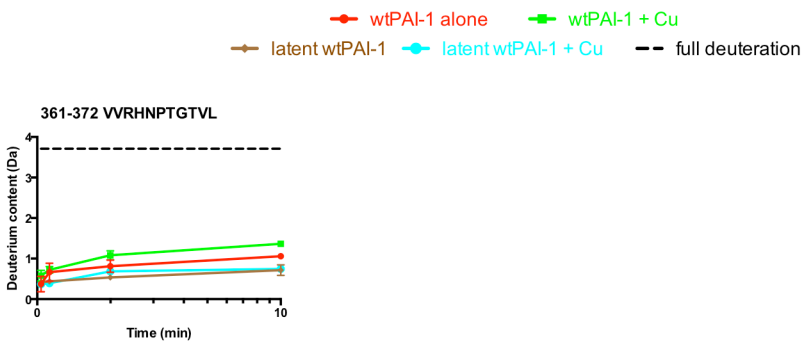

Figure 2.20 Deuterium Uptake Plots Active wtPAI-1 versus Latent wtPAI-1 in the Presence and Absence of Copper^{2+} (cont.): HDX-MS experiments were performed on wtPAI-1 (red), wtPAI-1 + copper^{2+} (green), latent wtPAI-1 (brown), and latent wtPAI-1 + copper^{2+} (teal). Deuterium uptake plots represent the increase in mass (Da) for the individual PAI-1 peptides as a function of time. The mass shift of each peptide having reached full experimental deuteration is denoted by the dashed black line.

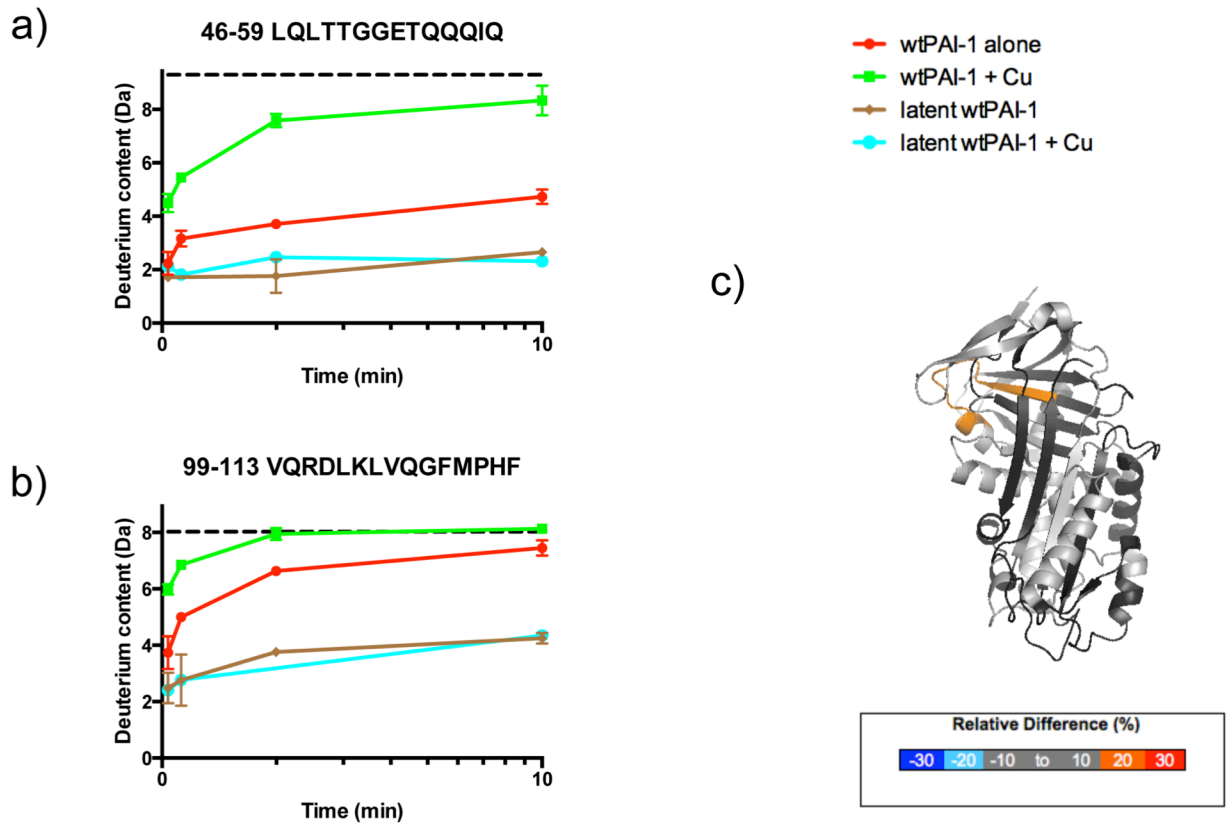

Figure 2.21 Latent wtPAI-1 Features Minimal Changes in HDX in the Presence and Absence of Copper^{2+}.

Panels a and b: Representative deuterium uptake plots comparing the effects of copper^{2+} addition in latent wtPAI-1. Deuterium uptake plots are shown for two PAI-1 peptides: 46-59 (LQLTTGGETQQQIQ) and 99-113 (FVQRDLKLVQGFMPHF). HDX-MS experiments were performed on active wtPAI-1 (red), active wtPAI-1 + copper^{2+} (green), latent wtPAI-1 (blue), and latent wtPAI-1 + copper^{2+} (brown). Deuterium uptake plots illustrate the increase is mass (Da) as a function of time for each PAI-1 peptic peptide.

Panel c: Heat map of copper^{2+} effects on a latent PAI-1 structure. The normalized percent difference of deuterium uptake of latent wtPAI-1 + copper^{2+} *versus* latent wtPAI-1 alone for the peptic peptides **Figure 2.22** was represented on a crystal structure for active PAI-1 (pdb: 3Q02). The percent difference in deuterium uptake is shown for the three minute HDX time point, represented in the following color scheme: > -20% in dark blue, -20 to -10% in light blue, -10 to 10% in dark gray, 10 to 20% in orange, and > 20% in red. Areas colored light gray signify residues for which there was no sequence coverage.

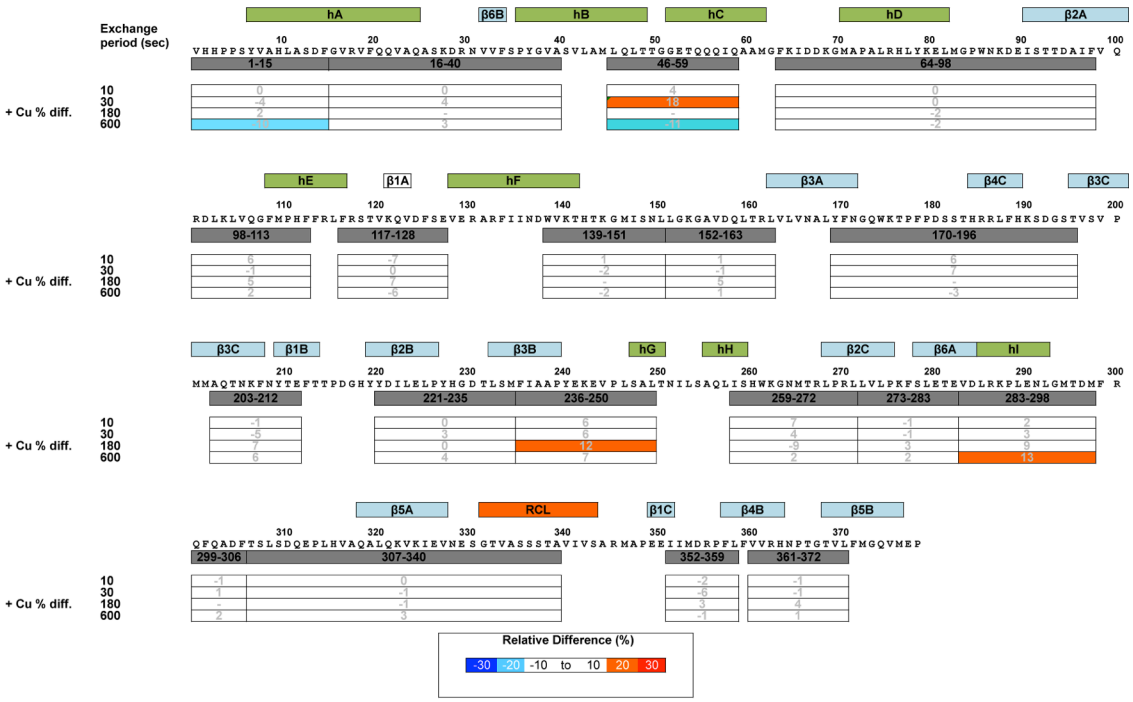

Figure 2.22 Determining the Effect of Copper^{2+} Binding on Latent PAI-1 Dynamics: Examining the Primary Sequence: Deuterium uptake of latent wtPAI-1 alone and latent wtPAI-1 + copper^{2+} were acquired for comparison with active wild type. Exchange data were collected for various periods listed on the far left. For each of the 4 time points, deuterium uptake of latent wtPAI-1+copper^{2+} is given as a percentage relative to that observed for wtPAI-1 alone. The data in both experimental conditions were normalized with respect to a fully deuterated control (100%) in which PAI-1 is denatured by guanidine in the presence of D_20 for 4 hours to determine the deuterium exchange in the unfolded form. The primary sequence is of PAI-1 is shown along the top of each row, with secondary structure α-helices (green) and β-strands (blue). The identity of individual peptic peptides that were analyzed is represented by the gray boxes along the sequence, and uptake results for each peptide at the four time points are displayed in the columns below each peptide. The listed deuterium uptake values are the percentage difference between the two experimental conditions ([latent wtPAI-1 + Cu] – [latent wtPAI-1 alone]). The normalized percent difference was color coded using the following

populations is proportional to the number of backbone amide hydrogens exposed to the solvent as a consequence of the unfolding event. The rate of unfolding can be measured as the rate at which the low mass and high mass populations interconvert. Three peptides detected in the HDX-MS experiments on PAI-1 demonstrated these events: 46-63 (hB-hC) with a $t_{1/2} \sim 80$ seconds at 15°C (< 10s at 37°C), 16-40 (hA-s6B) with a $t_{1/2} \sim 18$ minutes at 37°C, and 307-340 (s5A) with a $t_{1/2} \sim$ 24 minutes at 37°C [85]. As the HDX experiments conducted here were done at 25°C in MOPS buffer and terminated after 10 minutes of exchange, we did not sample the appropriate time and temperature to observe the unfolding of regions covered by peptides 16-40 and 307-340. The unfolding previously observed in the hB-hC peptide was much more frequent and is therefore sampled in the experiments conducted here (**Figure 2.23**). Interestingly, the change to MOPS buffer decreased the rate of unfolding significantly and only a negligible fraction of molecules have visited the unfolded state after 10 min incubation as judged by the limited peak broadening. Most importantly, addition of $copper^{2+}$ not only accelerates the unfolding event substantially ($t_{1/2}$ ~20 sec), but the spacing between the two mass populations resembles that previously observed when PAI-1 was analyzed in PBS buffer. This means that $copper^{2+}$ addition not only counteracts the effect of MOPS on the rate of unfolding, but $copper^{2+}$ also reverts the geometric extent of unfolding in the region to that observed in PBS. As expected, we also observed this bimodal peak distribution in the variant H2AH3A-PAI-1 (data not shown). Taken together, the correlation between accelerated local unfolding and accelerated latency transition upon addition of $copper^{2+}$ to PAI-1 further supports the hypothesis that unfolding events contribute in significant ways to the mechanism by which active PAI-1 rearranges to the latent inactive conformation.

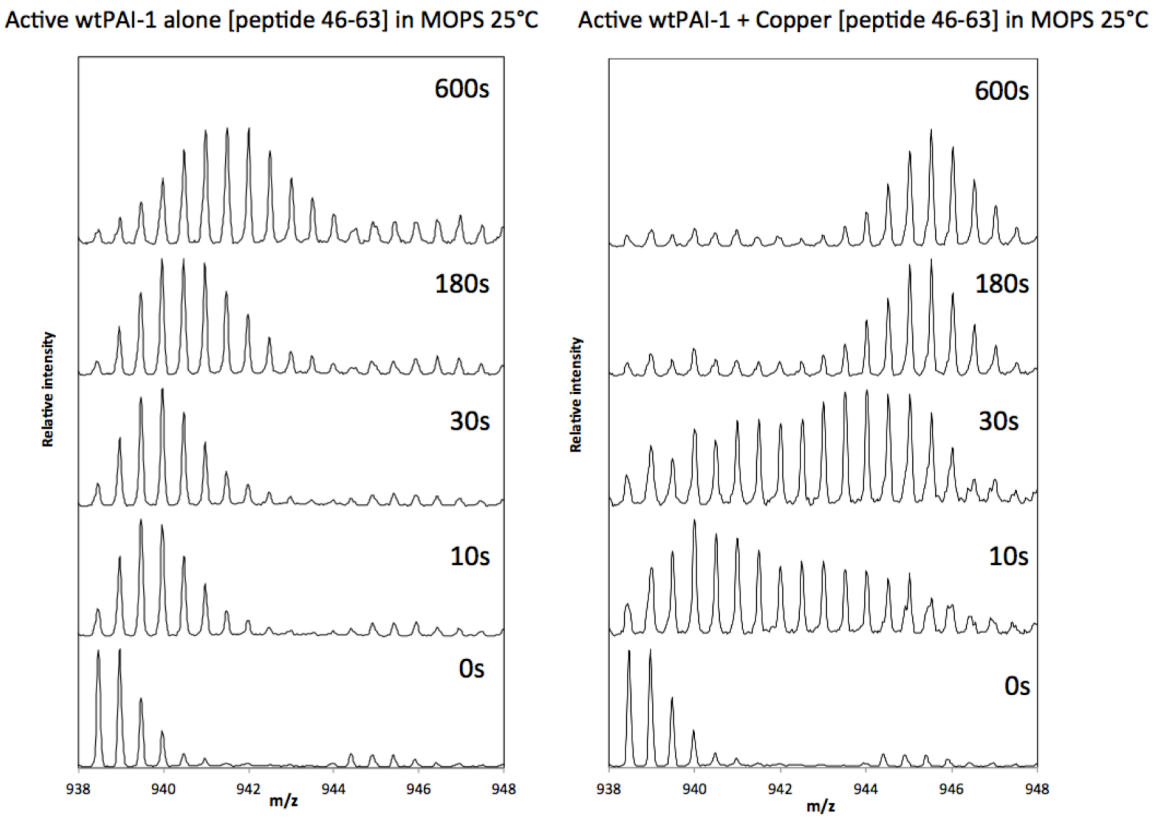

Figure 2.23 Local Unfolding Kinetics of PAI-1 Peptide 46-63 Accelerated in Presence of Copper^{2+}. The raw mass spectra of peptide 46-63 for active wtPAI-1 alone (left) and active wtPAI-1 + copper^{2+} (right) are shown for HDX time points 10, 30, 180, and 600 seconds. The peptic peptide (residues 46-63), is located underlying the shutter strands s3A/s5A), which is hypothesized to undergo local unfolding on a timescale consistent with early in the latency transition process.

2.5 Discussion

2.5.a. Copper^{2+} Increases Dynamics in Similar regions Protected by the SMB Domain

Copper^{2+} significantly destabilizes PAI-1 in the absence of VN, but substantially enhances the delay of latency conversion of the presence of VN. Since the SMB domain of VN curtails PAI-1 dynamics [91], we hypothesized that copper^{2+} addition would increase isotopic exchange if protein dynamics have a regulatory role in the rate of transition. We observed that the same regions that are more dynamic in the presence of copper$^{2+,}$ become stabilized in the presence of SMB domain, supporting our hypothesis. The flexible joint region, gate region, and shutter region are known to be involved in steps in the mechanism for the structural transition of PAI-1 from the active to latent form [83, 96, 105, 141]. The observed changes in dynamics were in predominantly overlapping regions affected by binding of the SMB domain and copper^{2+}, including the flexible joint region, and N-terminal part of hF [142]. Additionally, we observed changes due to copper^{2+} addition in the area underlying the shutter strands in hB-hC and the proximally located hI. Importantly, the altered dynamics were not a global effect, but were localized structurally. In other words, some dynamic, as well as protected regions of PAI-1 were unaffected as a result of copper^{2+} binding in our data.

Prior biochemical and HDX work was conducted on PAI-1 in the presence of Mab-1 antibody [138] and RNA aptamers [103] to evaluate their stabilizing effects. These ligands bind to PAI-1 in the flexible joint region as well as to hC in the case of the antibody [103]. Mab-1 binding stabilizes PAI-1 by 1.4 fold [138], while the aptamers do so by 3-4 fold [103]. Strikingly, peptides spanning

this region also reported decreased exchange in the presence of the Mab-1 [91], aptamers [139], and the SMB domain [91], albeit with differing protection patterns for the various ligands. The binding of copper^{2+} accelerates the latency transition [79] and strongly increased HDX exchange for peptides spanning helices hB, hC, and hI. Taken together, these findings add to the evidence that the dynamics of hB, hC, and hI have an important role in the latency transition process [139].

Our results feature more protection than in previous studies, caused by the buffer optimization from PBS to MOPS for metal ion studies. This switch was vital for maintaining an appropriate dynamic window for PAI-1 in the presence of a ligand that increases exchange. In the experiments using PBS buffer, many of the peptides reach full deuteration during the early time points [91]. The buffer change to MOPS helped maintain an adequate dynamic window for monitoring HDX with a ligand that increases PAI-1 dynamics. The tendency of phosphate to precipitate divalent metal ions precluded the use of PBS, but it allowed us to observe copper^{2+} effects that increased exchange rates of an already dynamic unligated form of active wtPAI-1. On the other hand, changing to MOPS buffer hindered our ability to measure changes in exchange of less dynamic species. For example, binding of the SMB domain to PAI-1 protected HDX in peptides of the flexible joint region in MOPS, but the effect was markedly less compared to the same HDX experiment in PBS [91]. Binding of SMB and copper^{2+} to PAI-1 results in a 2.5 fold stabilization compared with just binding of SMB [79]. One would expect to observe further protection from exchange with both ligands present compared to just SMB, but our experimental conditions showed no difference between them. The MOPS buffer system incurring a stabilizing structural effect on PAI-1 provides at least a partial explanation for this result.

2.5.b. Copper^{2+} Does Not Bind PAI-1 N-terminal Histidines to Mediate Changes in Dynamics

The most recent PAI-1 crystal structure provided amino acid residue targets from the N-terminus and gate region (H2, H3, E212, D222, E350, E242) as potential metal ion ligands [95]. We hypothesized that copper^{2+} may bind to the N-terminal residues to increase dynamics. If this hypothesis was correct, we would expect this increases of dynamics in a variant lacking these residues to be eradicated. We first observed a global decrease in dynamics as a result of the mutations, the source of which remains unclear. Nonetheless, it was clear that H2AH3A-PAI-1 follows a similar pattern as the wild-type protein regarding dynamic changes in the presence of copper^{2+}. Altogether, these data indicate that the N-terminal histidines are not the residues that coordinate metal to produce elevated dynamics and accelerated latency transition kinetics.

2.5.c. Latent wtPAI-1 is Insensitive to Copper^{2+} Effects on Dynamics

A global reduction in dynamics was observed when comparing active and latent PAI-1, due to the conformational change that yields a more compact, rigid structure. The only region with increased exchange in the latent form of PAI-1 is in the gate region, due to the widening of β-sheet C strands that is necessary to allow for the RCL to pass through during loop insertion. Addition of copper^{2+} to latent PAI-1 resulted in modest increases in exchange from a few isolated peptides, but had no effect on the flexible joint region. Copper^{2+} addition had minimal influences on dynamics near the gate region, an area that opens up as a result of conformational shift to the latent state. Although there could be several reasons for these observations, the most likely interpretation lies at the heart of the study. That is the metastable nature of PAI-1 that keeps it poised for protease inactivation

and drives it toward a timed inactivation as it converts to a latent form. Clearly, active PAI-1 is highly dynamic and sensitive to ligands that promote changes in protein dynamics that influence the overall conformation. Latent PAI-1 is inherently restricted in dynamics and thus not as prone to effects upon ligand binding.

2.5.d. Copper^{2+} Accelerates an Early Unfolding Related to the Latency Transition

As mentioned above, the need to perform experiments on copper^{2+}, a ligand that increases PAI-1 H-D exchange rates, required a modification of experimental conditions (temperature and buffer) to slow the exchange rates within a measurable window. This adjustment offered an opportunity for us to observe a local unfolding event that occurs in the timeframe of the experiment. This is local unfolding of peptide 46-63 (hB-hC) that occurs with a $t_{1/2}$ of 80 seconds at 15°C, and $t_{1/2}$ < 10 seconds at 37°C in PBS buffer [85]. The observation of local unfolding in this region provides some insight into the mechanism by which copper^{2+} exerts its effect and promotes the conformational change toward latency. In the present study, the same peptide (peptide 46-63) experiences local unfolding, in MOPS buffer in 10 minutes at 25°C, but the experimental timescale would have to be extended to view the local unfolding kinetics completely. The addition of copper^{2+} under these conditions decreased the $t_{1/2}$ to ~ 30 seconds. Since PAI-1 has a half-life for conversion to the latent form (37°C) of approximately 1 hour, with a decrease to 10 minutes upon binding of copper^{2+}, these rates of local peptide unfolding observed by HDX likely correspond to early events in the latency transition process. The other peptides (16-40 and 299-306) have $t_{1/2}$ for unfolding values on the order of the latency transition process itself [85]. It is important to note that we also observe local unfolding in peptide 46-63 of

H2AH3A-PAI-1 with copper^{2+} bound, indicating that copper^{2+} exerts it effects on PAI-1 by binding elsewhere than the two N-terminal histidines. Taken together, these results show that copper^{2+} binding facilitates an early transition presumed to be on the pathway to latency.

2.6. Conclusions

The major objective of this work was to investigate the effects of copper^{2+} on protein dynamics of PAI-1 in the active, latent, and SMB bound forms, as well as the active variant H2AH3A. PAI-1 functions in concert with VN at sites of injury in the vasculature to control hemostasis, and associates with the extracellular matrix of healthy and pathological states such as inflammatory response, tumor development, obesity. In circulation, tissue, and extracellular stores, copper^{2+} has involvement in these same pathophysiological conditions, although it is less well understood. Our recent finding of copper^{2+} effects on PAI-1 inhibitory activity and stability in the active form, which are dependent on the presence of VN [79], stimulated our interest in how protein dynamics could be correlated to function. In the presence of copper^{2+} concentrations that are physiologically relevant, PAI-1 converts to the latent form faster and exhibits increased dynamics. In the presence of SMB or both ligands, which stabilize PAI-1 in the active form, leads to decreases in dynamics of the very same regions within PAI-1. The binding of SMB domain negates copper^{2+} effects when both are present, resulting in similar protection to when SMB alone is bound to PAI-1. Since copper^{2+} accelerates the latency transition, but the SMB domain delays conversion to the latent state, these data on the dynamic behavior of PAI-1 agree well with the measurement of PAI-1 latency conversion in the presence of the ligands using kinetic approaches [79]. In addition to many of the known structural features of PAI-1 involved in the transition process, including the flexible joint region, shutter region, and gate region, the dynamics of

helices hB-hC-hI emerge as important factors that determine conformational stability. Moreover, local unfolding observed in a peptide spanning hB-hC, this unfolding transpires with an accelerated half-life in the presence of copper^{2+}. The timescales indicate this local unfolding event takes place early in the latency conversion process. Observation of the unfolding events upon copper^{2+} addition suggests that PAI-1 undergoes a similar path to the latent state in the presence and absence of copper^{2+}. The results of this study indicate that protein dynamics influence the PAI-1 latency transition process. Examination of ligands that stabilize and de-stabilize PAI-1 show that they decrease and increase dynamics, respectively. Therefore, physiologically important metal ion ligands that influence the latency transition in a VN-dependent manner affect changes by shifting protein dynamics in important regions of PAI-1. Our findings that ligands have specific effects on protein dynamics is particularly intriguing since PAI-1 is a metastable protein that converts from active to inactive conformations under physiological conditions. These effects of copper^{2+} on PAI-1 offer a mechanistic understanding of the peculiar metal ion effects, dependent on vitronectin, which can affect stability in a variety of biological compartments in which copper^{2+} and PAI-1 are implicated in disease.

Chapter 3 Identification and Functional Characterization of PAI-1 Metal Ion Binding Site

3.1. Introduction

3.1.a. Metal Ion Effects on PAI-1

Our laboratory has recently uncovered unexpected effects of transition metals on the rate of PAI-1 latency transition, and these effects are dependent on the presence of VN. PAI-1 transition metal ion affinity was first discovered through binding to an immobilized metal ion affinity column (IMAC) without requiring a 6x histidine tag [79]. IMAC resin charged with divalent metal ions such as maganese^{2+}, cobalt^{2+}, nickel^{2+}, copper^{2+}, and zinc^{2+} bound to PAI-1, albeit with varying affinities [79]. Several of the aforementioned transition metal ions, along with physiologically relevant alkali earth metal ions calcium^{2+}, and magnesium^{2+}, were incubated with PAI-1 to determine effects on the half-life of active PAI-1 in the presence and absence of VN [79]. PAI-1 alone remains active with a half-life of 70 minutes, whereas PAI-1 with VN exhibits some stabilization with a longer half-life of 90 minutes. PAI-1 is slightly stabilized in the presence of Ca^{2+}, Mg^{2+}, and Mn^{2+}, and the same modest stabilization is observed when these metal ions are incubated with PAI-1 and VN [79]. Cu^{2+}, Ni^{2+}, and Co^{2+} have a much more dramatic effect, significantly destabilizing PAI-1 ($t_{1/2}$ ~ 10 minutes). Notably, the binding of VN and the transition metal ions provide significant stabilization ($t_{1/2}$ ~ 3-4 hours) [79].

PAI-1 is stabilized primarily through the N-terminal SMB domain of VN interacting with the flexible joint region of PAI-1 [97]. However, the proteins have an extended binding interface that extends beyond the SMB domain of VN [98, 100]. Do the observed copper^{2+} effects on stability occur through binding to PAI-1, VN, or a combination of both proteins at their binding interface?

This was tested through stability measurements on PAI-1 in which the effects of SMB domain were compared with full length VN. In measurements including the SMB and copper^{2+}, the half-lives were comparable to those measured of full length VN with copper^{2+} [79], demonstrating that observed metal ion effects are mediated through PAI-1, the SMB domain, or a combination of both when they interact. Additionally, gel based activity assays were completed to monitor the relative amounts of tPA-bound, latent, and substrate-like PAI-1 in the presence of metal ions. Significantly more latent PAI-1 was observed for destabilizing metal ions Cu^{2+}, Ni^{2+}, and Co^{2+} compared to the stabilizing metal ions [79]. In addition, these metal ions (most notably copper^{2+}) appear to promote PAI-1 substrate-like behavior [79]. This indicates that copper^{2+} affects the rate limiting step of inhibition (refer to **Figure 1.4**) in which the rate of RCL insertion (k_{lim}) determines if full inhibition or release of the protease occurs.

The binding of different forms of PAI-1 to metal ions was also characterized by surface plasmon resonance (SPR), competition assays, and stopped-flow kinetics [109]. Active as well as latent PAI-1 bind immobilized nickel^{2+} on the SPR chip in the low micromolar range, with the latter binding 3.5 fold weaker [109]. High concentrations of Mg^{2+} were able to competitively inhibit PAI-1 binding to immobilized nickel^{2+}, which indicates that the metal ions bind in the same location, despite their difference in effects on PAI-1 stability [109]. Other methods were used to characterize ion binding to PAI-1 for each metal, since metal ions like Mg^{2+} and Mn^{2+} modestly stabilize PAI-1, whereas the transition metal ions display more dramatic effects. Stopped-flow experiments monitoring intrinsic tryptophan fluorescence determined binding differences in PAI-1 comparing the effects of the metal ions tested. Binding of metal ions that stabilize PAI-1 (Mg^{2+}, and Mn^{2+}) fit best to a double exponential equation while the binding behavior of those that

destabilized PAI-1 (Cu^{2+}, Ni^{2+}, and Co^{2+}) fit best to a triple exponential equation [109]. In other words, metal ions that featured the same effects in the stability assay exhibited the same binding via stopped-flow. In the case of the destabilizing metal ions, the intrinsic fluorescence has an initial decrease that is concentration dependent, indicating that it is likely a binding phase [109]. Following this initial binding, the intrinsic fluorescence exhibits a biphasic increase that is not concentration dependent [109]. The first of the two phases represents the occurrence of an unknown conformational change, and the last phase is attributed to the latency conversion, as this occurs with a rate constant near that of latency conversion measured by the stability kinetics assay [109]. $Copper^{2+}$ binds PAI-1 at low nanomolar concentrations, while $nickel^{2+}$ and $cobalt^{2+}$ bind at much higher micromolar concentrations, determined by the binding phases of the approach to equilibrium data [109]. Stability kinetics experiments involving two different metal ions provided further evidence that the metal ions bind in the same location [109]. When PAI-1 is incubated with saturating concentrations of Cu^{2+} and either Mg^{2+}, or Ni^{2+}, the kinetics of latency observed appear to represent an "average" of the effects exhibited by either individually [109], and support the notion that the metal ions were competing for binding to the same site on PAI-1.

The main aim of the work described in this chapter is to understand the molecular basis for metal ion effects on PAI-1. Several questions were raised- Where do metal ions, particularly $copper^{2+}$, bind to PAI-1? How does $copper^{2+}$ binding accelerate latency conversion of PAI-1? How do $copper^{2+}$ and VN (or SMB domain) stabilize PAI-1 more so than VN can alone? To address these questions, we pursued a mutagenesis approach to test for specific residues involved in metal ion binding, based on predictions from the PAI-1 crystal structure. Stability kinetics assays in the presence and absence of metal ions were performed on the PAI-1 variants to assess if the rate of latency conversion was altered due to the mutations. Also, we used a gel based metal ion titration

assay to determine metal ion sensitivity changes due to incorporation of mutations. Finally, we characterize copper^{2+} binding to wild-type and variant PAI-1 using isothermal titration calorimetry (ITC). Taken altogether, the results support a model with multiple specific metal-binding sites on PAI-1 that are localized to particular regions that influence the active to latent transition in different ways.

3.1.b. A Search for Potential Metal Ion Binding Sites on PAI-1

Interestingly, the active W175F PAI-1 crystal structure featured a zinc ion coordinated in the asymmetric dimer interface of the crystal (**Figure 3.1**) [95]. Carboxylate containing gate region residues E212, D222, E242, and E350 contribute to coordination from one PAI-1 molecule, and N-terminal histidine residues H2, and H3 from another PAI-1 [95]. This structure presented potential metal ion coordination residues that could be responsible for metal ion effects imparted on PAI-1. To computationally predict metal ion binding clusters within PAI-1, we also used a modified version of the MUltiple Geometries (MUG) algorithm that predicts calcium^{2+} binding clusters within proteins. The algorithm identifies several oxygen containing amino acid residues in close spatial proximity on crystal structures. Metal ions such as calcium^{2+} or magnesium^{2+} are classified as harder, less polarizable acid ligands, which are coordinated by relatively harder oxygen containing bases. These metal ions are often found in octahedral coordination geometry. By contrast, transition metal ions such as copper^{2+} or nickel^{2+} are softer, more polarizable acid ligands that are typically coordinated by softer nitrogen or sulfur containing bases. These metals are most often found in tetrahedral coordination geometry.

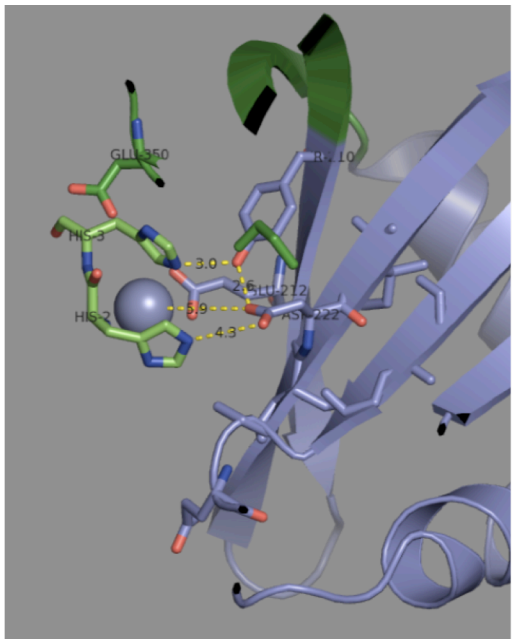

Figure 3.1: W175F PAI-1 Crystal Structure Residues Coordinating Zinc^{2+} Ion in Asymmetric Dimer Interface. The active PAI-1 crystal structure containing only one mutation (W175F) coordinated a zinc ion with N-terminal histidines (H2, H3) of one PAI-1 molecule (green, left), and carboxylate groups (E212, D222, E242, E350) of the gate region contributing to coordination from the second PAI-1 molecule (purple, right). This interface is situated at the asymmetric dimer interface of the crystal lattice. From Jensen et al., JBC. 2011.

Because of these differences, our collaborator, Dr. Jenny Yang, modified the MUG algorithm to include nitrogen and sulfur containing amino acids histidine and cysteine in the spatial cluster proximity prediction. It should be noted that there are 13 histidines and no cysteines within PAI-1. The modified metal ion binding cluster prediction was performed on the active 14-1b PAI-1 crystal structure (pdb code 1B3K). Five potential binding clusters were identified through the computational search (**Figure 3.2**). Of most interest were two binding clusters because of the functional relevance of their locations on PAI-1. A binding cluster featuring E212, D222, E242, and E350 residues of the gate region were the same residues observed to bind zinc in the crystal structure. There was also very interesting binding cluster that included E81 of hD, and H364 of s4B somewhat proximal to the N-terminal histidines in the crystal structure. Importantly, Mangs et al. completed a study in which all of the histidines of PAI-1 were mutated and characterized to investigate their role in stabilization of the active form at lower than physiological pH [92]. This work identified one histidine that is primarily responsible for the pH sensitive activity of PAI-1, and also showed that mutation of other histidines can produce significant amounts of latent PAI-1 in the purified fractions [92].

A sequence alignment was performed for the residues predicted in possible metal ion binding sites: H2, H3, E81, E212, D222, E242, E350, and H364, comparing different PAI-1 species, as well as other serpins (**Figure 3.3**). PAI-1 from different species retains strong sequence conservation of all the residues aligned except for H2, and H3. However, within serpins, these residues are far less conserved, with only E242 retaining conservation among different serpins. Based on this evidence, we chose to investigate the following sites in the study: Site A comprising the N-terminal histidines; Site B comprising E81 and H364; and Site C of the gate region

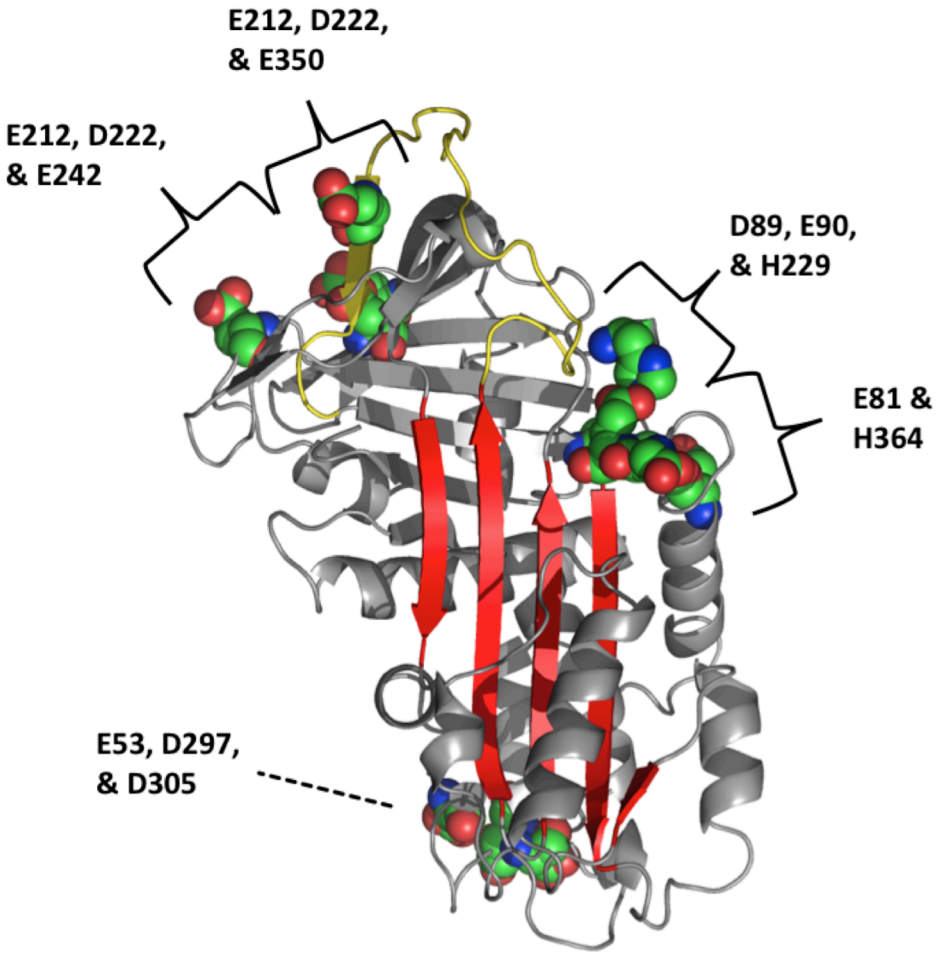

Figure 3.2 MUG Algorithm Copper^{2+} Binding Clusters within PAI-1. In collaboration with Jenny Yang at Georgia State, copper^{2+} ion binding clusters were predicted. The following clusters were identified in the prediction: E212, D222, E242; E212, D222, E350; D89, E90, H229; E81, H364; E53, D297, D305. The clusters are represented on the active PAI-1 structure (pdb 3q02) with the side chains as green, red, and blue space filling spheres. The RCL is represented in yellow, the central beta sheet is represented in red. The remainder of PAI-1 is shown in gray.

	PAI-1 amino acid position							
	2	**3**	**81**	**212**	**222**	**242**	**350**	**364**
Human	**H**	**H**	**E**	**E**	**D**	**E**	**E**	**H**
Rat	P	L	**E**	D	**D**	**E**	T	**H**
Pig	S	**H**	**E**	**E**	**D**	**E**	**E**	**H**
Mouse	P	L	**E**	**E**	**D**	**E**	T	**H**
Monkey	**H**	**H**	**E**	**E**	**D**	Q	**E**	**H**
Bull	Y	Q	**E**	**E**	**D**	**E**	**E**	**H**
α1-Antitrypsin			T	H	V	**E**	**E**	E
Antichymotrypsin			T	H	**D**	M	T	P
Antithrombin			K	R	Q	**E**	R	E
Neuroserpin	R	**H**	M	**E**	Q	**E**	Q	N
α2-Anti-Plasmin	K	S	R	L	Q	E	S	E

Figure 3.3: Sequence Alignment of Investigated Residues in PAI-1 Species and other Serpins. The human PAI-1 residues hypothesized to be involved in metal ion binding clusters were compared by sequence alignment with PAI-1 from with other species and other serpins using BLAST to assess the level of sequence identity of these residues within PAI-1 and the serpin family. Human PAI-1 was aligned with rat, pig, mouse, monkey, bull sequences, and also related serpins α1-anti-trypsin, anti-chymotrypsin, anti-thrombin, neuroserpin, and α2-anti-plasmin. The residues that retain identity with human PAI-1 are identified in bold.

containing E212, D222, E242, and E350. The three hypothesized metal ion clusters will be referenced in this way henceforth for clarity.

3.1.c. Isothermal Titration Calorimetry

Isothermal titration calorimetry (ITC) is a technique that directly measures the enthalpy change of an interaction to obtain thermodynamic parameters such as Gibbs free energy change (ΔG), enthalpy change (ΔH), entropy change ($T\Delta S$), affinity (Ka), and stoichiometry (n) (**Figure 3.4**). The instrument has a reference cell held at constant temperature, maintained by constant power from the reference heater. The instrument also has an experimental cell, where (in most experiments) the sample to be tested is loaded. Prior to the start of the experiment, the experimental cell temperature is equilibrated to the reference cell within tenths of a degree Celsius. The syringe typically contains the titrant, which is delivered into the experimental cell by sequential injections over set intervals. When ligand is injected and interacts with protein, the temperature changes depending on the type of reaction taking place. If an endothermic reaction takes place, the cell temperature decreases; it is then re-equilibrated to the reference cell by feedback power. If an exothermic reaction occurs, the temperature increases and the opposite occurs to re-equilibrate the temperature with the reference cell. This injection and re-equilibration process is repeated until the amount of ligand saturates the binding sites on the protein, manifested by injections with negligible heat change.

The raw data are displayed as the μcal/sec power used to re-equilibrate as a function of the experimental time over the course of the experiment with multiple injections. The reaction taking place as a result of each injection causes a release or absorption of heat (q_i), which is directly

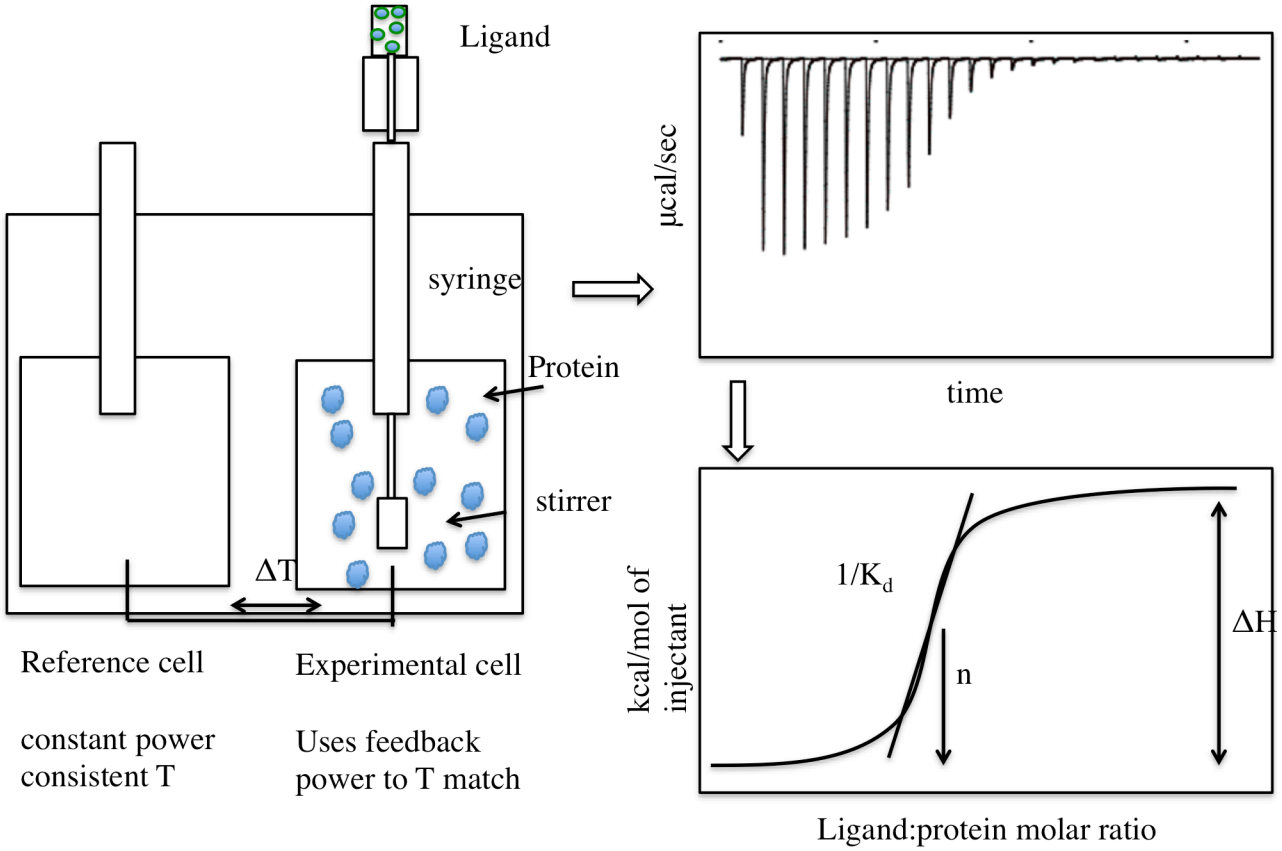

Figure 3.4: ITC Instrument and Data Output. A Schematic of the ITC instrument is displayed, showing the reference cell, experimental cells, and relative locations of the syringe, protein and ligand. Each injection brings a change in the heat of the experimental cell, and power is applied to bring the temperature back to the reference cell. That power is plotted in µcal/sec for each injection, as a function of time. From the preliminary data, each injection peak is integrated, and the values are plotted in kcal/mol of injectant as a function of the ligand to protein molar ratio. The enthalpy change of the reaction can be determined by the value of the difference between the lower and higher baselines of the data in the isotherm. A fitting the data to a mathematical model determines the thermodynamic parameters- stoichiometry, Kd, and ΔH, which can be used to calculate ΔG and ΔS using the Gibb's free energy equation. The stoichiometry of the reaction is the ligand concentration at the midpoint of the isotherm curve. The affinity of the interaction can be described as the slope of the isotherm transition from all available binding sites to all occupied binding sites.

proportional to the amount of ligand that binds to the protein (v x ΔL_i), and the binding reaction enthalpy (ΔH). This relationship of heat to protein ligand binding can be described by the equation $q_i = v \times \Delta H \times \Delta L_i$, where v is the reaction cell volume, i is the injection number, and ΔL_i is the change in ligand that is protein bound after each injection. The amount of heat change is calculated by integration of the area of each injection curve. As more ligand binds to protein, the concentration of unligated protein decreases with more injections, and the peak signal decreases until full saturation occurs. In a transformed plot, the peaks for each injection are integrated and plotted as kcal/mol of ligand injection as a function of the molar ratio of ligand to protein. The quantity of ΔLi, or change in ligand bound to protein [P] over the course of the injections (i to i-1) is directly related to the affinity between the ligand and the protein (K_a). This relies on the Gibb's free energy thermodynamic relationship, $\Delta G = \Delta H - T\Delta S$ and $\Delta G = -RT\ln K_a$ to obtain a full thermodynamic analysis of a ligand-protein interaction as a result of direct heat detection.

3.2. Materials and Methods

3.2.a. PAI-1 Stability Assay

To measure the latency conversion half-life of PAI-1, 0.1uM PAI-1 was incubated in 50mM MOPS, 100mM $(NH_4)_2SO_4$, 0.1 mM EDTA pH 7.4 at 37°C. At various time points, 0.1uM PAI-1 is mixed with 0.1uM two chain tPA in 50mM MOPS, 100mM $(NH_4)_2SO_4$, 2 mM EDTA, and 1% (w/v) BSA, pH 7.4 at 37°C. tPA substrate Spectrozyme tPA at 1mM (in the same buffer as tPA) is added to the PAI-1/tPA mixtures and the reaction is monitored for 5 minutes at 405 nm. Time points were collected for approximately 10 half-lives, and each assay is performed in triplicate. A

schematic of how the assay monitors PAI-1 activity over the time points is presented in **Figure 3.5** The tPA activity (linear slopes) of each time point are plotted as a function of time. The inverse of these values (PAI-1 activity) were normalized and fit to a single exponential decay function $x_t = x_0e^{-kt}$, in which x_0 is the starting PAI-1 activity, x_t is amount of PAI-1 activity at a specific time, t, and k is the rate of decay. The half-life is then determined by the calculation ln(2)/k. The data are fit in Graphpad Prism to determine the rate of latency conversion (k_{lat}) and half-life of latency conversion. An example fit with calculated k_{lat} and $t_{1/2}$ is shown in **Figure 3.6**. Assays containing metals were completed by incubation of 1.1 mM, or 300uM total $CuSO_4$ in the PAI-1 buffer. All proteins used in assays containing copper^{2+} are buffer exchanged into 50mM MOPS, 100mM $(NH_4)_2SO_4$ pH 7.4 at 37°C prior to dilution into assay buffer. Copper^{2+} addition resulted in a decrease of pH, so NaOH was used to correct the pH to 7.4.

3.2.b. Metal Ion Titration Gel Assay

A gel based assay was employed to measure the PAI-1/tPA complex formation in the presence of a wide range of metal ion concentrations. Buffer exchange of PAI-1 is performed using a PD25 column into 50mM MOPS, 100mM $(NH_4)_2SO_4$ pH 7.4 at 37°C. A copper stock solution is made in the same buffer, correcting the pH after copper addition to pH 7.4 at 37°C. PAI-1 at 4uM was incubated with copper^{2+} concentrations ranging from 5uM to 1331 uM (total Copper^{2+}, same buffer) for 30 minutes at 37°C, followed by addition of an equimolar amount of single chain tPA. For each assay, three control samples of PAI-1, tPA, and PAI-1/tPA are included that were not incubated with metal ion. SDS-PAGE loading dye is added, each sample is boiled for

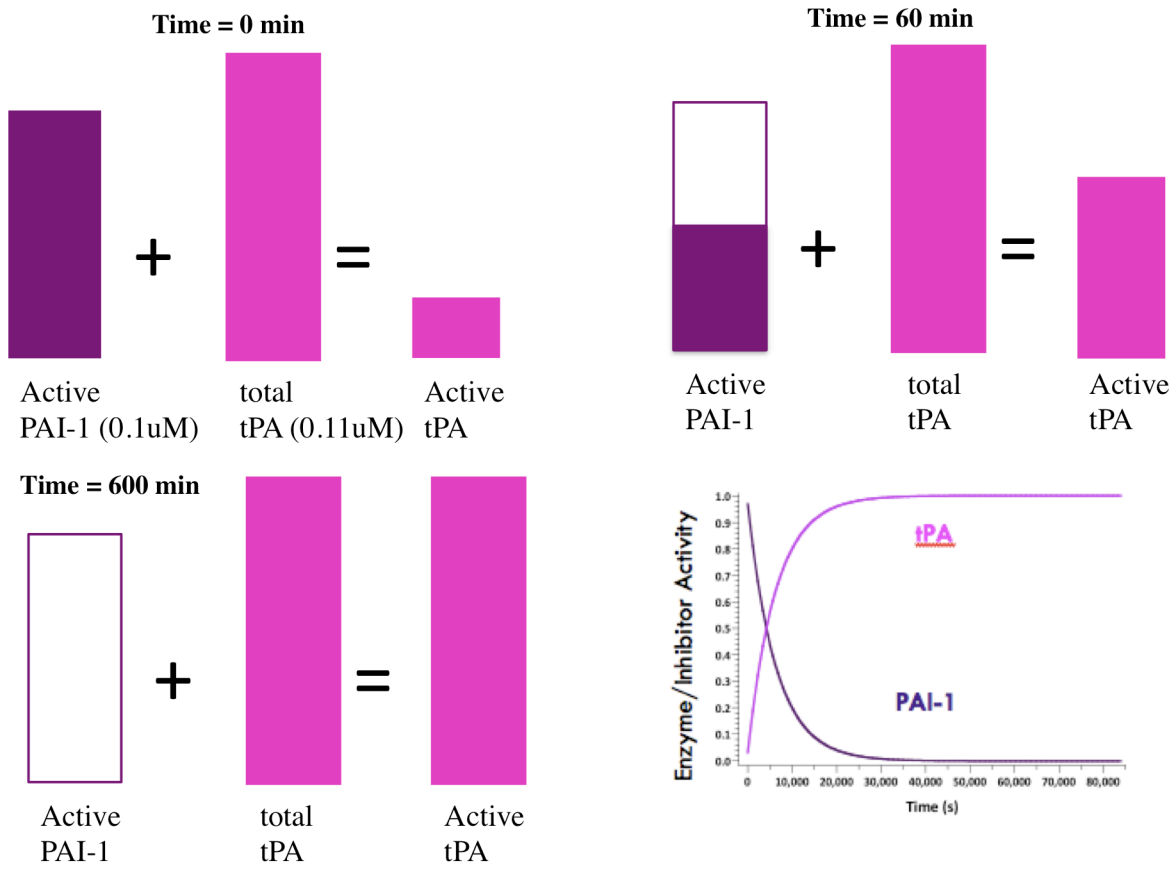

Figure 3.5 Stability Assay Protocol: In this assay, aliquots of PAI-1 are mixed with a slight access of tPA. Over time PAI-1 converts to the latent state, which equates to an increase in tPA activity, which is measured directly. This is illustrated by comparing time 0 representing completely active, then half active, then no active PAI-1 at the end of the assay. The graph on the right shows tPA activity over time, and the negative slope of tPA activity, which is how determining PAI-1 activity over time can calculate k_{lat} or $t_{1/2}$.

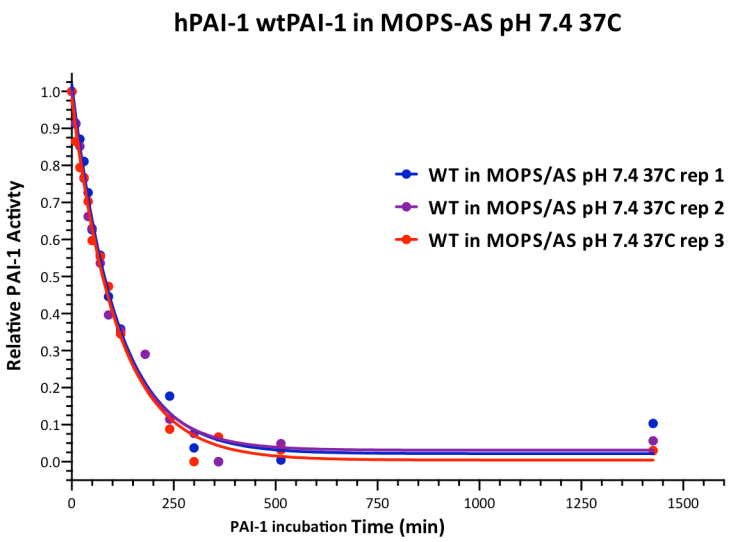

Figure 3.6 Wild-Type Stability Assay Sample Data Fit. The relative PAI-1 activity at each time point is normalized where 1.0 is at time 0 and 0.0 is at the lower baseline of the data fit. The data is plotted as a function of PAI-1 incubation time in minutes. The data are fit to a first order exponential decay equation to calculate k_{lat} and $t_{1/2}$. The blue, purple, and red curves represent independent experiments that are averaged, followed by calculation of standard error for the $t_{1/2}$ measurements.

10 minutes, and then electrophoresed on a 4-12% gradient gel. Gels are stained using Coommassie blue overnight, followed by three 90 minute destaining steps in deoionized water with 30% methanol, 7.5% glacial acetic acid. Imagelab (Biorad) software was used to create a photographic image of the gel and measure the densitometry for the PAI-1/tPA complex bands in each gel lane. The data are normalized to a 0% gel background and a 100% PAI-1/ tPA complex formation band in the absence of metal ions. An example gel using wild-type PAI-1 in the assay is shown in **Figure 3.7**. Each assay is completed in duplicate and the average percent complex formation is plotted as a function of the logarithm of the total copper^{2+} ion concentration in GraphPad Prism. The standard deviation was calculated for inclusion of error bars for wild-type PAI-1 and each variant. Samples containing SMB domain were incubated at 2:1 SMB:PAI-1 ratio and for 2 hours to account for intrinsic difference in rate of latency conversion (k_{lat}).

3.2.c. Isothermal Titration Calorimetry

ITC was used to determine the enthalpy change, stoichiometry, and K_d of copper^{2+} to wild-type and variant PAI-1. Active or inactive PAI-1 is exchanged into a buffer containing 50mM MOPS, 250mM $(NH_4)_2SO_4$, pH 7.4 at 10°C using a PD10 column. Following the column, buffer matching is ensured by dialysis for two hours at 4°C. Using dialysate, a copper^{2+} sulfate stock solution was prepared and the pH was corrected after copper^{2+} addition to yield a pH of 7.4 at 10°C. Protein samples were quantified by absorbance at 280nm. For each experiment, 2.2mL of 20uM PAI-1 was made, along with 4 mL of (300uM-2000uM depending on experiment) copper^{2+} solution. Both the protein solution and copper^{2+} solution undergo a degassing step for 10 minutes at 5°C prior to the experiment. The PAI-1 solution was loaded into the 1.394 mL ITC cell, the copper solution was loaded into the syringe. The instrument was set to 10°C, and set to dispense a

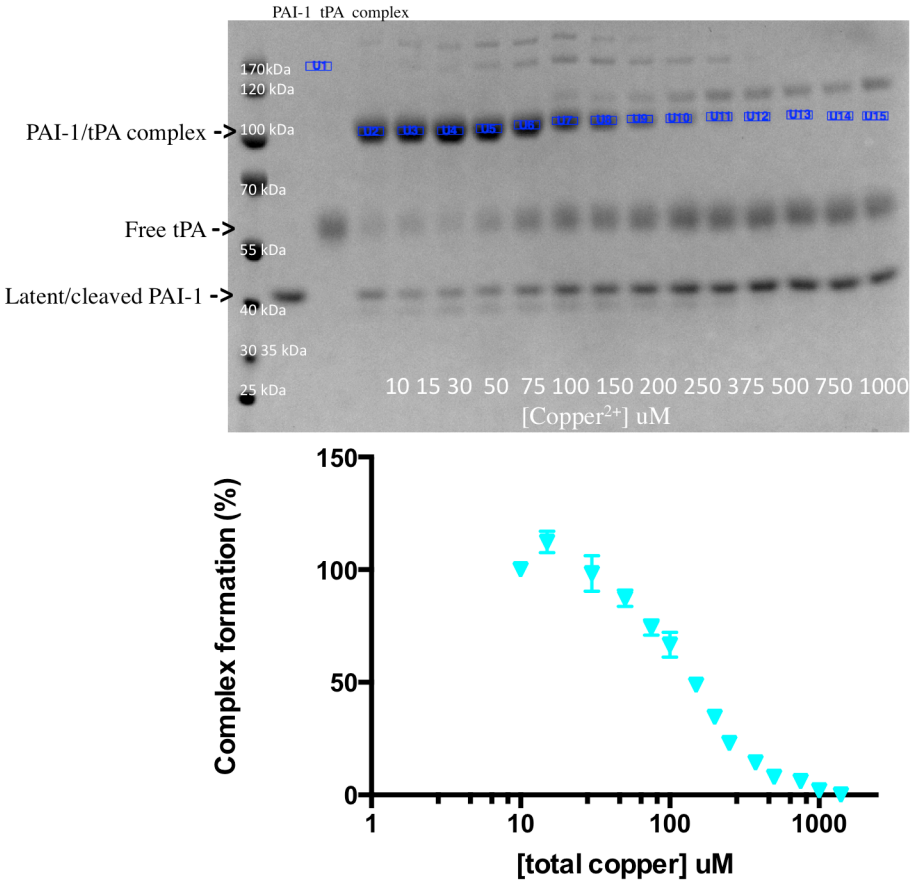

Figure 3.7 Gel Assay Densitometry for Wild-Type PAI-1. Each metal ion titration gel assay sample is a mixture of 1:1 PAI-1:tpA with a particular concentration of copper^{2+}. The samples electrophoresed by non-reducing SDS-PAGE to separate complex, free tPA, and latent/cleaved PAI-1. The first three lanes contain PAI-1, tPA and untreated complex, respectively. The following lanes contain increasing amounts of copper^{2+}. The amount of complex corresponding to the appropriate band in the gel is quantified by Imagelab software, and the data are normalized to the untreated complex sample (100%) and a gel background sample (0%). Assays are performed in duplicate and plotted as a function of copper^{2+} concentration.

2uL preliminary injection. This was followed by 5uL injections, each over 10 second duration, which occur at 120 second intervals so that the system to re-equilibrate to baseline temperature of in between injections. Each experiment uses a total of 54 injections, and each experiment was performed in at least duplicate. Control experiments measuring the heat of exchange between the copper solution and a matching buffer solution containing no protein were subtracted from all experimental data. Initial baseline correction was completed in NITPIC (University of Texas, Southwestern), followed by data fitting in SEDPHAT (National Institute of Health) using either a one site binding model, or a two site non-symmetric binding model, as appropriate. The data fits are represented using the software GUSSI (University of Texas, Southwestern).

3.3. Results

3.3.a. Mutations Modestly Affect the Stability of PAI-1

To determine the location of metal binding site(s) on PAI-1, we utilized site-directed mutagenesis to modify residues hypothesized to bind copper^{2+}. The rationale for the mutations comes from the W175F crystal structure [95], in which N-terminal histidines H2, H3 (site A), and gate region residues E212, D222, E242, and E350 (Site C) take part in copper^{2+} coordination. Additionally, the computationally predicted site involving E81A of hD and H364A of s4B (Site B), is proximal to the N-terminal histidines. Alanine replacements were generated at each of the individual positions to test for metal binding deficiency (**Figure 3.8**). We hypothesized that a PAI-1 variant deficient in metal ion binding would have a half-life of latency transition that is similar in the presence and absence of copper^{2+}.

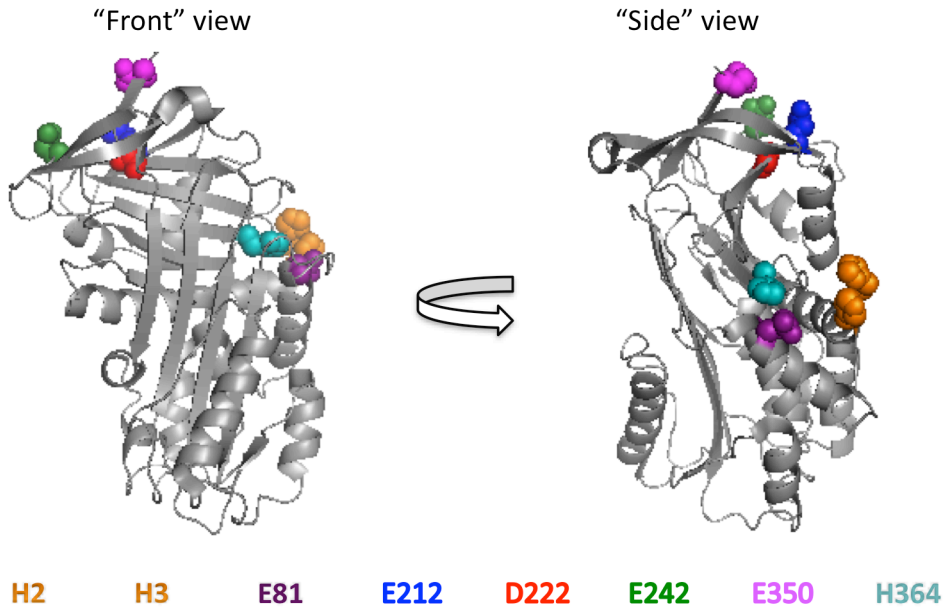

Figure 3.8: Location of Proposed Metal Binding Residues on PAI-1. The following residues are highlighted in the W175F crystal structure (pdb: 3Q02): H2A (orange), H3A (orange), E81 (purple) E212 (blue), D222 (red), E242 (green), E350 (magenta), and H364 (teal). These residues coordinated a zinc^{2+} ion from the crystallization media in the asymmetric dimer interface of the crystal in which the carboxylate containing residues (E212, D222, E242, E350) contributed from one PAI-1 molecule and histidine containing (H2A and H3A) residues contributed from another. The MUG algorithm (Jenny Yang, Georgia State) also computationally predicted this cluster of E212, D222, E242, and E350 as a metal binding cluster. A second cluster from the MUG algorithm containing E81, and H364 is also investigated.

We tested the stability of the PAI-1 variants with and without copper^{2+} to determine half-lives that reflect the rates of latency conversion. Copper^{2+} destabilizes wild-type PAI-1; in the absence of copper^{2+}, PAI-1 remains in the active form for a half-life of 70 minutes (**Figure 3.9**). While in the presence of a saturating concentration of copper^{2+}, it is significantly destabilized to an average half-life of 11 minutes. The three PAI-1 variants with N-terminal histidine replacements (Site A, ie. H2A, H3A, and H2AH3A) compare very closely to wild-type in the absence of metal ions, with average half-lives of 72, 69, and 70 minutes, respectively. As expected, addition of alanine at either H2, H3, or at both sites results loss of binding to the charged nickel IMAC column during purification. This indicates that a metal ion binding site was abolished as a result of the mutations. In the presence of saturating amounts of copper^{2+}, these variants exhibited rates of latency transition that were faster than wild-type PAI-1, with average half-lives for H2A, H3A, and H2AH3A of 4.1, 4.1, and 3.6 minutes in each, respectively, compared to 11 minutes for wild-type. This observation indicates that copper^{2+} does not promote latency conversion through interaction with the N-terminal histidines of PAI-1.

Next, we determined half-lives that reflect the latency conversion of the gate region predicted cluster (Site C). Introduction of alanine mutations into the gate region residues results in modest changes in stability in the absence of copper^{2+} (**Figure 3.10**). D222A and E212A PAI-1 have slightly shorter average half-lives of 56 and 60 minutes, respectively, and E242A and E350A PAI-1 have slightly longer average half-lives of 72 and 83 minutes, respectively, in comparison to a $t_{1/2}$ of 70 minutes with wild-type PAI-1. This region of the protein is known to play a key role in latency conversion, so it is not altogether surprising to see minor differences due to alanine mutations in this region.

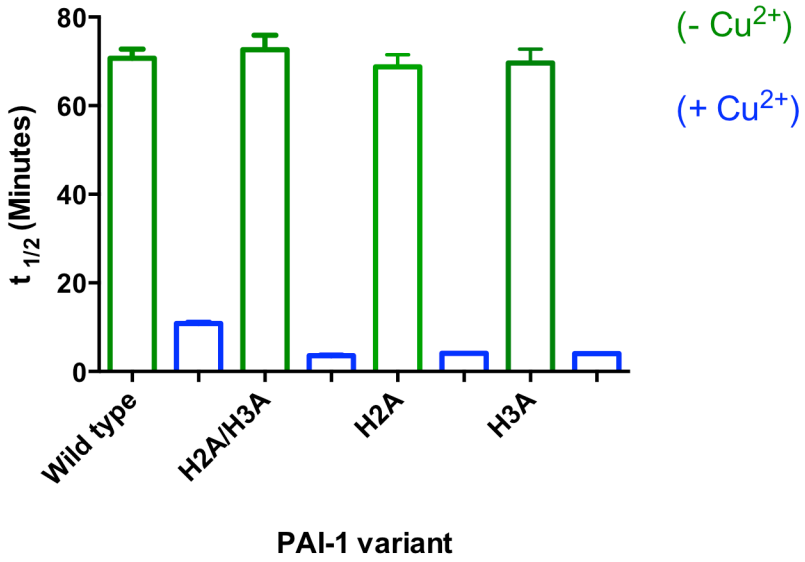

Figure 3.9: Stability Assays on N-Terminal Histidine Variants Site A(+/- Saturating Cu^{2+}). Stability assays were performed to measure the latency conversion half-life of wild-type PAI-1 for comparison to N-terminal region variants. PAI-1 at 0.1uM was incubated in 50mM MOPS, 100mM $(NH_4)_2SO_4$ 0.1mM EDTA pH 7.4 at 37°C, the total metal concentration of 1100uM copper^{2+} in the metal ion containing conditions. PAI-1 inhibition was indirectly measured through tPA activity at A_{405} over the course of the experiment. Each of the bars represent a stability assay completed in triplicate in which the PAI-1 half-life was calculated from a one phase exponential decay function. The data analysis and fit are performed in Graphpad Prism. The green bars represent PAI-1 half-lives in the absence of metal ion ligand, and the blue bars represent PAI-1 half-lives in the presence of metal ion ligand.

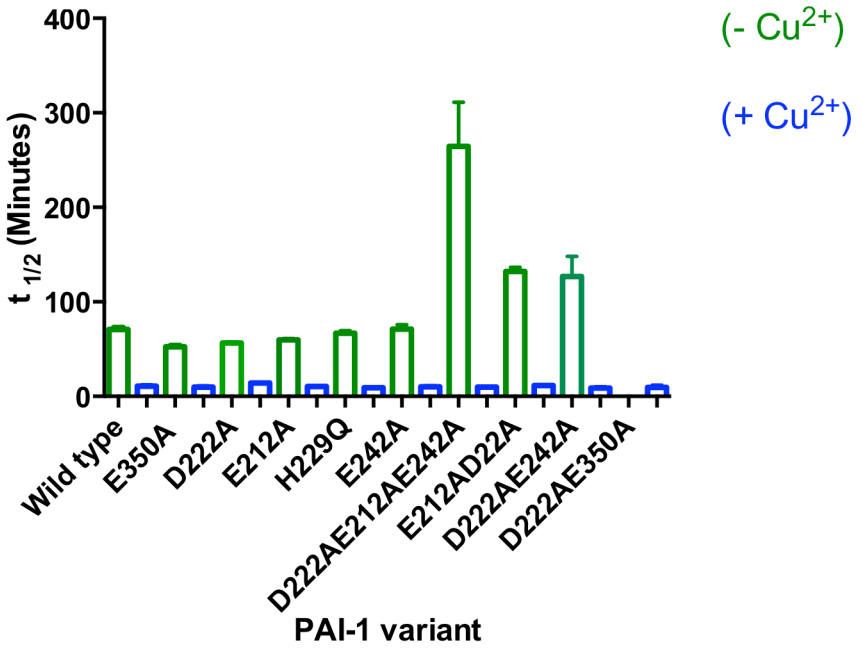

Figure 3.10: Stability Assays on Gate Region Variants Site C (+/- Saturating Cu^{2+}). Stability assays were performed to measure the latency conversion half-life of wild-type PAI-1 for comparison to gate region variants involved in coordination of zinc in the W175F structure. PAI-1 at 0.1uM was incubated in 50mM MOPS, 100mM $(NH_4)_2SO_4$ 0.1mM EDTA pH 7.4 at 37°C, the total metal concentration of 1100uM copper^{2+} in the metal ion containing conditions. PAI-1 inhibition was indirectly measured through tPA activity at A_{405} over the course of the experiment. Each of the bars represent a stability assay completed in triplicate in which the PAI-1 half-life was calculated from a one phase exponential decay function. The data analysis and fit are performed in Graphpad Prism. The green bars represent PAI-1 half-lives in the absence of metal ion ligand, and the blue bars represent PAI-1 half-lives in the presence of metal ion ligand.

The E212A, D222A, E242A, and E350A variant form of PAI-1 exhibit average half-lives of approximately 10-15 minutes in all variants at saturating copper^{2+} concentrations. None of the four individual amino acid replacements yielded a PAI-1 variant that was observed to be significantly different from wild-type PAI-1 at the same copper^{2+} concentration ($t_{1/2}$ = 11 minutes). On the surface, this result suggests that we did not succeed in making a metal-binding deficient form of PAI-1 with the single mutations in Site C. On the other hand, copper^{2+} binds almost always in tetrahedral binding geometry, using four ligands [129]. Removal of two or more of these ligands may be required to observe if significant changes to copper^{2+} binding are conferred.

With the hypothesis that one mutation might not be sufficient to alter PAI-1 metal ion binding, we introduced combinations of mutations to the proposed gate region-binding site, including E212AD222A PAI-1, D222AE242A PAI-1, and E212AD222AE242A PAI-1 (**Figure 3.10**). These variants were tested in the presence and absence of saturating amounts of copper^{2+} in the stability kinetics assay to determine if they exhibit deficiencies in metal ion binding. In the absence of copper^{2+}, there is significant stabilization as a result of combined mutations, where E212AD222A PAI-1 and D222AE242A PAI-1 have average half-lives of 131 minutes, and 126 minutes, respectively. Even more stabilized was the triple variant E212AD222AE242A PAI-1, with an average half-life of 264 minutes. Clearly, this is further indication that substitutions in this region have an impact on PAI-1 latency kinetics, presumably because the uncleaved RCL must pass through the two gate region loops during the latency conversion process. Nonetheless, these mutations had little effect on the PAI-1 latency transition in the presence of saturating amounts of copper^{2+}, with average half-lives that are not statistically different from that of wild-type PAI-1.

Finally, we measured the stability kinetics with and without copper^{2+} for variant forms of

PAI-1 with substitutions in site B (E81A, H364A, and H2AH3AE81A) that were computationally predicted from the MUG algorithm. E81A PAI-1 converts to the latent form in absence of metal ions with a measured average half-life of 70 minutes, while the H364A PAI-1 had an average half-life of latency conversion without copper^{2+} of 81 minutes (**Figure 3.11**). These compared well with the measured 70 minute $t_{1/2}$ of wild-type without metal ions present, albeit a modest stabilization of H364A PAI-1. By contrast, the triple variant H2AH3AE81A PAI-1 was stabilized to an average half-life of 102 minutes. When these variants were tested in the presence saturating amounts of copper^{2+}, they were even more destabilized than wild-type PAI-1, with half-lives of approximately 3 minutes for each, compared to 11 minutes for wild-type. This result also indicates that copper^{2+} does not promote latency conversion through interaction with these residues.

Stability kinetics assays were also performed at less than saturating concentrations of copper^{2+} with wild-type and variant forms of PAI-1. Assays were performed at 300uM copper^{2+}, with the aim to achieve measureable differences between wild-type and variant stabilities in the presence of copper^{2+} (**Figure 3.12**). With this sub-saturating level of copper^{2+}, wild-type PAI-1 average half-life of 16.8 minutes, thus the lower concentration of copper^{2+} still significantly accelerates the latency transition, although not as much as with the saturating 1.1mM copper^{2+} conditions. Measuring H2AH3A (Site A) PAI-1 latency conversion kinetics at lower copper^{2+} resulted in an average half-life of 5.4 minutes, which is significantly less when compared with wild-type PAI-1 at the same copper^{2+} concentration. This is an interesting, yet unexpected result since the mutations were designed to delay latency transition in the presence of copper^{2+}. Similarly, E81A (Site B) PAI-1 tested at this lower copper^{2+} concentration resulted in an average half-life of 3.9 minutes, which is also significantly less than wild-type. The absence of

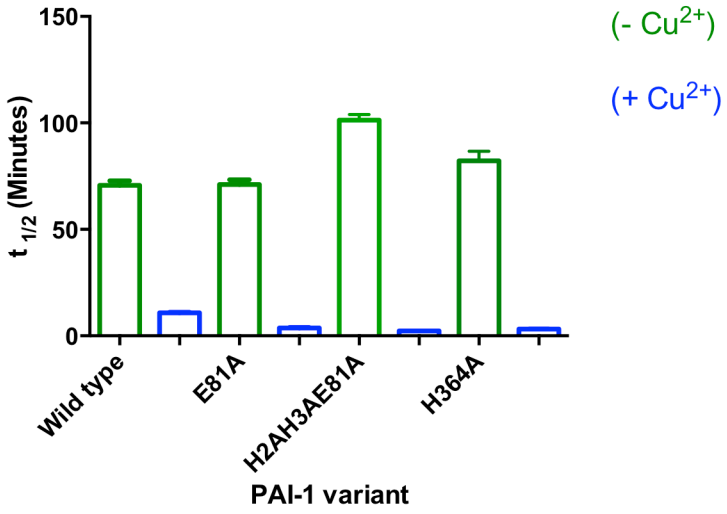

Figure 3.11: Stability Assays on Site B E81A, H364, and H2AH3AE81A PAI-1 Variants (+/- Saturating Cu^{2+}).
Stability assays were performed to measure the latency conversion half-life of wild-type PAI-1 for comparison to E81A, H364A, H2AH3AE81A PAI-1. PAI-1 at 0.1uM was incubated in 50mM MOPS, 100mM $(NH_4)_2SO_4$ 0.1mM EDTA pH 7.4 at 37°C, the total metal concentration of 1100uM copper^{2+} in the metal ion containing conditions. PAI-1 inhibition was indirectly measured through tPA activity at A_{405} over the course of the experiment. Each of the bars represent a stability assay completed in triplicate in which the PAI-1 half-life was calculated from a one phase exponential decay function. The data analysis and fit are performed in Graphpad Prism. The green bars represent PAI-1 half-lives in the absence of metal ion ligand, and the blue bars represent PAI-1 half-lives in the presence of metal ion ligand.

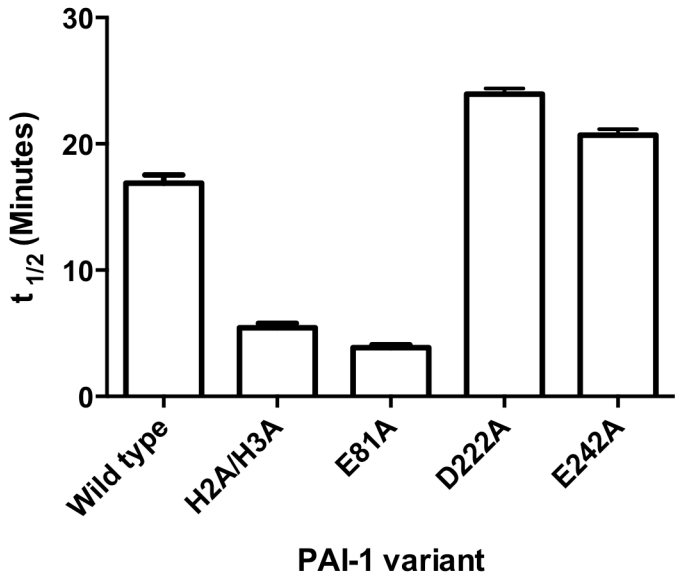

Figure 3.12: Stability Assays on Wild-Type, H2AH3A, E81A, D222A, and E242A PAI-1 Variants (+/- 300uM Cu^{2+}).
Stability assays were performed to measure the latency conversion half-life of wild-type PAI-1 for comparison to gate region variants involved in coordination of zinc in the W175F structure and E81 from the MUG algorithm. PAI-1 at 0.1uM was incubated in 50mM MOPS, 100mM $(NH_4)_2SO_4$ 0.1mM EDTA pH 7.4 at 37°C, the total metal concentration of 300uM copper^{2+} in the metal ion containing conditions. PAI-1 inhibition was indirectly measured through tPA activity at A_{405} over the course of the experiment. Each of the bars represent a stability assay completed in triplicate in which the PAI-1 half-life was calculated from a one phase exponential decay function. The data analysis and fit are performed in Graphpad Prism. The green bars represent PAI-1 half-lives in the absence of metal ion ligand, and the blue bars represent PAI-1 half-lives in the presence of metal ion ligand.

hypothesized copper^{2+} binding residues from sites A and B appear to impart the opposite of the intended effect, which is further accelerating latency transition in the presence of copper^{2+}. By contrast, D222A and E242A (Site C) PAI-1 exhibit different effects on PAI-1 stability in the presence of this lower copper^{2+} concentration. D222A PAI-1 tested at the lower copper^{2+} concentration resulted in an average half-life of 23.9 minutes, which is significantly longer than wild-type. Likewise, E242A PAI-1 tested at the lower copper^{2+} concentration resulted in an average half-life of 20.6 minutes, which is also statistically different than wild-type. **Figure 3.13** and **Figure 3.14** feature a compilation of the stability kinetics of latency transition data for PAI-1 variants with and without copper^{2+}. We decided next to test these variants at a wide range of copper^{2+} concentrations for comparison of copper^{2+} concentrations that induce latency conversion.

3.3.b. PAI-1 Variants Exhibit Differing Sensitivities to Copper^{2+} in Titration Assay

In a complementary approach to address our need to assess copper^{2+} effects on PAI-1, and on latency conversion in particular, we derived a means to measure the susceptibility of PAI-1 to undergo latency conversion at varying copper^{2+} concentrations. Rather than using a fixed copper^{2+} concentration and varying time, we used a fixed time and varied copper^{2+} concentration. We titrated copper^{2+} into a fixed concentration of PAI-1, and monitored tPA complex formation in a gel based assay, testing a concentration range of 5-1331 uM metal ions and incubating the PAI-1-metal ion complex for 30 minutes. Quantification by densitometry of the gel PAI-1/tPA complex bands at increasing copper^{2+} concentrations results in a sigmoidal semi-log plot, with an upper

	Activity eq. to inhbit tPA	klat (min-1)	Average t1/2 (min)	klat(min-1) with 1.1 mM Cu2+	Average t1/2 (min)	klat(min-1) with 300uM Cu2+	Average t1/2 (min)
Active WT	1.25	0.00921	70.7 (+/- 2.5)	0.0642	10.8 (+/- 0.4)	0.039	16.9 (+/- 0.8)
Active H2A	1.5	0.0099	68.6 (+/- 3.3)	0.169	4.1 (+/- 0.1)		
Active H3A	1.5	0.0097	69.6 (+/- 3.9)	0.1741	4.0 (+/- 0.1)		
Active H2AH3A	1.5	0.0091	72.7 (+/- 3.95)	0.1856	3.56 (+/- 0.1)	0.125	5.4 (+/- 0.4)
Active E212A	1.25	0.0112	59.9 (+/- 1.7)	0.066	10.4 (+/- 0.5)		
Active D222A	1.25	0.0113	56.4 (+/- 1.1)	0.058	14.0 (+/- 0.3)	0.029	23.9 (+/- 0.6)
Active E242A	1.25	0.0083	71.2 (+/- 5.61)	0.045	10.3 (+/- 1.1)	0.034	20.7 (+/- 0.6)
Active E350A	1.25	0.013	52.5 (+/- 1.4)	0.073	9.7 (+/- 0.6)		
Active E81A	1.25	0.009	71.1 (+/- 2.6)	0.26	3.73 (+/- 0.2)	0.17	3.9 (+/- 0.3)
Active H2AH3AE81A	1.5	0.0072	101.4 (+/- 3.1)	0.28	2.3 (+/- 0.2)		
Active H364A	2	0.0093	82.1 (+/- 5.5)	0.21	3.2 (+/- 0.4)		
Active H229Q	1.25	0.011	66.7 (+/- 3.6)	0.077	9.0 (+/- 0.2)		

Figure 3.13 Compiled Stability Kinetics Data. The activity of each variant in equivalents required to inhibit tPA, klat and average half-life in the presence and absence of 1.1mM Cu^{2+}, k_{lat} and average half-life in the presence and absence of 300 uM Cu^{2+} are presented for comparison.

	Activity eq. to inhbit tPA	klat (min-1)	Average t1/2 (min)	klat(min-1) with 1.1 mM Cu2+	Average t1/2 (min)
E212/D222A	1.25	0.0052	132.2 (+/- 5.1)	0.059	11.6 (+/- 0.4)
D222A/E242A	1.25	0.0055	126.9 (+/- 26.0)	0.079	8.8 (+/- 1.4)
D222A/E350A	1.25			0.074	9.4 (+/- 2.9)
E212A/D222A/E242A	1.25	0.0026	264.3 (+/- 57.6)	0.069	10.0 (+/- 0.7)

Figure 3.14 Compiled Stability Kinetics Data. The activity of each combination gate variant in equivalents required to inhibit tPA, klat and average half-life in the presence and absence of 1.1mM Cu^{2+} are presented for comparison.

baseline representing concentrations of metal ion to which PAI-1 is insensitive and mostly active, a transition region of metal ion sensitivity, and a lower baseline that represents metal concentrations that render PAI-1 latent. To compare wild-type PAI-1 with the variants, we used the midpoint in metal sensitivity, defined as the concentration of $copper^{2+}$ in which 50% complex formation with tPA was achieved.

When we measured wild-type PAI-1 in this gel based metal ion titration assay, the midpoint of the sigmoidal transition was at approximately 150uM $copper^{2+}$. We tested the N-terminal histidine variants Site A (H2A, H3A, H2AH3A) to determine what concentrations of metal ion induce latency conversion. In the stability assay, these variants converted to the latent form at comparable rates with wild-type PAI-1 in the absence of metal ions, but conversion of these variant forms occurs even faster than wild-type in the presence of $copper^{2+}$. Interestingly, we observed dramatically lower midpoints in the N-terminal histidine variants compared with wild-type regarding the concentration of $copper^{2+}$ that defines the range of sensitivity for the latency conversion. The double variant H2AH3A PAI-1, as well as the single variants H2A and H3A PAI-1 have approximate midpoints of 20uM $copper^{2}$ (**Figure 3.15**). These data compare well with stability kinetics data in the presence of $copper^{2+}$, in which $copper^{2+}$ accelerates latency of these variants faster than in wild-type PAI-1. The result indicates that $copper^{2+}$ binding to the Site A histidines produces a neutral or stabilizing effect on PAI-1 latency transition.

Next, we performed the gel based metal ion titration assay on the four individual gate region variants for comparison with wild-type. The stability assay data of the single variants from this predicted site C compare fairly well in the presence and absence of $copper^{2+}$, although at the lower $copper^{2+}$ concentration D222A and E242A PAI-1 have modestly delayed half-lives in the presence

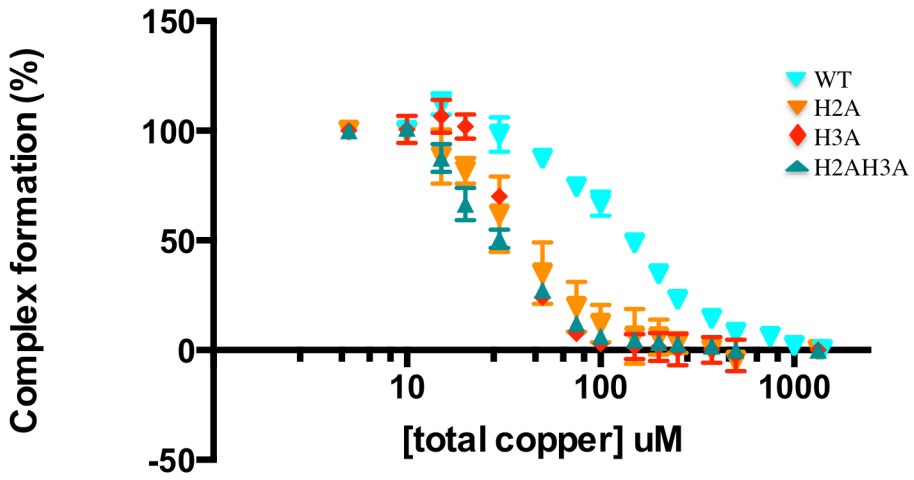

Figure 3.15: Metal Titration Gel Assays Comparing N-Terminal Region Variants and SMB Addition

PAI-1 at 4uM was incubated in 50mM MOPS,100mM $(NH_4)_2SO_4$ pH 7.4 at 37°C with total metal ion concentrations ranging from 5uM to 1331uM for 30 minutes at 37°C, followed by addition of an equimolar amount of tPA to form complex with remaining PAI-1 in the active form. This was monitored using a non-reducing SDS-PAGE. The PAI-1/tPA complex bands were quantified using densitometry on the program image lab, and normalized using an untreated PAI-1/tPA complex as 100% and a background gel sample as 0%. Each data point is a duplicate average of two assays. The wild-type PAI-1 data is represented in light blue triangles, H2A data is represented in orange triangles, H3A in red diamonds, and H2AH3A in teal triangles.

of copper^{2+}. The variants E212A and E350A PAI-1 have a midpoint value that occurs at a similar copper^{2+} concentration of approximately 150uM (**Figure 3.16**). The overlapping error bars comparing variants with wild-type PAI-1 suggest that these variants are not statistically different from wild-type in their metal ion sensitivity. These data agree well with the stability assay data with copper^{2+} present. However, the variants E242A and D222A PAI-1 have midpoint copper^{2+} concentrations of approximately 250uM total copper^{2+}, which are different compared with wild-type (**Figure 3.17**). These data also agree well with the stability assay results with lower copper^{2+} present. The results indicate that one or both of these Site C residues could be involved in a metal coordination event that accelerates the latency transition.

The variants from the MUG predicted site B residues (E81A, H364A, and E81AH364A) were tested in the gel metal ion titration assay next. Introducing these mutations caused modest stabilizations to PAI-1 in the absence of copper^{2+}, and yet when tested with copper^{2+}, the latency transition accelerated to rate faster than that of wild-type. Strikingly, E81A PAI-1 looks the most sensitive to copper^{2+}, with an approximate midpoint of 15uM (**Figure 3.18**). A triple variant containing H2AH3AE81A PAI-1 is also more sensitive than WT, but at an approximate sensitivity midpoint of 20uM, it is similar to the histidine variants. These results agree well with the stability kinetics in the presence of copper^{2+}. Finally, H364A PAI-1 had a similar copper^{2+} sensitivity midpoint as wild-type PAI-1, but the curve transition was markedly different (data not shown). From these data alone, it is difficult to determine if H364 PAI-1 plays a role in copper^{2+} binding that influences PAI-1 function. Overall, the results of Site B argue that a copper interaction with this region would provide a neutral or stabilizing effect on PAI-1 latency transition.

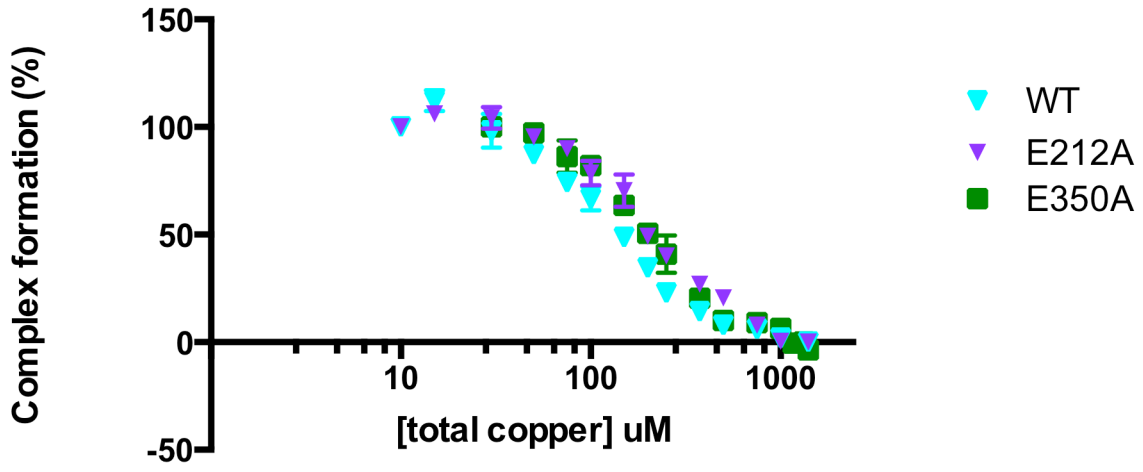

Figure 3.16: Metal Titration Gel Assays comparing Wild-Type and Gate Region PAI-1 Variants

PAI-1 at 4uM was incubated in 50mM MOPS, 100mM $(NH_4)_2SO_4$ pH 7.4 at 37°C with total metal ion concentrations ranging from 5uM to 1331uM for 30 minutes at 37°C, followed by addition of an equimolar amount of tPA to form complex with remaining PAI-1 in the active form. This was monitored using a non-reducing SDS-PAGE. The PAI-1/tPA complex bands were quantified using densitometry on the program image lab, and normalized using an untreated PAI-1/tPA complex as 100% and a background gel sample as 0%. Each data point is a duplicate average of two assays. The wild-type PAI-1 is represented in light blue triangles, E212A represented in purple triangles, and E350A in green squares.

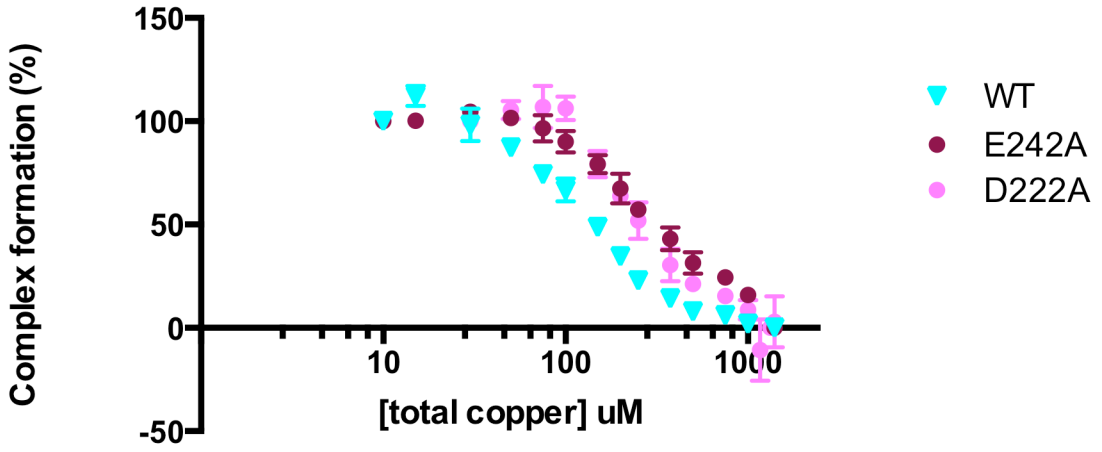

Figure 3.17: Metal Titration Gel Assays comparing Wild-Type and Gate Region PAI-1 Variants.
PAI-1 at 4uM was incubated in 50mM MOPS, 100mM $(NH_4)_2SO_4$ pH 7.4 at 37°C with total metal ion concentrations ranging from 5uM to 1331uM for 30 minutes at 37°C, followed by addition of an equimolar amount of tPA to form complex with remaining PAI-1 in the active form. This was monitored using a non-reducing SDS-PAGE. The PAI-1/tPA complex bands were quantified using densitometry on the program image lab, and normalized using an untreated PAI-1/tPA complex as 100% and a background gel sample as 0%. Each data point is a duplicate average of two assays. The wild-type PAI-1 is represented in light blue triangles, D222A represented in pink circles, and E242A in magenta circles.

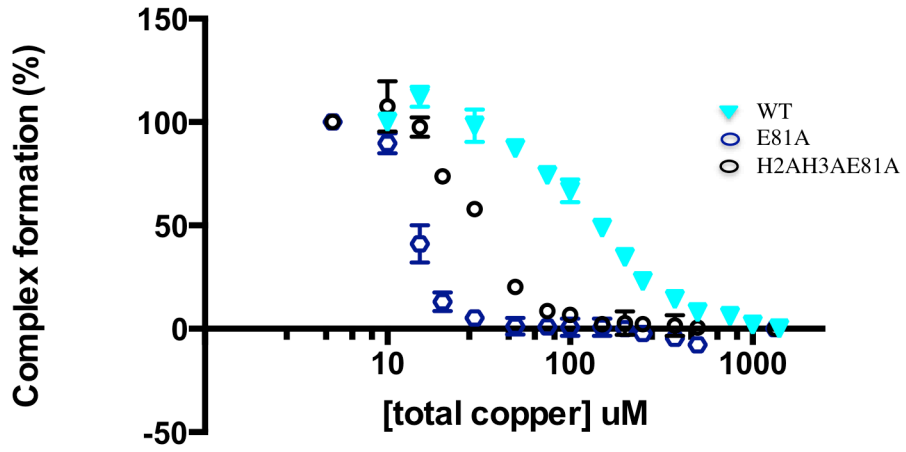

Figure 3.18: Metal Titration Gel Assays comparing E81A Variants to Wild-Type PAI-1.
PAI-1 at 4uM was incubated in 50mM MOPS,100mM $(NH_4)_2SO_4$ pH 7.4 at 37°C with total metal ion concentrations ranging from 5uM to 1331uM for 30 minutes at 37°C, followed by addition of an equimolar amount of tPA to form complex with remaining PAI-1 in the active form. This was monitored using a non-reducing SDS-PAGE. The PAI-1/tPA complex bands were quantified using densitometry on the program image lab, and normalized using an untreated PAI-1/tPA complex as 100% and a background gel sample as 0%. Each data point is a duplicate average of two assays. The wild-type PAI-1 data is represented in light blue triangles E81A in dark blue circles, and H2AH3AE81A in black circles.

We then investigated the influence of SMB domain on the midpoint concentrations of copper^{2+} sensitivity in the latency conversion. PAI-1 bound to SMB domain remains in the active form 1.5 longer than PAI-1 alone. Gel titration assays were performed on wild-type PAI-1 and H2AH3A PAI-1 in the presence of a 2 fold molar excess of SMB domain of VN. We observed similar midpoints in copper sensitivity (~200 uM copper^{2+}) for both the wild-type PAI-1 and H2AH3A PAI-1 with SMB bound (**Figure 3.19**). Since SMB changes the half live of PAI-1 without addition of metal ions, we were careful not to directly compare these two data sets with wild-type and H2AH3A alone. Nonetheless, with SMB present, the difference in metal ion sensitivity comparing wtPAI-1 and the H2AH3A variant is abolished, in stark contrast to the sensitivity of these two forms of PAI-1 without SMB bound. The compiled results from the metal ion titration gel assay are given in **Figure 3.20**. These results are consistent with our observation from HDX studies that binding of the SMB domain negates metal ion effects on protein dynamics (Refer to Chapter 2).

3.3.c. Differences in Latent/Variant PAI-1 Copper^{2+} Binding Identified by ITC

We performed ITC on various forms of PAI-1 to measure the enthalpy change of interaction (ΔH), and dissociation constant (K_d) for the interaction of the various forms of PAI-1 with copper^{2+}. First, we compared latent forms of wild-type PAI-1 with the H2AH3A variant, titrating in a buffer matched solution containing copper^{2+} sulfate in the injection syringe. Both proteins were confirmed to be latent by an activity assay, much like what is performed on active protein stocks. Previously, we determined by SPR that wild-type PAI-1 binds a nickel^{2+} charged NTA chip in both the active and latent forms, albeit tighter in the active form [109]. Since the H2AH3A does

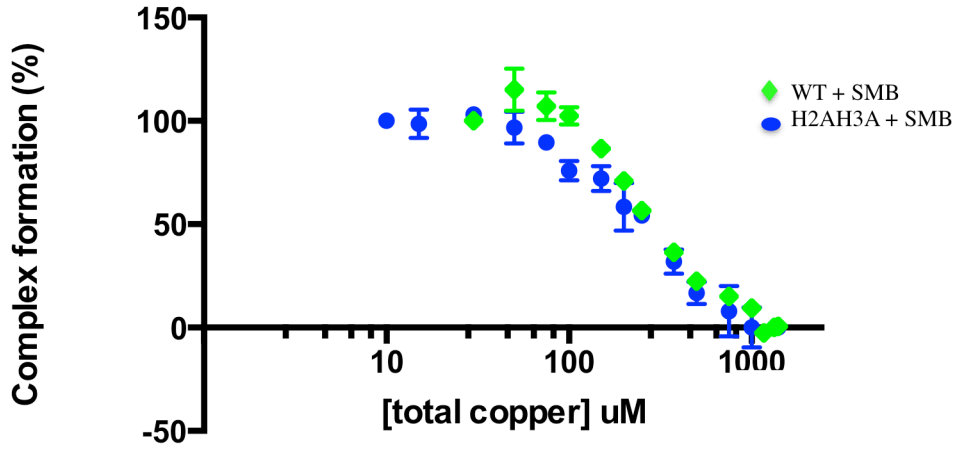

Figure 3.19: Metal Titration Gel Assays comparing Wild-Type and H2AH3A (+/- SMB).
PAI-1 at 4uM was incubated in 50mM MOPS,100mM $(NH_4)_2SO_4$ pH 7.4 at 37°C with total metal ion concentrations ranging from 5uM to 1331uM for 30 minutes at 37°C, followed by addition of an equimolar amount of tPA to form complex with remaining PAI-1 in the active form. The SMB containing samples were incubated for 2 hours at 37°C for adequate comparison. This was monitored using a non-reducing SDS-PAGE. The PAI-1/tPA complex bands were quantified using densitometry on the program image lab, and normalized using an untreated PAI-1/tPA complex as 100% and a background gel sample as 0%. Each data point is a duplicate average of two assays. The wild-type plus SMB data is represented in light green diamonds, and H2AH3A plus SMB in dark blue circles.

	Midpoint sensitivity (uM)
Active WT	~150
Active W175F	~150
Latent WT	N/A
Latent H2AH3A	N/A
Active WT + SMB	~200*
Active H2AH3A + SMB	~200*
Active H2A	~20
Active H3A	~20
Active H2AH3A	~20
Active E212A	~150
Active D222A	~250
Active E242A	~250
Active E350A	~150
Active E81A	~15
Active H2AH3AE81A	~20

*SMB alters latency kinetics of PAI-1 independent of metal effects

Figure 3.20 Compiled Metal Titration Gel Assay Data.
The compilation of metal titration gel assay data is shown, each midpoint copper^{2+} concentration is represented in micromolar concentration.

not bind an IMAC column, we hypothesized that these mutations would result in loss of a copper^{2+} binding transition in the ITC binding isotherm. Also, we chose to start with a comparison of the PAI-1 latent forms because the active form converts to the latent state quickly in the presence of metal ions. Fortunately though, the conformational changes during latency transition feature no detected enthalpy changes in the ITC [86]. This result was replicated in our lab by equilibrating the ITC control and experimental cells at 37°C, and titrating buffer into active PAI-1 for 16 hours (data not shown).

After optimizing the experimental conditions, we achieved binding isotherms with latent wild-type PAI-1. We first tested latent wild-type PAI-1 in the ITC with the cells set to 10°C, and higher salt (250mM) to prevent non-specific binding. Copper^{2+} titration into latent wild-type PAI-1 resulted in two clear transitions. Fitting to a two-site binding isotherm model resulted in K_d's of 50nM, and 2.1uM for the respective binding sites, with respective enthalpy changes of -12.2, and -4.6 kcal/mol (**Figure 3.21**). The data fit with a lower global chi squared to a two-site model, when compared with a one-site model, as illustrated in **Figure 3.21**. This makes sense given the prior knowledge that latent wild-type PAI-1 was able to bind to immobilized nickel^{2+} by SPR. We hypothesized that one of these transitions was due to binding at Site A N-terminal histidines. Copper^{2+} titration into latent H2AH3A PAI-1 was clearly weaker, as evidenced by the lack of an initial baseline using similar copper^{2+} concentrations to those used in the active protein titrations. As suspected, these data featured one binding transition. Fitting to a one-site binding isotherm model yielded a K_d of 1.96 uM, and an enthalpy change of -8.5 kcal/mol (**Figure 3.22**). Due to the close similarity in affinity of the one transition in latent H2AH3A PAI-1 and the second transition

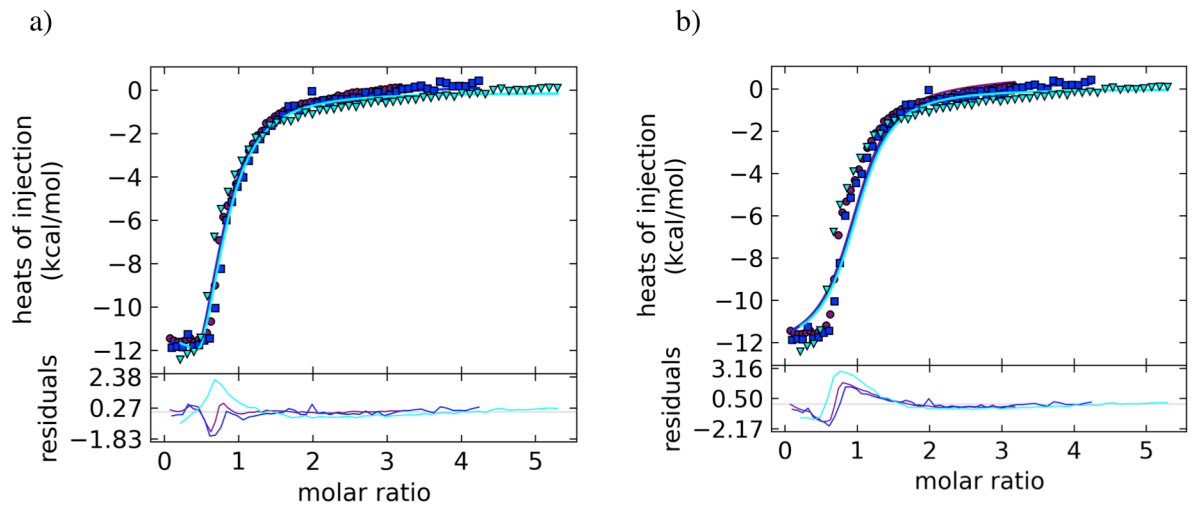

Figure 3.21: ITC on Latent Wild-type PAI-1, fit to a one and two site model.
Panel a) Latent 20uM wild-type PAI-1 was dialyzed into 50mM MOPS, 250mM $(NH_4)_2SO_4$ pH 7.4 at 10°C (two site model). Copper at 300, 400, and 500uM was added to the buffer matched dialysate from a concentrated stock, and pH corrected to pH 7.4 at 10°C. Syringe copper was injected into the cell containing PAI-1 in injections of 5uL over 10 second duration, over 120 second intervals, 54 injections total. The data are subtracted from runs in which $CuSO_4$ in the same buffer was titrated without protein to remove background metal ion-buffer heat of interaction. The data are converted into kcal/mol of injectant as a function of the molar ratio of copper to latent PAI-1. Global data fitting was performed in Sedphat Software to a two site binding model, and the fit is represented using Gussi software.
Panel b) Global data fitting of the same data was performed in Sedphat Software to a one site binding model, and the fit is represented using Gussi software.

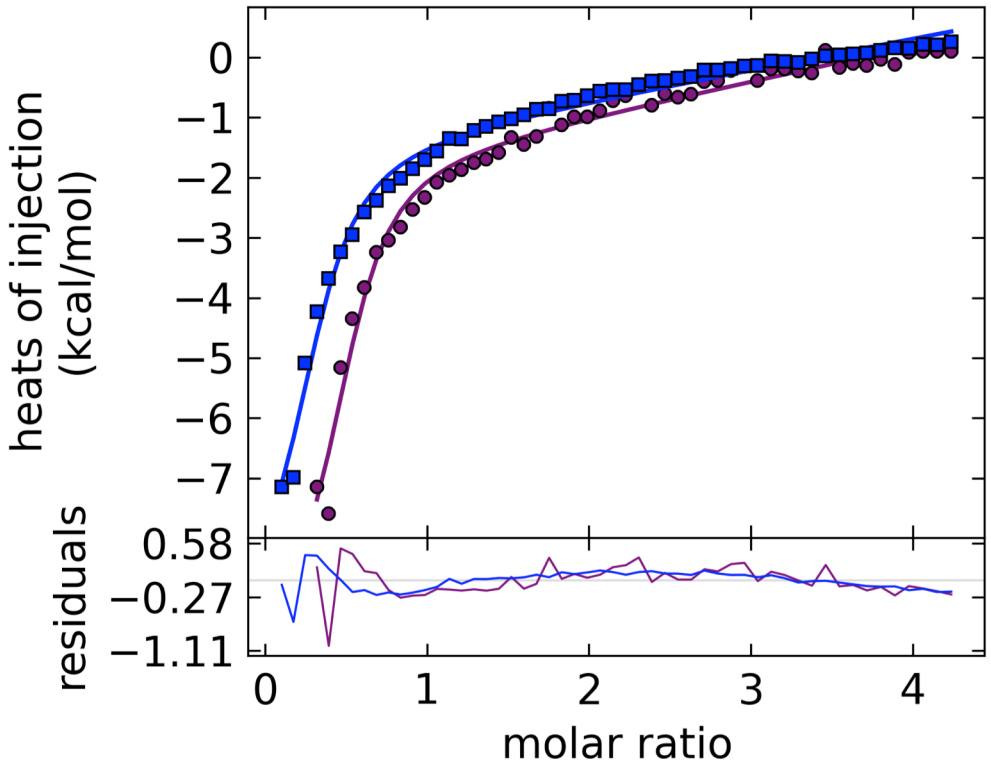

Figure 3.22: ITC on Latent H2AH3A PAI-1.
Latent 20uM H2AH3A PAI-1 was dialyzed into 50mM MOPS, 250mM $(NH_4)_2SO_4$ pH 7.4 at 10°C. Copper at 400uM was added to the buffer matched dialysate from a concentrated stock, and pH corrected to pH 7.4 at 10°C. Syringe copper was injected into the cell containing PAI-1 in injections of 5uL over 10 second duration, over 120 second intervals, 54 injections total. The data are subtracted from runs in which 400uM CuSO4 in the same buffer was titrated without protein to remove background metal ion-buffer heat of interaction. The data are converted into kcal/mol of injectant as a function of the molar ratio of copper to latent PAI-1. Data fitting was performed in Sedphat Software to a one site binding model, and the fit is represented using Gussi software.

of latent wild-type, we concluded that the tighter first transition of wild-type PAI-1 was contributed through binding of the N-terminal histidines. Also, it should be noted that even in the case of latent H2AH3A PAI-1 we observed copper^{2+} binding, which suggests the copper^{2+} binding site accelerating the rate of latency transition exists in one of the other hypothesized (Site B or C), or that this site only exists in the active form.

Our chief concern for testing active forms of PAI-1 in the ITC was ensuring that it does not convert to the latent form during the experiment. As mentioned, the temperature for all ITC experiments were 10°C, which prolongs the time PAI-1 remains active in the presence of metal ions. We also increased the salt concentration from 100mM as in the stability and titration assays, to 250mM for all ITC experiments. This change in particular resulted in two fortuitous effects. This eliminated detectable MOPS-copper^{2+} heats of interaction in control ITC experiments involving no PAI-1, and also lead to significantly decreased copper^{2+} sensitivity in wild-type, and H2AH3A in the gel based metal ion titration assay at this higher salt concentration (**Figure 3.23**).

As a further cautionary measure, we tested the active stabilized variant W175F as a standard for comparison with titrations of wild-type PAI-1. The single W175F PAI-1 variant is located on the PAI-1 structure in the hinge region of shutter strand s3A and is not located on the PAI-1 structure near the proposed metal ion binding clusters. Titration of copper^{2+} into wild-type PAI-1 revealed tight binding. Fitting of the data to a two-site binding isotherm model resulted in K_d's of 20 nM, and 60nM, with respective enthalpy changes of -12.2, and -9.2 kcal/mol (**Figure 3.24**). Additionally, the stabilized W175F PAI-1 had similar thermodynamics to wild- type, fitting to the

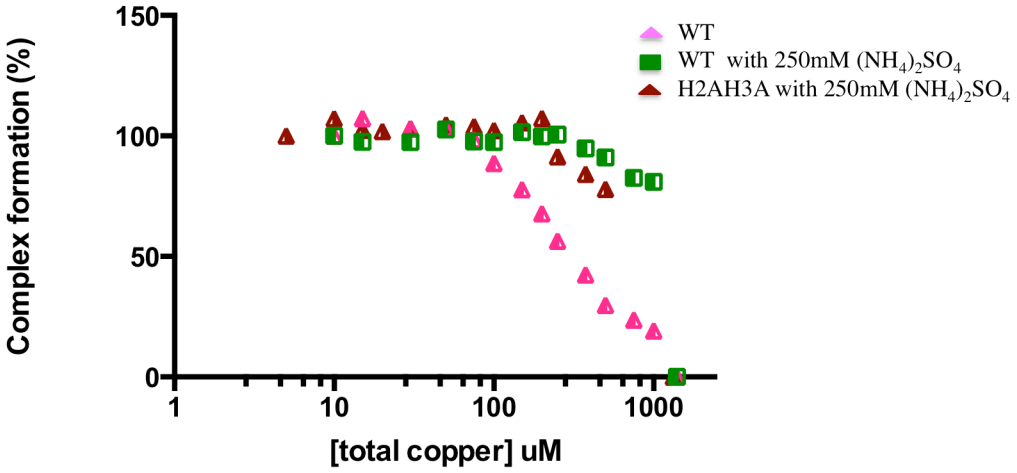

Figure 3.23: Metal Titration Gel Assays comparing Wild-Type and H2AH3A with Higher Salt.
PAI-1 at 4uM was incubated in 50mM MOPS,250mM $(NH_4)_2SO_4$ pH 7.4 at 37°C with total metal ion concentrations ranging from 5uM to 1331uM for 30 minutes at 37°C, followed by addition of an equimolar amount of tPA to form complex with remaining PAI-1 in the active form. This was monitored using a non-reducing SDS-PAGE. The PAI-1/tPA complex bands were quantified using densitometry on the program image lab, and normalized using an untreated PAI-1/tPA complex as 100% and a background gel sample as 0%. Each data point is a duplicate average of two assays. The wild-type PAI-1 data at normal conditions is represented in pink triangles, wild-type with higher salt in brown triangles, and H2AH3A with higher salt in green squares.

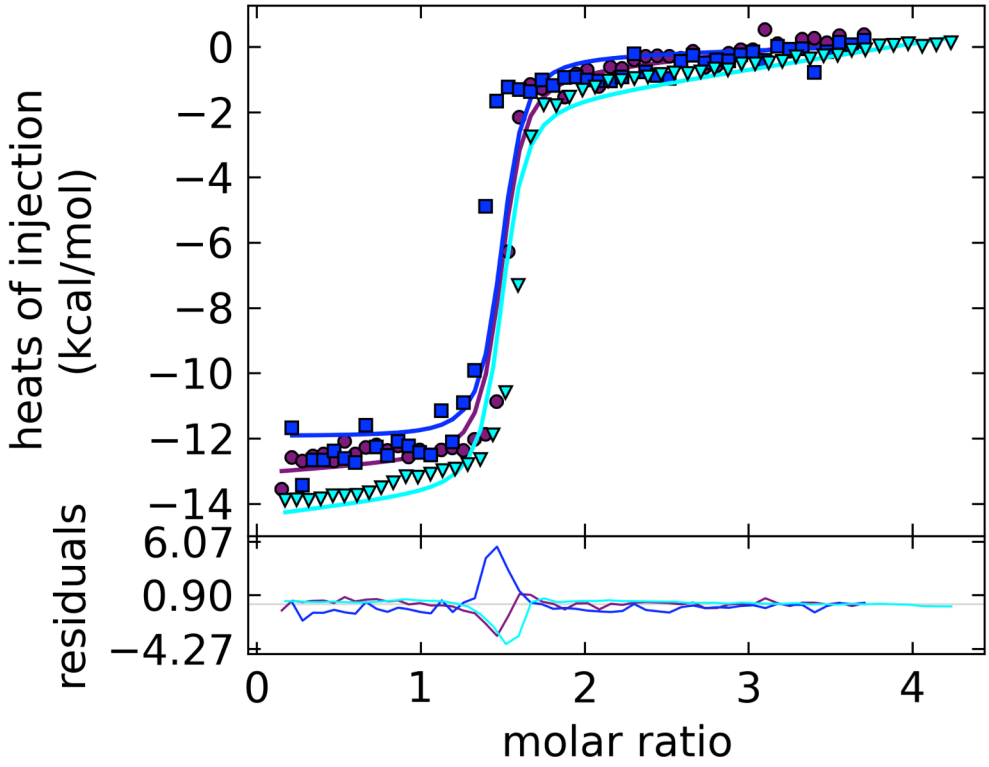

Figure 3.24: ITC Fit on the Tighter Transitions of Active Wild-Type PAI-1
Active 20uM wild-type PAI-1 was dialyzed into 50mM MOPS, 250mM $(NH_4)_2SO_4$ pH 7.4 at 10°C. $Copper^{2+}$ at 350, and 400uM was added to the buffer matched dialysate from a concentrated stock, and pH corrected to pH 7.4 at 10°C. Syringe copper was injected into the cell containing PAI-1 in injections of 5uL over 10 second duration, over 120 second intervals, 54 injections total. The data are subtracted from runs in which CuSO4 in the same buffer was titrated without protein to remove background metal ion-buffer heat of interaction. The data are converted into kcal/mol of injectant as a function of the molar ratio of copper to active PAI-1. Global data fitting was performed in Sedphat Software to a two non-symmetric site binding isotherm, and the fit is represented using Gussi software.

two-site model with K_d's of 10 nM and 20nM, and enthalpy changes of -14.9, and -15.1 kcal/mol, respectively (**Figure 3.25**). Due to the overlap in affinity of the transitions, it is difficult to determine the individual enthalpy of each transition in these titration data. There is a slope associated with the baseline at high metal ion concentrations, which opens the possibility of a weaker binding site. Testing ITC of active wild-type PAI-1 with higher copper concentrations did indeed reveal that a weaker binding site exists, as suggested from the baseline abnormalities existing at higher copper^{2+} concentrations in the active wild-type and W175F PAI-1 ITC experiments (**Figure 3.24, 3.25**). These experiments using higher copper^{2+} concentrations with active wild-type PAI-1 yielded a K_d of 2.1 uM and enthalpy change of -8.2 kcal/mol for this third transition (**Figure 3.26**). This affinity compares well with the second transition of latent wild-type, or the latent H2AH3A transition.

Copper titration into active forms of D222A, and E242A gate region PAI-1 variants of the MUG predicted Site C that exhibited lower copper^{2+} sensitivity in the metal ion gel assays. Interestingly, these variants resulted in tight transitions that fit to two site models. Fitting of the D222A PAI-1 data to a two-site binding isotherm model resulted in K_d's of 10 nM, and 10nM, and enthalpy changes of -20.2, and -20.2 kcal/mol, respectively. (**Figure 3.27**). Similarly, Fitting of the E242A PAI-1 isotherms to a two-site model resulted in K_d's of 9.2 nM and 20nM, with enthalpy changes of -17.2, and -17.0 kcal/mol, respectively (**Figure 3.28**). In this respect, these variants exhibited similar binding behavior as active wild-type or W175F PAI-1. However, close examination of the baseline at higher copper^{2+} in these experiments reveals interesting differences. The baseline at higher copper^{2+} concentrations for the D222A PAI-1 isotherm data suggests the presence of a weaker binding site, in which isotherms with increased amounts of copper^{2+} would be

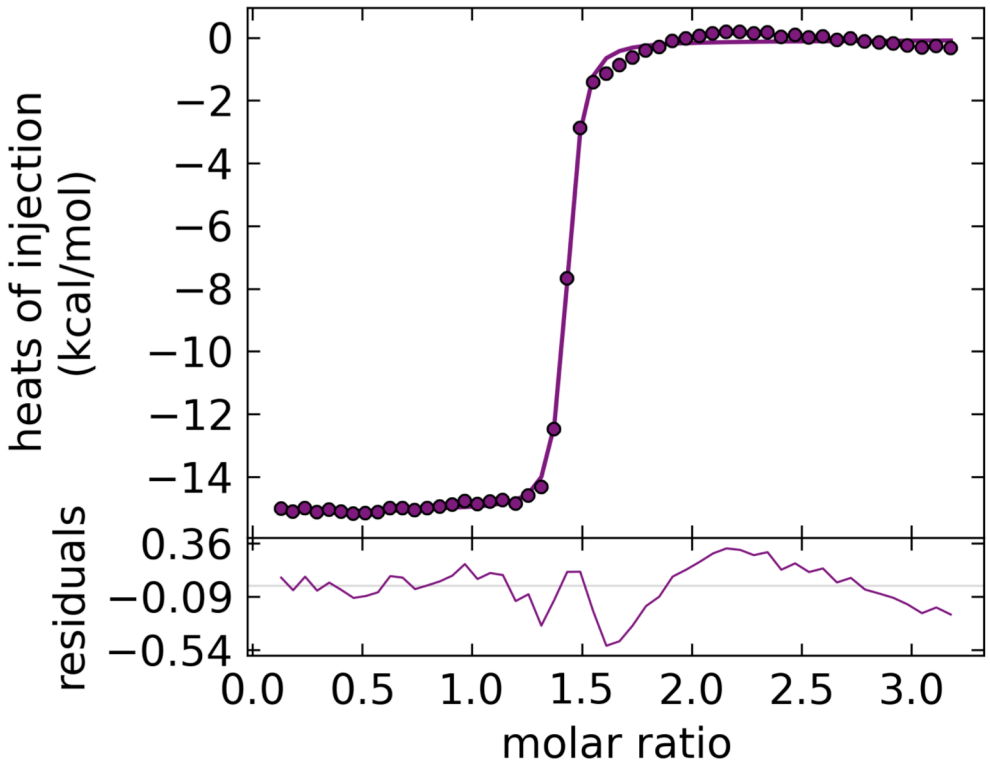

Figure 3.25: ITC of Active W175F PAI-1.
Active 20uM W175F PAI-1 was dialyzed into 50mM MOPS, 250mM $(NH_4)_2SO_4$ pH 7.4 at 10°C. Copper at 300uM was added to the buffer matched dialysate from a concentrated stock, and pH corrected to pH 7.4 at 10°C. Syringe copper was injected into the cell containing PAI-1 in injections of 5uL over 10 second duration, over 120 second intervals, 54 injections total. The data are subtracted from runs in which 300uM CuSO4 in the same buffer was titrated without protein to remove background metal ion-buffer heat of interaction. The data are converted into kcal/mol of injectant as a function of the molar ratio of copper to active PAI-1. Data fitting was performed in Sedphat software to a two site non-symmetric binding isotherm, and the fit is represented using Gussi software.

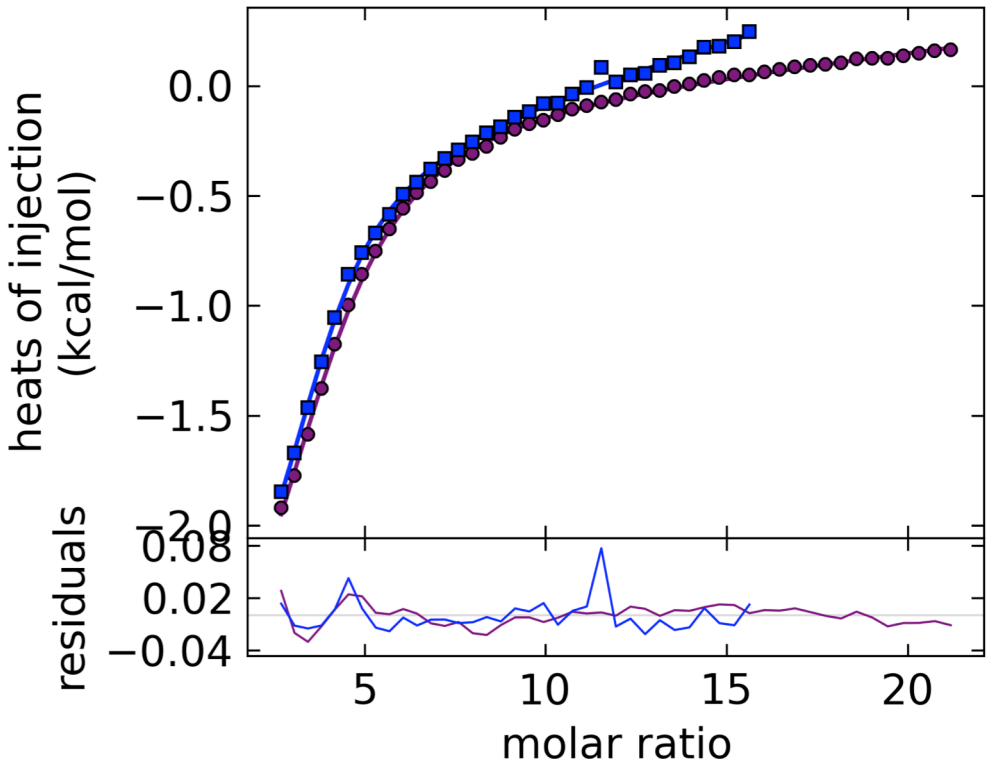

Figure 3.26 ITC Fit of the Weak Transition in Active Wild-Type PAI-1.
Active 20uM wild-type PAI-1 was dialyzed into 50mM MOPS, 250mM $(NH_4)_2SO_4$ pH 7.4 at 10°C. $Copper^{2+}$ at 2mM was added to the buffer matched dialysate from a concentrated stock, and pH corrected to pH 7.4 at 10°C. Syringe copper was injected into the cell containing PAI-1 in injections of 5uL over 10 second duration, over 120 second intervals, 54 injections total. The data are subtracted from runs in which 2mM CuSO4 in the same buffer was titrated without protein to remove background metal ion-buffer heat of interaction. The data are converted into kcal/mol of injectant as a function of the molar ratio of copper to active PAI-1. Data fitting was performed in Sedphat Software to a one site binding model, and the fit is represented using Gussi software.

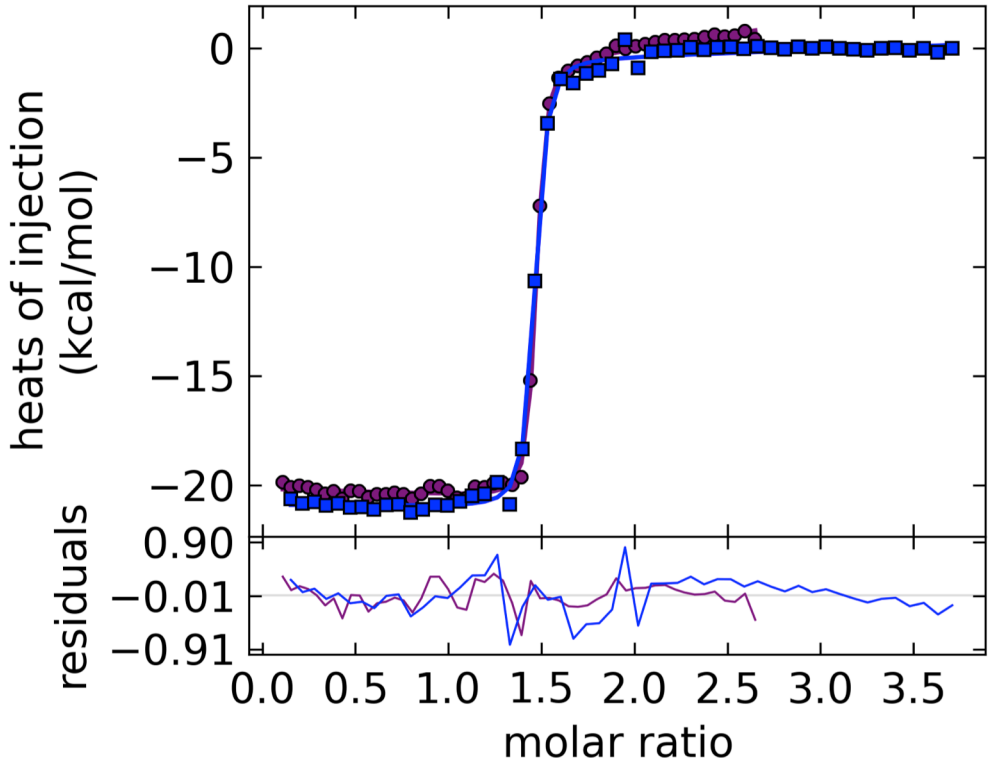

Figure 3.27: ITC Data Fit of Active D222A PAI-1
Active 20uM D222A PAI-1 was dialyzed into 50mM MOPS, 250mM $(NH_4)_2SO_4$ pH 7.4 at 10°C. $Copper^{2+}$ at 350uM was added to the buffer matched dialysate from a concentrated stock, and pH corrected to pH 7.4 at 10°C. Syringe copper was injected into the cell containing PAI-1 in injections of 5uL over 10 second duration, over 120 second intervals, 54 injections total. The data are subtracted from runs in which 350uM CuSO4 in the same buffer was titrated without protein to remove background metal ion-buffer heat of interaction. The data are converted into kcal/mol of injectant as a function of the molar ratio of copper to active PAI-1. Data fitting was performed in Sedphat Software to a two non-symmetric site binding model, and the fit is represented using Gussi software.

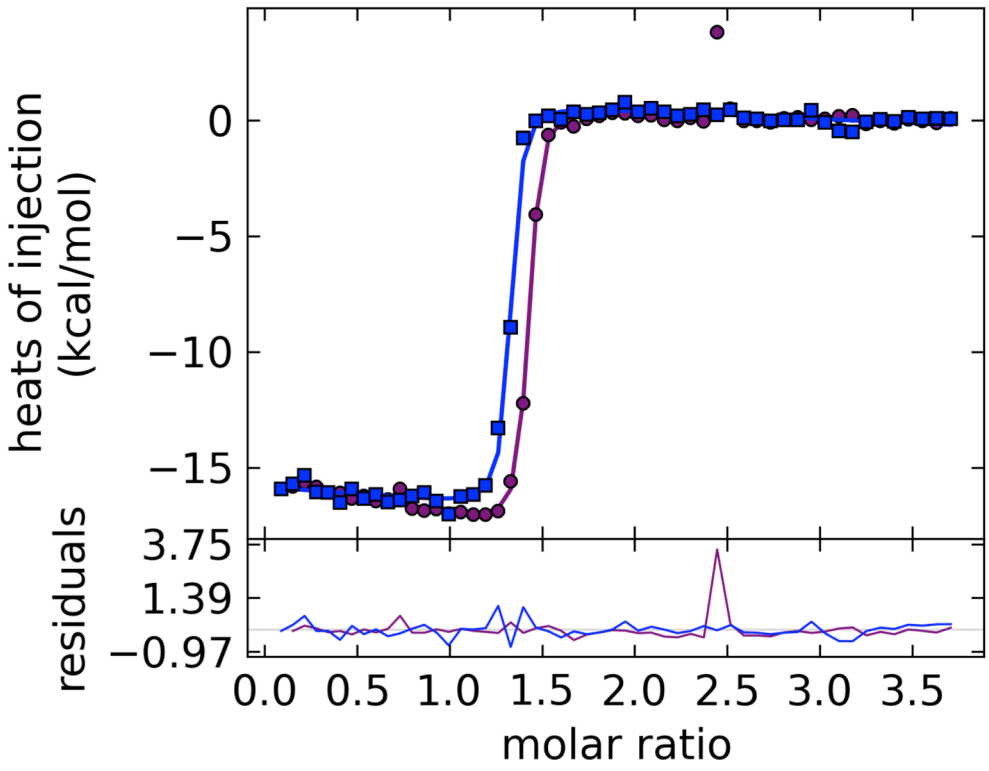

Figure 3.28: ITC Data Fit of Active E242A PAI-1
Active 20uM E242A PAI-1 was dialyzed into 50mM MOPS, 250mM $(NH_4)_2SO_4$ pH 7.4 at 10°C. $Copper^{2+}$ at 350uM was added to the buffer matched dialysate from a concentrated stock, and pH corrected to pH 7.4 at 10°C. Syringe copper was injected into the cell containing PAI-1 in injections of 5uL over 10 second duration, over 120 second intervals, 54 injections total. The data are subtracted from runs in which 350uM CuSO4 in the same buffer was titrated without protein to remove background metal ion-buffer heat of interaction. The data are converted into kcal/mol of injectant as a function of the molar ratio of copper to active PAI-1. Data fitting was performed in Sedphat Software to a two non-symmetric site binding model, and the fit is represented using Gussi software.

required to obtain a fit (data not shown). In the case of E242A PAI-1 however, there does not appear to be a weaker micromolar binding transition. The presence of a weaker transition will be determined in an E242A PAI-1 binding isotherm with higher concentrations of copper^{2+}. These data indicate that the gate region Site C may contain the site that accelerates PAI-1 latency, albeit at micromolar affinities. Additionally, the data argue for the involvement of E242 within this site, rather than D222.

Finally, we tested the effect of SMB domain on the thermodynamics of PAI-1 copper^{2+} binding. We used W175F PAI-1 with a 1.2 molar equivalent of SMB domain, otherwise keeping conditions constant. We observed a titration isotherm that was similar to W175F in the absence of SMB, fitting to a two-site model with K_d's of 20 nM and 30nM, and enthalpy changes of -14.3 and -13.8 kcal/mol, respectively (**Figure 3.29**). This result compares well with active W175F and wild-type PAI-1, further supporting that PAI-1 remains predominantly active during our ITC experiments. We next asked whether or not SMB domain directly interacts with copper^{2+}. Significantly, titration of the SMB domain with copper^{2+} did not result in a titrating heat signal (**Figure 3.30**). This is an important result as it indicates that copper^{2+} does not interact with SMB and exerts direct effects on PAI that are measured in the ITC experiments on the PAI-1-SMB complexes.

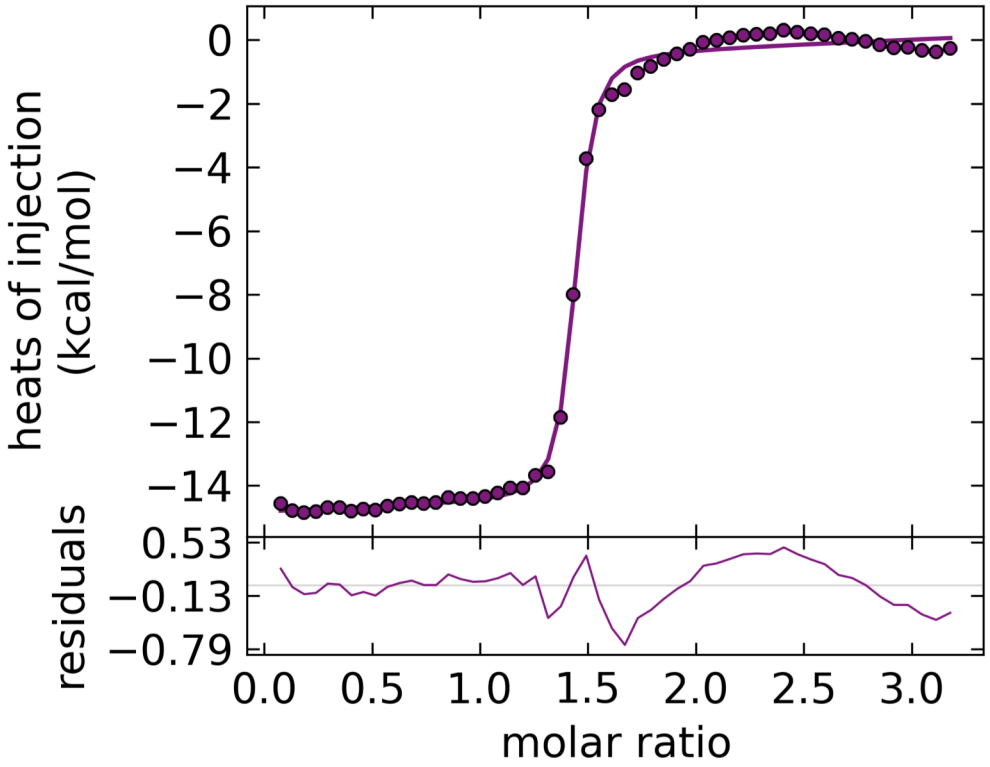

Figure 3.29: Copper^{2+} Binding to SMB Bound PAI-1
Active 20uM W175F PAI-1 with 24uM SMB domain was dialyzed into 50mM MOPS, 250mM $(NH_4)_2SO_4$ pH 7.4 at 10°C. Copper at 300uM was added to the buffer matched dialysate from a concentrated stock, and pH corrected to pH 7.4 at 10°C. Syringe copper was injected into the cell containing PAI-1 in injections of 5uL over 10 second duration, over 120 second intervals, 54 injections total. The data are subtracted from runs in which 300uM CuSO4 in the same buffer was titrated without protein to remove background metal ion-buffer heat of interaction. The data are converted into kcal/mol of injectant as a function of the molar ratio of copper to active PAI-1. Data fitting was performed in Sedphat Software to a two non-symmetric site binding model, and the fit is represented using Gussi Software.

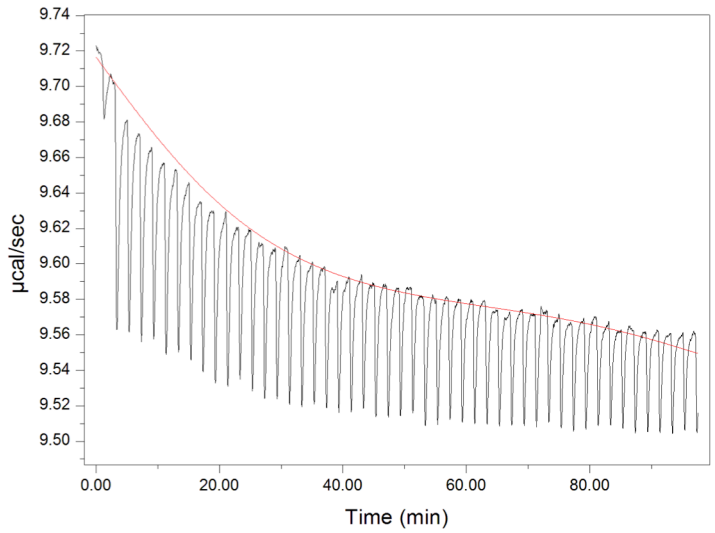

Figure 3.30 ITC of Copper^{2+} Titration into SMB Domain.
SMB domain at 20uM was dialyzed into 50mM MOPS, 250mM $(NH_4)_2SO_4$ pH 7.4 at 10°C. Copper at 400uM was added to the buffer matched dialysate from a concentrated stock, and pH corrected to pH 7.4 at 10°C. Syringe copper was injected into the cell containing PAI-1 in injections of 5uL over 10 second duration, over 120 second intervals, 54 injections total. No attempt was made to fit the data as there was no observable titrating signal.

3.4 Discussion/Conclusions

3.4.a. What Role do the N-terminal Histidines Play in Modulating PAI-1 Function?

The stability kinetics data for the N-terminal histidine variants (Site A) H2A, H3A, and H2AH3A showed that these variants retained the peculiar effect of metals ion to promote the latency transition. Indeed, half-lives in the presence of copper^{2+} were reduced to 4 minutes, compared with 11 in wild-type PAI-1. In the metal titration gel assays, we observed that these variants were even more sensitive to metal ions than wild-type PAI-1. These results clearly demonstrate that copper^{2+} binding to the N-terminal histidines is not responsible for promoting a more rapid latency transition. Strikingly however, H2AH3A PAI-1 appears even more sensitive to copper^{2+} effects than wild-type PAI-1. As observed on the structure, the N-terminal histidines are located on the opposite side of the protein from the central β-sheet A, proximal to but not overlapping with the flexible joints region. The H2AH3A amino acid substitutions remove the tightest first binding transition, and this supports a working model of the N-terminal histidines involvement in a tight binding site. Thus copper^{2+} binding to those residues must have a neutral or stabilizing effect on PAI-1 stability if their removal results in significantly faster conversion in the presence of copper^{2+}.

These results are consistent with HDX experiments comparing wild-type PAI-1 and H2AH3A PAI-1 in the presence of bound copper^{2+} (See Chapter 2). In wild-type PAI-1, copper^{2+} binding results in an increase to protein dynamics in specific regions of the protein, e.g. the flexible joints region underlying shutter region of hB-hC, and hI. Indeed, the same increases in protein dynamics are observed with H2AH3A PAI-1 in the presence of copper^{2+}, underscoring the conclusion that the N-terminal histidines do not comprise a site that accelerates the rate of latency

conversion. There is little evidence of metal ion effects on stability through binding at the N-terminus of PAI-1 via HDX, although local unfolding of proximal hA determined by HDX appears to occur on a timescale consistent with latency transition [85]. Interestingly, another circulatory protein, serum albumin contains an N-terminal histidine copper binding motif that has been characterized [143]. Prion protein PrC also binds to copper^{2+} via N-terminal histidines, which may initiate misfolding and aggregation in neurological disorders [144].

3.4.b. Evidence for Copper^{2+} Coordination Site in the Gate Region that Affects Stability

We observed in the metal titration gel assays that D222A and E242A PAI-1 had transition midpoints for copper sensitivity at higher copper^{2+} concentrations than wild-type PAI-1. In contrast, alanine mutations at residues E212 and E350 PAI-1 did not significantly influence the copper^{2+} concentrations that induce PAI-1 latency. D222 is located on the N-terminal portion of s2B, and E242 is located on the loop that connects s3B-hG. From the PAI-1 structure, it is observed that D222 is partially buried, whereas E242 is solvent exposed (**Figure 3.8**). This is of functional relevance because the gate region loops (s3C-s4C and s4B-hG) are the loops that open up to allow the RCL to pass through and eventually insert into the central β-sheet as s4A. E212 is located on s1B; although it is located proximally to D222 and E242 in the gate region, the data from the alanine switch do not suggest its involvement in metal binding. E350 is located on S1C, just C-terminal of the RCL loop. Strand s1C is of functional importance because it becomes unstructured and extends to allow the RCL passage through the gate region loops. However, in the active form, E350 is distal from D222 and E242. While the conformational change in s1C could affect a closer proximity for E350, evidence from the metal titration gel assays does not indicate a role for E350 in copper binding to the region.

Stability kinetics assays testing D222A and E242A PAI-1 in the presence and absence of copper^{2+} suggest that E242A PAI-1 has similar kinetics in the absence of metal ions, while D222A PAI-1 may be stabilized by the mutation itself. Additionally, ITC of both variants indicates that D222A PAI-1 binds copper^{2+} similar to wild-type, and E242A PAI-1 isotherms do not feature the weaker transition of micromolar affinity, which is proposed to be the copper^{2+} coordination site that accelerates PAI-1 latency. We have also identified that this binding transition is present in the latent forms of PAI-1 as well. A copper^{2+} binding site that favors conversion to the latent state should still exist in the latent form, and may even bind tighter than in the active state. Future ITC experiments with higher copper^{2+} concentrations in the latent and active forms of E242 could shed light on this hypothesis.

An interesting corroborating observation comes from comparing HDX for wild-type PAI-1 and H2AH3A PAI-1 in the presence of copper^{2+} (See Figure 2.17 HDX chapter). Comparison of the wild-type PAI-1:copper^{2+} complex with H2AH3A PAI-1 bound to copper^{2+} reveals protection from exchange for several peptides that span the binding site that contains E242. Copper^{2+} binding is preferred in Site A, which is an order of magnitude tighter than the proposed gate region site. Thus, changes in protection events in the HDX are more easily observed in copper^{2+} binding to gate region site in the variant lacking the Site A histidines, compared with wild-type PAI-1. A hypothesis from the current data is that copper^{2+} is coordinated by a site involving E242. This glutamate residue has proximal, but currently untested, metal ion binding residues such as E244 also of the s3B-hG loop, and H219 of s2B. This differs from the original predicted Site C, as the other three residues show no evidence of deficiencies in copper^{2+} binding, apart from the inclusion of E242. This proposed metal ion coordination involving E242 moving closer to H219 would

move the s3B-hG loop away from the other gate region loop, s3C-s4C, facilitating their opening and thus the path to the latent state.

3.4.c E81 and H364 Residues in Site B May Represent a Secondary Tight Binding Site within Active PAI-1

Amino acid substitution of the MUG algorithm predicted site B residues (E81, H364) resulted in comparable effects to H2AH3A PAI-1 in the stability assays with copper^{2+} and in the metal ion titration assay. In the presence of copper^{2+}, E81A PAI-1 converted to the latent state significantly faster than wild-type. E81A PAI-1 was also most sensitive to copper^{2+} in the titration assay. E81 is located on hD of the flexible joint region, and H364 is located proximally in s4B of the inner core of the protein. We suspect that E81 is part of a secondary binding site, in which copper^{2+} binding provides a neutral or stabilizing influence on rate of latency transition. This is because removal of E81 results in a faster conversion to the latent state in the presence of copper^{2+} compared with wild-type. However, robust copper^{2+} binding analysis of E81A PAI-1 in the active and latent forms by ITC is required to confirm this proposed site B. We hypothesize that as PAI-1 converts to the latent form, the shutter region strands spread out, moving helix D away (E81) from the protein core (H364) and the N-terminus (H2, H3), eliminating contribution to a binding site. This may be an explanation for the reduction in binding when comparing wild-type PAI-1 in the active form to the latent. Future testing with combination variants in the active and latent forms will be required to confirm this mechanism of the tight secondary site. Future testing with combination variants in the active and latent forms will be required to confirm this mechanism of the tight secondary site.

3.4.d. ITC Identifies Key Differences in Copper^{2+} Binding of Active and Latent Variants

A compilation of the K_d, and ΔH values from ITC are listed in **Figure 3.31**. Importantly, an enthalpy change associated with the active, latent, and variant PAI-1 binding to copper^{2+} is reasonably consistent with a copper^{2+} -protein interaction. The isotherms H2AH3A PAI-1 in the latent form, and to a lesser extent latent wild-type, lack lower baselines compared with the active forms. The latent H2AH3A PAI-1 fits to a one site model with weaker, micromolar binding. The latent form of wild-type fits to a two site model, the first of which is attributed to copper^{2+} binding to H2 and H3, and the second transition is of weaker affinity, comparable to the latent H2AH3A PAI-1 data. Fortunately, PAI-1 conversion to the latent form is not accompanied by an enthalpy change, making it possible to do experiments on the active form. The active form of wild-type supports a three binding site model, the first site involves the Site A N-terminal histidines, a second that may involve Site B (E81). The third site is of weaker micromolar affinity involving E242, and is proposed to cause the accelerated transition to the latent state. The first two sites have low nanomolar affinity, although the secondary site can only be observed in active PAI-1.

3.4.e. PAI-1 Bound to SMB negates Copper^{2+} Sensitivity (Wild-type and H2AH3A)

We separately tested wild-type and H2AH3A PAI-1 in the presence of the SMB domain to assess effects of ligand binding on metal ion sensitivity. Since H2AH3A PAI-1 has a similar half-life to wild-type, we were able to directly compare the two forms of PAI-1 bound to SMB. While there are significant differences in the copper sensitivity of wild-type and H2AH3A PAI-1 in the absence of SMB, the metal sensitivities of both forms of PAI-1 bound to SMB are virtually

	Dissociation constant (uM)	Enthalpy change (kcal/mol)	Model	Inc A
Active WT (global)	0.02 (+/- 0.04), 0.06 (+/-0.2), 2.1(+/- 0.05)	-12.2(+/- 1.1), -9.2(+/- 2.0), -8.2(+/- 0.11)	two, one	0.26
Active W175F	0.01(+/- 0.009), 0.02(+/- 0.014)	-14.9 (+/- 0.4), -15.1(+/- 0.8)	two site	0.3
Latent WT (global)	0.05 (+/- 0.04), 2.1 (+/- 0.2)	-12.2 (+/- 0.35), -4.6 (+/- 1.7)	two site	0.6
Latent H2AH3A	1.96 (+/- 0.1)	-8.5 (+/- 0.8)	one site	0.7
Active W175F + SMB	0.03(+/- 0.01), 0.02(+/- 0.015)	-14.3 (+/- 0.6), -13.8(+/- 0.8)	two site	0.29
Active D222A	0.01(+/- 0.002), 0.01(+/-0.005)	-20.2(+/- 0.7), 20.2(+/- 0.6)	two site	0.28
Active E242A	0.009(+/- 0.004), 0.02(+/- 0.006)	-17.2(+/- 0.3), -17.0(+/- 0.006)	two site	0.3

Figure 3.31: Compilation of Data Comparing Thermodynamics of Copper^{2+} Binding in Active versus Latent, Variant PAI-1. The compiled ITC results are contained in the table of wild-type and variant PAI-1 in the active and latent forms. The thermodynamic data (ie. Kd values in uM, and enthalpy changes in kcal/mol)was acquired by fitting in Sedphat software to either one site or two site non-symmetric binding models as appropriate for each experimental condition.

identical. How can SMB binding to PAI-1 produce this result? As observed on the structure, the SMB domain binds in the flexible joint region. The N-terminal histidines do not overlap with the PAI-1/SMB binding interface, and the gate region containing E242 is on the opposite pole of the molecule relative to this region. Since the N-terminus, SMB binding interface, and E242 are not close to one another, it is not reasonable to propose SMB domain sterically blocking $copper^{2+}$ binding to PAI-1. Furthermore, ITC studies titrating $copper^{2+}$ into SMB domain gave no evidence of metal binding to the SMB domain. It is possible that SMB binding could lower the affinity for copper binding at the either of the two binding sites. However, our ITC results that yield a similar K_d of active PAI-1 to $copper^{2+}$ in the presence or absence of SMB suggest otherwise. SMB binding most likely stabilizes PAI-1 in the same way in the presence or absence of metal ions, negating $copper^{2+}$ effects that induce latency.

3.5. Conclusions/Working Model

Figure 3.32 illustrates our working model of the molecular mechanisms by which $copper^{2+}$ affects PAI-1 activity. PAI-1 undergoes a number of structural rearrangements on the path to the latent form, including opening of the gate region loops (teal), and opening of the shutter strands (green) for the RCL (orange) to insert as a new strand in the central β-sheet. SMB domain binding to the flexible joint region confers conformational stabilization to the active form by disfavoring conversion to the latent form. Conversely, metal ions appear to induce conformational conversion that facilitates latency. Through the metal titration gel assays and ITC we were able to identify E242 as the metal binding ligand that results in accelerated latency conversion. We propose that $copper^{2+}$ binding to this region favors the opening of the gate region loops, facilitating the RCL loop to pass through and insert in the central β-sheet A. Since the loops remain open in the latent

Figure 3.32: **Working Model of the Molecular Effects of Copper^{2+} on PAI-1 Activity**. PAI-1 structural changes are highlighted in the RCL (orange), gate region loops (teal), shutter region strands (green), and the flexible joints region (red). The SMB domain binds to s1A (red), and the proposed copper^{2+} binding sites are shown on the structure. In the absence of copper^{2+}, PAI-1 undergoes latency by the opening of the gate region loops, followed by RCL passage and insertion into the central beta-sheet. In the presence of copper^{2+}, copper^{2+} binds to wild-type PAI-1 at the N-terminal histidines, and in proposed binding sites involving E81 and E242 of the gate region. The gate region binding site is the proposed as the metal binding site that induces latency. This results in facilitation of opening the gate region loops, and induced latency conversion. H2AH3A binds copper^{2+} in the proposed sites but not at the N-terminus that contains alanines. A secondary site involving E81 binds copper^{2+} in the active form. Mutation of these residues results in a neutral or stabilizing effect, since when mutated these residues convert to latent faster than wild-type in the presence of copper^{2+}. The SMB domain binds to favor PAI-1 in the active form, and also does so in a similar way when copper^{2+} is present. This stabilization of PAI-1 by SMB negates copper^{2+} induced latency.

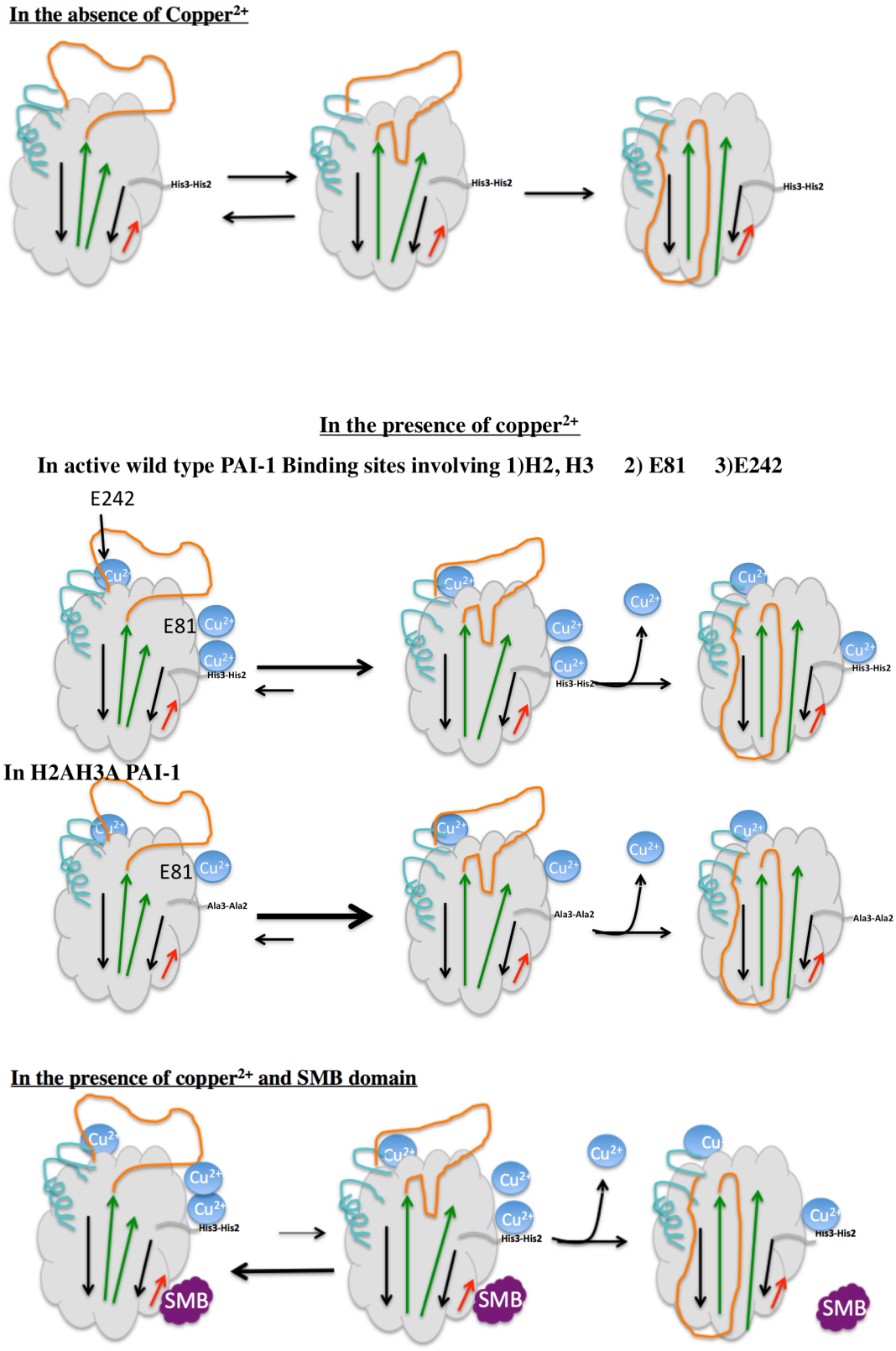

Figure 3.32: Working Model of the Molecular Effects of Copper^{2+} on PAI-1 Activity (Cont.)

state, this site is still functional in the latent form, and it would explain why we still observe this binding even in the latent form of H2AH3A PAI-1. Our experimental evidence suggests that SMB stabilizes PAI-1 in the same way in the presence of copper^{2+}, disfavoring conversion to the latent state. In other words, by this mechanism, SMB negates copper^{2+} effects that induce latency conversion. Mutation of the N-terminal histidines eliminates copper^{2+} binding to these residues. In the presence of copper^{2+}, H2AH3A PAI-1 converts to the latent state faster than wild-type. This indicates that copper^{2+} binding that occurs involving these residues must have a neutral or stabilizing effect on PAI-1 latency. The E81A PAI-1 variant also results in an even higher propensity of copper^{2+} induce latency conversion compared with wild-type. We suspect that E81 is part of a secondary binding site, in which copper^{2+} binding provides a neutral or stabilizing influence on rate of latency transition.

Chapter 4 Characterization of Halide Binding Site on PAI-1

This chapter is an adapted version of the published work:

Crystal Structure of Plasminogen Activator Inhibitor-1 in an Active Conformation with Normal Thermodynamic Stability. Jan K. Jensen, Lawrence C. Thompson, Joel C. Bucci, Poul Nissen, Peter G. W. Gettins, Cynthia B. Peterson, Peter A. Andreasen and J. Preben Morth, J. Biol. Chem. 2011. Volume 286, p.29709-29717.

4.1. Introduction

4.1.a. Evidence of PAI-1 Stabilization by Mutations and Halides

A high-resolution structural characterization (ie. crystal structure) of PAI-1 in the active form had remained elusive for many years due to the propensity of PAI-1 to convert to the latent from at an appreciable rate that corresponded to the timescale for the crystallization process. In order to stabilize active PAI-1, directed evolution studies identified residues that differ from the consensus serpin sequence [87, 90, 93]. Many of the resulting variants produced only modest stabilizing effects on PAI-1. The most dramatic stabilizing mutations came from a quadruple variant termed 14-1b PAI-1 (containing N150H, K154T, Q319L, and M354I mutations), with a half-life for the latency transition of approximately 145 hours [87]. The mutations were synergistic, with the effects of the four being greater than the sum of the effects of the single variants [87]. A caveat, however, is that the four amino acid replacements significantly altered the thermodynamics of PAI-1 folding, with 14-1b PAI-1 having a melting temperature 10°C higher than wild-type PAI-1 [87]. Halides such as chloride ions were also observed to stabilize PAI-1, so that varying NaCl concentrations from 50 mM to 1M resulted in dramatic stabilization to the active form [145]. This observation was part of a study that investigated the thermodynamic stability of PAI-1 active,

latent, and substrate-like forms under heat and chemical denaturation [145]. Thus, the stabilizing mutations and halide binding have interesting structural and functional implications on PAI-1 that prompted further study.

4.1.b. A Chloride Binding Model from the Active 14-1b PAI-1 Structure

The structure of active and latent forms of 14-1b PAI-1 was determined by x-ray crystallography. Three of the four mutations were located close to one another where the base of β-sheet A lies proximally to the loop connecting hF and s3A. The N150H and K154T substitutions are located on the hF-s3A loop, providing the potential for more hydrogen binding interactions with the central β-sheet A [1]. Nearby, the location of the Q319L amino acid switch can reinforce hydrophobic interactions in the hinge-like region at the base of s5A of the shutter [1]. Remote from these substitutions is M354I, which appears to stabilize hydrophobic interactions in s1C, just C-terminal of the RCL in the gate region [1]. The structures determined were consistent with previous work [82, 142], but of particular interest comparing 14-1b to wild-type PAI-1 was the identification of a chloride ion binding site in the central β-sheet A in the 14-1b variant. The structure depicted residues H150, S149 of the hF-s3A loop and K323, K325 of s5A participating in coordination of the chloride ion (**Figure 4.1**) [1]. Additionally, stability kinetics in the presence of halides determined the functional relevance of a halide-binding site within wild-type PAI-1. It was hypothesized that halide binding stabilized interactions between the hF-s3A loop and s5A that prevented translocation of hF, as well as opening of the shutter for RCL peptide insertion at the base of β-sheet A [1]. However, one of the stabilizing mutations of 14-1b PAI-1 was also one of the residues involved (H150) in the proposed chloride ion-binding site. Furthermore, two of the

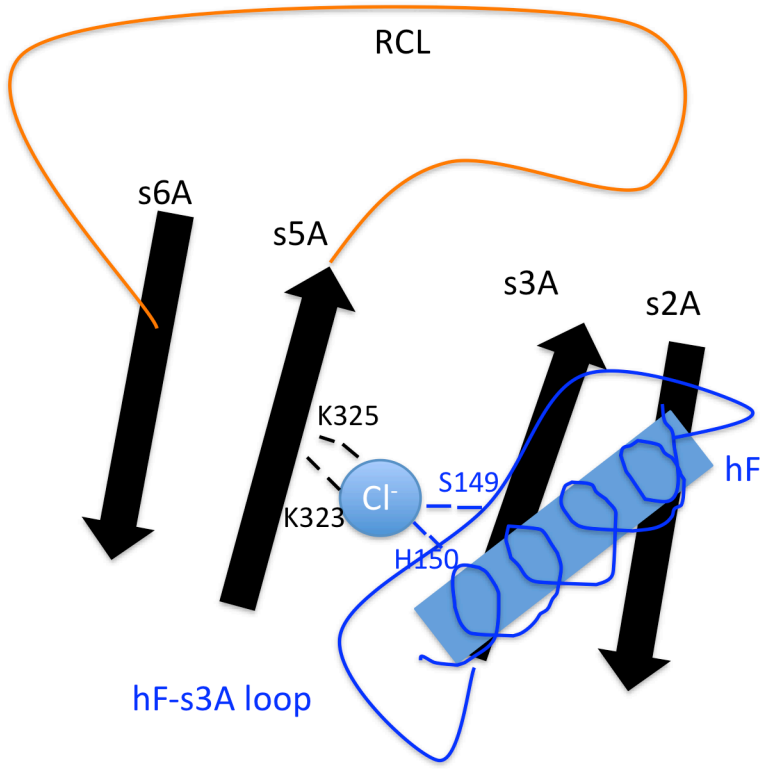

Figure 4.1 Shutter Region Chloride Ion Binding Model. The first hypothesis to explain salt stabilization of PAI-1 was through a chloride ion binding site in the shutter region of PAI-1 [1]. Residues S149 and H150 are shown in blue from the loop between helix hF and strand s3A, and residues K323 and K325 are shown in black from strand s5A. These four residues are shown to coordinate a chloride ion in the shutter. Since the RCL peptide insertion (orange) requires transient displacement of hF, chloride ion binding was presumed to stabilize interactions between hF-s3A loop and s5A. This would prevent full RCL peptide insertion and delay the latency transition time. However, further testing of the functional relevance of this hypothesis was required because H150 was one of the four mutations of 14-1b and is involved in the coordination. Also, two of the other three mutations of 14-1b are proximal to this area. Structural determination of the chloride ion binding in wild-type PAI-1 would determine the functional relevance of this model.

other three amino acid substitutions introduced in the 14-1b variant were located near to the proposed chloride ion binding site, which likely caused structural changes. Because of these reasons, further structural characterization of a potential halide-binding site was needed to determine whether wild-type PAI-1, without the relevant mutations in this region, also exhibit this binding site.

4.1.c. Functional Implication of W175F Crystal Structure and Alternative Chloride Binding Site

More recently, a crystal structure of PAI-1 with only one mutation (W175F) that produces a stable active form was determined by several collaborators, including our group (**Figure 4.2**). This amino acid substitution is located in the breach region on a structural hinge at the apex of shutter strand s3A (**Figure 4.3**). Functionally, this is the location where the first residues of the RCL loop are inserted into the space between shutter strands s3A, and s5A in the latency process. Although this mutation only results in a relatively modest stabilization of PAI-1 ($t_{1/2} \sim 7$ hours), of significance is that this variant retains similar thermodynamic characteristics in comparison to wild-type PAI-1. Circular dichroism (CD) and differential scanning calorimetry (DSC) experiments demonstrated that W175F PAI-1 has an indistinguishable melting point temperature compared with wild-type PAI-1. Conversely, 14-1b active PAI-1, and latent PAI-1 melting temperatures were significantly higher using the same techniques, indicating clear thermodynamic difference from wild-type PAI-1. The structural effect of the mutations was manifested upon successful crystallization of active W175F PAI-1.

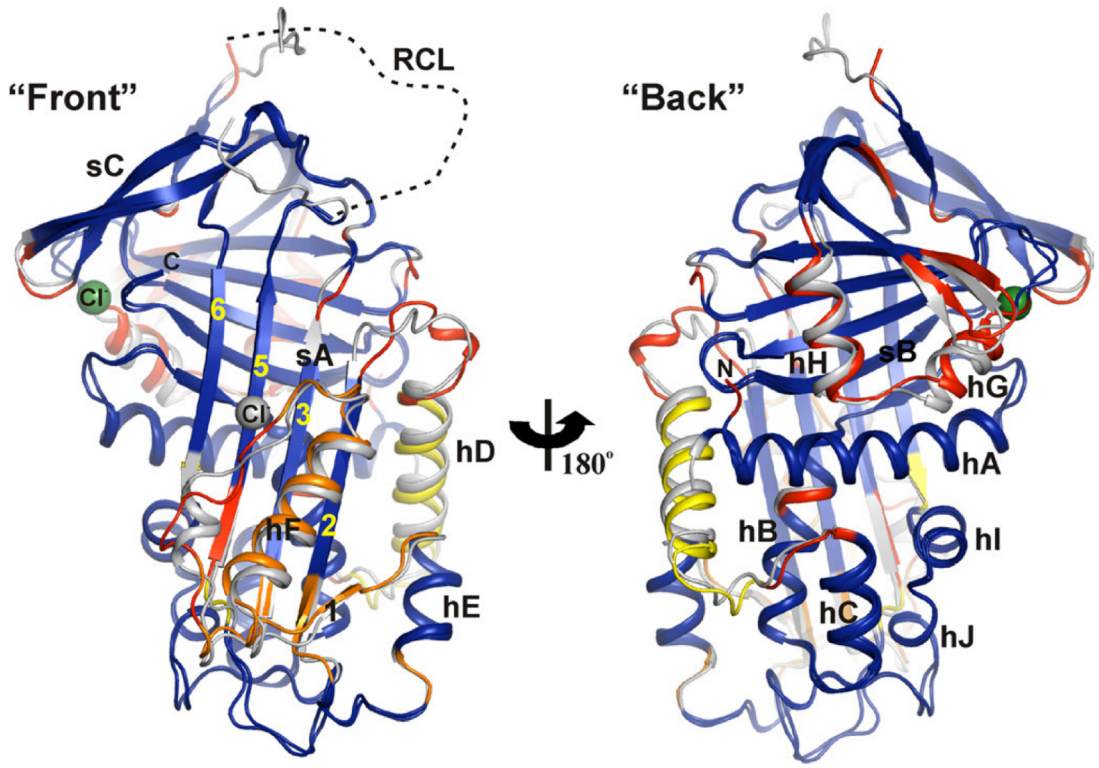

Figure 4.2 The Active W175F PAI-1 Structure. The structure of the active form of PAI-1 was determined with only one mutation W175F at the apex of s3A (pdb: 3q02). The RCL is shown in dotted black lines, with PAI-1 structure represented in ribbon style. The coloring scheme shows differences of this structure compared with the active 14-1b PAI-1 structure, in which blue is most similar, and then yellow, orange, or red are areas of increasing difference between the structures. The proposed shutter region chloride ion binding site is shown in gray, and the gate region chloride ion binding site is shown in green.

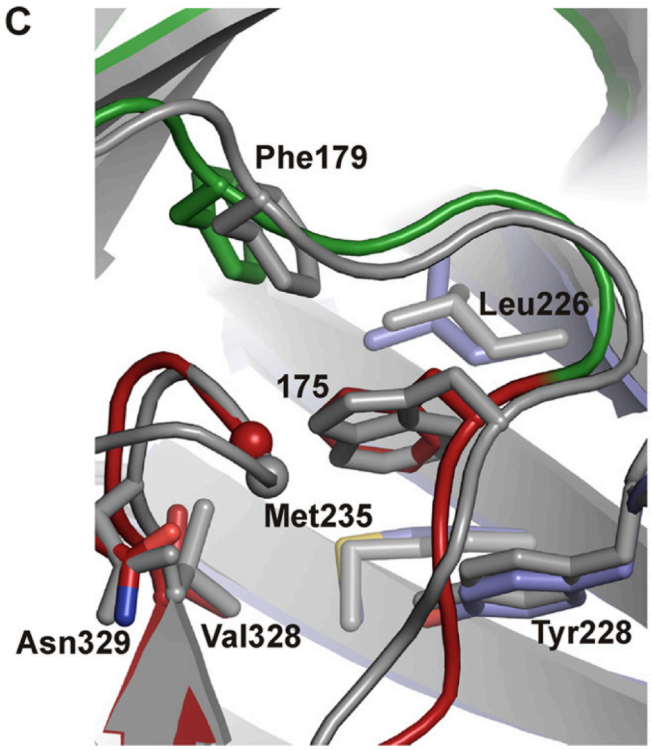

Figure 4.3 Breach Region of W175F PAI-1 Crystal Structure. The breach region at the apex of the shutter strand s3A is illustrated from the active W175F PAI-1 crystal structure. Residues within 5Å of residue 175 are colored and their respective side chains are represented in stick form. For structural comparison, the W175F variant structure is superimposed on the active 14-1b PAI-1 crystal structure (pdb: 1DVM, shown in gray).

The W175F PAI-1 structure featured several interesting differences from the original structural model of active PAI-1, 14-1b. The differences were most apparent in the locations of the mutations, but there were also changes remote from these areas. All but one of the previous PAI_1 structures [97] contained a 3_{10}-like helix in the region that connects hF to s3A. The W175F structure has an extended loop in this region, indicating that the 3_{10}-like helix likely was an artifact of the introduced amino acid substitutions (**Figure 4.4**). The interesting other exception is the 14-1b structure in which PAI-1 is bound to VN, which also does not produce the 3_{10}-like helix [97]. Another interested difference comparing the W175F and 4-1b structures is that hF has a slight clockwise rotation the W175F PAI-1 that propagates a structural change into the flexible joint region. Also, the loop connecting hD and s2A contains W86, which protrudes into the solvent in this structure compared to a buried inward orientation in previous work. There also is loss of a stabilizing salt bridge between D90 of this region and K145 that was previously observed in 14-1b PAI-1 structures. Overall, this results in a slightly different orientation of hD, and slightly shorter strands s2A, and s3A in the W175F PAI-1 structure. Importantly, the 14-1b PAI-1 chloride ion binding site in the center of β-sheet A was not observed in the W175F structure with the natural occurring amino acid residues present in the central β-sheet.

The W175F crystal structure did, however, contain a chloride binding site in the gate region of PAI-1, which has halide-binding contributions from a number of residues within the s3C-s4C loop, s3B-hG loop, and s1C, most notably R356 and S192 (**Figure 4.5**). The "back side" of PAI-1 shows the helices hG, hH shifted toward the chloride ion binding site, due to their contribution to coordination. It is hypothesized that intramolecular communication between the flexible joint

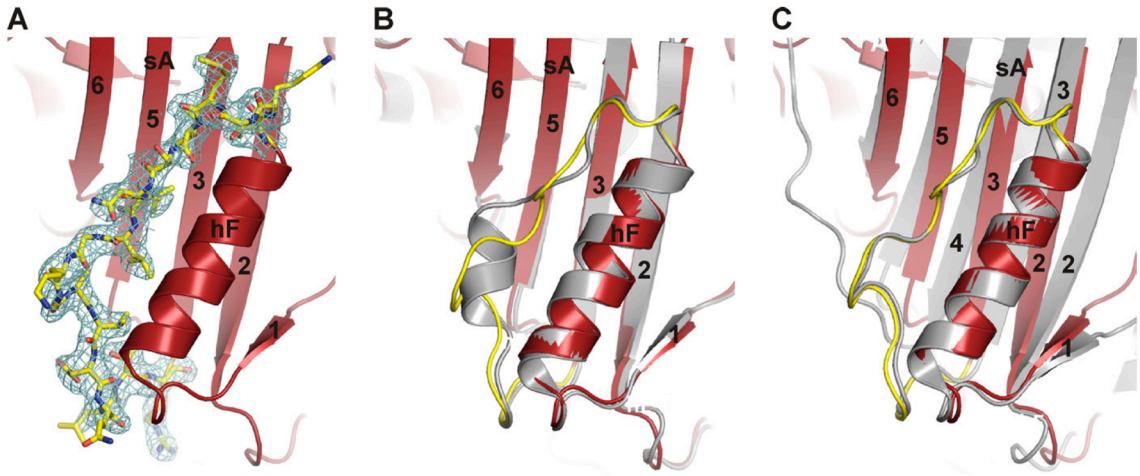

Figure 4.4 Central β-sheet A and Helix F of Active W175F PAI-1. The central β-sheet A and helix F of Active W175F PAI-1 are highlighted in cartoon style in red. The loop between hF and s3A (T144-R162) is shown in yellow to highlight differences in this part of the structure from the active 14-1b PAI-1 structure. On the left, the Fourier difference of electron density is shown for the hF-s3A loop, the residues therein represented in stick form. In the middle, this region is superimposed with the same region in the active 14-1b structure ((pdb: 1dvm, gray), where the loss of the 310 helix is shown. On the right, this region is superimposed with the same region in the latent PAI-1 structure (1LJ5, gray).

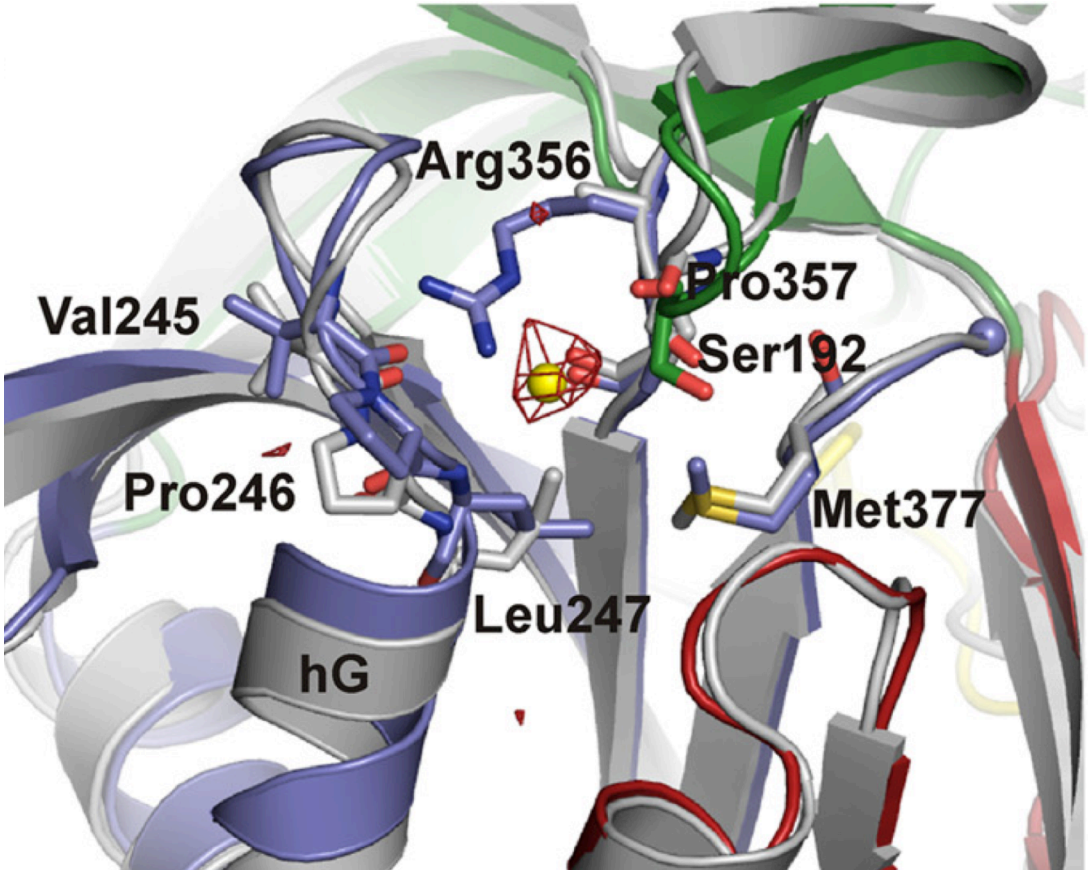

Figure 4.5 Gate Region Chloride Ion Binding Site. The chloride ion binding site in the gate region of the active W175F PAI-1 structure is illustrated in detail. The chloride ion is represented in yellow, immediately surrounded by the Fourier difference electron density map in red. All of the residues within 5Å of the chloride ion are highlighted in color and their respective side chains are represented in stick form. This structure is superimposed on the structure of active 14-1b (pdb: 1DVM, represented in gray) for structural comparison.

region and the gate region could be achieved through motion of these helices. These results suggest a new model for halide stabilization of PAI-1, in which the halide binds to the gate region, stabilizing interactions between the gate region loops s3C-s4C and s3B-hG. This mode of binding would disfavor opening of the gate region loops, and subsequent passage of the uncleaved RCL loop for peptide insertion.

To test the functional relevance of a gate region halide-binding site, we asked several questions. Does wild-type and W175F PAI-1 exhibit a stabilizing effect in the presence of halides? This would indicate whether or not the structural modifications due to the W175F mutation impact the halide binding. What halide concentrations are required to produce stabilizing effects? Finally, is there a preference for different halides binding in the site identified? To answer these questions, we tested wild-type and W175F PAI-1 in the presence of low and high concentrations of sodium halides, including NaF, NaCl, and NaBr. Out aim was to determine the physiological relevance and specificity of the newly proposed PAI-1 halide-binding site.

4.2. Materials and Methods

4.2.a. PAI-1 Stability Assay

To measure the latency conversion half-life of PAI-1, 100nM PAI-1 was incubated in 20mM HEPES, pH 7.4 at 37°C. The assays were performed using either low concentration (150 mM) of or a higher concentration (1.0M) of sodium halide (NaF, NaCl, NaBr). At various time points during the incubation with halides, 0.1uM PAI-1 is mixed with 0.1uM two chain tPA in 20mM

HEPES, 1% BSA, pH 7.4 at 37°C. Spectrozyme tPA substrate (1mM) is added to the PAI-1/tPA mixtures and the reaction is monitored for 5 minutes at 405 nm. Data were collected at various time points anticipated for the duration of ~10 expected half-lives, and each assay is done in triplicate. The tPA activities (linear slopes) at each time point are plotted as a function of time. The inverse of these values (PAI-1 activity) were normalized and fit to a single exponential decay function in Graphpad Prism to determine the rate of latency conversion (k_{lat}) and half-life of latency conversion.

4.3. Results

4.3.a. NaCl Stabilizes Wild-type and W175F PAI-1

We tested the kinetics of wild-type and W175F in the presence of low (150mM) and (1.0M) high concentrations of NaCl to determine the relative rates of conversation to latency and to probe the role of the chloride ion binding site in the gate region (**Figure 4.6-4.7**). At the lower concentration of NaCl (150mM), PAI-1 remained in the active form in the assay for a half-life of 49 minutes for wild-type PAI-1, and 199 minutes for W175F PAI-1. These values fall consistently within literature values for PAI-1, which can vary somewhat depending on buffer and experimental conditions [75, 79]. Furthermore, when PAI-1 is incubated with a high concentration of NaCl (1.0M), there is a marked reduction in latency transition rate in both wild-type and W175F PAI-1. Over the course of a 7-hour assay, less than 10% of PAI-1 was converted to the latent form. Thus, it is clear that high amounts of chloride significantly stabilize both wild-type and W175F PAI-1, with estimated half-lives that exceed 30 hours in the presence of 1.0M NaCl. This observation supports the existence of a halide-binding site in the gate region of PAI-1 in both wild-type protein and the W175F variant.

4.3.b. PAI-1 Stabilization Chloride Ion Specific

We next asked if the observed stabilization of PAI-1 was specific to chloride ions or if other halides, namely fluoride or bromide ions, could produce the same effect (**Figures 4.6-4.7**). We tested wild-type and W175F PAI-1 at the same concentrations of NaF and NaBr as used above with NaCl (either 150mM or 1.0M). When measured at the lower concentrations, wild-type PAI-1 incubated with NaF and NaBr converts to the latent form at comparable rates to the results observed with NaCl. The calculated half-lives at 150 mM NaF and NaBr are $t_{1/2}$ = 57 minutes, and 56 minutes, respectively, compared with 49 minutes with NaCl. This trend is also observed when we examine the same conditions for W175F PAI-1. The calculated half-lives for W175F PAI-1 with low NaF, and NaBr are $t_{1/2}$ = 246 minutes, 211 minutes, respectively compared with 199 minutes in NaCl. However, when wild-type PAI-1 is incubated at the higher concentration (1.0M) of NaF, and NaBr, moderate stabilization occurs but not nearly to the extent of stabilization when PAI-1 is incubated with 1.0M NaCl. The calculated half-lives are $t_{1/2}$ = 226 minutes, and 81 minutes, respectively for NaF and NaBr compared with a $t_{1/2}$ estimated to be over 1800 minutes with 1M NaCl. This result is recapitulated with W175F PAI-1 incubated with 1.0M sodium halides. The calculated half-lives are $t_{1/2}$ = 546 minutes, and 239 minutes for NaF and NaBr, respectively compared to an estimated half-life of over 1800 minutes at the same concentration in NaCl. Altogether, our observations suggest that PAI-1 high concentrations of sodium halide are capable of stabilizing PAI-1, and this effect is specific and varies according to the identify of the various halide ions.

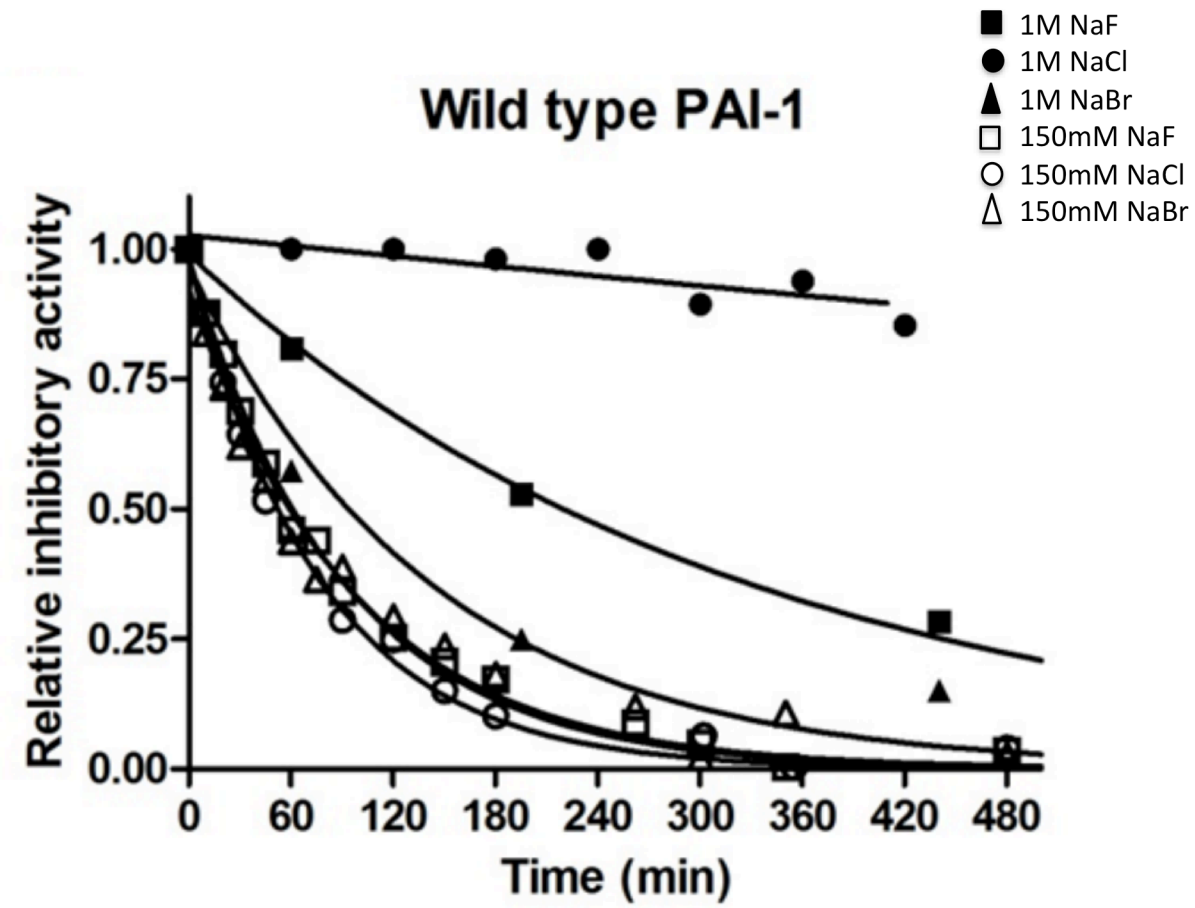

Figure 4.6 Wild-type PAI-1 Significantly Stabilized by High Concentrations of NaCl. The stability kinetics of PAI-1 in the presence of several sodium halides (NaF, NaCl, NaBr) was measured using the stability kinetics assay. The normalized PAI-1 inhibitory activity is plotted as a function of PAI-1 incubation time. The experimental conditions are represented as follows: NaF are squares, NaCl are circles, NaBr are triangles. The open shapes represent the 150mM concentration of each sodium halide, and the dark filled shapes represent 1.0 M concentration of each sodium halide. Data are fit to an exponential decay equation to calculate rate and half-lives of PAI-1 latency transition.

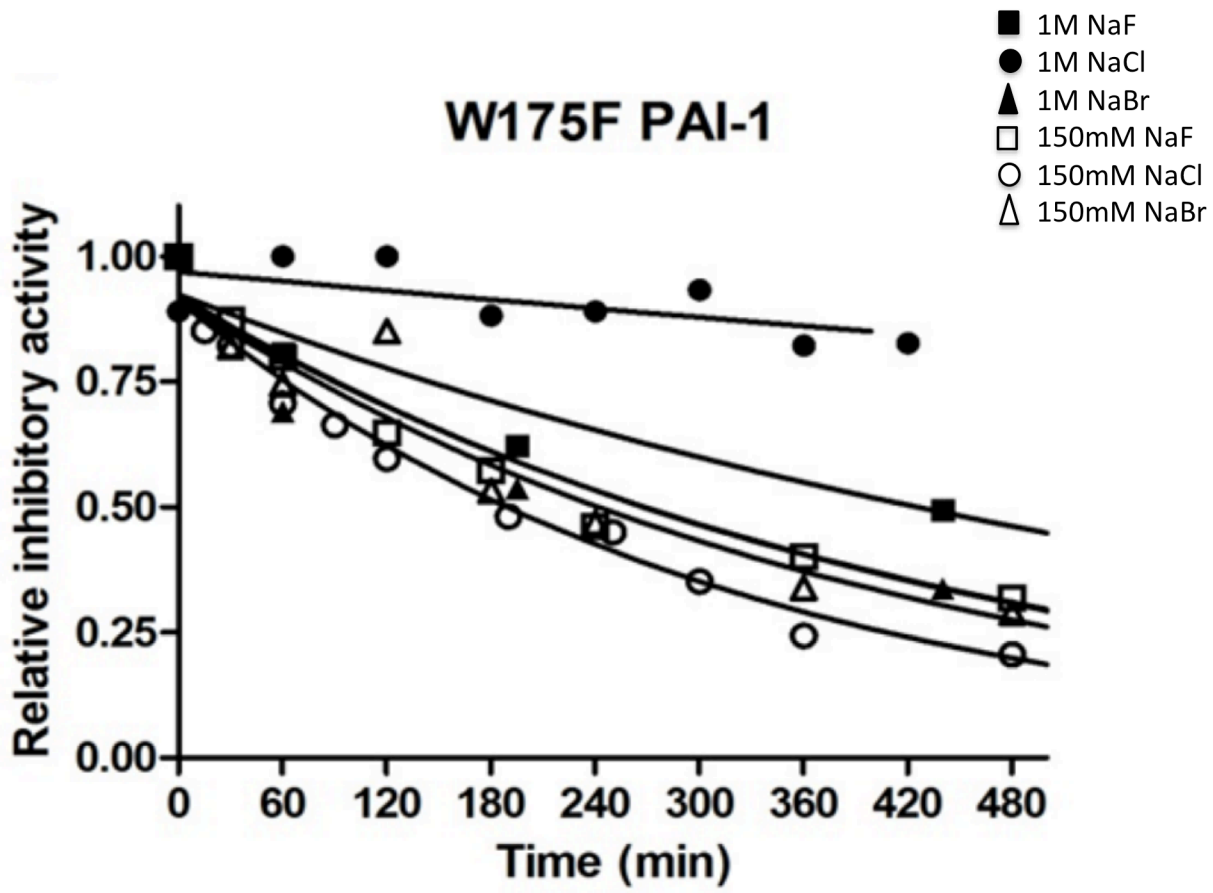

Figure 4.7 W175F PAI-1 Significantly Stabilized by High Concentrations of NaCl. The stability kinetics of PAI-1 in the presence of several sodium halides (NaF, NaCl, NaBr) was measured using the stability kinetics assay. The normalized PAI-1 inhibitory activity is plotted as a function of PAI-1 incubation time. The experimental conditions are represented as follows: NaF are squares, NaCl are circles, NaBr are triangles. The open shapes represent the 150mM concentration of each sodium halide, and the dark filled shapes represent 1.0 M concentration of each sodium halide. Data are fit to an exponential decay equation to calculate rate and half-lives of PAI-1 latency transition.

4.4 Discussion/Conclusions

4.4.a. A Chloride Specific Binding Site in Gate Region Stabilizes PAI-1

The original discovery of salt-dependent stabilization of PAI-1 through a possible chloride binding site that came from Stout et al. [1] with the 14-1b PAI-1 structure. The data presented here largely supports their hypothesis, with a specific site that appears to be chloride specific and which significantly stabilizes PAI-1 at high NaCl (1.0M) concentrations. However, the identity of the proposed chloride-ion binding site differs in the W175F structure. The retention of three wild-type amino acid residues near the hF-s3A loop and the base of the central β-sheet A in W175F relative to 14-1b gives different results for halide binding in the crystal structures. Notably, these three residues are in the vicinity of the proposed chloride ion binding site first proposed, in particular with regard to H150, which was implicated in original site for coordinating the chloride ion [1]. The absence of chloride ion binding to this region in W175F indicates that the binding event was presumably induced by the mutations of 14-1b, rather than naturally occurring in wild-type PAI-1. The kinetic results comparing wild-type and W175 PAI-1 show comparable half-lives in the presence of sodium halides, and then a similar and significant stabilization at high concentrations of NaCl. Other sodium halides tested stabilize both forms of PAI-1 somewhat, but more modestly than observed with NaCl (**Figure 4.8**).

The evidence with W175F and wild-type PAI-1 supports the presence of a physiologically relevant chloride ion binding site in the gate region of PAI-1. The location within the gate region positions chloride ion binding at a site that is remote from that of lone amino acid substitution in

	Wild type PAI-1, $t_{½}$ (min)	W175F PAI-1, $t_{½}$ (min)
NaCl (150 mM)	49 ± 3	199 ± 5
NaCl (1 M)	>1800	>1800
NaBr (150 mM)	56 ± 9	211 ± 12
NaBr (1 M)	81 ± 4	239 ± 80
NaF (150 mM)	57 ± 6	246 ± 17
NaF (1 M)	226 ± 35	546 ± 31

Figure 4.8: Compiled stability kinetics data of wtPAI-1 and W175F in the presence of sodium halides. The table in Figure 4.8 displays the average half-lives ($t_{1/2}$) of wtPAI-1 and W175F PAI-1 in the presence of either 150mM or 1M of sodium halides. Each assay was performed in triplicate of three independent measurements, and the resulting values were used to calculate standard error.

the W175F protein. Our data suggest that the binding site has highest affinity for chloride ions because it is optimally sized for this physiologically relevant ion. The observed coordination site for halides in this area of PAI-1 suggests a model by which chloride ion binding can stabilize the active form. During the process of latency conversion, the gate loops widen, and s1C stretches out as the RCL passes through. The significant reorganization of the gate region during latency distorts the positioning of the coordinating residues to such an extent that chloride ion binding to the latent form would be very weak or likely absent. With the gate region so intimately linked to the stability of PAI-1, it is logical that chloride ion binding could cause the drastic changes we observe in our data. Our data does not follow traditional halide binding size patterns. We have characterized a functionally relevant chloride ion binding site on PAI-1 that may have a physiological and/or pathophysiological roles in healthy and disease states.

Chapter 5 Overall Conclusions/Future Directions

This work has helped explain the molecular basis for ligand effects on PAI-1 stability and dynamics, namely copper^{2+}, SMB domain, and chloride ions. We have completed a full thermodynamic characterization of PAI-1 copper^{2+} binding in the active, latent, and SMB bound PAI-1 forms. Active PAI-1 binds copper^{2+} tightly, the affinity of which is the same with SMB bound, but with reduced binding in the latent form. Through site directed mutagenesis, we have identified three metal ion binding clusters that show functional and thermodynamic differences from wild-type PAI-1. We have fully characterized the dynamics of active and latent PAI-1 in the presence of copper^{2+}, and SMB domain. PAI-1 stability is tied to protein dynamics, as ligands that decrease dynamics result in stabilization of active PAI-1, and those that enhance dynamics accelerate conversion the latent form. Copper^{2+} increases PAI-1 dynamics of peptides structurally localized to the flexible joints region, underlying shutter region and proximal helices. Interestingly, these same regions are the regions of PAI-1 where dynamics is decreased by the stabilizing SMB ligand. Finally, the recent crystal structure of W175F represents the most accurate structural model for active wild-type PAI-1 to date. A halide ion binding site in the gate region is identified that significantly stabilizes PAI-1 at high concentrations. The halide ion binding site is specific to chloride ions, as fluoride and bromide can not produce the same stabilizing effects on PAI-1.

Several future experiments are required to completely understand how copper^{2+} can destabilize PAI-1 but stabilize it in the presence of VN or SMB. We aim to further investigate the gate region proposed site involving E242, E244, and H219 that may accelerate latency transition. Single and combination PAI-1 variants will be generated and tested for comparison to Wild-type for stability, sensitivity, and binding in the presence of copper^{2+}. Additionally, measurement of

H2AH3A, E81A, and H364A PAI-1 variants of latency conversion kinetics should be assayed in the presence of SMB domain and copper^{2+}, to determine if copper^{2+} binding to these residues is indeed involved in the observed further stabilization of PAI-1/SMB. These variants will also undergo full thermodynamic characterization to copper^{2+} in the ITC with SMB bound to observe copper^{2+} binding differences.

Additionally, early observations of PAI-1 tPA interaction suggest that copper^{2+} produces an increase in "substrate-like" PAI-1. The PAI-1 k_{lim} of inhibition for PAI-1 to tPA and uPA should be performed by stopped-flow kinetics in the presence of copper^{2+} for comparison with the PAI-1 alone or with SMB bound stopped-flow data. After these studies are complete, a cell culture and animal model could be designed with wild-type and metal ion binding deficient variants to assess physiological relevance of PAI-1 copper^{2+} regulation through their interaction.

References

1. Stout, T.J., et al., *Structures of active and latent PAI-1: a possible stabilizing role for chloride ions*. Biochemistry, 2000. **39**(29): p. 8460-9.
2. Silverman, G.A., et al., *Serpins flex their muscle: I. Putting the clamps on proteolysis in diverse biological systems*. J Biol Chem, 2010. **285**(32): p. 24299-305.
3. van Mourik, J.A., D.A. Lawrence, and D.J. Loskutoff, *Purification of an inhibitor of plasminogen activator (antiactivator) synthesized by endothelial cells*. J Biol Chem, 1984. **259**(23): p. 14914-21.
4. Budzynski, A.Z., *Fibrinogen and fibrin: biochemistry and pathophysiology*. Crit Rev Oncol Hematol, 1986. **6**(2): p. 97-146.
5. Loskutoff, D.J. and T.E. Edgington, *Synthesis of a fibrinolytic activator and inhibitor by endothelial cells*. Proc Natl Acad Sci U S A, 1977. **74**(9): p. 3903-7.
6. Fay, W.P., N. Garg, and M. Sunkar, *Vascular functions of the plasminogen activation system*. Arterioscler Thromb Vasc Biol, 2007. **27**(6): p. 1231-7.
7. Carmeliet, P., et al., *Physiological consequences of loss of plasminogen activator gene function in mice*. Nature, 1994. **368**(6470): p. 419-24.
8. Loskutoff, D.J., *A slice of PAI*. J Clin Invest, 1993. **92**(6): p. 2563.
9. Vaughan, D.E., *PAI-1 antagonists: the promise and the peril*. Trans Am Clin Climatol Assoc, 2011. **122**: p. 312-25.
10. Wiman, B., *Plasminogen activator inhibitor 1 in thrombotic disease*. Curr Opin Hematol, 1996. **3**(5): p. 372-8.
11. Alessi, M.C., et al., *Adipose tissue and atherothrombosis*. Pathophysiol Haemost Thromb, 2003. **33**(5-6): p. 290-7.
12. Berg, A.H. and P.E. Scherer, *Adipose tissue, inflammation, and cardiovascular disease*. Circ Res, 2005. **96**(9): p. 939-49.
13. Podor, T.J., et al., *Type 1 plasminogen activator inhibitor binds to fibrin via vitronectin*. J Biol Chem, 2000. **275**(26): p. 19788-94.
14. Podor, T.J., et al., *Incorporation of vitronectin into fibrin clots. Evidence for a binding interaction between vitronectin and gamma A/gamma' fibrinogen*. J Biol Chem, 2002. **277**(9): p. 7520-8.
15. Declerck, P.J., et al., *Purification and characterization of a plasminogen activator inhibitor 1 binding protein from human plasma. Identification as a multimeric form of S protein (vitronectin)*. J Biol Chem, 1988. **263**(30): p. 15454-61.
16. Lawrence, D.A., et al., *Characterization of the binding of different conformational forms of plasminogen activator inhibitor-1 to vitronectin. Implications for the regulation of pericellular proteolysis*. J Biol Chem, 1997. **272**(12): p. 7676-80.
17. Lawrence, D.A., et al., *Serpin reactive center loop mobility is required for inhibitor function but not for enzyme recognition*. J Biol Chem, 1994. **269**(44): p. 27657-62.
18. Wei, Y., et al., *Identification of the urokinase receptor as an adhesion receptor for vitronectin*. J Biol Chem, 1994. **269**(51): p. 32380-8.
19. Hedberg, K.K., et al., *High-molecular-weight serum protein complexes differentially promote cell migration and the focal adhesion localization of the urokinase receptor in human glioma cells*. Exp Cell Res, 2000. **257**(1): p. 67-81.
20. Memmo, L.M. and P. McKeown-Longo, *The alphavbeta5 integrin functions as an endocytic receptor for vitronectin*. J Cell Sci, 1998. **111 (Pt 4)**: p. 425-33.

21. Stefansson, S. and D.A. Lawrence, *The serpin PAI-1 inhibits cell migration by blocking integrin alpha V beta 3 binding to vitronectin*. Nature, 1996. **383**(6599): p. 441-3.
22. Nykjaer, A., et al., *Recycling of the urokinase receptor upon internalization of the uPA:serpin complexes*. EMBO J, 1997. **16**(10): p. 2610-20.
23. Conese, M., et al., *alpha-2 Macroglobulin receptor/Ldl receptor-related protein(Lrp)-dependent internalization of the urokinase receptor*. J Cell Biol, 1995. **131**(6 Pt 1): p. 1609-22.
24. Cao, C., et al., *Endocytic receptor LRP together with tPA and PAI-1 coordinates Mac-1-dependent macrophage migration*. EMBO J, 2006. **25**(9): p. 1860-70.
25. Stoop, A.A., F. Lupu, and H. Pannekoek, *Colocalization of thrombin, PAI-1, and vitronectin in the atherosclerotic vessel wall: A potential regulatory mechanism of thrombin activity by PAI-1/vitronectin complexes*. Arterioscler Thromb Vasc Biol, 2000. **20**(4): p. 1143-9.
26. Gutierrez, L.S., et al., *Tumor development is retarded in mice lacking the gene for urokinase-type plasminogen activator or its inhibitor, plasminogen activator inhibitor-1*. Cancer Res, 2000. **60**(20): p. 5839-47.
27. De Taeye, B., L.H. Smith, and D.E. Vaughan, *Plasminogen activator inhibitor-1: a common denominator in obesity, diabetes and cardiovascular disease*. Curr Opin Pharmacol, 2005. **5**(2): p. 149-54.
28. Lyon, C.J. and W.A. Hsueh, *Effect of plasminogen activator inhibitor-1 in diabetes mellitus and cardiovascular disease*. Am J Med, 2003. **115 Suppl 8A**: p. 62S-68S.
29. Nordt, T.K., et al., *Plasminogen activator inhibitor type-1 (PAI-1) and its role in cardiovascular disease*. Thromb Haemost, 1999. **82 Suppl 1**: p. 14-8.
30. Ploplis, V.A., *Effects of altered plasminogen activator inhibitor-1 expression on cardiovascular disease*. Curr Drug Targets, 2011. **12**(12): p. 1782-9.
31. Vaughan, D.E., *PAI-1 and atherothrombosis*. J Thromb Haemost, 2005. **3**(8): p. 1879-83.
32. Adibhatla, R.M. and J.F. Hatcher, *Tissue plasminogen activator (tPA) and matrix metalloproteinases in the pathogenesis of stroke: therapeutic strategies*. CNS Neurol Disord Drug Targets, 2008. **7**(3): p. 243-53.
33. Fuster, V., et al., *The pathogenesis of coronary artery disease and the acute coronary syndromes (2)*. N Engl J Med, 1992. **326**(5): p. 310-8.
34. Burke, A.P., et al., *Healed plaque ruptures and sudden coronary death: evidence that subclinical rupture has a role in plaque progression*. Circulation, 2001. **103**(7): p. 934-40.
35. Konstantinides, S., K. Schafer, and D.J. Loskutoff, *Do PAI-1 and vitronectin promote or inhibit neointima formation? The exact role of the fibrinolytic system in vascular remodeling remains uncertain*. Arterioscler Thromb Vasc Biol, 2002. **22**(12): p. 1943-5.
36. Minor, K.H. and C.B. Peterson, *Plasminogen activator inhibitor type 1 promotes the self-association of vitronectin into complexes exhibiting altered incorporation into the extracellular matrix*. J Biol Chem, 2002. **277**(12): p. 10337-45.
37. Garg, N., et al., *Plasminogen activator inhibitor-1 and vitronectin expression level and stoichiometry regulate vascular smooth muscle cell migration through physiological collagen matrices*. J Thromb Haemost, 2010. **8**(8): p. 1847-54.
38. Andreasen, P.A., R. Egelund, and H.H. Petersen, *The plasminogen activation system in tumor growth, invasion, and metastasis*. Cell Mol Life Sci, 2000. **57**(1): p. 25-40.

39. Chazaud, B., et al., *Promigratory effect of plasminogen activator inhibitor-1 on invasive breast cancer cell populations*. Am J Pathol, 2002. **160**(1): p. 237-46.
40. Naina, H.V., et al., *Systemic fibrinolysis caused by tissue plasminogen activator-producing metastatic breast cancer*. J Clin Oncol, 2010. **28**(11): p. e167-8.
41. Machowska, M., et al., *Nuclear location of tumor suppressor protein maspin inhibits proliferation of breast cancer cells without affecting proliferation of normal epithelial cells*. BMC Cancer, 2014. **14**(1): p. 142.
42. Kwaan, H.C., A.P. Mazar, and B.J. McMahon, *The apparent uPA/PAI-1 paradox in cancer: more than meets the eye*. Semin Thromb Hemost, 2013. **39**(4): p. 382-91.
43. Lee, Y.H. and G.G. Song, *Plasminogen activator inhibitor-1 4G/5G and the MTHFR 677C/T polymorphisms and susceptibility to polycystic ovary syndrome: a meta-analysis*. Eur J Obstet Gynecol Reprod Biol, 2014. **175**: p. 8-14.
44. Juhan-Vague, I., et al., *Plasminogen activator inhibitor-1, inflammation, obesity, insulin resistance and vascular risk*. J Thromb Haemost, 2003. **1**(7): p. 1575-9.
45. Alessi, M.C. and I. Juhan-Vague, *PAI-1 and the metabolic syndrome: links, causes, and consequences*. Arterioscler Thromb Vasc Biol, 2006. **26**(10): p. 2200-7.
46. Young, J.L., P. Libby, and U. Schonbeck, *Cytokines in the pathogenesis of atherosclerosis*. Thromb Haemost, 2002. **88**(4): p. 554-67.
47. Schleef, R.R., et al., *Cytokine activation of vascular endothelium. Effects on tissue-type plasminogen activator and type 1 plasminogen activator inhibitor*. J Biol Chem, 1988. **263**(12): p. 5797-803.
48. Slivka, S.R. and D.J. Loskutoff, *Platelets stimulate endothelial cells to synthesize type 1 plasminogen activator inhibitor. Evaluation of the role of transforming growth factor beta*. Blood, 1991. **77**(5): p. 1013-9.
49. Diebold, I., et al., *The 'PAI-1 paradox' in vascular remodeling*. Thromb Haemost, 2008. **100**(6): p. 984-91.
50. Vaughan, D.E., *PAI-1 and cellular migration: dabbling in paradox*. Arterioscler Thromb Vasc Biol, 2002. **22**(10): p. 1522-3.
51. Sobel, B.E., *Increased plasminogen activator inhibitor-1 and vasculopathy. A reconcilable paradox*. Circulation, 1999. **99**(19): p. 2496-8.
52. Irigoyen, J.P., et al., *The plasminogen activator system: biology and regulation*. Cell Mol Life Sci, 1999. **56**(1-2): p. 104-32.
53. Hou, B., et al., *Tumor necrosis factor alpha activates the human plasminogen activator inhibitor-1 gene through a distal nuclear factor kappaB site*. J Biol Chem, 2004. **279**(18): p. 18127-36.
54. Coffey, C.S., et al., *The Association of the Metabolic Syndrome with PAI-1 and t-PA Levels*. Cardiol Res Pract, 2011. **2011**: p. 541467.
55. Samad, F., et al., *Insulin continues to induce plasminogen activator inhibitor 1 gene expression in insulin-resistant mice and adipocytes*. Mol Med, 2000. **6**(8): p. 680-92.
56. Chen, Y.Q., et al., *Sp1 sites mediate activation of the plasminogen activator inhibitor-1 promoter by glucose in vascular smooth muscle cells*. J Biol Chem, 1998. **273**(14): p. 8225-31.
57. Juhan-Vague, I., M.C. Alessi, and P.E. Morange, *Hypofibrinolysis and increased PAI-1 are linked to atherothrombosis via insulin resistance and obesity*. Ann Med, 2000. **32 Suppl 1**: p. 78-84.

58. Dimova, E.Y. and T. Kietzmann, *Metabolic, hormonal and environmental regulation of plasminogen activator inhibitor-1 (PAI-1) expression: lessons from the liver*. Thromb Haemost, 2008. **100**(6): p. 992-1006.
59. Marques-Rocha, J.L., et al., *Noncoding RNAs, cytokines, and inflammation-related diseases*. FASEB J, 2015. **29**(9): p. 3595-611.
60. Tsantes, A.E., et al., *The effect of the plasminogen activator inhibitor-1 4G/5G polymorphism on the thrombotic risk*. Thromb Res, 2008. **122**(6): p. 736-42.
61. Binder, B.R., et al., *Plasminogen activator inhibitor 1: physiological and pathophysiological roles*. News Physiol Sci, 2002. **17**: p. 56-61.
62. Loskutoff, D.J., et al., *Regulation of PAI-1 gene expression in vivo*. Thromb Haemost, 1993. **70**(1): p. 135-7.
63. Kvassman, J.O., I. Verhamme, and J.D. Shore, *Inhibitory mechanism of serpins: loop insertion forces acylation of plasminogen activator by plasminogen activator inhibitor-1*. Biochemistry, 1998. **37**(44): p. 15491-502.
64. Gong, L., et al., *Crystal Structure of the Michaelis Complex between Tissue-type Plasminogen Activator and Plasminogen Activators Inhibitor-1*. J Biol Chem, 2015.
65. Lin, Z., et al., *Structural basis for recognition of urokinase-type plasminogen activator by plasminogen activator inhibitor-1*. J Biol Chem, 2011. **286**(9): p. 7027-32.
66. Lawrence, D.A., et al., *Serpin-protease complexes are trapped as stable acyl-enzyme intermediates*. J Biol Chem, 1995. **270**(43): p. 25309-12.
67. Lawrence, D.A., *The serpin-proteinase complex revealed*. Nat Struct Biol, 1997. **4**(5): p. 339-41.
68. Lawrence, D.A., et al., *Partitioning of serpin-proteinase reactions between stable inhibition and substrate cleavage is regulated by the rate of serpin reactive center loop insertion into beta-sheet A*. J Biol Chem, 2000. **275**(8): p. 5839-44.
69. Verhamme, I., et al., *Accelerated conversion of human plasminogen activator inhibitor-1 to its latent form by antibody binding*. J Biol Chem, 1999. **274**(25): p. 17511-7.
70. Olson, S.T., et al., *Resolution of Michaelis complex, acylation, and conformational change steps in the reactions of the serpin, plasminogen activator inhibitor-1, with tissue plasminogen activator and trypsin*. Biochemistry, 2001. **40**(39): p. 11742-56.
71. Blouse, G.E., et al., *Interactions of plasminogen activator inhibitor-1 with vitronectin involve an extensive binding surface and induce mutual conformational rearrangements*. Biochemistry, 2009. **48**(8): p. 1723-35.
72. York, J.D., P. Li, and S.J. Gardell, *Combinatorial mutagenesis of the reactive site region in plasminogen activator inhibitor I*. J Biol Chem, 1991. **266**(13): p. 8495-500.
73. Hekman, C.M. and D.J. Loskutoff, *Kinetic analysis of the interactions between plasminogen activator inhibitor 1 and both urokinase and tissue plasminogen activator*. Arch Biochem Biophys, 1988. **262**(1): p. 199-210.
74. Lawrence, D.A., et al., *Structure-function studies of the SERPIN plasminogen activator inhibitor type 1. Analysis of chimeric strained loop mutants*. J Biol Chem, 1990. **265**(33): p. 20293-301.
75. Blouse, G.E., et al., *Mutation of the highly conserved tryptophan in the serpin breach region alters the inhibitory mechanism of plasminogen activator inhibitor-1*. Biochemistry, 2003. **42**(42): p. 12260-72.

76. Whisstock, J.C. and S.P. Bottomley, *Molecular gymnastics: serpin structure, folding and misfolding*. Curr Opin Struct Biol, 2006. **16**(6): p. 761-8.
77. Dupont, D.M., et al., *Biochemical properties of plasminogen activator inhibitor-1*. Front Biosci (Landmark Ed), 2009. **14**: p. 1337-61.
78. Sherman, W.A., et al., *Enthalpy measurement using calorimetry shows a significant difference in potential energy between the active and latent conformations of PAI-1*. Biol Chem, 2005. **386**(2): p. 111-6.
79. Thompson, L.C., et al., *Metals affect the structure and activity of human plasminogen activator inhibitor-1*. Protein Sci, 2010.
80. Onda, M., et al., *Latent S49P neuroserpin forms polymers in the dementia familial encephalopathy with neuroserpin inclusion bodies*. J Biol Chem, 2005. **280**(14): p. 13735-41.
81. Beauchamp, N.J., et al., *Antithrombins Wibble and Wobble (T85M/K): archetypal conformational diseases with in vivo latent-transition, thrombosis, and heparin activation*. Blood, 1998. **92**(8): p. 2696-706.
82. Mottonen, J., et al., *Structural basis of latency in plasminogen activator inhibitor-1*. Nature, 1992. **355**(6357): p. 270-3.
83. Dupont, D.M., et al., *Evidence for a pre-latent form of the serpin plasminogen activator inhibitor-1 with a detached beta-strand 1C*. J Biol Chem, 2006. **281**(47): p. 36071-81.
84. Gettins, P.G., *The F-helix of serpins plays an essential, active role in the proteinase inhibition mechanism*. FEBS Lett, 2002. **523**(1-3): p. 2-6.
85. Trelle, M.B., et al., *Local transient unfolding of native state PAI-1 associated with serpin metastability*. Angew Chem Int Ed Engl, 2014. **53**(37): p. 9751-4.
86. Boudier, C., et al., *The conversion of active to latent plasminogen activator inhibitor-1 is an energetically silent event*. Biophys J, 2005. **88**(4): p. 2848-54.
87. Berkenpas, M.B., D.A. Lawrence, and D. Ginsburg, *Molecular evolution of plasminogen activator inhibitor-1 functional stability*. EMBO J, 1995. **14**(13): p. 2969-77.
88. Hekman, C.M. and D.J. Loskutoff, *Endothelial cells produce a latent inhibitor of plasminogen activators that can be activated by denaturants*. J Biol Chem, 1985. **260**(21): p. 11581-7.
89. Lambers, J.W., et al., *Activation of human endothelial cell-type plasminogen activator inhibitor (PAI-1) by negatively charged phospholipids*. J Biol Chem, 1987. **262**(36): p. 17492-6.
90. Stoop, A.A., et al., *Different structural requirements for plasminogen activator inhibitor 1 (PAI-1) during latency transition and proteinase inhibition as evidenced by phage-displayed hypermutated PAI-1 libraries*. J Mol Biol, 2001. **305**(4): p. 773-83.
91. Trelle, M.B., et al., *Hydrogen/deuterium exchange mass spectrometry reveals specific changes in the local flexibility of plasminogen activator inhibitor 1 upon binding to the somatomedin B domain of vitronectin*. Biochemistry, 2012. **51**(41): p. 8256-66.
92. Mangs, H., G.C. Sui, and B. Wiman, *PAI-1 stability: the role of histidine residues*. FEBS Lett, 2000. **475**(3): p. 192-6.
93. Gils, A., et al., *Identification of positively charged residues contributing to the stability of plasminogen activator inhibitor 1*. FEBS Lett, 1997. **415**(2): p. 192-5.

94. De Taeye, B., et al., *Immobilization of the distal hinge in the labile serpin plasminogen activator inhibitor 1: identification of a transition state with distinct conformational and functional properties*. J Biol Chem, 2003. **278**(26): p. 23899-905.
95. Jensen, J.K., et al., *Crystal structure of plasminogen activator inhibitor-1 in an active conformation with normal thermodynamic stability*. J Biol Chem, 2011. **286**(34): p. 29709-17.
96. Hansen, M., M.N. Busse, and P.A. Andreasen, *Importance of the amino-acid composition of the shutter region of plasminogen activator inhibitor-1 for its transitions to latent and substrate forms*. Eur J Biochem, 2001. **268**(23): p. 6274-83.
97. Zhou, A., et al., *How vitronectin binds PAI-1 to modulate fibrinolysis and cell migration*. Nat Struct Biol, 2003. **10**(7): p. 541-4.
98. Schar, C.R., et al., *Characterization of a site on PAI-1 that binds to vitronectin outside of the somatomedin B domain*. J Biol Chem, 2008. **283**(42): p. 28487-96.
99. Xu, D., et al., *Model for the three-dimensional structure of vitronectin: predictions for the multi-domain protein from threading and docking*. Proteins, 2001. **44**(3): p. 312-20.
100. Schar, C.R., et al., *A deletion mutant of vitronectin lacking the somatomedin B domain exhibits residual plasminogen activator inhibitor-1-binding activity*. J Biol Chem, 2008. **283**(16): p. 10297-309.
101. Mayasundari, A., et al., *The solution structure of the N-terminal domain of human vitronectin: proximal sites that regulate fibrinolysis and cell migration*. J Biol Chem, 2004. **279**(28): p. 29359-66.
102. Lynn, G.W., et al., *A model for the three-dimensional structure of human plasma vitronectin from small-angle scattering measurements*. Biochemistry, 2005. **44**(2): p. 565-74.
103. Madsen, J.B., et al., *RNA aptamers as conformational probes and regulatory agents for plasminogen activator inhibitor-1*. Biochemistry, 2010. **49**(19): p. 4103-15.
104. Gils, A., et al., *Biochemical importance of glycosylation of plasminogen activator inhibitor-1*. Thromb Haemost, 2003. **90**(2): p. 206-17.
105. Bager, R., et al., *Protein conformational change delayed by steric hindrance from an N-linked glycan*. J Mol Biol, 2013. **425**(16): p. 2867-77.
106. Gorlatova, N.V., et al., *Mapping of a conformational epitope on plasminogen activator inhibitor-1 by random mutagenesis. Implications for serpin function*. J Biol Chem, 2003. **278**(18): p. 16329-35.
107. Gooptu, B., et al., *Inactive conformation of the serpin alpha(1)-antichymotrypsin indicates two-stage insertion of the reactive loop: implications for inhibitory function and conformational disease*. Proc Natl Acad Sci U S A, 2000. **97**(1): p. 67-72.
108. Komissarov, A.A., P.J. Declerck, and J.D. Shore, *Mechanisms of conversion of plasminogen activator inhibitor 1 from a suicide inhibitor to a substrate by monoclonal antibodies*. J Biol Chem, 2002. **277**(46): p. 43858-65.
109. Thompson, L.C., S. Goswami, and C.B. Peterson, *Metals affect the structure and activity of human plasminogen activator inhibitor-1*. Protein Sci, 2010.
110. Stadler, N., R.A. Lindner, and M.J. Davies, *Direct detection and quantification of transition metal ions in human atherosclerotic plaques: evidence for the presence of elevated levels of iron and copper*. Arterioscler Thromb Vasc Biol, 2004. **24**(5): p. 949-54.

111. Linder, M.C. and M. Hazegh-Azam, *Copper biochemistry and molecular biology*. Am J Clin Nutr, 1996. **63**(5): p. 797S-811S.
112. Osterberg, R., *Physiology and pharmacology of copper*. Pharmacol Ther, 1980. **9**(1): p. 121-46.
113. Nalbandyan, R.M., *Copper in brain*. Neurochem Res, 1983. **8**(10): p. 1211-32.
114. Hartter, D.E. and A. Barnea, *Brain tissue accumulates 67copper by two ligand-dependent saturable processes. A high affinity, low capacity and a low affinity, high capacity process*. J Biol Chem, 1988. **263**(2): p. 799-805.
115. Ji, H.F., et al., *Evolutionary formation of new protein folds is linked to metallic cofactor recruitment*. Bioessays, 2009. **31**(9): p. 975-80.
116. Cartledge, B.T., et al., *The impact of particle size, relative humidity, and sulfur dioxide on iron solubility in simulated atmospheric marine aerosols*. Environ Sci Technol, 2015. **49**(12): p. 7179-87.
117. Jomova, K. and M. Valko, *Advances in metal-induced oxidative stress and human disease*. Toxicology, 2011. **283**(2-3): p. 65-87.
118. Brem, S.S., et al., *Inhibition of angiogenesis and tumor growth in the brain. Suppression of endothelial cell turnover by penicillamine and the depletion of copper, an angiogenic cofactor*. Am J Pathol, 1990. **137**(5): p. 1121-42.
119. Finney, L., et al., *X-ray fluorescence microscopy reveals large-scale relocalization and extracellular translocation of cellular copper during angiogenesis*. Proc Natl Acad Sci U S A, 2007. **104**(7): p. 2247-52.
120. Finney, L., et al., *Copper and angiogenesis: unravelling a relationship key to cancer progression*. Clin Exp Pharmacol Physiol, 2009. **36**(1): p. 88-94.
121. Haidari, M., et al., *Enhanced susceptibility to oxidation and diminished vitamin E content of LDL from patients with stable coronary artery disease*. Clin Chem, 2001. **47**(7): p. 1234-40.
122. Uriu-Adams, J.Y. and C.L. Keen, *Copper, oxidative stress, and human health*. Mol Aspects Med, 2005. **26**(4-5): p. 268-98.
123. Ohrvik, H. and D.J. Thiele, *How copper traverses cellular membranes through the mammalian copper transporter 1, Ctr1*. Ann N Y Acad Sci, 2014. **1314**: p. 32-41.
124. Horn, D. and A. Barrientos, *Mitochondrial copper metabolism and delivery to cytochrome c oxidase*. IUBMB Life, 2008. **60**(7): p. 421-9.
125. Lutsenko, S., *Human copper homeostasis: a network of interconnected pathways*. Curr Opin Chem Biol, 2010. **14**(2): p. 211-7.
126. Tumer, Z., *An overview and update of ATP7A mutations leading to Menkes disease and occipital horn syndrome*. Hum Mutat, 2013. **34**(3): p. 417-29.
127. Wu, F., et al., *Wilson's disease: a comprehensive review of the molecular mechanisms*. Int J Mol Sci, 2015. **16**(3): p. 6419-31.
128. Shim, H. and Z.L. Harris, *Genetic defects in copper metabolism*. J Nutr, 2003. **133**(5 Suppl 1): p. 1527S-31S.
129. Rubino, J.T. and K.J. Franz, *Coordination chemistry of copper proteins: how nature handles a toxic cargo for essential function*. J Inorg Biochem, 2012. **107**(1): p. 129-43.
130. Danielsson, J., et al., *Global structural motions from the strain of a single hydrogen bond*. Proc Natl Acad Sci U S A, 2013. **110**(10): p. 3829-34.

131. Redinbo, M.R., et al., *The 1.5-A crystal structure of plastocyanin from the green alga Chlamydomonas reinhardtii*. Biochemistry, 1993. **32**(40): p. 10560-7.
132. Koch, M., et al., *Crystal structures of oxidized and reduced stellacyanin from horseradish roots*. J Am Chem Soc, 2005. **127**(1): p. 158-66.
133. Morgan, C.R. and J.R. Engen, *Investigating solution-phase protein structure and dynamics by hydrogen exchange mass spectrometry*. Curr Protoc Protein Sci, 2009. **Chapter 17**: p. Unit 17 6 1-17.
134. Takehara, S., et al., *The 2.1-A crystal structure of native neuroserpin reveals unique structural elements that contribute to conformational instability*. J Mol Biol, 2009. **388**(1): p. 11-20.
135. Kaslik, G., et al., *Effects of serpin binding on the target proteinase: global stabilization, localized increased structural flexibility, and conserved hydrogen bonding at the active site*. Biochemistry, 1997. **36**(18): p. 5455-64.
136. Sarkar, A., et al., *Local conformational flexibility provides a basis for facile polymer formation in human neuroserpin*. Biophys J, 2011. **101**(7): p. 1758-65.
137. Zheng, X., P.L. Wintrode, and M.R. Chance, *Complementary structural mass spectrometry techniques reveal local dynamics in functionally important regions of a metastable serpin*. Structure, 2008. **16**(1): p. 38-51.
138. Bodker, J.S., et al., *Mapping of the epitope of a monoclonal antibody protecting plasminogen activator inhibitor-1 against inactivating agents*. Eur J Biochem, 2003. **270**(8): p. 1672-9.
139. Trelle, M.B., et al., *Dissecting the effect of RNA aptamer binding on the dynamics of plasminogen activator inhibitor 1 using hydrogen/deuterium exchange mass spectrometry*. ACS Chem Biol, 2014. **9**(1): p. 174-82.
140. Magyar, J.S. and H.A. Godwin, *Spectropotentiometric analysis of metal binding to structural zinc-binding sites: accounting quantitatively for pH and metal ion buffering effects*. Anal Biochem, 2003. **320**(1): p. 39-54.
141. Egelund, R., et al., *A regulatory hydrophobic area in the flexible joint region of plasminogen activator inhibitor-1, defined with fluorescent activity-neutralizing ligands. Ligand-induced serpin polymerization*. J Biol Chem, 2001. **276**(16): p. 13077-86.
142. Egelund, R., et al., *Type-1 plasminogen-activator inhibitor -- conformational differences between latent, active, reactive-centre-cleaved and plasminogen-activator-complexed forms, as probed by proteolytic susceptibility*. Eur J Biochem, 1997. **248**(3): p. 775-85.
143. Zhang, Y. and D.E. Wilcox, *Thermodynamic and spectroscopic study of Cu(II) and Ni(II) binding to bovine serum albumin*. J Biol Inorg Chem, 2002. **7**(3): p. 327-37.
144. Gogineni, D.P., A.M. Spuches, and C.S. Burns, *Calorimetric investigation of copper binding in the N-terminal region of the prion protein at low copper loading: evidence for an entropically favorable first binding event*. Inorg Chem, 2015. **54**(2): p. 441-7.
145. Sancho, E., et al., *Purification and characterization of active and stable recombinant plasminogen-activator inhibitor accumulated at high levels in Escherichia coli*. Eur J Biochem, 1994. **224**(1): p. 125-34.

Vita

Joel Bucci is originally from Tewksbury, Massachusetts. He grew up with his parents Mary Jane, and John, as well as younger brothers Jason, and Joseph. Joel enjoyed a public primary school education, attending the Dewing Elementary School, followed by the Wynn Middle School, and Tewksbury Memorial High School. Joel attended college at Merrimack College in North Andover, Massachusetts, where he graduated with a B.S. in Biochemistry. During his senior year, he worked on a senior project with Dr. Janine LeBlanc-Straceski that aimed to determine the expression location of specific myosin protein iosforms in developing *Xenopus laevis* embryos. Following a short stint in industry, Joel decided to pursue a graduate degree in Biochemistry in at the University of Tennessee. He chose to work under the mentorship of Dr. Cynthia B. Peterson, to investigate the metal ion effects on PAI-1 stability, which is the primary focus of this document. In his free time, Joel enjoys playing soccer, reading, hiking, camping, and traveling.